GOLD-COATED BLACK SILICON NANOSTRUCTURED SURFACES FOR SERS AND SALDI-MS MULTIMODAL IMAGING OF BIOLOGICAL APPLICATIONS

Stefania-Alexandra Iakab

ADVERTIMENT. L'accés als continguts d'aquesta tesi doctoral i la seva utilització ha de respectar els drets de la persona autora. Pot ser utilitzada per a consulta o estudi personal, així com en activitats o materials d'investigació i docència en els termes establerts a l'art. 32 del Text Refós de la Llei de Propietat Intel·lectual (RDL 1/1996). Per altres utilitzacions es requereix l'autorització prèvia i expressa de la persona autora. En qualsevol cas, en la utilització dels seus continguts caldrà indicar de forma clara el nom i cognoms de la persona autora i el títol de la tesi doctoral. No s'autoritza la seva reproducció o altres formes d'explotació efectuades amb finalitats de lucre ni la seva comunicació pública des d'un lloc aliè al servei TDX. Tampoc s'autoritza la presentació del seu contingut en una finestra o marc aliè a TDX (framing). Aquesta reserva de drets afecta tant als continguts de la tesi com als seus resums i índexs.

ADVERTENCIA. El acceso a los contenidos de esta tesis doctoral y su utilización debe respetar los derechos de la persona autora. Puede ser utilizada para consulta o estudio personal, así como en actividades o materiales de investigación y docencia en los términos establecidos en el art. 32 del Texto Refundido de la Ley de Propiedad Intelectual (RDL 1/1996). Para otros usos se requiere la autorización previa y expresa de la persona autora. En cualquier caso, en la utilización de sus contenidos se deberá indicar de forma clara el nombre y apellidos de la persona autora y el título de la tesis doctoral. No se autoriza su reproducción u otras formas de explotación efectuadas con fines lucrativos ni su comunicación pública desde un sitio ajeno al servicio TDR. Tampoco se autoriza la presentación de su contenido en una ventana o marco ajeno a TDR (framing). Esta reserva de derechos afecta tanto al contenido de la tesis como a sus resúmenes e índices.

WARNING. Access to the contents of this doctoral thesis and its use must respect the rights of the author. It can be used for reference or private study, as well as research and learning activities or materials in the terms established by the 32nd article of the Spanish Consolidated Copyright Act (RDL 1/1996). Express and previous authorization of the author is required for any other uses. In any case, when using its content, full name of the author and title of the thesis must be clearly indicated. Reproduction or other forms of for profit use or public communication from outside TDX service is not allowed. Presentation of its content in a window or frame external to TDX (framing) is not authorized either. These rights affect both the content of the thesis and its abstracts and indexes.

UNIVERSITAT ROVIRA I VIRGILI
GOLD-COATED BLACK SILICON NANOSTRUCTURED SURFACES FOR SERS AND SALDI-MS MULTIMODAL IMAGING OF BIOLOGICAL APPLICATIONS
Stefania-Alexandra Iakab

Stefania - Alexandra Iakab

UNIVERSITAT ROVIRA i VIRGILI

Gold-Coated Black Silicon Nanostructured Surfaces for SERS and SALDI-MS Multimodal Imaging of Biological Applications

Stefania - Alexandra Iakab

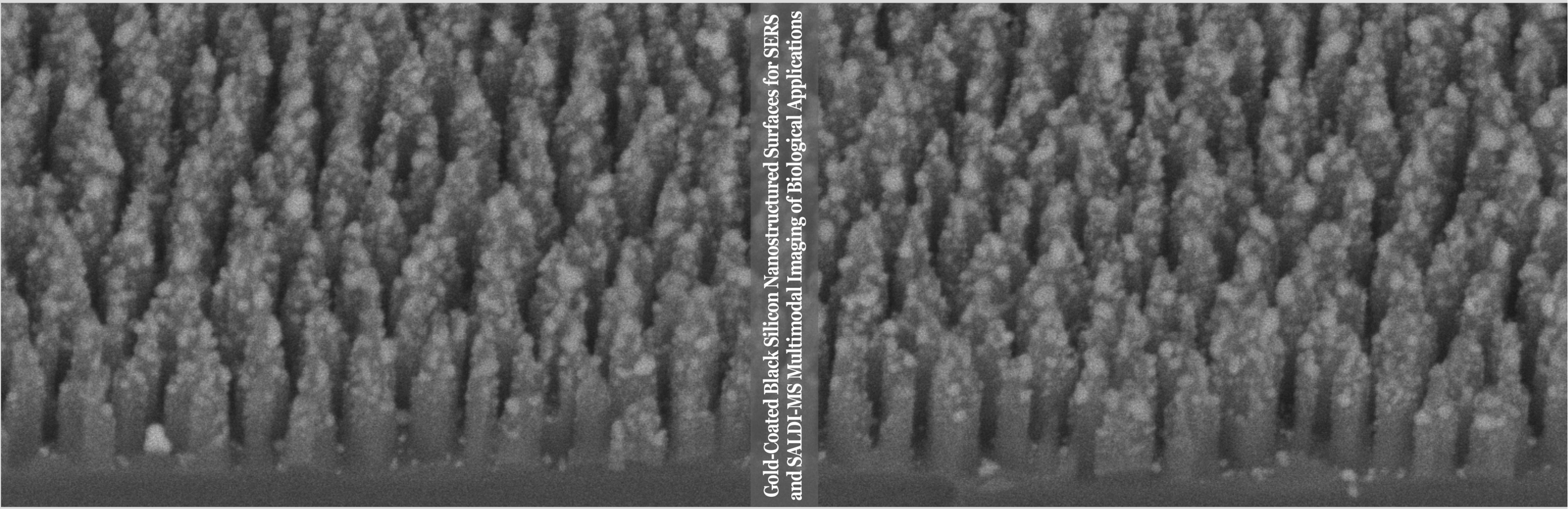

Gold-Coated Black Silicon Nanostructured Surfaces for SERS and SALDI-MS Multimodal Imaging of Biological Applications

UNIVERSITAT ROVIRA i VIRGILI

Doctoral Thesis 2021

Doctoral Thesis
2021

UNIVERSITAT ROVIRA I VIRGILI
GOLD-COATED BLACK SILICON NANOSTRUCTURED SURFACES FOR SERS AND SALDI-MS MULTIMODAL IMAGING OF BIOLOGICAL APPLICATIONS
Stefania-Alexandra Iakab

UNIVERSITAT ROVIRA I VIRGILI
GOLD-COATED BLACK SILICON NANOSTRUCTURED SURFACES FOR SERS AND SALDI-MS MULTIMODAL IMAGING OF BIOLOGICAL APPLICATIONS
Stefania-Alexandra Iakab

Stefania-Alexandra Iakab

Gold-Coated Black Silicon Nanostructured Surfaces for SERS and SALDI-MS Multimodal Imaging of Biological Applications

DOCTORAL THESIS

Supervised by Prof. Xavier Correig Blanchar and Dr. María García-Altares

Department of Electronic, Electric and Automatic Engineering

UNIVERSITAT ROVIRA i VIRGILI

Tarragona

2021

UNIVERSITAT ROVIRA I VIRGILI
GOLD-COATED BLACK SILICON NANOSTRUCTURED SURFACES FOR SERS AND SALDI-MS MULTIMODAL IMAGING OF BIOLOGICAL APPLICATIONS
Stefania-Alexandra Iakab

UNIVERSITAT
ROVIRA i VIRGILI

Escola Tècnica Superior d'Enginyeria
Departament d'Enginyeria Electrònica, Electrica i Automatica
Av. Paisos Catalans 26
Campus Sescelades
43007 Tarragona

We STATE that the present study, entitled "**Gold-Coated Black Silicon Nanostructured Surfaces for SERS and SALDI-MS Multimodal Imaging of Biological Applications**", presented by **Stefania-Alexandra Iakab** for the award of the degree of Doctor, has been carried out under or supervision at the Department of Electronic, Electric and Automatic Engineering of this university and meets the requirements to qualify for International Mention.

Tarragona, March 2021

Doctoral thesis supervisors:

Prof. Xavier Correig Blanchar

Dr. María García-Altares

UNIVERSITAT ROVIRA I VIRGILI
GOLD-COATED BLACK SILICON NANOSTRUCTURED SURFACES FOR SERS AND SALDI-MS MULTIMODAL IMAGING OF BIOLOGICAL APPLICATIONS
Stefania-Alexandra Iakab

ACKNOWLEDGEMENTS

This thesis is the fruit of many people's labour. Thanks to their patience and effort I was able to reach this point in my life which I was looking forward to for many years. For this reason, I would like to thank them:

Thank you to the greatest thesis supervisors I could have Xavier and Maria. Thank you, Xavier, for giving me the opportunity to work with your marvellous group, for giving me freedom in the lab and for supporting my ideas (good or bad). Thank you, Maria, for inspiring me every day, in the lab, the office or working from home and for teaching me how to navigate through the field of metabolomics imaging. You both have made my journey a memorable one.

Thank you to all the members of Mil@b. To my outstanding office mates Pere, Sonia, Carla, Gerard, Lluc, Laura, and ex-office mates Bea, Hamza, Dani, Pep, thank you for making me feel included in the group, for bearing with all my questions - research related or not-, for keeping English the official office language and for showing me how to respect the breakfast/coffee break mid-morning (I'm talking about you Sonia). Special thanks to Pere, Lluc and Gerard for all the informatics-related help, especially teaching me the R language and its terrific world. To Serena and Pineda, I would like to thank all the help with the complicated paperwork, without you I would not have been able to travel around the world in the name of science. Mariona, Noelia, Oscar, thank you for your ideas, feedback and support, you were the best "external supervisors".

I would like to thank all the technicians who showed me how to operate all kinds of expensive toys. From the SRCiT, I would like to acknowledge the help of Merce, Lukas, Eric, Rita, Mariana, and Sonia. Special thanks to Lukas for showing me the wonders of a clean room, which I already miss. From COS

I would like to thank Isabel and Elisabet for the training with the MALDI. From the DEEEA, thank you Jose for 3D printing my ideas. Thank you, Xavi and Miriam, for drawing for me with the inkjet printer. Of course, you never work alone in the lab, nor does the office stand alone in the building, so I would like to thank Miriam, Eric, Juan, Ernesto, Xavi, Mohamed, you were the best office neighbours and lab mates. Special thanks to Eric for also making me feel at home outside the lab, going out dancing was so much fun (pre-pandemic of course).

During my internship in Krakow, I had a fruitful and wonderful time thanks to a wonderful group of people: thank you Malgosia and Kamilla for hosting me and to your group members for welcoming me, especially Karolina and Ewelina W.

Four years of PhD have taught me a lot about research but also about cherishing the people who support you from near and far. Christi, Timi, Laura, Rebeca, Karina, Irene, Trudi, Ander, thank you for diminishing my homesickness whether it was through video calls, weekend getaways or visiting the beautiful town of Tarragona. Special thanks to Ander for bringing me home-made goodies (and not only) when in dire need.

Last but not least, without the support of my family I would never have been able to write this thesis. Tati, you were the one who inspired me to pursue a career in science and I thank you for that. Mami, you were there for me whenever I needed a recipe, instructions for how to wash my clothes but also when I had a bad day far from home, so thank you for always supporting me. To my brother Isti and all my dear grandparents, thank you for your never-ending questions about my work - which I'm sure I still did not clarify - you made me realize how far I had come but also how I should appreciate the simple things in life. And finally, I am thanking my two cats, Lucifer and Pit, for the emotional support throughout these years.

UNIVERSITAT ROVIRA I VIRGILI
GOLD-COATED BLACK SILICON NANOSTRUCTURED SURFACES FOR SERS AND SALDI-MS MULTIMODAL IMAGING OF BIOLOGICAL APPLICATIONS
Stefania-Alexandra Iakab

UNIVERSITAT ROVIRA I VIRGILI
GOLD-COATED BLACK SILICON NANOSTRUCTURED SURFACES FOR SERS AND SALDI-MS MULTIMODAL IMAGING OF BIOLOGICAL APPLICATIONS
Stefania-Alexandra Iakab

"*Simplicity is the ultimate sophistication.*"

Leonardo da Vinci

UNIVERSITAT ROVIRA I VIRGILI
GOLD-COATED BLACK SILICON NANOSTRUCTURED SURFACES FOR SERS AND SALDI-MS MULTIMODAL IMAGING OF BIOLOGICAL APPLICATIONS
Stefania-Alexandra Iakab

ABSTRACT

Understanding the fundamentals of biological processes is imperative for advancements in diagnostics and therapeutics. Molecular imaging is an indispensable tool for shedding light not only on morphological and anatomical details of biological samples (of plant, animal and human origin), but also on the *in situ* characterization of their molecular composition. Label-free imaging modalities such as mass spectrometry imaging and Raman spectroscopy imaging are some of the most common methods employed in basic research. However, these methods have drawbacks: Raman imaging is limited by low sensitivity and specificity, while mass spectrometry imaging is limited by low lateral resolution and ionization yield. Nanostructured materials are often used for addressing these challenges, but the majority of applications still lack reproducibility and are limited to targeted analyses. Multimodal imaging strategies employing mass spectrometry imaging (MSI) and Raman imaging are currently on demand, but they do not use the same substrate, enhancing agents nor the same data format which complicates sample preparation, data analysis and image coregistration.

The aim of this thesis was to design, fabricate, evaluate and apply a gold- and silicon-based nanostructured substrate compatible with surface-assisted laser desorption/ionization mass spectrometry imaging (SALDI-MSI) and surface-enhanced Raman spectroscopy (SERS) imaging applications. Our nanostructure fabrication strategy relies exclusively on dry etching methods (reactive ion etching and sputtering) because they provide reproducible, user-friendly, cost effective, highly reliable and contaminant free substrates. The substrate created resembles a nano-asparagus forest structure and it is made of biocompatible nanomaterials: gold nanoparticles decorating a silicon nanopillar array, also known as black silicon, thus the substrate received the name “AuBSi". The AuBSi substrate possesses the optimal

physico-chemical properties for enhancing the Raman signal and promoting laser desorption/ionization, as demonstrated by scanning electron and atomic force microscopy, contact angle measurements, and UV-vis spectroscopy. It has large surface area, sufficient mechanical stability, and stable hydrophobic properties. Moreover, it absorbs most of the visible light (>95%), and the gold nanoparticles permit surface modification methods such as thiol-terminated oligonucleotides, aptamers, and ethylene glycol for improved selectivity of various biomolecules.

The AuBSi substrate is compatible with SALDI-MSI. Standard solutions and fingermarks were deposited onto the sample by contact, while mouse liver, kidney and brain tissues were imprinted. This is a sample preparation method that allows efficient transference of metabolites from the tissues to the substrate surface, without compound delocalization. All samples measured from the AuBSi substrate were characterized by high quality ion images. Furthermore, the AuBSi surface chemistry was modified using hydrophobic and hydrophilic plasma treatments, which stimulated specific interactions between surface and sample, leading to a selective analysis of molecules. For example, we could selectively detect lipids and nonpolar lipids (e.g. wax esters) from fingermarks using the hydrophobic-AuBSi, and lactic acid using the hydrophilic-AuBSi.

The AuBSi substrate is also compatible with SERS imaging. Imaging measurements of Raman reporter solutions of various concentrations demonstrated the AuBSi surface homogeneity at the micron scale, which enables imaging fine morphological details. The AuBSi substrate's analytical enhancement factor is in the order of 105, attributed to the synergy of several phenomena: the effective adsorption of molecules to the surface, the high absorption of the laser energy by the black silicon and the presence of Au nanoparticles which lead to enhanced electromagnetic fields. For example,

using AubSi the intensity of rhodamine 6G signal was linearly correlated with its concentrations between micromolar and millimolar concentrations.

Since the AuBSi substrate can be used in SALDI-MS and SERS imaging, we integrated both modalities. Our multimodal approach uses the same substrate, sample preparation and data analysis software on the same sample, allowing the coregisteration of both images - linking two types of spectra to the same spatial location. We used clean and stained fingermarks to demonstrate our approach. For straightforward data analysis of the obtained orthogonal information, we developed a Raman imaging data converter, which converts .txt files into imzML, the standard format for MSI. Therefore, we used a single software for image coregistration and univariate and multivariate data analysis to gain chemical information of residues adhered to fingerprints.

In conclusion, the gold-coated black silicon substrate can be used to measure liquids, tissues and fingerprints with both SALDI and SERS imaging, while dealing with the challenges of each technique independently. Our substrate and Raman image data converter encourage multimodal imaging, as coregistration of images from the same sample and substrate is straightforward. The multimodal approach developed in this thesis facilitates targeted and/or untargeted in situ metabolomics studies for various fields such as clinical, environmental, forensics, and pharmaceutical research.

UNIVERSITAT ROVIRA I VIRGILI
GOLD-COATED BLACK SILICON NANOSTRUCTURED SURFACES FOR SERS AND SALDI-MS MULTIMODAL IMAGING OF BIOLOGICAL APPLICATIONS
Stefania-Alexandra Iakab

Table of Contents

UNIVERSITAT ROVIRA I VIRGILI
GOLD-COATED BLACK SILICON NANOSTRUCTURED SURFACES FOR SERS AND SALDI-MS MULTIMODAL IMAGING OF BIOLOGICAL APPLICATIONS
Stefania-Alexandra Iakab

CHAPTER 1: Introduction

UNIVERSITAT ROVIRA I VIRGILI
GOLD-COATED BLACK SILICON NANOSTRUCTURED SURFACES FOR SERS AND SALDI-MS MULTIMODAL IMAGING OF BIOLOGICAL APPLICATIONS
Stefania-Alexandra Iakab

1.1. Context

The research presented in this thesis was carried out between January 2017 and March 2021 in the Metabolomics Interdisciplinary Laboratory (MiL@b) group. MiL@b is a research group of the Department of Electronic, Electrical and Automation Engineering (DEEEA) at the Rovira i Virgili University (URV). The MiL@b group is also a part of the Metabolomics Platform from the Pere Virgili Health Research Institute (IISPV) and the Center for Biomedical Research Network on Diabetes and Associated Metabolic Diseases (CIBERDEM).

The research for this thesis was sponsored by the Spanish Ministry of Science Innovation and Universities within the projects: “Development of nanosurfaces and signal processing algorithms for the obtention and treatment of metabolic images by Laser Desorption Ionization Mass Spectrometry (LDI-MS)” TEC2015-69076-P and “Development of new molecular histology technologies based on imaging spectroscopy and its application to the study of cancer and diabetes” RTI2018-096061-B-I00. In the first project, this research focused on designing and developing nanostructured surfaces for obtaining enhanced metabolic images by Laser Desorption Ionization Mass Spectrometry (LDI-MS), and in the second project, it aimed for advancing the use of Au-functionalized black silicon surfaces for molecular imaging applications across several imaging techniques: vibrational spectroscopy and mass spectrometry imaging. Our research group is specialized in developing and optimizing both experimental and data processing workflows for spatial metabolomics data.

This thesis is the first one carried out in the MiL@b group in the field of nanotechnology for multimodal label-free molecular imaging applications. The main goal was to develop a novel nanostructured substrate which allows

mapping the molecular context of biological tissue sections with Mass Spectrometry and Raman imaging. As our group is specialized in MSI, a three-month long research internship (September – December 2019) was carried out at the Raman Imaging Group from the Faculty of Chemistry of the Jagiellonian University of Krakow, under the guidance of Prof. Kamilla Malek. The group specializes in developing spectroscopic methodology for the diagnosis of lifestyle diseases which includes the design of Surface-Enhanced Raman Spectroscopy (SERS) nanosensors. The internship focused on two goals: (1) mastering the experimental part of collecting Raman images from biological samples, including the use of nanostructured substrates, and (2) mastering chemometrics approaches for Raman imaging data analysis.

During this thesis other short-term collaborations have been carried out. The collaboration with the group of Prof. Pilar Pina at the Institute of Nanoscience of Aragon from Zaragoza was essential for establishing that the nanostructured surface developed in this thesis is suitable for SERS measurements, and included experimental activities: fabrication of gold nanoparticles through wet chemistry methods, evaluation of AuBSi for Raman measurements and nanostructure characterization using FIB-SEM. This evaluation was done in comparison with the substrate developed during the thesis. The collaboration with the group of Prof. Eduard Llobet from the Department of Electric Engineering of the Rovira i Virgili involved technical support for using the inkjet printer as reflected in Chapter 4.

The work carried out in this thesis has been published in 3 international journals and presented at 6 national and international scientific meetings, as listed in section 1.6.

1.2. Label-free molecular imaging methods

1.2.1. Classical histopathology techniques

Histopathology is the standard technique used for characterizing biological tissues for clinical applications. It is based on the optical microscopy images acquired from formalin fixed and paraffin embedded (FFPE) tissues. The tissues are stained to create a better contrast for light microscopy in order to characterize the anatomy, or the morphology of specific parts of an organism.[1] Immunohistochemistry employs special staining solutions, which target certain molecules within tissues and create a specific colour or contrast in the histopathological image.[2] Specifically, chromogenic (mediated by an enzyme) or fluorescent dyes are binding the molecules in tissues by antigen-antibody interactions. Once the target antigen in a tissue is determined, the antibody is created and labelled with a chromogenic or fluorescent molecule. This protocol enables the characterization of both morphology and composition but, once the tissue is stained, it cannot be used for any other kind of measurement.[3]

Pathologists are experts in differentiating healthy from diseased regions, with the ability to recognize several stages of disease based only on morphological architecture and colouring. Unfortunately, histopathology is made difficult by the variety of fixation and staining protocols, which have to be chosen carefully for each type of tissue, and it is limited to visual (or optical) information exclusively. For example, there is no standard staining protocol to study neurons and the currently available methods are not specific, reproducible, nor stable over time, and might modify sample morphology.[4] Also, the possibility of human error, which is always a variable in any experiment, can result in flawed interpretation. In fact, there are insufficient trained pathologists to support both hospital laboratories and

research groups,[5] restricting the latter to opt for interpretations from pathologists with limited training and experience.

1.2.2. Imaging in the clinics

In vivo imaging methods used in the clinical environment to characterize anatomical or molecular features include a wide range of techniques: positron emission tomography (PET), computed tomography (CT), single photon emission CT (SPECT), magnetic resonance imaging (MRI), ultrasound (US) or optical imaging.[6] All these techniques need a contrasting agent to obtain relevant images: CT, PET and SPECT use radioactive isotopes (*e.g.*^{123}I, ^{18}F, ^{68}Ga, ^{99m}Tc, ^{111}In), MRI needs iron or manganese oxide nanoparticles, US uses contrast microbubbles and optical imaging needs fluorescent molecules, dyes or light absorbing nanoparticles. The majority of the contrasting agents are expensive, cannot be applied for all kinds of tissues (soft *vs.* hard tissues), can be harmful to the patient in higher dosage, and cannot detect non targeted molecular information. That is why methods that allow detection of multiple biomolecules with both *in vivo* and *ex vivo* modalities are in high demand.

1.2.3. Label free imaging techniques

With the discovery of lasers and laser-based spectroscopy techniques, more complex molecular imaging approaches have emerged such as mass spectrometry imaging (MSI) and vibrational spectroscopy imaging (VSI). These techniques are label-free, as they do not employ synthetic molecules or contrast agents to target biomolecules or tissues, but they rely on some specific interactions between laser light and biomolecules.

1.2.3.1. Mass Spectrometry Imaging

MSI is a key tool in proteomics, lipidomics and metabolomics studies as it is highly specific.[7] For this reason, it is frequently used in various fields: pharmaceutics,[8] clinics,[9] forensics,[10] microbiology[11] and plant biology.[12] The most popular MSI techniques are matrix-assisted laser desorption/ionization (MALDI), surface-assisted laser desorption/ionization (SALDI), desorption electrospray ionization (DESI), laser ablation inductively coupled plasma (LA-ICP) and secondary ion mass spectrometry (SIMS).[13]

The typical SALDI-MSI experiment workflow consists of sample sectioning, sample mounting on a substrate (generally indium tin oxide (ITO) coated glass slides), nanomaterial deposition over the sample section (through wet or dry methods), image acquisition, spectra pre-processing and data analysis.[14] This workflow is illustrated in Figure 1.

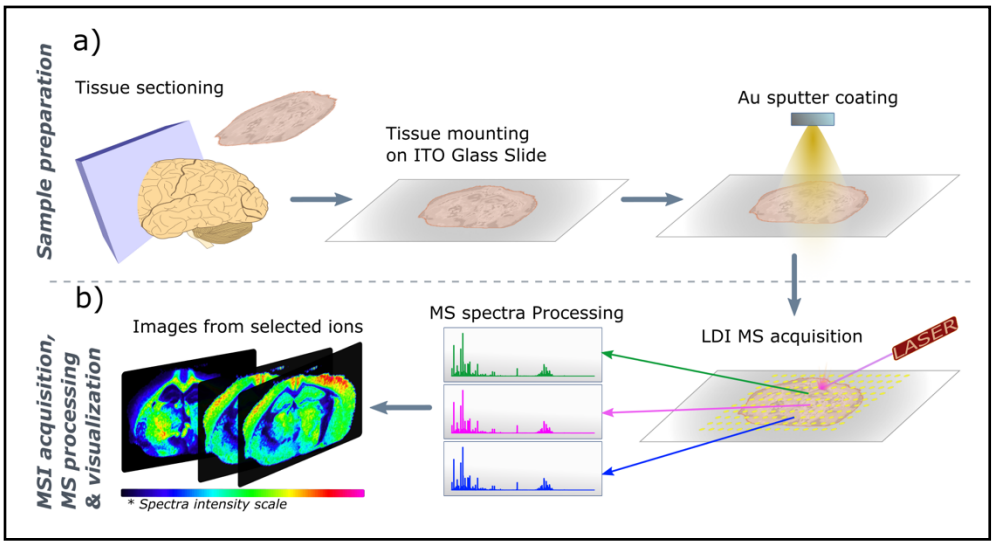

Figure 1. SALDI-MSI imaging workflow. Reprinted with permission from Rafols et. al.[14] Copyright © 2018 Ràfols et al.

Fundamentals

In mass spectrometry each ionized molecule is detected as a mass-to-charge ratio (*m/z*) and then represented in a mass spectrum. In mass spectrometry imaging, each pixel over an area is represented by a spectrum, and a data cube of pixel position and spectral information (mass spectra spatially correlated with sample morphology) is generated. With this kind of dataset, the position of each *m/z* can be represented as a map of intensities. Each MSI technique has a different approach to ionizing molecules (illustrated in Figure 2). MALDI, SALDI and LA-ICP employ a UV laser to desorb and ionize the molecules from the surface, but the ionization is different for each technique: MALDI uses organic matrices,[15] SALDI uses nanostructured materials[16] and LA-ICP uses an inductively coupled plasma.[17] DESI employs an electrospray to remove molecules from the sample surface[18] while SIMS relies on a collimated ion beam to remove the analytes from the sample surface.[19]

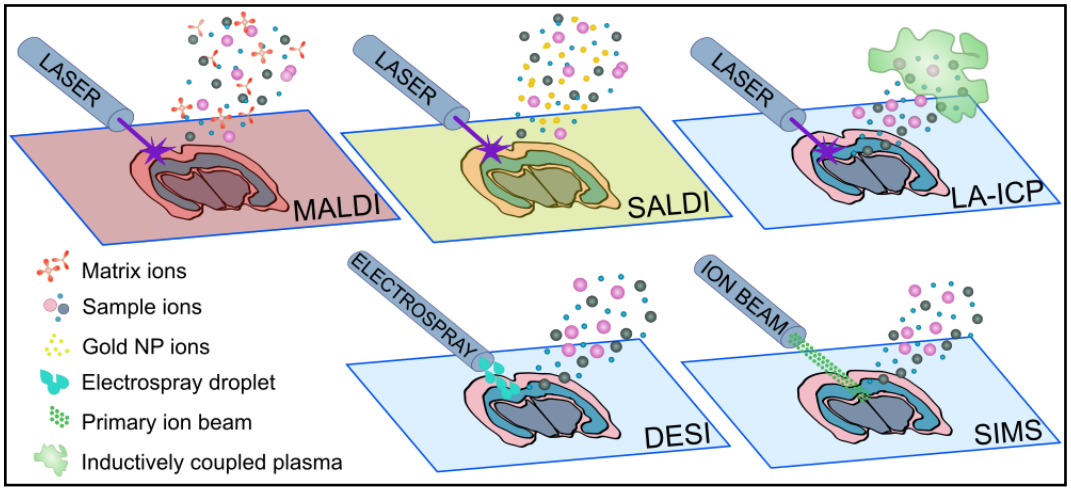

Figure 2. Schematic illustration of different ionization mechanisms used in MSI.

Characteristics

MSI provides abundant high-quality biological information regarding molecular composition and distribution. The chemical information obtained from biological tissues encompasses all classes of biomolecules: small metabolites, medium-sized molecules such as lipids, and large biomolecules such as proteins and polymers, and also biologically relevant elements (in the case of SIMS). MSI techniques are highly specific: depending on the mass analyser (Time of flight - TOF, Orbitrap or Fourier transform ion cyclotron resonance - FTICR, *etc.*), the spectral resolution can offer mass accuracy better than 1 ppm (accurate to four decimal places) and so can identify ions – single or multiple charged isotopes, adducts and fragments – by their mass-to-charge ratio.[20] For accurate identification, especially in untargeted studies, tandem MS (MS/MS) analysis is often used.[13] However, MS cannot identify molecules with the same molecular weight, such as isomers and enantiomers, and is not suitable for analysing neutral molecules or the secondary structure of proteins. The typical lateral resolution in MSI for imaging biological tissues starts from 10-20 μm, but, depending on the technique, can be as low as 0.02 μm (in the case of SIMS).[13]

Despite being such powerful tools, these techniques have some limitations. Generally, MSI instruments are expensive, they require vacuum-compatible samples (except for DESI), the mass range detection is limited (depending on the type of ionization - hard *vs.* soft ionization), and some methods are constrained to reduced lateral resolution (10 μm for MALDI and 40 μm for DESI due to heterogeneous co-crystallization, analyte delocalization, the spray tip-to-surface distance, and the spray tip and nebulizer orifice diameters).[20–23] Lastly, the MSI data collected demands large storage capabilities and powerful computational tools for data preprocessing and analysis.

Sample preparation

Sample preparation is a critical step for any imaging technique. Normally biological samples for mass spectrometry imaging are fresh-frozen tissues[15] although some applications have reported the use of paraffin embedded tissues.[24,25] The typical sample processing before analysis consists of: tissue sectioning, tissue section handling, choosing the right ionization agent and solvent, deposition of the ionization agent, sample transportation and storage.[20] Sometimes, extra steps are included, such as deparaffinization or other specific tissue treatments (*e.g.* on-tissue washes, enzymatic digestion, chemical derivatization, *etc.*) when necessary.[20]

Data acquisition

The typical MS image measurement starts with the selection and optimization of the acquisition parameters such as mass range, mass resolution, laser power, laser spot size, number of shots per pixel, pixel size, and area of acquisition, but it also includes mass analyser calibration. Optimizing acquisition parameters is crucial for a successful experiment, as the sensitivity of MSI depends strongly on lateral resolution and ionization efficiency while sample viability can suffer during long experiments.[13] To avoid the acquisition of big datasets in the range of tens to hundreds of gigabytes, all parameters should be optimized to preserve the image quality while also minimizing data size: fewer pixels, precise area of measurement, reduced mass range, *etc.*

Data analysis

The raw data collected from MSI studies goes through several preprocessing algorithms to ensure high quality MS images and optimal statistical analysis. Usually, MSI data consists of a large volume of mass

spectra that presents experimental variability – such as chemical noise and mass spectra shifts – due to sample preparation and small changes during image acquisition. Preprocessing algorithms improve image reconstruction and spectral quality. Rafols *et al.* described in great detail each step in the general pipeline of preprocessing MSI data.[14] After preprocessing, the data is usually analysed first by the univariate analysis – or simply spatial visualization – of one specific peak (or ion), and then by more sophisticated analysis such as supervised or unsupervised multivariate analysis. Rafols *et al.* outlined all aspects necessary for powerful bioinformatics tools reviewing data handling strategies with both commercial and open-source software.[14] Fortunately the mass spectrometry imaging community developed a common data format called imzML,[26] which facilitates progress in MSI processing algorithms, as well as inter-laboratory collaborations in which instruments are not from the same manufacturer.[27]

Nanomaterials for MSI

In spite of its popularity, MSI has some challenges. For example, standard spatial metabolomics studies such as MALDI and DESI are limited either by complicated sample preparation, low sensitivity for small molecules, cluttered spectra due to the presence of matrices, and/or low spatial resolution.[23] To this end, nanostructured materials have been employed to enhance the detection of small molecules, to collect better signals and to enable mapping at increased spatial resolution.[28–30] Nanostructures present advantages such as reproducibility, reliability, low cost, easy fabrication, and the possibility to be functionalized for targeted analysis. Silicon, carbon and carbon-derivative materials, and metal nanoparticles (TiO_2, Fe_2O_3, Au, Ag, Pt, *etc.*) are common choices for LDI-MSI applications.[31] For example, matrix-free LDI uses AuNPs as an alternative to organic matrices because they promote ionization, produce clean spectra and permit higher resolution

images.[14] Other nanomaterial-based MSI methods are surface-assisted laser desorption ionization (SALDI),[16,32] desorption ionization on silicon (DIOS)[33] and nanostructure-initiator mass spectrometry (NIMS)[29] in which the ionization is supported by nanostructured materials, porous silicon, and molecules trapped in nanostructured surfaces, respectively.

1.2.3.2. Vibrational Spectroscopy Imaging

Vibrational spectroscopy techniques are highly popular choices in the fields of pharmaceuticals, biomedicine and threat-detection of dangerous molecules.[34] They rely on detecting spectral irregularities within tissues that stray from the typical patterns. Therefore, anomalies such as cancerous tissue, different stages of disease, drugs, contaminants or illegal substances show very distinct spectral features compared to the inherent tissue or sample. The most popularly used VSI techniques are Raman, surface-enhanced Raman spectroscopy (SERS), infrared (IR), Fourier-transform IR (FTIR) and attenuated total reflection FTIR (ATR-FTIR) spectroscopy.[23] The typical VSI imaging experiment workflow consists of mounting the sample on a low-fluorescence substrate, image acquisition and data processing. For example, the SERS imaging workflow described in Figure 3 contains an additional sample preparation step which incorporates the enhancing agent (in this case AuNPs) into the sample.

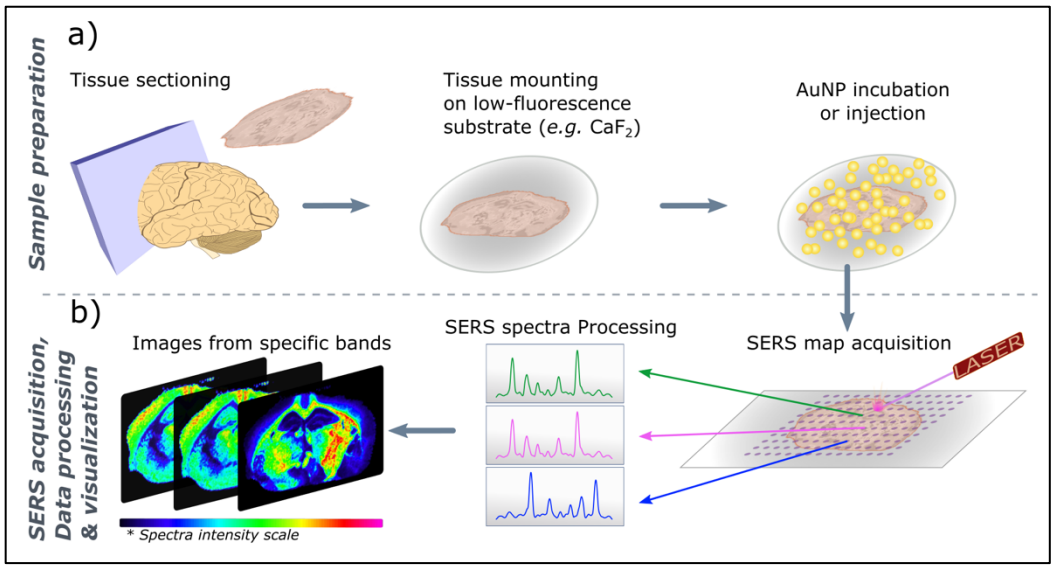

Figure 3. SERS imaging workflow example. Adapted from Rafols et al.[14]

Fundamentals

Vibrational spectroscopy is based on light interacting with molecules from a sample. Specifically, the recorded spectrum represents a collection of the molecular vibrations of chemical bonds from all molecules within the illuminated area.[35] This information gives the fingerprint signature of the sample. For Raman spectroscopy, the incident light of a fixed wavelength interacts with the sample and the frequency-shifted scattered light is detected and represented in the Raman shift spectrum;[36] for IR/FTIR spectroscopy the incident light is absorbed by the sample and the transmitted (or reflected) light is detected, resulting in a spectrum of absorption (illustrated in Figure 4).[37] Just as for MSI, each pixel of an area of the sample is represented by a single spectrum, while the full image contains a data cube of pixel position and spectral information.

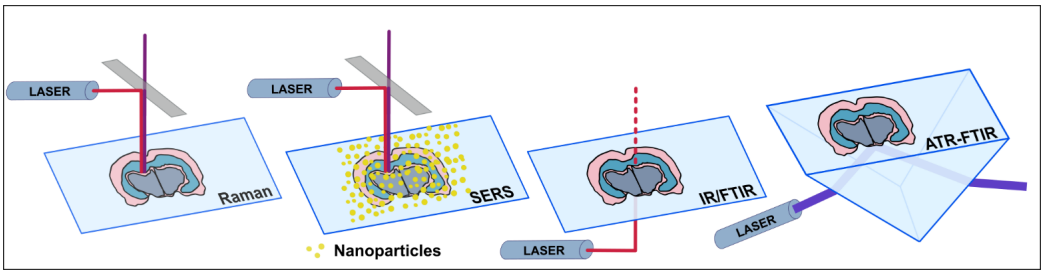

Figure 4. Vibrational spectroscopy methods

Characteristics

Raman and IR spectroscopy describe the physical and chemical properties of molecules by collecting signals that represent the stretching, bending and rotating vibrations of their chemical bonds. Vibrational spectroscopy is label-free and non-destructive, enabling imaging with lateral resolutions from several mm (for mid-IR) to below 1 μm (for Raman). Hence, Raman can be used for single-cell and intracellular imaging[38] while IR is employed for imaging larger areas on tissues.[39] The resulting spectral information gives valuable insights into tissue organization, secondary structure of molecules, lipid and protein content, cell metabolism, drug delivery and even *in vivo* prediction of diseases in clinical research. This information is typically obtained from the strong vibrations of specific bonds: for example, lipid droplets and the myelin sheath of neurons are represented by CH_2 vibrations of lipids and CH_3 vibrations of proteins, respectively.[40,41] The lateral resolution in vibrational spectroscopy depends on the optical configuration of the microscope (objective numerical aperture, NA) and the incident laser wavelength (λ), following the laws of physics and optics: spatial resolution = 0.61 λ / NA.[42] Therefore, submicron lateral resolution is easily accessible for various combinations of laser wavelengths and objectives. However, VSI techniques have some limitations. Raman has low sensitivity, due to its lack of signal strength (*ca.* 1 scattered photon in 10^9 incident photons) and low

chemical specificity.[23] IR techniques present strong interference from water absorption, which hampers data acquisition and analysis.[38]

Sample preparation

Raman samples can be either liquids or solids: fresh frozen (*e.g.* tissues) or immersed in liquid (*e.g.* cell cultures in aqueous media). Frozen samples follow a similar procedure to MSI: tissue sectioning, tissue section handling, optional deparaffinization or other specific treatments, transportation and sample storage. Tissue sections are typically placed on calcium fluoride slides because their low refractive index and absorption mean that their natural fluorescence is also low.[43] The case of live samples (such as cell cultures) requires an immersion objective that permits live-cell analysis in real time.[44,45] On the other hand, IR imaging samples are usually solid (*e.g.* tissue sections[24,25,46,47]) and they need to be placed on transparent slides with low absorption in the IR range, such as IR-reflecting microscope slides or calcium fluoride windows. Sample preparation for vibrational spectroscopy can be as simple as choosing the sample substrate that does not interfere with the sample signals.

Data acquisition

Raman image acquisition parameters strongly depend on the optical configuration of the microscope and the lasers used with the instrument. Laser parameters (wavelength, power, spot shape, *etc.*), the objective's numerical aperture, the type of measurement (in air or immersed in liquid), the spectral grating (for spectral resolution), and the exposure time are the typical acquisition parameters that need to be optimized for spectroscopy measurements. Due to the weakness of Raman scattering and the intrinsic fluorescence of biological samples, the laser wavelength and the objective have to be chosen properly for each experiment so that the spot size, laser

power and exposure time provide the best Raman signal without "burning" the samples.[48] Autofluorescence can be reduced by photobleaching[49] and high resolution images can be achieved with small laser spot sizes (<1μm). Unfortunately, these conditions together with high laser power damage samples by the localized heat induced on the sample surface. For IR measurements – in transmission, transflection and ATR modes – the spatial resolution depends on the configuration of the IR instrument (single aperture resolution $2\lambda/3$ and confocal arrangement resolution $\lambda/2$ [50] and on measuring the right background signal. IR spectroscopy is sensitive to substrate transparency (in transmission mode), sample thickness, and water content. In biological samples such as tissue sections, the water content is reflected in the spectra by the OH band.[51] IR measurements are mostly held in atmospheric environments, so sample viability over time is also an issue, which is why both Raman and IR spectroscopy seek substrates that allow the temperature to be controlled.

Data analysis

Data analysis for spectroscopic datasets consists of a pre-processing step that prepares the Raman and IR data for analysis.[51] Lasch described in detail the aims of signal pre-processing for both IR and Raman data: (i) robust and accurate spectra; (ii) comprehensible data for both humans and machines; (iii) outlier and trend removal and (iv) dimensionality reduction.[51] Similarly, Vidal et. al highlighted the importance of first removing background, dead pixels, spikes and outliers and then pre-processing the remaining spectral data.[52] This approach eliminates all the unwanted effects during acquisition that are both intrinsic (*e.g.* autofluorescence, cell media or water content, substrate, *etc.*) and extrinsic (*e.g.* detector noise, calibration errors, cosmic rays, laser power fluctuations, *etc.*). Gautam *et al.* described all the shared pre-processing algorithms between Raman and IR data: background

correction (or baseline removal), smoothing, normalization and outlier removal.[53] However, some data processing steps are specific for each type of data: Raman imaging spectra need to be aligned through wavelength calibration and cleaned of cosmic ray artifacts; IR spectra need to pass a quality test, undergo water vapor correction and finally go through a first or second derivative filter for interpretation.[52] Data processing usually consists of univariate analysis in which the spatial visualization of one specific band generates a heatmap, and then of supervised or unsupervised multivariate analysis which finds important structural information, image segmentation, and tissue classification.[53] Unfortunately, unlike for MSI data, there is no standard or common file format for VSI data storage and processing.

Nanostructures for Raman

Raman spectroscopy lacks signal strength and specificity which lead to the development of SERS.[54] SERS uses nanostructured materials such as silver and gold nanoparticles (NPs) to enhance the Raman signal through electromagnetic and chemical enhancement[55] without introducing interference. Additionally, Au and Ag NPs are popular choices in SERS, due to their surface plasmon resonance properties, biocompatibility, stability, and surface binding properties, which allows the functionalization of the nanoparticle surface for targeted analysis. For example, AuNPs were used to monitor through SERS imaging the intracellular exosome uptake.[56] Unfortunately, SERS is strongly dependent on the nanostructured substrate which implies reduced spot-to-spot homogeneity. This limits reproducible imaging experiments.[23]

UNIVERSITAT ROVIRA I VIRGILI
GOLD-COATED BLACK SILICON NANOSTRUCTURED SURFACES FOR SERS AND SALDI-MS MULTIMODAL IMAGING OF BIOLOGICAL APPLICATIONS
Stefania-Alexandra Iakab

1.3. Motivation and objectives

This thesis aims at exploiting the symbiosis between non-labelled MSI and VSI techniques for the analysis of biological tissues. The final goal of the thesis is to provide a solution that ensures compatibility of surface-assisted laser desorption/ionization (SALDI) and surface-enhanced Raman spectroscopy (SERS) imaging applications on the same sample at each stage of the analysis, from sample preparation to data analysis. This goal is accomplished by following four specific objectives:

Objective 1: To design, fabricate and characterize a nanostructured substrate based on black silicon and gold nanoparticles compatible with both SALDI-MS and SERS imaging of biological samples

Since SALDI-MS and SERS imaging use nanomaterials to enhance the signal of biological samples, the first objective of the thesis focuses on designing, fabricating and characterizing a silicon-based nanostructured surface decorated with Au nanoparticles, which promote desorption/ionization processes in mass spectrometry imaging and enhance the Raman signal in vibrational spectroscopy. This novel substrate has to be reproducible, user-friendly, cost effective, highly reliable and contaminant free to ensure successful imaging experiments. Thus, the nano-substrate geometry and physicochemical properties have to be tailored for collecting optimal MS and Raman signals.

Objective 2: To obtain SALDI-MS images of biological samples using the nanostructured substrate and to implement data processing methods

The second objective focuses on obtaining molecular images using the nanostructured substrate in SALDI-MSI. This includes: optimizing the sample preparation for liquids and solids (*e.g.* immersion and spotting for

solutions, and imprinting for animal tissues and fingermarks, *etc.*), evaluating the reproducibility of the acquisition and the reliability of the surface properties. It also includes the optimization of acquisition parameters for imaging (*e.g.* laser power, spot size, mass range, no-to-low fragmentation, *etc.*). MSI data analysis procedures - such as univariate and multivariate processing - have to be implemented, aiming to extract maximum information. For this, open-source tools developed in our research group will be employed.

Objective 3: To collect optimal SERS images using the nanostructured substrate and to implement data analysis methods

The third objective focuses on evaluating the performance of the nanostructured substrate for SERS imaging. This includes: evaluating the reproducibility of imaging measurements, the reliability of the subtrate's surface properties (*e.g.* submicron homogeneity, laser absorption, nanostructure enhancing properties) and the simplicity of the sample preparation methods for liquids and solids (*e.g.* solutions, fingermarks, *etc.*). It also includes the optimization of acquisition parameters for imaging (*e.g.* type of laser, laser power, exposure time, *etc.*). SERS imaging data analysis will include pre-processing methods (cosmic ray removal, baseline subtraction, smoothing, *etc.*) and univariate and multivariate (*e.g.* principal component analysis, clustering, *etc.*) approaches.

Objective 4: To develop a multimodal imaging workflow

The fourth objective is to obtain molecular images using a multimodal strategy based on the nanostructured substrate. The aim is to (1) combine the two complementary imaging techniques (SALDI-MS and SERS) in a synergistic manner by measuring the same sample from the same substrate, and to collect the complete information regarding morphology and chemical

composition; and (2) implement computational solutions to visualize and analyze both SALDI and SERS imaging data using the same open-source software. Multimodal data analysis strategies - such as image registration - will be assessed and implemented.

1.4. Thesis outline and development

The thesis is divided into five chapters (timeline represented in Figure 5). The first chapter *Introduction* describes the environment in which the thesis was developed (funding, collaborations, internships *etc.*) and the academic drive (background, motivation and objectives) of the thesis. The second chapter *State-of-the-art of Nanostructured surfaces for SALDI-MS and SERS imaging applications* includes two review papers which summarize the latest findings in the fields of nanomaterials used for singular and multimodal imaging of MSI and VSI. The third chapter *Gold Nanoparticle-Assisted Black Silicon Substrates for Mass Spectrometry Imaging Applications* encompasses the first two objectives of the thesis by fabricating and evaluating the gold-coated black silicon substrates for SALDI-MSI applications. The fourth chapter *Gold Nanoparticle-Assisted Black Silicon Substrates and Data Converters for Multimodal Imaging* focuses on the development of a multimodal imaging platform combining SALDI MSI and SERS imaging with the help of the nanostructured substrate and it is strongly related to objectives three and four. The fifth chapter *Discussion, Conclusions and Perspectives* discusses the main findings of the research carried out in this thesis, focusing on the impact on the field of multimodal imaging combining SALDI and SERS imaging; it includes the main conclusions of the thesis and their associated perspectives.

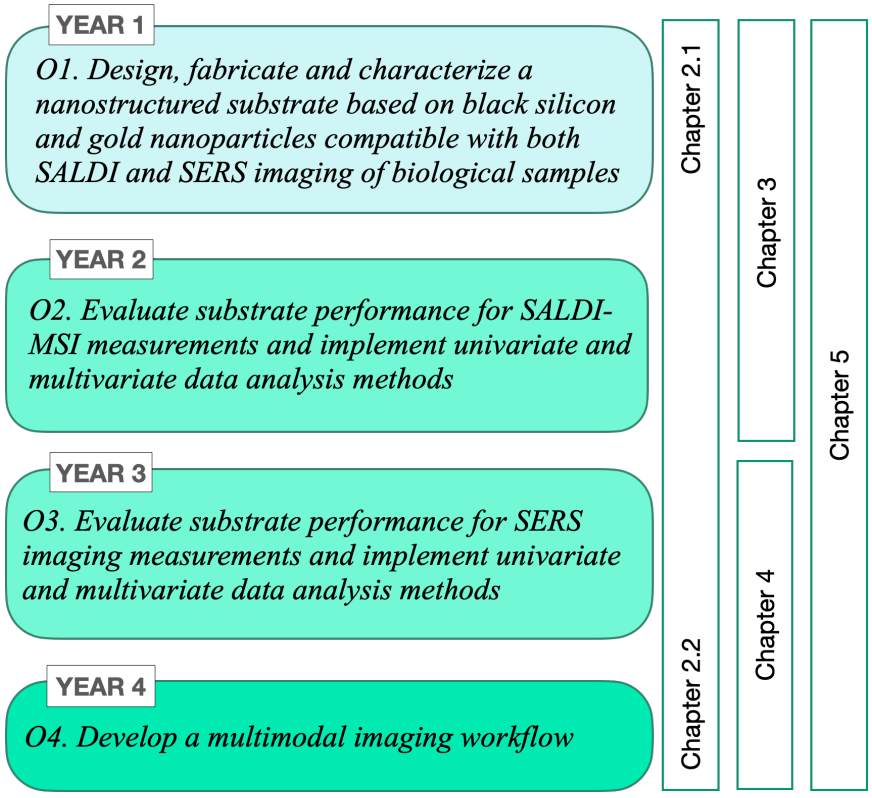

Figure 5. Timeline of planned execution of each objective, indicating where the objectives have been achieved in the thesis.

1.5. Acronyms

CT	Computed Tomography
DESI	Desorption Electrospray Ionization
DIOS	Desorption Ionization on Silicon
FFPE	Formalin Fixed and Paraffin Embedded
FTICR	Fourier Transform Ion Cyclotron Resonance
ITO	Indium Tin Oxide
IR	Infrared
LA-ICP	Laser Ablation Inductively Coupled Plasma
LDI-MS	Laser Desorption Ionization Mass Spectrometry
MRI	Magnetic Resonance Imaging
MSI	Mass Spectrometry Imaging
m/z	Mass-to-charge Ratio
MALDI	Matrix-assisted Laser Desorption/Ionization
NP	Nanoparticle
NIMS	Nanostructure-initiator Mass Spectrometry
NA	Numerical Aperture
PET	Positron Emission Tomography
SIMS	Secondary Ion Mass Spectrometry
SPECT	Single Photon Emission CT
SALDI	Surface-assisted Laser Desorption/Ionization
SERS	Surface-enhanced Raman Spectroscopy
TOF	Time of Flight
US	Ultrasound
VSI	Vibrational Spectroscopy Imaging

1.6. List of Contributions

1.6.1. Publications

"Silicon-Based Laser Desorption Ionization Mass Spectrometry for the Analysis of Biomolecules: A Progress Report" S. A. Iakab, P. Rafols, M. García- Altares, O. Yanes, X. Correig, Advanced Functional Materials 2019, 29 (45), https://doi.org/10.1002/adfm.201903609

"Gold Nanoparticle-Assisted Black Silicon Substrates for Mass Spectrometry Imaging Applications" S. A. Iakab, P. Ràfols, M. Tajes, X. Correig-Blanchar, M. García-Altares, ACS Nano 2020, 14, 6, 6785–6794, https://doi.org/10.1021/acsnano.0c00201

"*Raman2imzML* converts Raman imaging data into the standard mass spectrometry imaging format" S. A. Iakab, L. Sementé, M. García-Altares, X. Correig, P. Ràfols, BMC Bioinformatics 2020, 21, 448 https://doi.org/10.1186/s12859-020-03789-8

"Perspective on multimodal imaging techniques coupling mass spectrometry and vibrational spectroscopy: picturing the best of both worlds" S. A. Iakab, P. Ràfols, X. Correig, M. García-Altares, accepted in Analytical Chemistry (Manuscript ID ac-2020-04986u.R1)

"SALDI-MS and SERS Multimodal Imaging: one nanostructured substrate to rule them both" S. A. Iakab, G. Baquer, M. Lafuente, P. Pina, M. Alvarado, J. L. Ramírez, P. Ràfols, X. Correig, M. García-Altares, in preparation

1.6.2. Conferences

Twitter Poster Conference 2019 organized by Royal Society of Chemistry; **Poster:** "Nanostructured surfaces for molecular imaging applications" [**First prize**]

10th International Conference on Advanced Vibrational Spectroscopy 2019 Auckland, New Zealand, **Oral presentation**: "Label free SERS Imaging for Molecular Images"

22nd International Mass Spectrometry Conference IMSC 2018 Florence, Italy, **Poster**: "Selective MS imaging of hydrophobic/hydrophilic compounds with a novel Au-coated black silicon substrate"

9th Franco Spanish Workshop. IBERNAM CMC2 2018 Tarragona, Spain, **Oral presentation**: "Gold coated Black Silicon: An Efficient Substrate for Laser Desorption Ionization Mass Spectrometry"

17th International Meeting on Chemical Sensors 2018 Vienna, Austria. **Poster**: "Gold coated Black Silicon: An Efficient Substrate for Laser Desorption Ionization Mass Spectrometry" [**First prize**]

14th IBERNAM Reunion 2017, Tordesillas, Spain, **Poster**: "Design and fabrication of gold-coated nanostructured silicon wafers for LDI-MS analysis"

1.7. References

(1) Alturkistani, H. A.; Tashkandi, F. M.; Mohammedsaleh, Z. M. Histological Stains: A Literature Review and Case Study. *Global journal of health science* **2015**, *8* (3), 72–79. https://doi.org/10.5539/gjhs.v8n3p72.

(2) Orakpoghenor, O.; Avazi, D. O.; Markus, T. P.; Olaolu, O. S. Immunogenetics : Open Access A Short Review of Immunochemistry. *Immunogenet Open Access* **2018**, *3* (1), 1–6.

(3) Kim, S. W.; Roh, J.; Park, C. S. Immunohistochemistry for Pathologists: Protocols, Pitfalls, and Tips. *Journal of Pathology and Translational Medicine* **2016**, *50* (6), 411–418. https://doi.org/10.4132/jptm.2016.08.08.

(4) Kang, H. W.; Kim, H. K.; Moon, B. H.; Lee, S. J.; Lee, S. J.; Rhyu, I. J. Comprehensive Review of Golgi Staining Methods for Nervous Tissue. *Applied Microscopy* **2017**, *47* (2), 63–69. https://doi.org/10.9729/am.2017.47.2.63.

(5) Wilson, M. L. The Future of Pathology and Laboratory Medicine - Again. *American Journal of Clinical Pathology* **2018**, *150* (2), 93–95. https://doi.org/10.1093/ajcp/aqy058.

(6) Pysz, M. A.; Gambhir, S. S.; Willmann, J. K. Molecular Imaging: Current Status and Emerging Strategies. *Clin Radiol* **2010**, *65* (7), 500–516. https://doi.org/10.1016/j.crad.2010.03.011.

(7) McDonnell, L. A.; Heeren, R. M. A. IMAGING MASS SPECTROMETRY. *Mass Spectrometry Reviews* **2007**, *26*, 606–643. https://doi.org/10.1002/mas.20124.

(8) Nishidate, M.; Hayashi, M.; Aikawa, H.; Tanaka, K.; Nakada, N.; Miura, S. ichi; Ryu, S.; Higashi, T.; Ikarashi, Y.; Fujiwara, Y.; Hamada, A. Applications of MALDI Mass Spectrometry Imaging for Pharmacokinetic Studies during Drug Development. *Drug Metabolism and Pharmacokinetics* **2019**, *34* (4), 209–216. https://doi.org/10.1016/j.dmpk.2019.04.006.

(9) Aichler, M.; Walch, A. MALDI Imaging Mass Spectrometry: Current Frontiers and Perspectives in Pathology Research and Practice. *Laboratory Investigation* **2015**, *95* (4), 422–431. https://doi.org/10.1038/labinvest.2014.156.

(10) Francese, S.; Bradshaw, R.; Denison, N. An Update on MALDI Mass Spectrometry Based Technology for the Analysis of Fingermarks-Stepping into Operational Deployment. *Analyst* **2017**, *142* (14), 2518–2546. https://doi.org/10.1039/c7an00569e.

(11) DeMarco, M. L.; Ford, B. A. Beyond Identification: Emerging and Future Uses for Maldi-Tof Mass Spectrometry in the Clinical Microbiology Laboratory. *Clinics in Laboratory Medicine* **2013**, *33* (3), 611–628. https://doi.org/10.1016/j.cll.2013.03.013.

(12) Boughton, B. A.; Thinagaran, D.; Sarabia, D.; Bacic, A.; Roessner, U. Mass Spectrometry Imaging for Plant Biology: A Review. *Phytochemistry Reviews* **2016**, *15* (3), 445–488. https://doi.org/10.1007/s11101-015-9440-2.

(13) Wang, T.; Cheng, X.; Xu, H.; Meng, Y.; Yin, Z.; Li, X.; Hang, W. Perspective on Advances in Laser-Based High-Resolution Mass Spectrometry Imaging. *Analytical Chemistry* **2020**, *92* (1), 543–553. https://doi.org/10.1021/acs.analchem.9b04067.

(14) Rafols, P.; Vilalta, D.; Brezmes, J.; Cañellas, N.; del Castillo, E.; Yanes, O.; Ramírez, N.; Correig, X. Signal Preprocessing, Multivariate Analysis and Software Tools for MA(LDI)-TOF Mass Spectrometry Imaging for Biological Applications. *Mass Spectrometry Reviews* **2018**, No. 37, 281–306. https://doi.org/10.1002/mas.

(15) Cornett, D. S.; Reyzer, M. L.; Chaurand, P.; Caprioli, R. M. MALDI Imaging Mass Spectrometry: Molecular Snapshots of Biochemical Systems. *Nature Methods* **2007**, *4* (10), 828–833. https://doi.org/10.1038/nmeth1094.

(16) Law, K. P.; Larkin, J. R. Recent Advances in SALDI-MS Techniques and Their Chemical and Bioanalytical Applications. *Analytical and Bioanalytical Chemistry* **2011**, *399* (8), 2597–2622. https://doi.org/10.1007/s00216-010-4063-3.

(17) Wang, H. A. O.; Grolimund, D.; Giesen, C.; Borca, C. N.; Shaw-Stewart, J. R. H.; Bodenmiller, B.; Günther, D. Fast Chemical Imaging at High Spatial Resolution by Laser Ablation Inductively Coupled Plasma Mass Spectrometry. *Analytical Chemistry* **2013**, *85* (21), 10107–10116. https://doi.org/10.1021/ac400996x.

(18) Lanekoff, I.; Heath, B. S.; Liyu, A.; Thomas, M.; Carson, J. P.; Laskin, J. Automated Platform for High-Resolution Tissue Imaging Using Nanospray Desorption Electrospray Ionization Mass Spectrometry. *Analytical Chemistry* **2012**, *84* (19), 8351–8356. https://doi.org/10.1021/ac301909a.

(19) Kollmer, F.; Paul, W.; Krehl, M.; Niehuis, E. Ultra High Spatial Resolution SIMS with Cluster Ions - Approaching the Physical Limits.

Surface and Interface Analysis **2013**, *45* (1), 312–314. https://doi.org/10.1002/sia.5093.

(20) Norris, J. L.; Caprioli, R. M. Analysis of Tissue Specimens by Matrix-Assisted Laser Desorption/Ionization Imaging Mass Spectrometry in Biological and Clinical Research. *Chemical Reviews* **2013**, *113* (4), 2309–2342. https://doi.org/10.1021/cr3004295.

(21) Porta Siegel, T.; Hamm, G.; Bunch, J.; Cappell, J.; Fletcher, J. S.; Schwamborn, K. Mass Spectrometry Imaging and Integration with Other Imaging Modalities for Greater Molecular Understanding of Biological Tissues. *Molecular Imaging and Biology* **2018**, *20* (6), 888–901. https://doi.org/10.1007/s11307-018-1267-y.

(22) Alberici, R. M.; Simas, R. C.; Sanvido, G. B.; Romão, W.; Lalli, P. M.; Benassi, M.; Cunha, I. B. S.; Eberlin, M. N. Ambient Mass Spectrometry: Bringing MS into the "Real World." *Analytical and Bioanalytical Chemistry* **2010**, *398* (1), 265–294. https://doi.org/10.1007/s00216-010-3808-3.

(23) Masyuko, R.; Lanni, E. J.; Sweedler, J. v.; Bohn, P. W. Correlated Imaging-a Grand Challenge in Chemical Analysis. *Analyst* **2013**, *138* (7), 1924–1939. https://doi.org/10.1039/c3an36416j.

(24) le Naour, F.; Bralet, M. P.; Debois, D.; Sandt, C.; Guettier, C.; Dumas, P.; Brunelle, A.; Laprévote, O. Chemical Imaging on Liver Steatosis Using Synchrotron Infrared and ToF-SIMS Microspectroscopies. *PLoS ONE* **2009**, *4* (10). https://doi.org/10.1371/journal.pone.0007408.

(25) Balbekova, A.; Lohninger, H.; van Tilborg, G. A. F.; Dijkhuizen, R. M.; Bonta, M.; Limbeck, A.; Lendl, B.; Al-Saad, K. A.; Ali, M.; Celikic, M.; Ofner, J. Fourier Transform Infrared (FT-IR) and Laser Ablation Inductively Coupled Plasma–Mass Spectrometry (LA-ICP-MS) Imaging of Cerebral

Ischemia: Combined Analysis of Rat Brain Thin Cuts Toward Improved Tissue Classification. *Applied Spectroscopy* **2018**, *72* (2), 241–250. https://doi.org/10.1177/0003702817734618.

(26) Schramm, T.; Hester, A.; Klinkert, I.; Both, J. P.; Heeren, R. M. A.; Brunelle, A.; Laprévote, O.; Desbenoit, N.; Robbe, M. F.; Stoeckli, M.; Spengler, B.; Römpp, A. ImzML - A Common Data Format for the Flexible Exchange and Processing of Mass Spectrometry Imaging Data. *Journal of Proteomics* **2012**, *75* (16), 5106–5110. https://doi.org/10.1016/j.jprot.2012.07.026.

(27) McDonnell, L. A.; Heeren, R. M. A.; Andrén, P. E.; Stoeckli, M.; Corthals, G. L. Going Forward: Increasing the Accessibility of Imaging Mass Spectrometry. *Journal of Proteomics* **2012**, *75* (16), 5113–5121. https://doi.org/10.1016/j.jprot.2012.05.016.

(28) Sekuła, J.; Nizioł, J.; Rode, W.; Ruman, T. Gold Nanoparticle-Enhanced Target (AuNPET) as Universal Solution for Laser Desorption/Ionization Mass Spectrometry Analysis and Imaging of Low Molecular Weight Compounds. *Analytica Chimica Acta* **2015**, *875*, 61–72. https://doi.org/10.1016/j.aca.2015.01.046.

(29) Northen, T. R.; Yanes, O.; Northen, M. T.; Marrinucci, D.; Uritboonthai, W.; Apon, J.; Golledge, S. L.; Nordström, A.; Siuzdak, G. Clathrate Nanostructures for Mass Spectrometry. *Nature* **2007**, *449* (7165), 1033–1036. https://doi.org/10.1038/nature06195.

(30) Palermo, A.; Forsberg, E. M.; Warth, B.; Aisporna, A. E.; Billings, E.; Kuang, E.; Benton, H. P.; Berry, D.; Siuzdak, G. Fluorinated Gold Nanoparticles for Nanostructure Imaging Mass Spectrometry. *ACS Nano* **2018**, *12* (7), 6938–6948. https://doi.org/10.1021/acsnano.8b02376.

(31) Silina, Y. E.; Volmer, D. A. Nanostructured Solid Substrates for Efficient Laser Desorption/Ionization Mass Spectrometry (LDI-MS) of Low Molecular Weight Compounds. *Analyst* **2013**, *138* (23), 7053–7065. https://doi.org/10.1039/c3an01120h.

(32) Sunner, J.; Dratz, E.; Chen, Y. C. Graphite Surface-Assisted Laser Desorption/Ionization Time-of-Flight Mass Spectrometry of Peptides and Proteins from Liquid Solutions. *Analytical Chemistry* **1995**, *67* (23), 4335–4342. https://doi.org/10.1021/ac00119a021.

(33) Thomas, J. J.; Shen, Z.; Crowell, J. E.; Finn, M. G.; Siuzdak, G. Desorption/Ionization on Silicon (DIOS): A Diverse Mass Spectrometry Platform for Protein Characterization. *Proceedings of the National Academy of Sciences of the United States of America* **2001**, *98* (9), 4932–4937. https://doi.org/10.1073/pnas.081069298.

(34) Stewart, S.; Priore, R. J.; Nelson, M. P.; Treado, P. J. Raman Imaging. *Annual Review of Analytical Chemistry* **2012**, *5* (1), 337–360. https://doi.org/10.1146/annurev-anchem-062011-143152.

(35) Prentice, B. M.; Caprioli, R. M.; Vuiblet, V. Label-Free Molecular Imaging of the Kidney. *Kidney International* **2017**, *92* (3), 580–598. https://doi.org/10.1016/j.kint.2017.03.052.

(36) Talari, A. C. S.; Movasaghi, Z.; Rehman, S.; Rehman, I. U. Raman Spectroscopy of Biological Tissues. *Applied Spectroscopy Reviews* **2015**, *50* (1), 46–111. https://doi.org/10.1080/05704928.2014.923902.

(37) Bhargava, R. Infrared Spectroscopic Imaging: The next Generation. *Applied Spectroscopy* **2012**, *66* (10), 1091–1120. https://doi.org/10.1366/12-06801.

(38) Willetts, K.; Farr, L.; Foreman, L.; Willetts, K.; Farr, L.; Foreman, L. From Stellar Composition to Cancer Diagnostics From Stellar Composition to Cancer Diagnostics. *Contemporary Physics* **2019**, *0* (0), 1–15. https://doi.org/10.1080/00107514.2019.1645492.

(39) Rabe, J. H.; Sammour, D. A.; Schulz, S.; Munteanu, B.; Ott, M.; Ochs, K.; Hohenberger, P.; Marx, A.; Platten, M.; Opitz, C. A.; Ory, D. S.; Hopf, C. Fourier Transform Infrared Microscopy Enables Guidance of Automated Mass Spectrometry Imaging to Predefined Tissue Morphologies. *Scientific Reports* **2018**, *8* (1), 1–11. https://doi.org/10.1038/s41598-017-18477-6.

(40) Cheng, J. X.; Xie, X. S. Vibrational Spectroscopic Imaging of Living Systems: An Emerging Platform for Biology and Medicine. *Science* **2015**, *350* (6264). https://doi.org/10.1126/science.aaa8870.

(41) Freudiger, C. W.; Pfannl, R.; Orringer, D. A.; Saar, B. G.; Ji, M.; Zeng, Q.; Ottoboni, L.; Ying, W.; Waeber, C.; Sims, J. R.; de Jager, P. L.; Sagher, O.; Philbert, M. A.; Xu, X.; Kesari, S.; Xie, X. S.; Young, G. S. Multicolored Stain-Free Histopathology with Coherent Raman Imaging. *Laboratory Investigation* **2012**, *92* (10), 1492–1502. https://doi.org/10.1038/labinvest.2012.109.

(42) Murphy, D. B.; Davidson, M. W. *Fundamentals of Light Microscopy and Electronic Imaging*; John Wiley & Sons, Inc.: Hoboken, NJ, USA, 2012. https://doi.org/10.1002/9781118382905.

(43) Fullwood, L. M.; Griffiths, D.; Ashton, K.; Dawson, T.; Lea, R. W.; Davis, C.; Bonnier, F.; Byrne, H. J.; Baker, M. J. Effect of Substrate Choice and Tissue Type on Tissue Preparation for Spectral Histopathology by Raman Microspectroscopy. *Analyst* **2013**, *139* (2), 446–454. https://doi.org/10.1039/c3an01832f.

(44) Drescher, D.; Zeise, I.; Traub, H.; Guttmann, P.; Seifert, S.; Büchner, T.; Jakubowski, N.; Schneider, G.; Kneipp, J. In Situ Characterization of SiO 2 Nanoparticle Biointeractions Using BrightSilica. *Advanced Functional Materials* **2014**, *24* (24), 3765–3775. https://doi.org/10.1002/adfm.201304126.

(45) Ahlf, D. R.; Masyuko, R. N.; Hummon, A. B.; Bohn, P. W. Correlated Mass Spectrometry Imaging and Confocal Raman Microscopy for Studies of Three-Dimensional Cell Culture Sections. *Analyst* **2014**, *139* (18), 4578–4585. https://doi.org/10.1039/c4an00826j.

(46) Bedia, C.; Sierra, À.; Tauler, R. Application of Chemometric Methods to the Analysis of Multimodal Chemical Images of Biological Tissues. *Analytical and Bioanalytical Chemistry* **2020**, *412* (21), 5179–5190. https://doi.org/10.1007/s00216-020-02595-8.

(47) Lasch, P.; Noda, I. Two-Dimensional Correlation Spectroscopy for Multimodal Analysis of FT-IR, Raman, and MALDI-TOF MS Hyperspectral Images with Hamster Brain Tissue. *Analytical Chemistry* **2017**, *89* (9), 5008–5016. https://doi.org/10.1021/acs.analchem.7b00332.

(48) Oshima, Y.; Shinzawa, H.; Takenaka, T.; Furihata, C.; Sato, H. Discrimination Analysis of Human Lung Cancer Cells Associated with Histological Type and Malignancy Using Raman Spectroscopy. *Journal of Biomedical Optics* **2010**, *15* (1), 017009. https://doi.org/10.1117/1.3316296.

(49) Cebeci, D.; Alam, A.; Wang, P.; Pinal, R.; Ben-amotz, D. Photobleaching Profile of Raman Peaks and Fluorescence Background. *European Pharmaceutical Review* **2017**, *22* (6), 18–21.

(50) Baranska, M. *Optical Spectroscopy and Computational Methods in Biology and Medicine*; 2014. https://doi.org/10.1007/978-94-007-7832-0.

(51) Lasch, P. Spectral Pre-Processing for Biomedical Vibrational Spectroscopy and Microspectroscopic Imaging. *Chemometrics and Intelligent Laboratory Systems* **2012**, *117*, 100–114. https://doi.org/10.1016/j.chemolab.2012.03.011.

(52) Vidal, M.; Amigo, J. M. Pre-Processing of Hyperspectral Images. Essential Steps before Image Analysis. *Chemometrics and Intelligent Laboratory Systems* **2012**, *117*, 138–148. https://doi.org/10.1016/j.chemolab.2012.05.009.

(53) Gautam, R.; Vanga, S.; Ariese, F.; Umapathy, S. Review of Multidimensional Data Processing Approaches for Raman and Infrared Spectroscopy. *EPJ Techniques and Instrumentation* **2015**, *2* (1). https://doi.org/10.1140/epjti/s40485-015-0018-6.

(54) Singh, N.; Kumar, P.; Riaz, U. Spectrochimica Acta Part A : Molecular and Biomolecular Spectroscopy Applications of near Infrared and Surface Enhanced Raman Scattering Techniques in Tumor Imaging : A Short Review. *Spectrochimica Acta Part A: Molecular and Biomolecular Spectroscopy* **2019**, *222*, 117279. https://doi.org/10.1016/j.saa.2019.117279.

(55) Sharma, B.; Frontiera, R. R.; Henry, A. I.; Ringe, E.; van Duyne, R. P. SERS: Materials, Applications, and the Future. *Materials Today* **2012**, *15* (1–2), 16–25. https://doi.org/10.1016/S1369-7021(12)70017-2.

(56) Chen, H.; Luo, C.; Yang, M.; Li, J.; Ma, P.; Zhang, X. Intracellular Uptake of and Sensing with SERS-Active Hybrid Exosomes: Insight into a Role of Metal Nanoparticles. *Nanomedicine* **2020**, *15* (9), 913–926. https://doi.org/10.2217/nnm-2019-0419.

UNIVERSITAT ROVIRA I VIRGILI
GOLD-COATED BLACK SILICON NANOSTRUCTURED SURFACES FOR SERS AND SALDI-MS MULTIMODAL IMAGING OF BIOLOGICAL APPLICATIONS
Stefania-Alexandra Iakab

UNIVERSITAT ROVIRA I VIRGILI
GOLD-COATED BLACK SILICON NANOSTRUCTURED SURFACES FOR SERS AND SALDI-MS MULTIMODAL IMAGING OF BIOLOGICAL APPLICATIONS
Stefania-Alexandra Iakab

CHAPTER 2: State-of-the-art of Nanostructured Surfaces for Laser Desoprtion/Ionization Mass Spectrometry (LDI-MS) and Surface Enhanced Raman Spectroscopy (SERS) Imaging Applications

UNIVERSITAT ROVIRA I VIRGILI
GOLD-COATED BLACK SILICON NANOSTRUCTURED SURFACES FOR SERS AND SALDI-MS MULTIMODAL IMAGING OF BIOLOGICAL APPLICATIONS
Stefania-Alexandra Iakab

CHAPTER 2.1: Silicon-based Laser Desorption Ionization Mass Spectrometry for the Analysis of Biomolecules: A Progress Report

UNIVERSITAT ROVIRA I VIRGILI
GOLD-COATED BLACK SILICON NANOSTRUCTURED SURFACES FOR SERS AND SALDI-MS MULTIMODAL IMAGING OF BIOLOGICAL APPLICATIONS
Stefania-Alexandra Iakab

State of the article:

Published in Advanced Functional Materials 2019, 29, 1903609, DOI: 10.1002/adfm.201903609 and reproduced by permission from © 2019 WILEY-VCH Verlag GmbH & Co. KGaA, Weinheim

Journal metrics:

Impact factor 16.83 (2019)

Q1 (Nanoscience and Nanotechnology)

Contributing authors:

Stefania Alexandra Iakab, Pere Rafols, María García-Altares, Oscar Yanes, Xavier Correig

Department of Electronic Engineering, Rovira i Virgili University, Tarragona, 43007, Spain

Spanish Biomedical Research Centre in Diabetes and Associated Metabolic Disorders (CIBERDEM), Madrid, 28029, Spain

UNIVERSITAT ROVIRA I VIRGILI
GOLD-COATED BLACK SILICON NANOSTRUCTURED SURFACES FOR SERS AND SALDI-MS MULTIMODAL IMAGING OF BIOLOGICAL APPLICATIONS
Stefania-Alexandra Iakab

2.1.1. Abstract

Matrix-assisted laser desorption/ionization mass spectrometry (MALDI-MS) is widely used in the biomedical field for the label-free analysis of molecules such as drugs, lipids, peptides, proteins, and biological tissues for molecular imaging. However, organic matrices used in traditional MALDI-MS applications introduce excessive interferences in the low m/z range. For this reason, nanostructured materials —and in particular silicon-based LDI strategies— have become a promising alternative, since they provide a much weaker background. Herein, we review the recent developments in fabrication, functionalization and practical applications of silicon-based LDI-MS methods. We also report the basic requirements of silicon-based substrates for optimal LDI analysis by providing an overview of the LDI mechanisms that use silicon-based substrates instead of organic matrices. Finally, we discuss the considerable potential of silicon-based substrates and give suggestions for topics for future research.

Keywords: silicon nanostructures, surface functionalization, laser desorption ionization (LDI), mass spectrometry imaging (MSI)

UNIVERSITAT ROVIRA I VIRGILI
GOLD-COATED BLACK SILICON NANOSTRUCTURED SURFACES FOR SERS AND SALDI-MS MULTIMODAL IMAGING OF BIOLOGICAL APPLICATIONS
Stefania-Alexandra Iakab

2.1.2. Introduction

Matrix-assisted laser desorption/ionization mass spectrometry (MALDI-MS) is one of the most versatile mass spectrometry techniques for detecting a wide range of molecules in complex biological samples. It can be used to detect chemical compounds in liquid samples (i.e. urine, serum, etc.), but its great advantage is that it can map the concentration of chemical compounds on animal or plant tissue surfaces. The molecular images obtained correlate spatially with the morphology of such tissues.[1–4]

Traditionally, MALDI deposits an organic matrix onto the sample that is to be subject to laser desorption/ionization. A successful MALDI matrix needs to have high optical absorption at the laser irradiation wavelength, be able to incorporate the analyte effectively into the matrix, have a proton donor or acceptor available for efficient ionization and fragment the analyte only minimally.[3] Two of the most common organic matrices are α-cyano-4-hydroxycinnamic acid (CHCA) and 2,5- dihydroxybenzoic acid (DHB).

Although organic matrices efficiently ionize a wide variety of molecules, they do have some important limitations:

1. The use of an organic matrix hampers the analysis in the low mass range due to the presence of many background ion signals generated from the organic matrix clusters.[5] This results in major disadvantages for the use of MALDI-MS in metabolomics.
2. Inhomogeneity in the co-crystallization of the organic matrix with the analyte leads to a lack of reproducibility. The dried organic matrix crystals vary in size and shape across the surface, leading to differences in pixel-to-pixel MS signal intensities and making quantitative MALDI analysis difficult.[5]

3. Although there are a wide range of commercial organic matrices, the optimization of their selection and deposition is a complex process that can only be done manually. Each experiment may require a specific matrix which has to be optimized, and in some cases, there may be chemical interactions between analyte and matrix.[2]
4. Poor lateral resolution is frequently associated with the presence of matrix. It is mainly caused by heterogeneous co-crystallization of the matrix and analyte. Additionally, the solvent often interacts with tissues and induces the delocalization of molecules.[6] This problem was partially solved by finely controlled matrix deposition methods.[3]

To overcome heterogeneous co-crystallization between matrix and analyte during spray-coating, organic matrices were directly deposited uniformly and homogeneously onto analytes via sublimation.[7] This improves the lateral resolution, but given the long acquisition times needed in tissue imaging, the matrix may evaporate during measurement, which renders this approach largely unusable.[8] Of the two deposition methods, spray-coating results in higher analyte extraction efficiency (i.e., increased sensitivity) whereas sublimation improves lateral resolution.[7]

In the attempt to find alternatives to depositing organic matrices on the sample, attention has now turned to substrates that can promote the ionization and desorption of compounds without introducing exogenous material that might interfere with the detection of endogenous compounds. As a consequence, new solid-state substrate materials have been developed and used. Several reviews [5,9–13] have described inorganic materials based on

carbon, silicon, metals or metal-oxides that have been used extensively in LDI-MS applications as substitutes for the organic matrices for the analysis of small molecules. The main function of these materials is to promote the ionization and desorption processes of the compounds. They have to be stable under vacuum, absorb the laser irradiation and not cause ion interferences in the low mass range of the spectra. Moreover, other properties such as low thermal conductivity, high electrical conductivity and high surface-area-to-volume ratio may increase the efficiency of the LDI process.[14] They are synthesized as nanoparticles or nanostructured surfaces to enhance the absorption at UV wavelengths and have a high area/volume ratio. The use of metal nanoparticles, especially noble metals,[15–17] metal oxide nanoparticles,[18] and silicon- and carbon-based substrates as nanostructured surfaces[11,19] is now being investigated.

Silicon has a clear advantage over other alternatives: it is a versatile material with enormous potential for a large number of applications. Its chemical stability, high thermal conductivity, excellent biocompatibility, rich abundance, and unique electronic, optical and mechanical properties have established silicon as a material that is widely used in biomedical applications.[20,21] From the technological point of view, the microelectromechanical systems industry has developed numerous advanced technologies that rely on silicon-based materials. These technologies, based mainly on high vacuum processes, have the advantage of being able to fabricate highly homogeneous, reliable and repetitive surfaces. Using all these resources, scientists have spent time and effort on using intrinsic or functionalized silicon in several forms (porous, nanostructured) as a substrate for LDI-MS applications.[12]

Silicon-based substrates for matrix-free LDI-MS first appeared in 1998 in the form of porous silicon (pSi) as desorption ionization on silicon (DIOS)

technique.[22] This technique has further developed into nanostructure-initiator mass spectrometry (NIMS) which impregnates the pSi with a fluorinated compound (an initiator) [23] in order to make the whole surface stable and increase the ion desorption and ionization yield. Other silicon-based nanostructures have also been used: silica nanoparticles, silicon nanowires and nanostructured silicon surfaces (e.g. nanocone array).[12] The mass spectrometry techniques that use these substrates are known as surface-assisted laser desorption/ionization mass spectrometry (SALDI-MS) and nanostructure-assisted laser desorption ionization mass spectrometry (NALDI-MS).[14]

In this review, we describe the various kinds of silicon-based substrates that have successfully been used in all types of LDI-MS experiments. The first section describes the fabrication methods for pSi substrates and various types of 2D and 3D silicon nanostructures. The second section describes the surface modification techniques together with the applications of these substrates. The third section focuses on the LDI mechanism of each type of substrate in order to provide a better understanding of the current technologies and ideologies. Finally, we discuss important current issues affecting the silicon substrate technologies for LDI-MS applications and give some guidelines for selecting the most suitable substrate for LDI-MS experiments for a variety of applications.

2.1.3. Fabrication of nanostructured silicon substrates

2.1.3.1. Porous Silicon – DIOS MS and NIMS

DIOS was first developed in 1999 by Siuzdak et al.[22,24] who were the first to use silicon as a pSi substrate to trap the analytes deposited on the surface. Subsequently they were vaporized and ionized by laser irradiation. This matrix-free method proved its value by detecting compounds such as

peptides and small drug molecules at concentrations as low as femtomole and attomole levels and with little or no fragmentation. Budimir et al. reported using a commercial DIOS chip, which was patented by Dr Gary Siuzdak from Mass Consortium Corporation (San Diego, CA, USA).[25]

2.1.3.1.1. Anodization

The basic DIOS fabrication is anodization and its process starts from a flat crystalline silicon wafer etched by a simple galvanostatic procedure as described elsewhere by Cullis et al. in 1997.[26] Basically, n- or p-type silicon wafers can be etched in a solution of ethanol/hydrofluoric acid in the presence of current with or without illumination, depending on the type of silicon wafer. The schematic diagram of the electrochemical etching set-up used for pSi fabrication can be seen in the supporting information (see **Figure S1**). Many groups [27–31] have adjusted this fabrication method by varying parameters such as pre-etching cleaning methods, current density, ethanol/HF solution concentrations, etching time and illumination (see **Table S1**). In most cases, the electrochemical etching was carried out in custom-built Teflon cells. The typical pSi structure created by Guinan et al. [32] is illustrated in **Figure 1**. Some groups used the electrochemical etching method on silicon wafers previously patterned with standard lithography methods,[33,34] while others developed a new processing method by combining electrochemical etching and laser processing.[35]

2.1.3.1.2. Other fabrication methods

To create pSi, unconventional techniques have also been used. Densely packed vertically oriented pores in silicon have been created using a combination of colloidal lithography and metal-assisted chemical etching (MACE).[36] This technique combines both dry and wet etching methods to obtain an array of straight submicron pores in silicon not only for SALDI-MS

analysis but also for electrochemical and optical biosensors and for enzyme nanoreactors.[36] Silicon nanocavity arrays with low (9%) or high (92%) porosities have been obtained using an electron beam lithography system for high-resolution nanopatterning, and then a reactive ion etching (RIE) protocol was used to create the pSi.[37] Compared to electrochemically etched surfaces, this method uses dry chemistry that drastically reduces surface contamination and safety risks inherent to the use of HF solutions. Another atypical method for obtaining pSi for DIOS-MS was reported by Gaspari et al.[38] In this study, the pSi was fabricated by coating silicon wafer pieces with a 500 nm thick nanoporous film of silicon oxide. Goto et al. used evaporation-induced self-assembly (EISA) to create mesoporous organosilica films with open surface pores.[39] The pSi surface was created using an amphiphilic block copolymer as a structure-directing surfactant template for the triphenylamine (TPA)-derived sol-solution that was spin-coated onto the Si substrate. The film was treated with ammonia vapor and heat to obtain a condensed stable siloxane network. Lastly, the surfactant was removed by heating in toluene at elevated temperatures.[39] However, all fabrication methods for DIOS substrates are incomplete without the stabilization and/or functionalization of the surface.

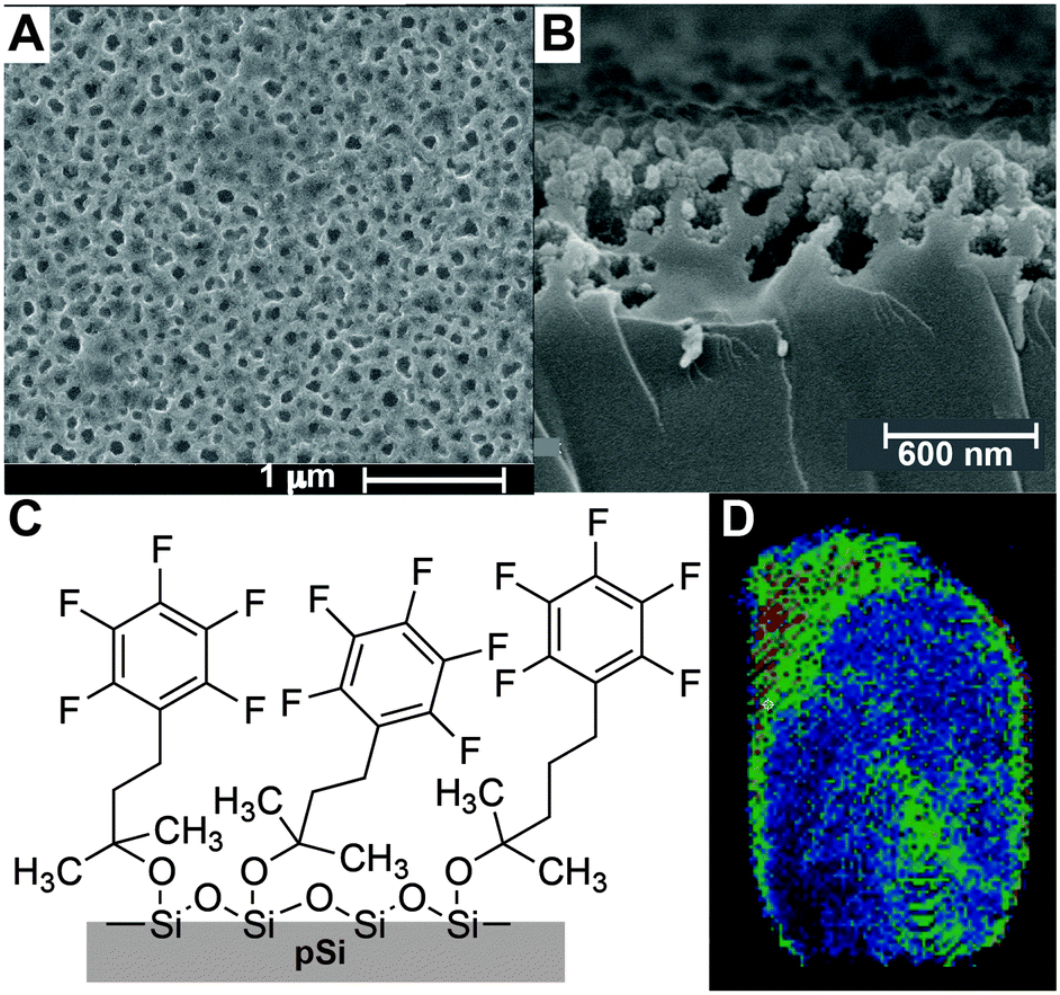

Figure 1. SEM of a DIOS chip in A) the top view and B) the cross-sectional view. C) The schematic of pSi functionalized with F5PhPr and D) DIOS-MSI of fingerprint sweat at 200 µm resolution. Reproduced with permission.[32] Copyright 2015, The Royal Society of Chemistry.

2.1.3.2. Silicon/silica nanoparticles

Silicon and silica-containing nanoparticles have emerged as a reliable alternative to organic matrices for LDI ever since pSi demonstrated its extensive value in MS applications. As a result, many groups have developed a variety of silica and silicon nanostructures. Silica nanoparticles can be

easily synthesized by wet chemical methods but they can also be purchased from several commercial distributors. Dupre et al. chose to prepare SiO_2 nanoparticles through the well-known sol-gel method. They used a solution of ammonium hydroxide in methanol and tetraethoxysilane (TEOS) as the precursor for the silica NPs. After completing all the necessary steps, they dried the SiO_2 NPs at room temperature.[40] Following the example of SiO_2 NPs, core-shell nanoparticles (CSNPs) have also been used as matrix-free substrates for LDI-MS experiments. These nanostructures proved to be more complex and required a rigorous design for each application. These nanoparticles have largely been synthesized using sol-gel processes. For example, several groups have prepared magnetite core-shell particles,[41–44] in which the core is a magnetite nanoparticle and the shell a thin silica layer. Briefly, the CSNPs are synthesized by coating the magnetite particles with a thin silica layer by the sol-gel process with TEOS as the silica source. Xiong et al.[44] designed and synthesized aptamer-immobilized magnetic mesoporous silica/Au nanocomposites (MMANs) (**Figure 2**) for the highly selective detection of unlabeled insulin in complex biological media using MALDI-TOF MS (with CHCA matrix). Briefly, the aptamer was anchored onto the gold nanoparticles in the mesochannels of MMANs for the efficient and specific enrichment of insulin. Zhu et al. approached the CSNP method differently. They substituted the magnetite core with AuNPs (between 18 and 50 nm) and the outer layer was an ultrathin silica shell (~2-4 nm). The adhesion between gold and silica was made possible by the prior functionalization of the AuNPs' surface with amino groups.[45] However, other groups [46–48] chose to purchase the SiNPs and experimented with storage and functionalization methods.

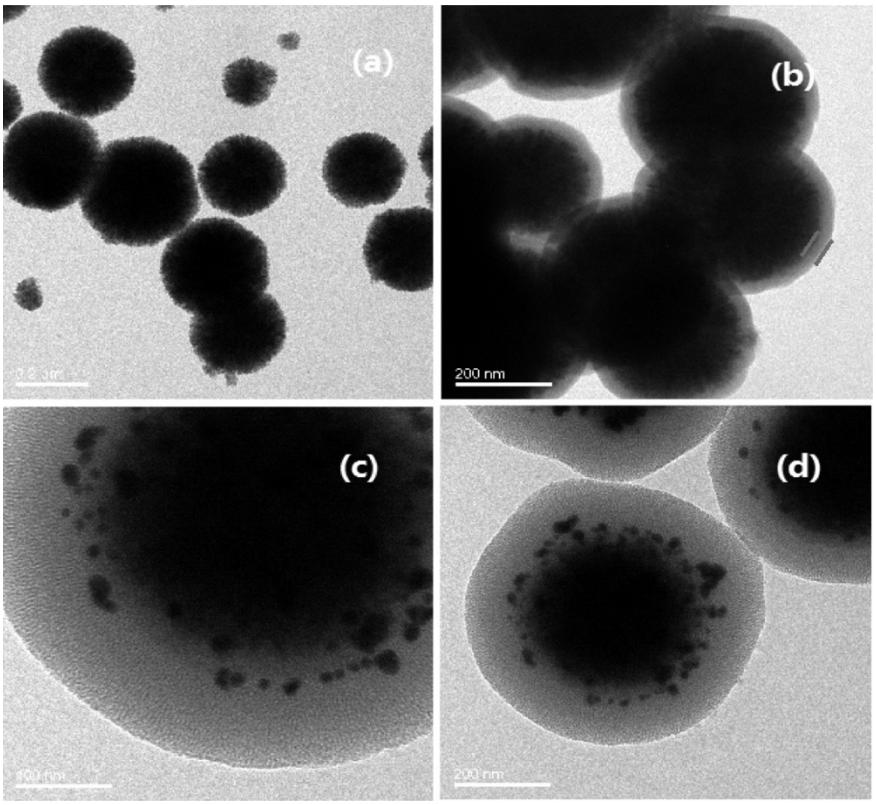

Figure 2. Electron microscope images of silicon nanoparticles. Reproduced and adapted with permission.[44] Copyright 2015, American Chemical Society.

2.1.3.3. Silicon nanowires

Silicon nanowires (SiNWs) used in LDI-MS experiments have primarily been synthesized using the vapor-liquid-solid (VLS) growth mechanism.[49–51] This method uses a nano-sized catalyst metal (deposited onto the silicon wafer) that can rapidly adsorb the gaseous precursors from which nanowires grow. The growth and diameter of SiNWs are directly dependent on the size of the Au colloid particles. In this case, the groups that developed SiNWs used Au-nanocluster-catalyzed VLS growth. Briefly, Au nanoparticles are distributed on a silicon substrate by spin-coating, then solvents and organic residues are removed and finally the SiNWs grow during chemical vapor

deposition with silane as the vapor-phase reactant. Muck et al. [51] combined the VLS growth method with the typical fabrication methods of patterned silicon: photolithography, wet-chemical etching, and dry plasma etching. Firstly, the silicon substrates were patterned with holes (~50 μm depth) arranged in arrays of 2.5 μm circles with a 4.5 μm pitch (**Figure 3**). Finally, the patterned silicon served as the substrate on which the SiNWs were grown at the bottom of the etched holes by the VLS method using chemical vapor deposition from silane. SiNWs were commercially available for a limited time from Bruker.[52]

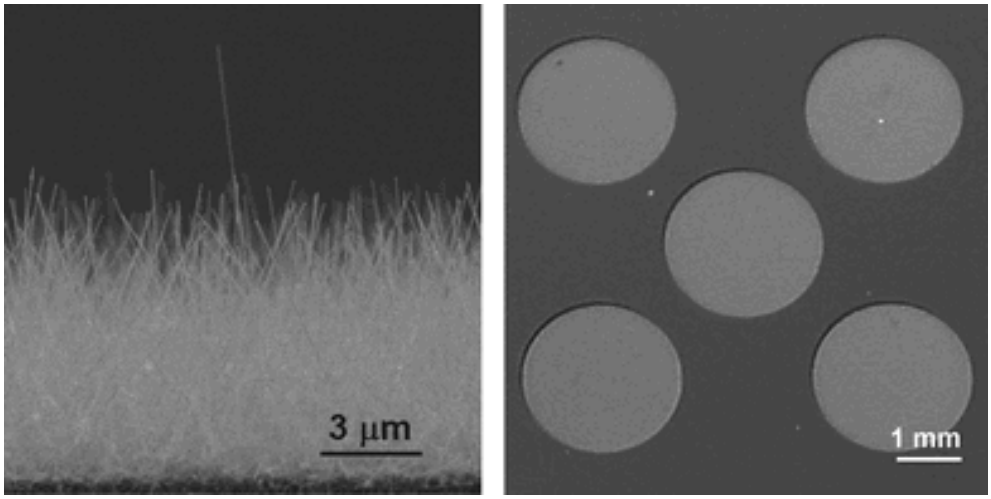

Figure 3. Electron microscope images of silicon nanowires. Reproduced and adapted with permission.[51] Copyright 2010, The Royal Society of Chemistry.

2.1.3.4. Nanostructured silicon surfaces

Along with the use of silicon nanoparticles and nanowires, silicon nanostructured surfaces have also been tested as LDI-MS substrates. In most of the studies, the nanostructured surfaces are referred to as ordered silicon nanowire arrays. These are densely packed arrays of vertical nanopillars, also called black silicon (BSi), not to be confused with silicon nanowires. The

fabrication methods of these substrates can be divided into two categories: wet etching and dry etching.

The most popular fabrication method for ordered silicon nanowire arrays is chemical etching (see **Figure 4**).[53–56] Briefly, Si wafers are cleaned using well-known methods (Piranha solution, sonicating in acetone, isopropanol, methanol, rinsing with deionized water, etc.) to obtain clean and oxide-free Si surfaces. Then the wafers are etched in a solution of $AgNO_3/H_2O/HF$ of different concentrations to form bare silicon nanopillars. This classical method was slightly modified and replaced by metal-assisted chemical etching (MACE).[57–60] In this case, a new step is added to the process. After Si wafer cleaning, a thin layer of Au is deposited onto Si substrates and then immersed in an $HF/H_2O_2/EtOH$ etching mixture to create nanostructured silicon on the wafer.

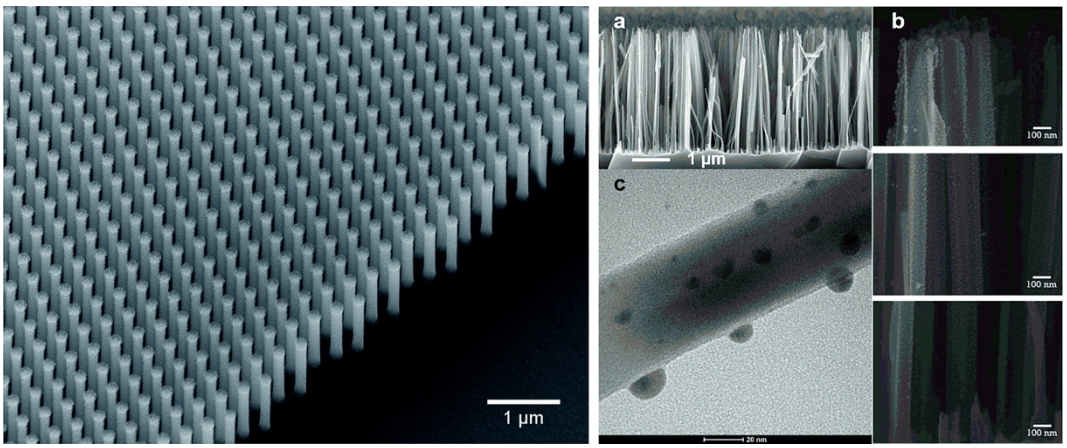

Figure 4. Electron microscope images of a silicon nanopost array (left) and Ag-functionalized silicon nanowire array (right). Left figure reproduced and adapted with permission.[63] Copyright 2015, The Royal Society of Chemistry. Right figure reproduced and adapted with permission.[56] Copyright 2016, John Wiley & Sons, Ltd.

However, all chemical etching methods use substances that are highly toxic and dangerous for the user. For example, the piranha solution is a mixture of H_2SO_4/H_2O_2, which is a strong oxidant that reacts violently with organic materials and can cause severe skin burns. Another dangerous substance is HF, which is a hazardous acid that can cause serious tissue damage if burns are not appropriately treated. All etching processes must be handled with extreme care in a well-ventilated fume hood while wearing appropriate chemical safety protection: face shield, double layered nitrile gloves, etc.[46,53,57] All these factors can reduce interest in using these methods.

Alternative solutions, consisting of variations of dry etching methods used to create nanostructures on silicon wafers have quickly emerged. Basically, the silicon wafers are covered with a protective mask and etched using plasma. In the study by Gulbakan et al.[61] an alumina mask was used together with argon plasma and various etching parameters to form several pore depth nanowell arrays. In the study by Wang et al.,[62] the mask was a polystyrene (PS) nanosphere monolayer and the plasma was formed by a mixture of etching gases: SF_6, CHF_3 and O_2. In this case, the resulting nanostructure was a silicon nanocone array, with cone heights ranging between 200 and 600 nm. Morris et al.[63] used traditional microelectronic fabrication steps for the whole process: first they patterned the silicon wafer using deep-UV-photolithography and then they performed silicon etching using both ICP and RIE and a mixture of etchant gases: C_4F_8, SF_6 and Ar. This resulted in well-ordered silicon nanopost surfaces (NAPA) that were useful for small molecule analysis (Figure 4).[63,64] The fabrication method of Chen et al.[65] is slightly unconventional compared to the techniques presented above. The silicon wafers were exposed to repeated laser irradiations in the presence of air, SF_6 gas or deionized water. This method,

however, generated mostly microcolumn arrays but in special conditions (600 laser shots at 0.13 J/cm^2 in water environment) submicrometer microcolumns were generated with an average height of 800 nm and a periodicity of 600 nm.

2.1.4. Surface modification methods

Nanostructured silicon substrates were developed to avoid the unnecessary background signals from the organic matrices largely so that low molecular weight molecules could be easily detected. Interestingly, nanostructured silicon together with organic matrices can have a synergistic effect and provide enhanced signals for detecting larger molecules such as peptides and proteins. However, to be able to use pSi substrates, the pSi needs to be stabilized (or passivated) because the freshly etched pSi surface is metastable due to the silicon-hydride terminations. The surface energy configuration is easily affected by neighboring energies, so stabilization processes are applied, one of the most common of which is oxidation. Other methods for stabilizing pSi can be seen in **Table S2**. The stabilized pSi surfaces are resistant to air and other external factors (or environments), and they present good longevity (lifetimes greater than 9 months)[66] and constant DIOS-MS activity over an extended period of time.

All the dry techniques presented in this review produced stable substrates without additional modifications, unlike the surfaces produced by chemical attack. The latter were stabilized during derivatization or functionalization.

Silicon nanostructures are functionalized by modifying the surface with functional groups that promote specific bonding between nanostructure and analyte. In this way some classes of molecules can be detected which would not be otherwise. Functionalization methods are also used to improve ionization. First, the nanostructured Si surface is derivatized, which results

in slight changes in the chemical properties of the surface because specific derivatization agents are added. The most common derivatization methods are described below in section **2.2.4.1. Derivatization**. After the nanostructured Si has been derivatized, functional groups can be added for specific bonding. The bonding can be designed for hydrophobic, electrostatic, coordination-bond, or Lewis acid-base interactions between functional group and analyte. For example, nanostructured Si is commonly functionalized to create antibody-antigen, receptor–enzyme or DNA–protein interactions.[67] Common functionalization methods are described below in sections **2.2.4.3. Functionalization with metals** and **2.2.4.4. Other functionalization methods**, and all surface modification methods together with their applications are represented in **Table 1.**

2.1.4.1. Derivatization

The most frequently used derivatization method is called silylation, often used together with ozone oxidation.[32,66,68–70] Essentially, the hydride-terminated substrates are oxidized by exposure to ozone plasma and the hydroxyl-terminated surface is modified by adding silylating reagents. The silylating reagents used will depend on the application of the substrate. For instance, Trauger et al. [68] derivatized the pSi surface with N,O-bis(trimethylsilyl)trifluoroacetamide (BSTFA), N-methyl-N-(trimethylsilyl)fluoroacetamide (MSTFA), hexamethyldisilazane (HMDS), octyldimethylchlorosilane (ODMCS), chloro(dimethyl)octadecylsilane (CDOS), 3-Aminopropyl)dimethylethoxysilane (APDMES), (3,3,4,4,5,5,6,6,6-nona- fluorohexyl)chlorosilane (FHCS), or (pentafluorophenyl)propyl-dimethylchlorosilane (PFPPDCS) that generated trimethylsilyl- (TMS), amine-, C8-, C18-, perfluoroalkyl-, and perfluorophenyl-derivatized surfaces, from which the most effective terminal groups proved to be amino- and pentafluorophenyl-. Protein model systems

(BSA and hemoglobin tryptic digests), three small drug molecules (propafenone, verapamil, midazolam), simple neutral carbohydrates (maltotriose, sucrose) and four amino acids (phenylalanine, alanine, isoleucine/leucine, glutamic acid) were analyzed and detected. The hydrophobic perfluorophenyl-derivatized surface is more responsive to hydrophobic molecules while the amine-derivatized surface is more responsive to hydrophilic molecules, demonstrating that silyl derivatization is a flexible approach for preparing functionalized DIOS chips for analyte-specific applications and for the selective adsorption of analytes. The studies in [69,71] used the same method to obtain derivatized DIOS chips by adding neat silane (PFPPDCS). These chips were used to study the distribution of bioactive compounds synthesized in the hypobranchial gland of the marine sea snail, *D. orbita*. Results showed a strong correlation between histological regions and the localization of both known and unknown metabolites. Guinan et al.[32,66,70,72] have also used neat silane (functional group F5PhPr) as a silylating agent to detect three illicit drugs —methamphetamine (MA), 3,4-methylenedioxymethamphetamine (MDMA) and cocaine— with detection limits comparable to current techniques.[66] They also detected exogenous and endogenous drug compounds from fingerprints,[32] using functional group bis(Heptadecafluorodecyl)-tetramethyldisiloxane (BisF17) for high throughput quantitative analysis of methadone in saliva, plasma and urine and the functional group tridecafluoro-1,1,2,2-tetrahydrooctyldimethylchlorosilane (F13) to detect amphetamines, opiates, benzodiazepines and tropane alkaloids at concentrations relevant to body fluid testing.[72] Other more uncommon derivatization agents for pSi were used by Tuomikonski et al.[73] They chemically derivatized the pSi samples with 10-undecenoic acid and ethyl undecenoate to obtain organic monolayers covalently attached to the surface by Si–C bonds. With this substrate, they analyzed solutions of midazolam, propranolol, buprenorphine, psilocin, 1-

naphthalene methylamine, and 2-naphthylacetic acid, dichloromethylene bisphosphonate and dichloromethyl phosphonate. The results reinforced the analysis method's validity because the detection sensitivity was at the 100–150 fmol level for the pharmaceutical compounds.

In case of silicon or silica nanoparticles, several groups [46,47] chose to silylate purchased SiO_2 nanoparticles with [(Pentafluorophenyl)propyl] dimethylchlorosilane (PFP), chlorodimethylphenethylsilane (PHP), trimethylsilane (TMS), short chain fatty acids (C10, C6, and C3), and test silicon-nanoparticle-assisted laser desorption/ionization (SPALDI) on pharmaceuticals, peptides, pesticides, nucleic acids and salt derivatives. The SiNPs were oxidized with HNO_3 before silylation, and after silylation they were mixed with the analyte solutions and spotted on standard MALDI plates.

Nanowires have also been silylated with PFPPDCS.[49,50] In both cases the SiNWs were first etched in HF solution to remove the oxide layer and then reoxidized with ozone, followed by the final silylation step. Go et al. [49] examined the effect of laser energy, nanowire density, nanowire size and growth orientation of the SiNWs while performing mass spectrometry experiments on peptides and small drug molecules. Luo et al. focused on studying the internal energy transfer in SALDI from SiNWs and its relationship to nanoporous silicon in DIOS and to conventional MALDI.[50] Using benzyl-substituted benzylpyridinium thermometer ions, they proved that very low laser fluence is needed for LDI, due to the high thermal energy confinement achieved in SiNWs.

The chemically etched nanostructured silicon substrates from different studies [53–55] were modified with octadecyltrichlorosilane (OTS), perfluorodecyltrichlorosilane (FDTS) or octyldimethylchlorosilane (ODCS).

These studies mostly focused on validating the use of the new substrates by detecting various types of peptides and small molecules. Finally, a MACE substrate silylated (functional group F_{13}) was used to detect peptides (middle range 1–3 kDa) and methadone (low range <500 Da).[58] The substrate made it possible to detect methadone in saliva, blood plasma and urine from clinical samples of real methadone-treated patients.

2.1.4.2. Nanostructure initiator mass spectrometry (NIMS)

The combination of nanoporous surfaces and functionalization methods made DIOS so versatile that scientists were inspired to develop it further: nanostructure-initiator mass spectrometry (NIMS), which combines the properties of nanostructured materials and fluorinated compounds. This new MS analysis technique uses compounds called 'initiators', which are trapped on nanostructured surfaces where they release and ionize intact molecules adsorbed on the surface.[23] NIMS is different from silylated pSi because the fluorinated compounds are bound differently. In the case of silylated pSi, the fluorinated compounds are chemically bound to the surface while in the case of NIMS they are physically adsorbed onto the surface. In other words, NIMS exploits the nanostructured surface's ability to trap liquids and does not use any derivatization methods to activate the hydride-terminated surface. However, the authors suggest silanization with chlorosilane of the oxidized NIMS substrate as an optional step for preparing the surface before the addition of the initiator. Most research groups use pSi as the nanostructured substrate and Bis17 as the initiator.[23,72,74–77] However, the first reports on NIMS studied a variety of initiators.[23,77] Perfluorinated siloxanes are preferred for NIMS because they are effectively trapped within the nanostructured surface and perform best.

The well-known manufacturing process of pSi and the fact that initiators are straightforward to use has led to NIMS being successfully used in various applications. The versatility of NIMS was demonstrated by Northen et al.,[23] who tested several initiators for a large number of applications: direct analysis of blood and urine, characterization of peptide microarrays, detection of endogenous phospholipids of a MDA-MB-231 cancer cell line and MSI analysis of mouse embryo tissue. A protocol for preparing and applying NIMS surfaces has been published by the same group in which they give detailed step by step instructions accompanied by supplementary movies.[23,77] NIMS performance was compared with DIOS and (nanostructure assisted laser desorption ionization) NALDI for the detection of four drug classes: amphetamines, benzodiazepines, opiates and tropane alkaloids.[72] NIMS produced better LODs for oxycodone in both water and PBS. A study on pSi morphology showed the pore-size-dependent analyte selectivity of NIMS. This selective behavior manifests mainly through physical interactions of analyte molecules and NIMS surfaces. The sensitivity of NIMS is directly affected by the pore and analyte size. This study analyzed analytes ranging from m/z 175.12 to m/z 3657.92 and substrates of pore size from ~4 to 12 nm (porosity from ~7% to 70%).[78]

Variations in NIMS technology soon emerged. In the first place, NIMS was modified by using new augmenting components such as organic matrices or metal nanoparticles. Moening et al. used a sublimated organic matrix (DHB) together with NIMS to develop a new hybrid ionization approach called matrix-enhanced nanostructure initiator mass spectrometry (ME-NIMS).[75] ME-NIMS improved the performance of conventional NIMS by reducing the limit of detection of pentamidine by at least one order of magnitude. This improvement was also seen in the detection of lipids and small drug molecules during tissue imaging.[75] Patti et al.[74] replaced the organic matrix

with an $AgNO_3$ coating of the NIMS substrate and focused on localizing perturbations in the metabolism in pathological tissues by MSI. They showed that the deposition of cationization agents ($AgNO_3$) on the NIMS surface enables otherwise difficult sterol molecules such as cholesterol to be imaged. Finally, to modify NIMS, they redesigned the nanostructured silicon by replacing the highly dangerous electrochemical etching of silicon with plasma dry-etching. Gao et al.[76] used black silicon instead of conventional pSi. The relationship between black silicon morphology and its NIMS sensitivity was studied using several biomolecules: spermidine, arginine, adenosine, palmitoyl carnitine, verapamil, bradykinin, and STAL-2. It was found that the black silicon pillars absorb enough initiator to promote the desorption of analytes, and that large surface areas can efficiently improve NIMS sensitivity due to the enhanced energy transfer from substrates to analytes. The same dry-etching method was used to create an integrated microfluidics-NIMS device.[79] In this study, the novel NIMS substrate is compatible with droplet and digital microfluidics and can be used on-chip to assay glycoside hydrolase enzyme in vitro.

2.1.4.3. Functionalization with metals

Several studies presented the use of metals to functionalize the pSi surface. Zhou et al.[80] used several chemical reactions to obtain phosphonate-terminated pSi which was immersed in $ZrOCl_2$ solution to yield zirconium phosphonate-modified porous silicon (ZrP-pSi) wafers. These wafers were sensitive to phosphopeptide detection and their high specificity was demonstrated by analyzing the tryptic digest product of α-casein, β-casein and BSA. The latest research has specifically focused on the use of silver as a surface functionalizing agent for pSi. Yan et al.[81] used different mixtures of silver nitrate in water, 4-ATP in ethanol and trifluoroacetic acid (TFA) to prepare substrates with and without well-organized 4-ATP self-assembled monolayers. They demonstrated that the 4-ATP capped substrate was more efficient

than the substrate covered by naked Ag nanoparticles, because it produced greater ionization and less fragmentation. The substrate performance was excellent, with limits of detection down to several femtomoles for tetrapyridinporphyrin (TPyP), sub-picomoles for oxytocin, and picomoles for PEG 400 and PEG 2300. A different approach to obtain silver-covered pSi was described by Gustafsson et al.[82] The DIOS substrates were prepared by electrochemical etching and immediately sputter-coated with a 1.4nm-thick Ag layer. To test this new DIOS/Ag-DIOS MSI method, distributions of fingermark compounds and tissue metabolites of 6-bromoisatin were mapped. Fingermark analysis showed a broad range of small molecule classes, including environmental contaminants (ditallow dimethyl ammonium chloride, DTDMAC), lipids (fatty acids - FAs, triglycerides - TAGs), sterols and wax esters (WEs). The imprinted murine fore-stomach tissue analysis showed a phosphatidylcholine head group (PC), 6,6'-dibromoindirubin (6,6'-DBI), fatty acids (FAs), cholesterol and Ag cluster peaks. This novel approach exhibited minimal observable depletion and has the potential to simplify the analysis of multiple compound classes by using a single analytical platform to acquire multi-tiered spatial data sets. Gold was also used by Li et al. to functionalize pSi.[29] They used electrochemical deposition to obtain a new pSi chip functionalized with gold nanoparticles (PSi-GNPs) that allows direct serum peptide profiling with a high-quality MS signal. Both silver and gold nanoparticles can also be used. Wang et al.[83] used chemical-assisted etching to create patterned nanoporous silicon chips embedded with Ag and Au NPs for the detection of thiol compounds. The selectivity of the chips embedded with Ag and Au NPs towards thiol compounds was monitored in cells. These novel chips were also used to determine the effect of irinotecan, 7-ethyl-10-[4-(1-piperidino)−1-piperidino]-carbonyloxy camptothecin (CPT-11), a potent anticancer drug.

Au was also used by various groups as a functionalization agent for 2D and 3D silicon nanostructures. Xiong et al.[44] modified magnetite core-shell

nanoparticles with Au NPs on the silica outer shell to obtain aptamer-immobilized magnetic mesoporous silica/Au nanocomposites (MMANs). These composite nanoparticles are mainly used for insulin detection, although other proteins were also detected: immunoglobulin G, human serum albumin, α1-antitrypsin, horseradish peroxidase, lysozyme and cytochrome C. Another group [48] attached purchased silica nanoparticles to a silicon wafer using polymers for adhesion. Then they modified the SiNPs with Au by immersing the wafer into an AuNP solution. In this way the AuNPs constructed the outer layer of the substrate and facilitated the formation of a self-assembled monolayer (SAM) of Capture DNA-1. The final substrate was an Au and SiO2 NP-assembled hybrid porous nanostructure and was used to analyze confined DNA structures. Another method to create AuNPs on nanostructured surfaces was developed by Tsao et al.[59] The nanostructured Si surface was oxidized with O_2 plasma and immersed in $HF/HAuCl_4$ solution to graft the Au nanoparticles. The resulting AuNPs-nSi chip was used as a LDI-MS substrate for analyzing glucose from standard solutions and urine. The high detection sensitivity and specificity for glucose in a biological sample confirmed the potential of the substrate.

Other metals that have been used to create functional substrates are Cu,[42] Li,[51] and Ag.[56] Copper was used for surface grafting magnetite core-shell nanoparticles with Cu^{2+} ions. The functional microspheres captured small peptides from complex sample systems (human serum and urine) although not the large proteins because of the porosity of mesoporous silica and the specific affinity of Cu^{2+} ions toward peptides.[42] Muck et al. chose Li as a doping agent. They deposited the sample solutions on the silicon nanowire substrate and the ^{7}LiOH solution after the sample had dried. The ^{7}LiOH solution was prepared in methanol–dichloromethane 1:4 at 7.5 mg mL^{-1}. Most of the compounds were detected as clean $[M+^{7}Li]^{+}$ signals.[51] Finally,

AgNPs were used to decorate silicon nanowire arrays by a pulsed laser deposition method.[56] The applicability of AgNP-decorated SiNWs was demonstrated by the detection of unsaturated compounds (SQ and oleic acid) in a complex matrix.

2.1.4.4. Other functionalization methods

For some applications that characterize bio-systems, the functionalization of pSi forms particular Si- bonds on the surface of pSi. This method was used together with an organic matrix to enhance the detection of slightly larger molecules such as peptides or proteins. Analytical methods were developed by several research groups. Chen et al.[33] analyzed a specific protein system, NTA-Ni2+/His-tagged protein, with a carboxyl (–COOH) functionalized pSi microarray. Chen et al. [67] and Yan et al. [34] immobilized antibodies on the pSi surface by physical adsorption. These experiments resulted in the detection of biomarker B-type natriuretic peptide (BNP) with a detection limit as low as 10pg/mL BNP in human plasma [67] and the specific detection of angiotensin I at a 10 fmol level in diluted plasma samples (10 μL, 1 nM). [34] Selective detection of benzodiazepines in the presence of illicit drugs has been achieved by covalent immobilization of antibenzodiazepine antibodies on pSi surfaces.[27] Dizepam, cocaine and alprazolam in small concetrations (50 pmol) were detected using this specific pSi strategy. Another specific biological system characterization method was developed by Sweetman et al. [28] to study the attachment of mammalian cells to pSi. To this end, *N*-hydroxysuccinimide (NHS) ester and PEG-functionalized pSi surfaces were conjugated with adhesion mediator protein fibronectin (FN) and used for the selective immobilization of human neuroblastoma cell line SK-N-SH.

Some groups adopted a different approach to the functionalization method. The study by Chen et al.[41] modified the surface of magnetite core-

shell nanoparticles (CSNPs) first by modification with MPS and finally by a seeded aqueous-phase radical polymerization with MMA. These CSNPs were specifically designed for the enrichment of peptides and proteins for mass spectrometric analysis. Other groups have also designed their novel substrate based on magnetite CSNPs roughly for the same purpose: selective enrichment of peptides.[43] In this case, the microspheres were dried and calcined in nitrogen to improve the hydrophobic property of the surface. Another study developed CSNPs with AuNP cores and ultra-thin silica shells.[45] These Au@utSiO2 CSNPs were stabilized by further growth of the silica shell using the Stöber method. Small functional molecules and small polymers were successfully detected by CSNP-based LDI-TOF-MS. In 2008 Daniels et al.[52] functionalized commercially available NALDI target plates from Bruker Daltonics, Billerica, MA. The surface of the silicon nanowires was modified by depositing organic layers to change the hydrophobicity of the substrate. The new target plate was used for the detection of small molecules. Unfortunately, there is no mention of the type of organic layer and the NALDI plates are no longer available for purchase.

Table 1. Silicon nanostructures: fabrication, surface modification and applications

	Fabrication Method	Surface modification method [a)]	Analyzed Molecules	Sample type	Matrix [b)]	Ref.
Porous silicon	Anodization = Electrochemical etching	N/A	Choline (40 μM), BSA, FHV, adenovirus penton protein, β-lactoglobulin	Liquid	-	[22]
			Four-residue peptide (MRFA), des-arg-bradykinin, bradykinin, angiotensin, adrenocorticotropic hormone (2 pmol each); caffeine, antiviral drug WIN, reserpine (1	Liquid	-	[24]

		pmol each); N-octyl β-D-glucopyranoside			
		Prednisolone, dalargin, bradykinin, adrenocorticotropic hormone (ACTH) 1–17	Liquid	-	[35]
		Arginine, tryptophan, histidine, methionine, glutamine, and glycine (5 μg/mL each)	Liquid	-	[30]
		4-amino-1-benzylpyridinium bromide (0.5 mM), 1,2-dihexadecanoyl-sn-glycero-3-phosphocholine (0.01 mM), angiotensin III (2.5 mg/mL)	Liquid	-	[37]
		Substance P, renin substrate tetrapeptide, angiotensin I (ng/ml standard solutions) and calcitonin	Liquid	CHCA SA	[38]
	Silylation	Verapamil (700 ymol), BSA (500 amol), phospholipids; bradykinin 2-9, bradykinin 1-7 and neurotensin (1 fmol peptide array), phosphatidylcholine, phosphatidylethanolamine, codeine (15 ng/ml)	Liquid Cells Tissue	-	[23]
		Perfluorophenyl silylated pSi: midazolam (200 fmol); propafenone (200 fmol); verapamil (200 fmol), des-Arg9-bradykinin (800 ymol) amine silylated pSi: sucrose (25 pmol); maltotriose (25 pmol) phenylalanine, alanine, isoleucine/leucine, glutamic acid	Liquid	-	[68]
		Tyrindoxyl sulfate; 6,6′-dibromoindigo	Tissue	-	[69]
		MA (2.88 ng/mL); MDMA (0.66 ng/mL); cocaine (0.86 ng/mL)	Liquid	-	[66]

	Methadone (14.74ng/mL in saliva; 18.84ng/mL in plasma; 19.50ng/mL in urine)	Liquid	-	[70]
	Methadone (100 ng/mL); oxycodone (2.5 ng/mL in water and 10 ng/mL in PBS); flunitrazepam (100 ng/mL); MDMA (100 ng/mL); cocaine (100 ng/mL)	Liquid	-	[72]
	Murexine; tyrindoxyl hydrogen sulfate; tyrindoleninone; Tyrian purple	Tissue	-	[71]
	Cholesterol; nicotine; methamphetamine; amphetamine; nonanoic acid; methadone; EDDP; codeine	Fingerprint	-	[32]
Two levels of derivatization (aminopropyl then phosphonate) and functionalization with Zr	Phosphopeptides from α-casein, β-casein and BSA	Liquid	DHB	[80]
Two levels of functionalization (Ag and 4-ATP)	TPyP (5.2 fmol); oxytocin (0.4 pmol); PEG 400 (3 pmol); PEG 2300 (30 pmol)	Liquid	-	[81]
Functionalization with nanometer Ag layer	Fingermark: DTDMA C16/C16; DTDMA C16/C18; DTDMA C18/C18; TAG 48:1; oleic acid; stearic acid; WE 36:1; Behentrimonium	Fingerprint	-	[82]
	tissue section: PC head group; oleic acid; stearic acid; 6,6′-dibromoindirubin (Tyrian purple); cholesterol	Tissue		
Functionalization with $AgNO_3$ solution and addition of physically adsorbed initiator	Cholesterol and 7DHC	Tissue	-	[74]

Two levels of derivatization (10-undecenoic acid and ethyl-10-undecenoate)	Buprenorphine (100 fmol); midazolam (150 fmol); psilocin (5 pmol); propranolol (4 pmol); 1-Naphthalene methylamine (6 pmol); 2-Naphthylacetic acid (5 pmol); dichloromethyl phosphonate (60 pmol); dichloromethylene bisphosphonate (40 pmol); Leu-Enkephalin-Arg (4 pmol); Des-Arg1-Bradykinin (4 pmol); Substance P (3 pmol)	Liquid	-	[73]
Two levels of derivatization (undecylenic acid and NHS) and functionalization with BNP antibodies	Different BNP concentration solutions prepared in PBS buffer and in human plasma (10pg/mL)	Liquid	CHCA	[67]
Two levels of silylation (alkene 1 and alkene 3) and functionalization with FITC-BSA or FN	Tryptic peptides of fibronectin from human neuroblastoma cell line SK-N-SH	Cells	CHCA	[28]
Functionalization with electrochemically deposited Au	Model sample consisting of HRP digest (100 mg/mL); excess BSA; serum peptides, insulin	Liquid	CHCA	[29]
Addition of BisF17 initiator	Angiotensin III, bradykinin, and angiotensin I (0.3 μM each), lipid species	Liquid	DHB	[75]
Functionalization with $AgNO_3$ solution and addition of initiator	Testosterone, vitamin D3, glucose (300 fmol), sucrose (500 fmol), maltotriose (800 amol), maltohexaose, maltoheptaose, β- and γ-cyclodextrin; trans-androsterone, progesterone, corticosterone, and prednisone (500 fmol each), cholesterol	Liquid, Tissue	-	[31]
Addition of BisF17 initiator	Arginine, palmitoylcarnitine, streptomycin, bradykinin, angiotensin, ACTH residues ("clip" 1–17, 18–39, 7–38), insulin B, neurotensin	Liquid	-	[78]

	Silanization followed by functionalization with antibodies	Diazepam, cocaine, alprazolam (50 pmol in solution mixture)	Liquid	-	[27]
commercial DIOS chip	N/A	Heptadecanoic acid, stearic acid, nonadecanoic acid, arachidic acid, heneicosanoic acid, behenic acid (2 nmol each)	Liquid	-	[25]
Photolithography and reactive ion etching	Silanization	Dextromethorphan and CelE-CBM3a enzymatic assay	Liquid	-	[79]
evaporation-induced self-assembly (EISA) method	Derivatization by RIE etching in gas mixture O_2/CF_4	Peptide and oligosaccharide molecules	Liquid	-	[39]
Photolithography and anodization	Four levels of derivatization (OH, carboxyl, NHS and NTA) and functionalization with Ni^{2+}	Trx-urodilatin (1 pM)	Liquid	SA	[33]
	Functionalization with angiotensin I antibodies	Angiotensin I (1 nM in diluted plasma)	Liquid	CHCA	[34]
Photolithography and silver-assisted chemical etching	Functionalization with AuNPs	GSH (10 μg/mL in standard solution), GSH (healty and Irinotecan-treated Caco-2 cells) and l-cysteine (10 μg/mL)	Liquid and Cell (lysate = extraction?)	-	[83]
Reactive ion etching	Addition of BisF17	Spermidine, arginine, adenosine, palmitoylcarnitine, verapamil, STAL-2 (100 fmol-10 pmol), Bradykinin	Liquid	-	[76]
Metal-assisted chemical etching (using Au nanostructures and aqueous HF etching solution)	N/A	Methadone solutions at 1000 ng/mL	Liquid	-	[36]

Nanoparticles and nano-powders	Sol-gel synthesis (SiO_2 NPs)	N/A	48 sequences from synthetic peptides mimicking protein digests	Liquid	-	[40]
	Sol-gel synthesis (magnetite core-shell Fe_3O_4@SiO_2 microspheres)	Modification with MPS and polymerization of MMA	Standard peptide angiotensin II (DRVYIHPF), standard protein cytochrome C	Liquid	CHCA	[41]
		Functionalization with Cu^{2+} ions by surface grafting	Angiotensin II, tryptic BSA digest, peptides from human serum and urine	Liquid	CHCA	[42]
		CSNPs dried and calcined in N_2	Angiotensin II, MYO digest and BSA digest	Liquid	CHCA	[43]
		Functionalization with Au	Human insulin, immunoglobulin G, human serum albumin, α1-antitrypsin, horseradish peroxidase, β-casein, lysozyme, cytochrome C	Liquid	CHCA	[44]
	AuNPs coated with an ultrathin silica shell	Au@SiO_2 CSNPs by growth of the silica shell	Stabilization of hydroxyphenyl)acetamide, 2-(2-methyl-5-nitro-1H-imidazole-1-yl)ethanol, norfloxacin, amoxicillin, erythromycin, PEG1000, roxithromycin and temporin-SHf	Aspartic acid, N-(4-Liquid	-	[45]
	Particles purchased from distributors	Etching with HF, oxidation with HNO_3 and derivatization with PFP, PHP or TMS	Peptides leucine encephalin (200 μg/mL), angiotensin II (DRVYIHPF) (100 μg/mL), nucleobase adenine (400 μg/mL), propafenone (10 pmol/μL), verapamil (10 pmol/μL), trioctylamine (80 μg/mL)	Liquid	-	[46]
			morphine and propafenone from spiked urine			
			ametryn and altretamine from spiked soil			
		Oxidation with HNO_3 and silylation with C6 or C3	2-methyl, 4-methyl, 3-methoxy, 4-methoxy and 4-chloro C10,benzylpyridiniums	Liquid	-	[47]

		Functionalization with Au by dipping in AuNP solution	Surface-confined DNA: ss-DNA and ds-DNA	Liquid	3-HPA	[48]
Nanowires	Au nanocluster-catalyzed vapor-liquid-solid (VLS) growth mechanism	Oxidation with ozone and silylation with PFP	Cocaine (3 μM spiked saliva), BSA and FHV tryptic digests (1 μM), and des-Arg9-bradykinin, midazolam, propafenone, and verapamil (all 1 mg/mL aqueous solution)	Liquid	-	[49]
			Chloride salts of seven benzyl-substituted benzylpyridinium ions (70 μM standard solution)	Liquid	-	[50]
		Doping with LiOH after sample deposition	Diglycerides, tristearin, tripalmitin, fatty acids and glyceride	Liquid		[51]
Nanostructured surfaces	Chemical etching (variations on HF/$AgNO_3$ aq. solution)	Oxidation by UV/ozone and silylation with OTS, FDTS, or ODCS	Peptide mixture: Des-Arg-bradykinin, angiotensin I, fibrinopeptide B and neurotensin (10 fmol/μL), verapamil (5 fmol/μL) and Sutent (10 fmol/μL)	Liquid	-	[53]
		Silylation with OTS	Peptide mixture (fmol/mL): Des-Arg-Bradykinin, angiotensin I, fibrinopeptide B and neurotensin	Liquid	-	[54]
			15 tryptic peptides and 14 Lys-N peptides	Liquid	-	[55]
		Functionalization with AgNPs by pulsed laser deposition	Linoleic acid, oleic acid, arachidonic acid, squalene, diacylglycerol	Liquid	-	[56]
	Metal-assisted chemical etching (using Ag or Au nanostructures and aqueous HF etching solution)	N/A	Single model peptide sample des-Arg9 Bradykinin (1 pM)	Liquid	-	[57]
		Oxidation by ozone and silylation with F13	Methadone (100 ng/mL aqueous solution), EDDP from clinical samples of blood plasma, saliva, and urine and peptide mixture: angiotensin I, angiotensin II, substance P, bombesin, ACTH clip 1–17, ACTH clip 18–39, somatostatin 28	Liquid	-	[58]

	Oxidation by plasma and grafting by immersion in $HF/HAuCl_4$ solution	O_2Glucose (100 μM aqueous solution) AuNP(50 mM spiked urine samples)	Liquid	-	[59]
	Au deposited by e-beam evaporation, immersion in 1:1:1 volume ratio of HF/H2O2/EtOH solution	Natural products in microbial interactions: metabolites, peptides	Microbial cells	-	[60]
Reactive ion etching (mask and gas mixture plasma)	N/A	Adenosine, Pro-Leu-Gly tripeptide, and bradykinin, fentanyl, BSA digest and standard carnitine metabolite cocktail	Liquid	-	[61]
	N/A	PEG, bradykinin, Arg, and TMZ (100 μM in standard solutions) and glucose from urine samples from healthy and diabetic patients	Liquid	CHCA DHB	[62]
	N/A	Buprenorphine, norbuprenorphine, ropivacaine, amiodarone, chlorpheniramine, fentanyl, clonidine, nordiazepam, metoprolol, verapamil	Liquid	-	[63]
	Photopatterning, RIE etching and cleaning using standard microelectronic steps	Metabolites from hepatocyte extracts or urine aliquots	Liquid Cell extracts	-	[64]
Laser irradiation (in air, SF_6 gas, or DI water)	N/A	Angiotensin I, bovine insulin, PPG1000 and PEG400 (0.5 nmol/μL)	Liquid	-	[65]
Commercial NALDI targets	Hydrophobic organic coating	Clonidine, propranolol, quinidine, papaverine, verapamil, ketoconazol, prazosin, haloperidol	Liquid	-	[52]

[a] N/A= information not available; [b] - no matrix used

2.1.5. LDI mechanism: ionization and desorption processes

Matrix-assisted laser desorption/ionization mass spectrometry (MALDI-MS) has become an indispensable analysis technique for many research communities since it was first used by Karas et al. in the 1980s.[84] The fundamental strategy of a complete MALDI-MS analysis consists of several steps: sample preparation, excitation of the sample and desorption of the condensed phase, ionization of analyte molecules by generating charges, and extraction and detection of ions.[85] The processes that occur between the excitation of the sample and the extraction of ions are collectively called laser desorption/ionization (LDI). This mechanism is widely regarded as the convolution of two processes —desorption and ion formation— and has been previously studied in detail by several groups.[85–89] LDI is portrayed as a complex process that involves both optical and mechanical phenomena as well as the thermodynamic and physicochemical processes of phase transition and ionization. Ionization, in particular, has been described as a collection of chemical and physical pathways including gas-phase photoionization, ion-molecule reactions, disproportionation, excited-state proton transfer, energy pooling, thermal ionization and desorption of preformed ions.[86] The LDI mechanism is an active topic of research and was revisited by Chang et al. and Jaskolla et al. in 2007 and 2011, respectively.[88,89]

Since the beginning of MALDI analysis, the ionization of analytes was helped by an organic matrix with various essential functions. First, it has to isolate analyte molecules by preventing analyte aggregation. Then, it has to absorb the laser energy while the condensed phase disintegrates without excessive destructive heating of the analyte molecules. Finally, the matrix should efficiently ionize analyte molecules.[86] With all these specificities of the matrices, however, the spectra generated are far from ideal and a matrix

is not as suitable for use in untargeted MS experiments focused on small molecules. The matrix complicates the sample preparation, introduces background ions into the spectra, hampers quantitative analysis and also complicates the acquisition of MS images at high lateral resolutions. These difficulties can be reduced by replacing the organic matrix with a less invasive component that has at least the same specific/required properties as the matrix. Therefore, by understanding the LDI mechanism of molecules adsorbed onto a specific substrate, especially nanostructured silicon, ion yields can be maximized, analyte charge states controlled, spectra can be obtained with less fragmentation, and new classes of compounds analyzed.

This section provides an overview of the LDI mechanisms described in LDI-MS experiments using silicon-based substrates instead of organic matrices. The specific physicochemical properties that the substrate needs to aid desorption and ion formation will be discussed, as will the specific LDI processes for each substrate type. We have summarized the main characteristics of MALDI and Silicon-based LDI in **Table 2**.

2.1.5.1. Influence of physical properties

For pSi, the factors that most influence the LDI process are the physical properties of the material surface. The pSi structure has a high surface area which provides an optimal environment for the co-adsorption or entrapment of the analyte and solvent.[24,25,30,35] High pore density and smaller pore sizes might produce better results as the increase in the ion signal can be correlated with the increase in the overall surface area and analyte coverage. Furthermore, the tendency of energy to localize near defects, protrusions and edge sites makes these areas more active in LDI processes.[24,30] In addition, it is critical for the analytes to penetrate into the pSi because the pSi also manifests quantum confinement effects: high optical absorption and low

thermal conductivity. These effects cause rapid heating of the pSi in the presence of laser and the resulting energy can be transferred from silicon to the trapped analyte. Basically, instant heating of the pSi provides the energy required for analyte desorption and ionization.[24,35]

Silicon nanostructures such as nanoparticles, nanowires and nanostructured surfaces have specific physical properties that favor LDI processes. Although many different nanostructures have been fabricated, most of their properties are the same: specific dimensions that maximize laser light absorption, specific heat capacity and conductivity of the nanostructured silicon and geometric effects that promote molecule adhesion and desorption.

In case of functionalized silica nanoparticles, the layer of silicon oxide shell affects the ionization process by two mechanisms: (1) the mesoporous silica shell produces a size-exclusion effect which reduces background interference[44] and (2) the thickness of the silica shells affects the energy transfer from the nanoparticle core to the analyte.[45]

For silicon nanowires, the main features that correlate with efficient LDI are morphology and low thermal conductivity. For example, the ionization performance of nanowires was described as strongly dependent on wire length and density.[49] Here, SiNWs act as tiny antennas where the laser energy is efficiently absorbed. When the energy is focused on a small area it generates a field desorption effect which results in the gas-phase generation of the deposited analyte molecules. This energy focusing effect primarily promotes the desorption of molecules and results in very few surface-related background ions.[49] The SiNW arrays showed superior laser desorption properties because they required less laser energy to desorb molecules.[51] In this case, the signal obtained was enhanced for three main reasons: the

increased absorption of the nanowire forest near the wavelength of the laser, the rapid heating of the silicon core within the insulating oxide sheath and the large surface area of the nanostructures.[51] Vertes et al.[50] made a thorough study of internal energy transfer in laser desorption/ionization from silicon nanowires. They also state that the geometry and thermal properties of the SiNWs are the main factors that increase the efficiency of energy transfer, which, in turn, increases the efficiency of desorption.

The key physical features of nanostructured silicon surfaces that promote efficient ionization are their morphology and their optical and thermal properties. For example, the dimensions of the nanostructured silicon surfaces described by several groups [56,58,62,63] were directly associated with ionization efficiency. In these cases the ion intensity decreased considerably as the length increased, because the longer structures (> 450 nm [58]) did not allow efficient energy transfer from the laser to the analyte. Morris et al.[63] correlated three main features of their nanopost arrays with optimum LDI: namely, (1) well-ordered nanopost arrays; (2) dimensions that maximize laser light absorption and subsequent resonance effects that promote analyte desorption and ionization, and (3) a highly porous surface to maximize analytical sensitivity. Gulbakan et al.[61] have also suggested that these factors generate a local environment to which analytes adhere with optimal heat capacity and heat conductivity. This results in the effective absorption of laser light followed by effective sublimation.

Another morphological aspect that has been associated with increased ionization efficiency is surface roughness. It has been suggested that surface roughness has a more direct effect on the ion intensity efficiency than the silicon nanostructure pore size, depth and surface area/volume ratio.[57]

2.1.5.2. Influence of the functional group

The LDI mechanism of pSi is also affected by the chemical properties of the surface. Hydrophobic or hydrophilic groups can cover the substrate surface and affect the adsorption of the analyte onto the pSi. Hydrophobic surfaces can give intense MS signals for hydrophobic analytes from an aqueous medium because the solvent is not confined to the porous area.[24] On the other hand, hydrophilic surfaces enhance the adsorption of all molecules from an aqueous medium onto the pSi and decrease the ion desorption efficiency.[73] In the case of derivatized substrates with terminal hydride and silanol groups, the deposition of the analyte leads to the adsorption and trapping of the solvent.[30] The interaction between the analyte and metal cations can also influence LDI. Ag is a well-known cationization agent that produces enhanced D/I processes.[82] The LDI of analyte molecules is obtained using Ag nanoparticles through the high absorption and low reflection of energy. The laser energy is quickly absorbed by the Ag nanoparticles, which are rapidly heated, resulting in the vaporization and ionization of the analyte molecules.[81] In the same study, the surface is also functionalized with 4-ATP, which acted as a matrix. This small aromatic molecule enhanced the absorption of energy in the ultraviolet region. Gold is another well-known metal used to functionalize pSi surfaces for enhanced ionization.[29,83] Li et al.[29] describe the effect of the plasmonic property of AuNPs on ionization. They assume that AuNPs act primarily as antennae, which concentrate the laser-induced field within the nanoporous channel and enhance the MS signal. They also postulate that plasmonic metals absorb resonant photons, and the energetic electrons formed by the SPR excitation are transferred to the semiconductor (Si), leading to the accumulation of positive charges on the metal surface.

Chemically derivatized silicon nanostructures have been designed and synthesized to improve LDI efficiency mainly by separating targeted molecules from biological media and inducing a controlled ionization of the selected analytes. Liu et al.[42] functionalized the magnetic mesoporous microspheres with immobilized Cu^{2+} to increase the efficiency of peptide enrichment. Aptamer-functionalized magnetic nanoparticles have also been used to enhance the MS intensity of insulin, because aptamer and magnetism facilitate immunoreactions between the aptamer and the target, and improve detection sensitivity.[44]

A more traditional chemical improvement of nanostructured silicon was reported by Morris et al.[63] They used silanol groups as the proton source for ionization and to induce increased analyte sensitivity. They described the presence and electronegativity of fluorine as a factor that increased the acidity of the silanol group, thus providing a favorable environment for the protonation of molecules. The altered chemical composition of the silicon nanostructures also affected optical absorption. In the study by Chen et al. the absorption values of microcolumns were increased throughout the UV-visible spectrum, and significant absorption extended into the near-IR region.[65]

2.1.5.3. Influence of other interactions

It has also been speculated that the proton affinity of some analytes affects ionization.[30,66,73] The ionization efficiency is similar for analytes with comparable secondary amino groups (e.g. structurally related MA and MDMA) while the ionization efficiency is higher for other analytes (e.g. cocaine) which contain tertiary amino groups and have higher proton affinity.[66] Functional groups and solvents are the primary proton sources, so the right combination of substrate, analyte, and solvent could be critical

for optimal DIOS efficiency. External elements, such as laser fluence and substrate storage, impact the D/I process as well. High laser fluence results in analyte fragmentations that could lead to crowded mass spectra in the low mass range. The laser fluence adjustment was previously studied by monitoring the intensity of the ion *m/z* 184 typical for the phosphatidylcholines head group fragment.[90]

Some LDI mechanisms are directly affected not by the physicochemical properties of the substrate but by the inherent physicochemical properties of analytes such as pI (isoelectric point), hydrophobicity, hydrophilicity, number of charges and their concentration. For example, due to each molecule's specific pI and the sample pH, some molecules appear as negatively charged ions and cannot be detected in positive mode and vice versa. One example of a negatively charged molecule is fibrinopeptide B because it has one aspartic acid and three glutamic acid residues in its sequence.[54] In this study, the super-hydrophilic pattern of the surface was also investigated. This specific surface promoted the better ionization efficiency of peptides because most peptides are positively charged and adsorb specifically to the SiO_2 surface. This specific adhesion property of biological samples has been attributed to amino acid residues which adhere differently to inorganic interfaces such as SiO_2, Si_3N_4, and metals, largely because of differences in their side chains.[54]

Other external factors that affect the LDI mechanism are the laser energy and laser plume. Laser energy can be varied to induce different effects on the D/I processes. Zenobi and Knochenmuss [86] described ion formation and the effect of laser fluency in the classical MALDI process in great detail. A similar description could be given for nanostructure-assisted LDI. However, several authors have suggested that the optimal laser intensity required to get good MS signals is typically much lower than that required for both standard

MALDI and DIOS.[91–93] This is assumed to be due to the optical and thermal properties of silicon nanostructures. The low laser fluencies are also beneficial in the ionization of thermally labile compounds because they can reduce both fragmentation and the energy required for desorption.[65]

The laser plume effect has been described as the presence of electrons in the laser plume due to photoelectric effects. Ions can be generated through electron impact ionization or recombination between electrons emitted from the plume and analyte surface. In this way the desorbed species mix with the plume and protonated species are generated after ion-molecule reactions. At increased laser power, the elevated electron density can neutralize the protons to form hydrogen-free radicals while more alkali ions are released from the hot silicon surface, which results in the formation of peptide-alkali adduct ions.[65]

Another interesting hypothesis suggested that desorption was caused by absorbed UV laser energy being transferred from the surface to pre-charged analytes.[65] However, it is unclear whether the protonation process takes place in solution (before laser interaction) or whether it is a laser-induced proton transfer on/near the surface. Also, residual solvents retained in the cavities of the nanostructured surfaces are probable sources of protons that help to ionize analytes.[65] Tsao et al. proposed another ionization process: they catalyzed glucose samples to negatively charged gluconic acid molecules by on-chip AuNPs-nSi surface Au-based catalyst reactions, thus the MS analysis was carried out in negative mode.[59] In this case, the grafting of the Au nanoparticles to the nanostructured silicon surface enhanced detection sensitivity.

Table 2. Laser desorption/ionization characteristics of MALDI and Silicon-based LDI

	MALDI	Silicon based-LDI
LDI promoting agent	• Organic matrix	• Porous nanostructure • Initiator [a)] • Nanoparticles • Nanowires • Nanostructured surfaces
Properties of promoting agent that influence LDI	• Efficient absorption of laser energy • Embedding of analytes by co-crystallization • Ability to donate/accept protons to/from the sample molecules	• High surface area as a consequence of high pore density • Edges and protrusions facilitate energy accumulation • Surface characteristics that promote molecule adhesion • Specific dimensions that maximize optical absorption • Low thermal conductivity
Selectivity of LDI	• Choice of matrix for ionization mode (positive or negative) • Choice of matrix for analyte molecular properties	• Surface modification using functional groups to mimic analyte properties • Functionalization with ligands that bind specific analytes • Cationization using metals

[a)]In case of NIMS

2.1.6. Discussion

2.1.6.1. Fabrication

Silicon is one of the prime candidates for fabricating LDI-MS substrates for three main reasons: it is biologically inert; the technology is advanced and flexible, and silicon nanostructures can be designed with controllable morphology and properties for LDI-MS. It is important to mention that silicon is a material that can be easily stabilized, derivatized and functionalized.

In the case of silicon substrates designed for LDI-MS experiments, the wet (chemical) fabrication techniques used to create pSi slowly evolved to dry (physical) techniques. Wet techniques use highly toxic compounds (e.g., piranha solution for cleaning and HF for etching) in dangerous fabrication methods (e.g., electrochemical etching in a closed Teflon cell). The dry fabrication techniques that have emerged eliminate all these dangers to the user. These techniques also improve all the aspects of a good quality substrate: the fabrication process is highly repetitive, the surface is free of air and liquid contaminants, fabrication can be automated and, most importantly, they are safe. Most dry fabrication techniques are derived from micro/nanoelectronic fabrication methods. This is another reason why dry fabrication methods are becoming more popular: silicon technology and silicon nanostructure fabrication methods are improving day by day.

2.1.6.2. Surface modification

Silicon nanostructures of all types —nanoparticles, nanowires, black silicon, pSi, etc.— have been stabilized and derivatized using different strategies for many purposes. There is no standard procedure for all the types of experiments. Muthu et al.[92] suggested that sample preparation is an art

form, and, given its complexity, the surface modification of any silicon nanostructure can be considered likewise. Surfaces can be modified with a variety of agents: from metal nanoparticles (Ag, Au, Cu, etc.) to small (amine groups, perfluorophenyls, etc.) and large (antibodies, etc.) molecules (see Table 1). Depending on the application of the substrate, a targeted analysis method can be designed by choosing the appropriate functionalization method and/or combining various functionalization methods to reduce unwanted signals or to obtain a broader range of detection. All these surface-modified matrix-free methods can be used together with an organic matrix to expand the detection range from small to large molecules.

2.1.6.3. Analysis of liquid samples

Although silicon nanostructures can be very repetitive and homogeneous, the reliability of the LDI-MS measurements also depends on the sample deposition method. Irreproducible sample deposition leads to irreproducible results. This is largely due to the uneven crystallization of liquid samples on the substrate, which induces signal variation between different spots of the same sample. For this reason, sample deposition was rigorously studied for silicon nanostructures. In the case of pSi, acoustic printing was used to make liquid sample deposition reproducible.[76,94]]

As we have described above, silicon-based nanoparticles/nanowires have been used as LDI substrates. In this case, the sample analyte is usually mixed with the nanoparticle/nanowire solution in the appropriate concentrations prior to spotting on the MALDI target plate and subsequent co-crystallization.[45,46] Although this wet chemistry deposition technique is very flexible, it has the same problems as organic matrices (i.e. heterogeneous spots).

2.1.6.4. Analysis of tissue samples

Most of the studies mentioned in this report focus on liquid samples. However, the analysis of tissues is also in high demand. The most important consideration in an MSI experiment is the performance of the substrate-tissue-air system. In standard MALDI analysis, the tissue is cut into slices ~10 μm thick and each slice is mounted onto a glass slide coated with indium tin oxide (ITO), and then the tissue is covered with a thin layer of matrix.[8] The thickness of the tissue does not affect the transfer of energy from the laser to the matrix and from the matrix to the tissue for LDI processes. On the other hand, when the matrix and the ITO glass slide are replaced by a nanostructured surface on which the tissue is mounted, the thickness of the tissue is important. The laser energy has to pass through the tissue and reach the nanostructured surface in order to promote ion desorption and ionization processes. In NIMS applications, to allow the laser to get to the tissue-nanostructure interface, the tissue slices are 3-5 □m thick, much thinner than in usual MSI experiments.[31,74,75] Even in this case, laser power needs to be high, which often burns the tissue and produces harder ionization.

An alternative technique that avoids the effect of tissue thickness is imprinting (or stamping) a tissue on the surface.[68] The imprinting process consists of placing the tissue in contact with the nanostructured substrate and then removing it, leaving only the molecules from the tissue sample that adhere to the substrate. Although the imprinting process does not require thin tissue samples to be cut and deposited on the surface, it has been reported that it lacks reliability because of possible smears.[95] This method means that MSI can have new applications in clinical practice: for example, a tissue can be imprinted on a silicon-based substrate for needle biopsy processes, where the biopsy probe containing the silicon substrate touches the tissue sample to be analyzed.[96]

The imprinting process is compatible with the new strategies that can be developed to allow the adhesion of specific molecules to the nanostructured surface through surface functionalization. The silicon-based nanoparticle methods presented in this review often use linker molecules for the specific detection of analytes. This approach should be considered for nanostructured silicon surfaces as well.

2.1.6.5. Clinical applications of Si-based LDI-MS

The emerging field of Si-based LDI-MS has already yielded several applications that can be directly translated to the clinics. For instance:

- *High-throughput screening and quantification*: pSi SALDI-MS has been used in the compliance monitoring of opioid addiction programs. Guinan et al.[70] analyzed samples of saliva, urine, and plasma from 13 opioid dependent patients by pSi SALDI-MS and Liquid Chromatography-MS (LC-MS). Quantitation of methadone by pSi SALDI-MS was in agreement with LC-MS results, adding the advantages of shorter analysis times, and lower volumes of samples and solvents.

- *Improved detection of biomarkers for diagnosis*: pSi-Au nanoparticles have been used to improve the detection of peptides in serum by diminishing the signal suppression effect caused by proteins. With this strategy, Li et al.[29] obtained clear peptide fingerprints that were used to correctly discriminate colorectal cancer patients.

- *Non-invasive tests*: DIOS-MSI has been used to detect and visualize the distribution of compounds from sweat of fingerprints.[32] As a non-invasive test, it is a great alternative to monitor illicit drugs, since the

samples cannot be adulterated and the MSI analysis definitively link the identity of individuals to its results by their fingerprints. Moreover, it could be used to monitor excreted metabolites from the detoxification of contaminants and medicines, and biomarkers of diseases from sweat and skin.

2.1.6.6. Guidelines for detecting molecules by Si-based LDI-MS

All the detected molecules and the detection strategies used in the publications presented in this progress report are listed in **Table S3** and summarized in **Figure 5**. The bar charts in **Figure 5** show the great versatility of Si-based substrates, as all types of Si substrate have been used to detect most types of analytes. Since there are no standard protocols for detecting all kinds of molecules simultaneously, each strategy focuses on detecting specific analytes. As such, we highlight the following trends in Si LDI-MS:

A. Peptides and proteins are often detected with the help of organic matrices while small molecules are detected without this help. Larger molecules are known to be thermally labile and they need controlled energy transfer from an organic matrix if they are to be analyzed by the laser desorption method.
B. Most of the pSi, SiNW and SiNP surfaces are modified, while half of the work published on nano Si does not use surface modification. This suggests that dry fabrication techniques produce stable surfaces, while wet chemistry fabrication techniques produce surfaces that need stabilization.
C. Si LDI-MS first appeared as DIOS (pSi), then evolved into NIMS (pSi) and lately it has appeared as nanostructured silicon LDI. Organic matrices are rarely used together with Si-based LDI nanostructures in recent works.

We envision that matrix-free strategies will be the LDI strategy of choice in the future.

D. The evolution of Si-based substrates for LDI MS indicates two major trends as future perspective: (1) functionalized Si-based strategies for targeted analysis of molecules and (2) Si-based substrates for MS imaging applications.

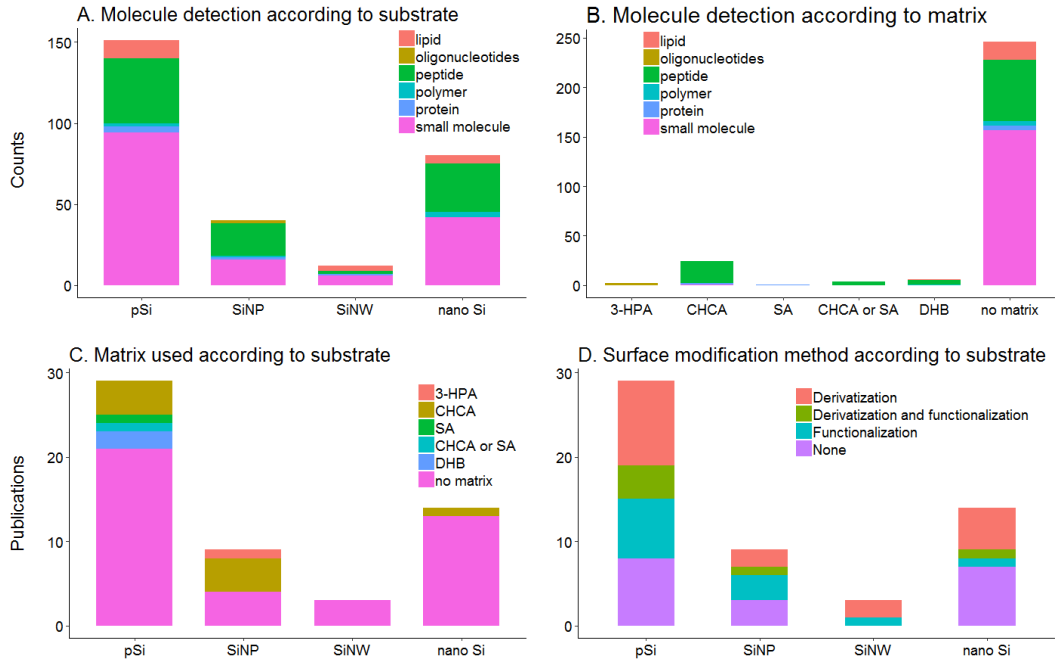

Figure 5. Bar charts summarizing the detection strategies used in the publications reviewed in this study.

2.1.7. Conclusion

The wide variety of silicon nanostructures used for MS applications illustrate the major prerequisites for successful LDI-MS analysis. The basic requirements for all silicon-based substrates are the following: they must (1) absorb UV laser irradiation without being deteriorated by it; (2) provide a surface that can be easily functionalized; (3) be stable under vacuum; (4)

improve and enhance the analyte's ionizability; (5) not cause interferences or clusters with the target analyte; (6) be easy to fabricate; (7) allow reproducible results and, finally, (8) be cheap. Bearing in mind that silicon technology (regardless of the field of study) is constantly advancing, the fabrication and functionalization of silicon-based substrates will rapidly adapt to the necessities of mass spectrometry applications. Silicon-based LDI-MS will become a solid matrix-free alternative to traditional MALDI-MS and will speed up the transition of MSI into the clinic.

2.1.8. References

[1] D. S. Cornett, M. L. Reyzer, P. Chaurand, R. M. Caprioli, *Nat. Methods* **2007**, *4*, 828.

[2] H. N. Abdelhamid, *TrAC - Trends Anal. Chem.* **2017**, *89*, 68.

[3] L. A. McDonnell, R. M. A. Heeren, *Mass Spectrom. Rev.* **2007**, *26*, 606.

[4] J. L. Norris, R. M. Caprioli, *PROTEOMICS - Clin. Appl.* **2013**, *7*, 733.

[5] C.-K. Chiang, W.-T. Chen, H.-T. Chang, *Chem. Soc. Rev.* **2011**, *40*, 1269.

[6] C. Gregson, *Biosci. Horizons* **2009**, *2*, 134.

[7] E. Gemperline, S. Rawson, L. Li, *Anal. Chem.* **2014**, *86*, 10030.

[8] N. Ogrinc Potočnik, T. Porta, M. Becker, R. M. A. Heeren, S. R. Ellis, *Rapid Commun. Mass Spectrom.* **2015**, *29*, 2195.

[9] D. S. Peterson, *Mass Spectrom. Rev.* **2007**, *26*, 19.

[10] L. Qiao, B. Liu, H. H. Girault, *Nanomedicine* **2010**, *5*, 1641.

[11] C. Y. Shi, C. H. Deng, *Analyst* **2016**, *141*, 2816.

[12] K. P. Law, J. R. Larkin, *Anal. Bioanal. Chem.* **2011**, *399*, 2597.

[13] T. Guinan, P. Kirkbride, P. E. Pigou, M. Ronci, H. Kobus, N. H. Voelcker, **2014**.

[14] Y. E. Silina, D. A. Volmer, *Analyst* **2013**, *138*, 7053.

[15] J. Sekuła, J. Nizioł, W. Rode, T. Ruman, *Anal. Chim. Acta* **2015**, *875*, 61.

[16] M. Dufresne, A. Thomas, J. Breault-Turcot, J.-F. Masson, P. Chaurand, *Anal. Chem.* **2013**, *85*, 3318.

[17] H. Kawasaki, T. Ozawa, H. Hisatomi, R. Arakawa, *Rapid Commun. Mass Spectrom.* **2012**, *26*, 1849.

[18] Y. Gholipour, S. L. Giudicessi, H. Nonami, R. Erra-Balsells, *Anal. Chem.* **2010**, *82*, 5518.

[19] A. Y. Lim, J. Ma, Y. C. F. Boey, *Adv. Mater.* **2012**, *24*, 4211.

[20] Y. He, C. Fan, S. T. Lee, *Nano Today* **2010**, *5*, 282.

[21] F. Peng, Y. Su, Y. Zhong, C. Fan, S. T. Lee, Y. He, *Acc. Chem. Res.* **2014**, *47*, 612.

[22] J. J. Thomas, Z. Shen, J. E. Crowell, M. G. Finn, G. Siuzdak, *Proc. Natl. Acad. Sci. U. S. A.* **2001**, *98*, 4932.

[23] T. R. Northen, O. Yanes, M. T. Northen, D. Marrinucci, W. Uritboonthai, J. Apon, S. L. Golledge, A. Nordström, G. Siuzdak, *Nature* **2007**, *449*, 1033.

[24] J. Wei, J. M. Buriak, G. Siuzdak, *Nature* **1999**, *399*, 243.

[25] N. Budimir, J. C. Blais, F. Fournier, J. C. Tabet, *Rapid Commun. Mass Spectrom.* **2006**, *20*, 680.

[26] A. G. Cullis, L. T. Canham, P. D. J. Calcott, *J. Appl. Phys.* **1997**, *82*, 909.

[27] R. D. . Lowe, E. J. Szili, P. Kirkbride, H. Thissen, G. Siuzdak, N. H. Voelcker, *Anal. Chem.* **2010**, *82*, 4201.

[28] M. J. Sweetman, M. Ronci, S. R. Ghaemi, J. E. Craig, N. H. Voelcker, *Adv. Funct. Mater.* **2012**, *22*, 1158.

[29] X. Li, J. Tan, J. Yu, J. Feng, A. Pan, S. Zheng, J. Wu, *Anal. Chim. Acta* **2014**, *849*, 27.

[30] Y. Chen, H. Chen, A. Aleksandrov, T. M. Orlando, *J. Phys. Chem. C* **2008**, *112*, 6953.

[31] G. J. Patti, H. K. Woo, O. Yanes, L. Shriver, D. Thomas, W. Uritboonthai, J. V Apon, R. Steenwyk, M. Manchester, G. Siuzdak, *Anal. Chem.* **2009**, *82*, 4271.

[32] T. Guinan, C. Della Vedova, H. Kobus, N. H. Voelcker, *Chem. Commun.* **2015**, *51*, 6088.

[33] L. Chen, Z.-T. Chen, J. Wang, S.-J. Xiao, Z.-H. Lu, Z.-Z. Gu, L. Kang, J. Chen, P.-H. Wu, Y.-C. Tang, J.-N. Liu, *Lab Chip* **2009**, *9*, 756.

[34] H. Yan, A. Ahmad-Tajudin, M. Bengtsson, S. Xiao, T. Laurell, S. Ekstr??m, *Anal. Chem.* **2011**, *83*, 4942.

[35] J. Li, C. Lu, X. K. Hu, X. Yang, A. V. Loboda, R. H. Lipson, *Int. J. Mass Spectrom.* **2009**, *285*, 137.

[36] D. Brodoceanu, R. Elnathan, B. Prieto-Simo, B. Delalat, T. Guinan, E. Kroner, N. H. Voelcker, T. Kraus, **2014**.

[37] X. Yongsheng, T. R. Scott, K. T. Darrell, T. Jia-Yuan, H. Lin, *J. Phys. Chem. C* **2009**, *113*, 3076.

[38] M. Gaspari, M. M. Cheng, R. Terracciano, X. Liu, A. J. Nijdam, L. Vaccari, E. Fabrizio, E. F. Petricoin, L. A. Liotta, G. Cuda, S. Venuta, M. Ferrari, *J. Proteome Res.* **2006**, *5*, 1261.

[39] Y. Goto, N. Mizoshita, Y. Yamada, Y. Maegawa, J. Amano, S. Inagaki, *Microporous Mesoporous Mater.* **2018**, *268*, 125.

[40] M. Dupré, S. Cantel, J. O. Durand, J. Martinez, C. Enjalbal, *Anal. Chim. Acta* **2012**, *741*, 47.

[41] H. Chen, C. Deng, X. Zhang, *Angew. Chemie Int. Ed.* **2010**, *49*, 607.

[42] S. Liu, H. Chen, X. Lu, C. Deng, X. Zhang, P. Yang, *Angew. Chemie - Int. Ed.* **2010**, *49*, 7557.

[43] H. Chen, S. Liu, H. Yang, Y. Mao, C. Deng, X. Zhang, P. Yang, *Proteomics* **2010**, *10*, 930.

[44] Y. Xiong, C. Deng, X. Zhang, P. Yang, *ACS Appl. Mater. Interfaces* **2015**, *7*, 8451.

[45] X. Zhu, L. Wu, D. C. Mungra, S. Xia, J. Zhu, *Analyst* **2012**, *137*, 2454.

[46] X. Wen, S. Dagan, V. H. Wysocki, *Anal. Chem.* **2007**, *79*, 434.

[47] S. Dagan, Y. Hua, D. J. Boday, A. Somogyi, R. J. Wysocki, V. H. Wysocki, *Int. J. Mass Spectrom.* **2009**, *283*, 200.

[48] M. Hong, X. Zhou, J. Li, Y. Tian, J. Zhu, *Anal. Chem.* **2009**, *81*, 8839.

[49] E. P. Go, J. V. Apon, G. Luo, A. Saghatelian, R. H. Daniels, V. Sahi, R. Dubrow, B. F. Cravatt, A. Vertes, G. Siuzdak, *Anal. Chem.* **2005**, *77*, 1641.

[50] G. Luo, Y. Chen, H. Daniels, R. Dubrow, A. Vertes, *J. Phys. Chem. B* **2006**, *110*, 13381.

[51] A. Muck, T. Stelzner, U. Hübner, S. Christiansen, A. Svatos, *Lab Chip* **2010**, *10*, 320.

[52] R. Daniels, S. Dikler, E. Li, C. Stacey, *J. Assoc. Lab. Autom.* **2008**, *13*, 314.

[53] G. Piret, H. Drobecq, Y. Coffinier, O. Melnyk, R. Boukherroub, *Langmuir* **2010**, *26*, 1354.

[54] F. Lapierre, G. Piret, H. Drobecq, O. Melnyk, Y. Coffinier, V. Thomy, R. Boukherroub, *Lab Chip* **2011**, *11*, 1620.

[55] M. Dupré, Y. Coffinier, R. Boukherroub, S. Cantel, J. Martinez, C. Enjalbal, *J. Proteomics* **2012**, *75*, 1973.

[56] R. A. Picca, C. D. Calvano, M. J. Lo Faro, B. Fazio, S. Trusso, P. M. Ossi, F. Neri, C. D'Andrea, A. Irrera, N. Cioffi, *J. Mass Spectrom.* **2016**, 849.

[57] W. Y. Chen, J. T. Huang, Y. C. Cheng, C. Chien, C. W. Tsao, *Anal. Chim. Acta* **2011**, *687*, 97.

[58] H. Z. Alhmoud, T. M. Guinan, R. Elnathan, H. Kobus, N. H. Voelcker, *Analyst* **2014**, *139*, 5999.

[59] C. W. Tsao, Z. J. Yang, *ACS Appl. Mater. Interfaces* **2015**, *7*, 22630.

[60] P. Y. Chen, C. Y. Hsieh, C. J. Shih, Y. J. Lin, C. W. Tsao, Y. L. Yang, *J. Nat. Prod.* **2018**, *81*, 1527.

[61] B. Gulbakan, D. Park, M. Kang, K. Kececi, C. R. Martin, D. H. Powell, W. Tan, *Anal. Chem.* **2010**, *82*, 7566.

[62] Y. Wang, Z. Zeng, J. Li, L. Chi, X. Guo, N. Lu, *J. Am. Soc. Mass Spectrom.* **2013**, *24*, 66.

[63] N. J. Morris, H. Anderson, B. Thibeault, A. Vertes, M. J. Powell, T. T. Razunguzwa, *RSC Adv.* **2015**, *5*, 72051.

[64] A. R. Korte, N. J. Morris, A. Vertes, *Anal. Chem.* **2019**, *91*, 3951.

[65] Y. Chen, A. Vertes, *Anal. Chem.* **2006**, *78*, 5835.

[66] T. Guinan, M. Ronci, H. Kobus, N. H. Voelcker, *Talanta* **2012**, *99*, 791.

[67] Y.-Q. Chen, F. Bi, S.-Q. Wang, S.-J. Xiao, J.-N. Liu, *J. Chromatogr. B* **2008**, *875*, 502.

[68] S. A. Trauger, E. P. Go, Z. Shen, J. V Apon, B. J. Compton, E. S. P. Bouvier, M. G. Finn, G. Siuzdak, *Anal. Chem.* **2004**, *76*, 4484.

[69] M. Ronci, D. Rudd, T. Guinan, K. Benkendorff, N. H. Voelcker, *Anal. Chem.* **2012**, *84*, 8996.

[70] T. M. Guinan, D. Neldner, P. Stockham, H. Kobus, C. B. Della Vedova, N. H. Voelcker, *Drug Test. Anal.* **2017**, *9*, 769.

[71] D. Rudd, M. Ronci, M. R. Johnston, T. Guinan, N. H. Voelcker, K. Benkendorff, *Sci. Rep.* **2015**, *5*, 1.

[72] T. Guinan, M. Ronci, R. Vasani, H. Kobus, N. H. Voelcker, *Talanta* **2015**, *132*, 494.

[73] S. Tuomikoski, K. Huikko, K. Grigoras, P. Ostman, R. Kostiainen, M. Baumann, J. Abian, T. Kotiaho, S. Franssila, *Lab Chip* **2002**, *2*, 247.

[74] G. J. Patti, L. P. Shriver, C. A. Wassif, H. K. Woo, W. Uritboonthai, J. Apon, M. Manchester, F. D. Porter, G. Siuzdak, *Neuroscience* **2010**, *170*, 858.

[75] T. N. Moening, V. L. Brown, L. He, *Anal. Methods* **2016**, *8*, 8234.

[76] J. Gao, M. De Raad, B. P. Bowen, R. N. Zuckermann, T. R. Northen, *Anal. Chem.* **2016**, *88*, 1625.

[77] H. K. Woo, T. R. Northen, O. Yanes, G. Siuzdak, *Nat. Protoc.* **2008**, *3*, 1341.

[78] J. Gao, K. B. Louie, P. Steinke, B. P. Bowen, M. De Raad, R. N. Zuckermann, G. Siuzdak, T. R. Northen, *Anal. Chem.* **2017**, *89*, 6521.

[79] J. Heinemann, K. Deng, S. C. C. Shih, J. Gao, P. D. Adams, A. K. Singh, T. R. Northen, *Lab Chip* **2017**, *17*, 323.

[80] H. Zhou, S. Xu, M. Ye, S. Feng, C. Pan, X. Jiang, X. Li, G. Han, Y. Fu, H. Zou, *J. Proteome Res.* **2006**, *5*, 2431.

[81] H. Yan, N. Xu, W.-Y. Huang, H.-M. Han, S.-J. Xiao, *Int. J. Mass Spectrom.* **2009**, *281*, 1.

[82] O. J. R. Gustafsson, T. M. Guinan, D. Rudd, H. Kobus, K. Benkendorff, N. H. Voelcker, *Rapid Commun. Mass Spectrom.* **2017**, *31*, 991.

[83] J. Wang, M. Jie, H. Li, L. Lin, Z. He, S. Wang, J. M. Lin, *Talanta* **2017**, *168*, 222.

[84] M. Karas, D. Bachmann, F. Hillenkamp, *Anal. Chem.* **1985**, *57*, 2935.

[85] K. Dreisewerd, *The desorption process in MALDI*; 2003; Vol. 103.

[86] R. Zenobi, R. Knochenmuss, *Mass Spectrom. Rev.* **1998**, *17*, 337.

[87] M. Karas, R. Krüger, *Chem. Rev.* **2003**, *103*, 427.

[88] W. C. Chang, L. C. L. Huang, Y. S. Wang, W. P. Peng, H. C. Chang, N. Y. Hsu, W. Bin Yang, C. H. Chen, *Anal. Chim. Acta* **2007**, *582*, 1.

[89] T. W. Jaskolla, M. Karas, *J. Am. Soc. Mass Spectrom.* **2011**, *22*, 976.

[90] P. Ràfols, D. Vilalta, S. Torres, R. Calavia, B. Heijs, L. A. McDonnell, J. Brezmes, E. del Castillo, O. Yanes, N. I. Ramírez, X. CorreigID, **2018**.

[91] J. A. Stolee, B. N. Walker, V. Zorba, R. E. Russo, A. Vertes, *Phys. Chem. Chem. Phys.* **2012**, *14*, 8453.

[92] M. Muthu, S. Chun, H.-F. Wu, M. W. Duncan, J. Gopal, *J. Mass Spectrom.* **2018**, 525.

[93] R. A. Picca, C. D. Calvano, N. Cioffi, F. Palmisano, *Nanomaterials* **2017**, *7*, 75.

[94] J. L. Norris, R. M. Caprioli, *Chem Rev*. **2013**, *113*, 2309.

[95] Y. J. Lee, D. C. Perdian, Z. Song, E. S. Yeung, B. J. Nikolau, *Plant J*. **2012**, *70*, 81.

[96] J. Kriegsmann, M. Kriegsmann, R. Casadonte, *Int. J. Oncol*. **2015**, *46*, 893.

2.1.9. Supporting Information

Table S1. Electrochemical etching fabrication methods

Pre-etch cleaning process	Current density (mA/cm^2)	Etching solution (vol/vol)	Time (sec)	Illumination	Teflon cell	Ref.
n-type	71	1:1 EtOH/49% HF	60-180	300-W tungsten filament bulb	N/A	[24]
p-type	37	1:1 EtOH/49% HF	10800	in the dark	N/A	[24]
5% HF/ethanol solution and then rinsed in deionized water, acetone and methanol	40	1:1 EtOH/48% HF	300 prior laser and 900 with laser	4 ns pulses of a 355 nm frequency-tripled Nd:YAG laser operating at a 20Hz repetition rate and with an intensity of 4 W/cm^2	Yes	[35]
N/A	5	25% EtOH/HF	60	white-light 50 mW/cm^2	N/A	[22]
Methanol wash 3-5 times	48	EtOH /25%HF	1800	N/A	Yes	[23]
N/A	10 - 50	1:1 EtOH/50%HF	N/A	300–500 W halogen lamp	Yes	[73]
N/A	5	25% EtOH/HF	120	white light	N/A	[68]
N/A	4	2:3 EtOH/49%HF	100	250 W tungsten filament bulb	Yes	[80]
Boiled in 3:1 (v/v) concentrated H_2SO_4/30% H_2O_2 for 30min and then rinsed extensively with Milli-Q water	100	1:3 EtOH/40%HF	180	N/A	N/A	[67]
Cleaned with 3:1 (v/v) H_2SO_4/H_2O_2 for 30 min, rinsed with copious amounts of	60	1:3 EtOH/40%HF	600	In the dark	Yes	[81]

water and absolute ethanol, and then immersed in water prior to the etching procedure						
Piranha solution for 30 min, rinsed with nano-pure water, and blown dry with nitrogen gas	300	EtOH /25%HF	1800	N/A	N/A	[74]
N/A	20	1:1 EtOH/HF	120	fiber optic light source*	Yes	[69]
Rinsed with methanol, acetone and DCM	20	1:3 EtOH/48%HF	300	N/A	Yes	[28]
Sonicated in 99.9% methanol and dried under a stream of nitrogen	4	1:1 EtOH/HF	120	fiber optic light source*	Yes	[66]
N/A	20	1:1 EtOH/HF	120	fiber optic light source*	Yes	[32]
N/A	27	1:2 EtOH/HF	300	fiber optic light source*	Yes	[70]
N/A	20	1:1 EtOH/HF	120	fiber optic light source*	Yes	[82]
Sonicated in 99.9% methanol and dried under a stream of nitrogen	3.2	1:1 EtOH/HF	120	fiber optic light source*	Yes	[72]
N/A	20	1:1 EtOH/HF	120	fiber optic light source*	Yes	[71]
N/A	30	1:4 EtOH/40%HF	30–600	N/A	Yes	[29]
Piranha solution for 30 min, thoroughly washed in DI H_2O and dried with N_2	32	EtOH /25%HF	1800	In the dark	N/A	[75]
Three solvent baths: trichloroethylene, acetone, and methanol for 15 min sequentially	2360	EtOH /24%HF	120-4800	N/A	Yes	[78]
N/A	N/A	HF/HNO3/ H2O (1:3:5) solution	60-240	N/A	N/A	[30]
Piranha solution for 30 min and rinsed by nanopure water and dried with N_2	300	EtOH /25%HF	1800	N/A	Yes	[31]

N/A - information not available; * - no mention of light source or type

Table S2. Stabilization methods of porous silicon substrates

Stabilization method	Ref
Ozone oxidation and immersion in diluted aqueous HF solution	[22]
Ozone oxidation (hydroxyl-terminated surface)	[23,66, 68–72,82]
Ozone oxidation and re-etching in ethanol containing 5% HF	[80]
Wash with absolute ethanol and drying with nitrogen	[81]
pSi rinsed with a mixture of ethanol–deionized water, kept in ethanol for 5 min and dried carefully under nitrogen flow	[73]
pSi was rinsed with pure ethanol and pentane, and then dried with nitrogen	[67]
pSi washed with methanol, acetone and DCM and dried with nitrogen	[28]
Immersion in deionized water, then in ethanol and pentane, dried with nitrogen and stored in a vacuum chamber	[38]

Table S3. Molecules and their respective detection strategies

Molecule	Class	Substrate	Surface modification	Matrix	Ref.	Year
1,2-dihexadecanoyl-sn-glycero-3-phosphocholine (DPPC)	small molecule	pSi	None	no matrix	30	2009
1,4-b-D-cellotetraose-probe	peptide	nano Si	None	no matrix	51	2017
14 Lys-N peptides	peptide	nano Si	Derivatization	no matrix	73	2012
15 tryptic peptides	peptide	nano Si	Derivatization	no matrix	73	2012
1-Naphthalene methylamine	small molecule	pSi	Derivatization	no matrix	43	2002
2-(2-methyl-5-nitro-1H-imidazole-1-yl)ethanol	small molecule	SiNP	None	no matrix	59	2012

2-Naphthylacetic acid	small molecule	pSi	Derivatization	no matrix	43	2002
4-amino-1-benzylpyridinium bromide	small molecule	pSi	None	no matrix	30	2009
4-chloro benzylpyridinium salts	small molecule	SiNP	Derivatization	no matrix	61	2009
6,6′-dibromoindigo	small molecule	pSi	Derivatization	no matrix	35	2012
7DHC	small molecule	pSi	Functionalization	no matrix	42	2010
ACTH clip 1–17	peptide	nano Si	Derivatization	no matrix	75	2014
ACTH clip 18–39	peptide	nano Si	Derivatization	no matrix	75	2014
ACTH residues (“clip” 1–17, 18–39, 7–38)	peptide	pSi	None	no matrix	50	2017
adenosine	small molecule	nano Si	None	no matrix	49	2016
adenosine	small molecule	nano Si	None	no matrix	77	2010
adenovirus penton protein	protein	pSi	None	no matrix	21	2001
adrenocorticotropic hormone	peptide	pSi	None	no matrix	23	1999
Adrenocorticotropic Hormone (ACTH) 1–17	peptide	pSi	None	no matrix	29	2009
alanine	small molecule	pSi	Derivatization	no matrix	34	2004
altretamine	small molecule	SiNP	Derivatization	no matrix	60	2007
ametryn	small molecule	SiNP	Derivatization	no matrix	60	2007
amiodarone	small molecule	nano Si	None	no matrix	65	2015
amoxicillin	small molecule	SiNP	None	no matrix	59	2012
amphetamine	small molecule	pSi	Derivatization	no matrix	26	2015
angiotensin	peptide	pSi	None	no matrix	23	1999
angiotensin	small molecule	pSi	None	no matrix	50	2017
angiotensin I	peptide	pSi	Derivatization	CHCA or SA	31	2006
angiotensin I	peptide	pSi	Functionalization	CHCA	28	2011
angiotensin I	peptide	nano Si	Derivatization	no matrix	72	2010
angiotensin I	peptide	nano Si	Derivatization	no matrix	75	2014
angiotensin I	peptide	nano Si	Derivatization	no matrix	76	2011
angiotensin I	peptide	pSi	None	DHB	47	2016
angiotensin I	peptide	nano Si	None	no matrix	70	2006

angiotensin II	peptide	SiNP	Functionalization	CHCA	56	2010
angiotensin II	peptide	nano Si	Derivatization	no matrix	75	2014
Angiotensin II	peptide	SiNP	None	CHCA	58	2010
angiotensin II (DRVYIHPF)	peptide	SiNP	Derivatization and functionalization	CHCA	55	2010
angiotensin II (DRVYIHPF)	peptide	SiNP	Derivatization	no matrix	60	2007
angiotensin III	peptide	pSi	None	no matrix	30	2009
angiotensin III	peptide	pSi	None	DHB	47	2016
antiviral drug WIN	small molecule	pSi	None	no matrix	23	1999
Arachidic acid	small molecule	pSi	None	no matrix	24	2006
arachidonic acid	lipid	nano Si	Functionalization	no matrix	64	2016
arginine	small molecule	nano Si	None	no matrix	49	2016
arginine	small molecule	pSi	None	no matrix	50	2017
arginine	small molecule	pSi	None	no matrix	52	2008
arginine acids	small molecule	nano Si	None	CHCA	69	2013
Aspartic acid	small molecule	SiNP	None	no matrix	59	2012
Behenic acid	small molecule	pSi	None	no matrix	24	2006
Behentrimonium	small molecule	pSi	Functionalization	no matrix	41	2017
benzylpyridinium ions	small molecule	SiNW	Derivatization	no matrix	67	2006
beta-cyclodextrin	peptide	pSi	Functionalization	no matrix	48	2009
beta-lactoglobulin	protein	pSi	None	no matrix	21	2001
BNP	peptide	pSi	Derivatization and functionalization	CHCA	33	2008
bombesin	peptide	nano Si	Derivatization	no matrix	75	2014
bovine insulin	peptide	nano Si	None	no matrix	70	2006
bradykinin	peptide	pSi	None	no matrix	23	1999
Bradykinin	peptide	pSi	None	no matrix	29	2009
bradykinin	peptide	pSi	None	DHB	47	2016
Bradykinin	peptide	nano Si	None	no matrix	49	2016

bradykinin	small molecule	pSi	None	no matrix	50	2017
bradykinin	peptide	nano Si	None	CHCA	69	2013
bradykinin	peptide	nano Si	None	no matrix	77	2010
bradykinin 1-7	peptide	pSi	Derivatization	no matrix	22	2007
bradykinin 2-9	peptide	pSi	Derivatization	no matrix	22	2007
BSA	peptide	pSi	Derivatization	no matrix	22	2007
BSA	peptide	pSi	None	no matrix	21	2001
BSA	peptide	SiNW	Derivatization	no matrix	66	2005
BSA digest	peptide	SiNP	None	CHCA	58	2010
BSA digest	peptide	nano Si	None	no matrix	77	2010
Buprenorphine	small molecule	pSi	Derivatization	no matrix	43	2002
buprenorphine	small molecule	nano Si	None	no matrix	65	2015
butyrylcarnitine (C4)	small molecule	nano Si	None	no matrix	77	2010
caffeine	small molecule	pSi	None	no matrix	23	1999
calcitonin	peptide	pSi	Derivatization	CHCA or SA	31	2006
carnitine (C1)	small molecule	nano Si	None	no matrix	77	2010
cellobiose-probe	peptide	nano Si	None	no matrix	51	2017
cellotriose-probe	peptide	nano Si	None	no matrix	51	2017
chlorpheniramine	small molecule	nano Si	None	no matrix	65	2015
cholesterol	lipid	pSi	Functionalization	no matrix	41	2017
cholesterol	small molecule	pSi	Functionalization	no matrix	42	2010
cholesterol	small molecule	pSi	Functionalization	no matrix	48	2009
cholesterol	small molecule	pSi	Functionalization	no matrix	48	2009
cholesterol	small molecule	pSi	Functionalization	no matrix	48	2009
cholesterol	lipid	pSi	Derivatization	no matrix	26	2015
choline	small molecule	pSi	None	no matrix	21	2001
clonidine	small molecule	nano Si	Derivatization	no matrix	68	2008
clonidine	small molecule	nano Si	None	no matrix	65	2015
cocaine	small molecule	pSi	Derivatization	no matrix	32	2012

cocaine	small molecule	pSi	Derivatization	no matrix	38	2015
cocaine	small molecule	SiNW	Derivatization	no matrix	66	2005
codeine	small molecule	pSi	Derivatization	no matrix	22	2007
codeine	small molecule	pSi	Derivatization	no matrix	26	2015
corticosterone	small molecule	pSi	Functionalization	no matrix	48	2009
cytochrome C	protein	SiNP	Derivatization and functionalization	CHCA	55	2010
Dalargin	small molecule	pSi	None	no matrix	29	2009
decanoylcarnitine (C6)	small molecule	nano Si	None	no matrix	77	2010
des-Arg1-Bradykinin	peptide	pSi	Derivatization	no matrix	43	2002
des-Arg9 Bradykinin	peptide	nano Si	None	no matrix	74	2011
des-Arg9-bradykinin	peptide	pSi	Derivatization	no matrix	34	2004
des-Arg9-bradykinin	peptide	SiNW	Derivatization	no matrix	66	2005
des-Arg-bradykinin	peptide	nano Si	Derivatization	no matrix	72	2010
des-Arg-Bradykinin	peptide	nano Si	Derivatization	no matrix	76	2011
des-arg-bradykinin	peptide	pSi	None	no matrix	23	1999
dextromethorphan	small molecule	nano Si	None	no matrix	51	2017
diacylglycerol	lipid	nano Si	Functionalization	no matrix	64	2016
dibutylphosphoric acid	small molecule	SiNP	Derivatization	no matrix	60	2007
dichloromethyl phosphonate	small molecule	pSi	Derivatization	no matrix	43	2002
dichloromethylene bisphosphonate	small molecule	pSi	Derivatization	no matrix	43	2002
diglycerides	lipid	SiNW	Functionalization	no matrix	63	2010
ds-DNA	oligonucleotides	SiNP	Functionalization	3-HPA	62	2009
DTDMA C16/C16	small molecule	pSi	Functionalization	no matrix	41	2017
DTDMA C16/C18	small molecule	pSi	Functionalization	no matrix	41	2017
DTDMA C18/C18	small molecule	pSi	Functionalization	no matrix	41	2017
EDDP	small molecule	pSi	Derivatization	no matrix	26	2015
EDDP	small molecule	nano Si	Derivatization	no matrix	75	2014
erythromycin	small molecule	SiNP	None	no matrix	59	2012

fatty acids and glyceride	small molecule	SiNW	Functionalization	no matrix	63	2010
fentanyl	small molecule	nano Si	None	no matrix	65	2015
fentanyl	small molecule	nano Si	None	no matrix	77	2010
FHV	protein	pSi	None	no matrix	21	2001
FHV tryptic digests	protein	SiNW	Derivatization	no matrix	66	2005
fibrinopeptide B	peptide	nano Si	Derivatization	no matrix	72	2010
fibrinopeptide B	peptide	nano Si	Derivatization	no matrix	76	2011
flunitrazepam	small molecule	pSi	Derivatization	no matrix	38	2015
four-residue peptide (MRFA)	peptide	pSi	None	no matrix	23	1999
glucose	small molecule	pSi	Functionalization	no matrix	48	2009
glucose	small molecule	pSi	Functionalization	no matrix	48	2009
glucose	small molecule	nano Si	None	no matrix	69	2013
glucose	small molecule	nano Si	Derivatization and functionalization	no matrix	71	2015
glucose	small molecule	nano Si	Derivatization and functionalization	no matrix	71	2015
glucose-probe	peptide	nano Si	None	no matrix	51	2017
glutamic acid	small molecule	pSi	Derivatization	no matrix	34	2004
glutamine	small molecule	pSi	None	no matrix	52	2008
glycine	small molecule	pSi	None	no matrix	52	2008
GSH	small molecule	pSi	Functionalization	no matrix	46	2017
GSH	small molecule	pSi	Functionalization	no matrix	46	2017
haloperidol	small molecule	nano Si	Derivatization	no matrix	68	2008
heneicosanoic acid	small molecule	pSi	None	no matrix	24	2006
heptadecanoic acid	small molecule	pSi	None	no matrix	24	2006
histidine	small molecule	pSi	None	no matrix	52	2008
insulin	peptide	pSi	Functionalization	CHCA	45	2014
insulin	peptide	SiNP	Functionalization	CHCA	57	2015
insulin B	peptide	pSi	None	no matrix	50	2017

isoleucine/leucine	small molecule	pSi	Derivatization	no matrix	34	2004
ketoconazol	small molecule	nano Si	Derivatization	no matrix	68	2008
L-cysteine	small molecule	pSi	Functionalization	no matrix	46	2017
Leu-Enkephalin-Arg	peptide	pSi	Derivatization	no matrix	43	2002
linoleic acid	lipid	nano Si	Functionalization	no matrix	64	2016
lipid species	lipid	pSi	None	DHB	47	2016
maltoheptaose	peptide	pSi	Functionalization	no matrix	48	2009
maltohexaose	peptide	pSi	Functionalization	no matrix	48	2009
maltotriose	small molecule	pSi	Functionalization	no matrix	48	2009
maltotriose	small molecule	pSi	Derivatization	no matrix	34	2004
MDMA	small molecule	pSi	Derivatization	no matrix	32	2012
MDMA	small molecule	pSi	Derivatization	no matrix	38	2015
methadone	small molecule	pSi	Derivatization	no matrix	26	2015
methadone	small molecule	pSi	Derivatization	no matrix	37	2017
methadone	small molecule	pSi	Derivatization	no matrix	37	2017
methadone	small molecule	pSi	Derivatization	no matrix	37	2017
methadone	small molecule	pSi	Derivatization	no matrix	38	2015
methadone	small molecule	nano Si	Derivatization	no matrix	75	2014
methamphetamine	small molecule	pSi	Derivatization	no matrix	26	2015
methamphetamine	small molecule	pSi	Derivatization	no matrix	32	2012
methionine	small molecule	pSi	None	no matrix	52	2008
metoprolol	small molecule	nano Si	None	no matrix	65	2015
midazolam	small molecule	pSi	Derivatization	no matrix	43	2002
midazolam	small molecule	pSi	Derivatization	no matrix	34	2004
midazolam	small molecule	SiNW	Derivatization	no matrix	66	2005
model sample of HRP digest and BSA	peptide	pSi	Functionalization	CHCA	45	2014
morphine	small molecule	SiNP	Derivatization	no matrix	60	2007
murexine	small molecule	pSi	Derivatization	no matrix	36	2015
MYO digest	peptide	SiNP	None	CHCA	58	2010

myristoylcarnitine (C9)	small molecule	nano Si	None	no matrix	77	2010
N-(4-hydroxyphenyl)acetamide	small molecule	SiNP	None	no matrix	59	2012
neurotensin	peptide	pSi	Derivatization	no matrix	22	2007
neurotensin	peptide	nano Si	Derivatization	no matrix	72	2010
neurotensin	peptide	nano Si	Derivatization	no matrix	76	2011
neurotensin	peptide	pSi	None	no matrix	50	2017
nicotine	small molecule	pSi	Derivatization	no matrix	26	2015
N-octyl beta-D-glucopyranoside	peptide	pSi	None	no matrix	23	1999
nonadecanoic acid	small molecule	pSi	None	no matrix	24	2006
nonanoic acid	lipid	pSi	Derivatization	no matrix	26	2015
norbuprenorphine	small molecule	nano Si	None	no matrix	65	2015
nordiazepam	small molecule	nano Si	None	no matrix	65	2015
norfloxacin	small molecule	SiNP	None	no matrix	59	2012
nucleobase adenine	peptide	SiNP	Derivatization	no matrix	60	2007
octanoylcarnitine (C5)	small molecule	nano Si	None	no matrix	77	2010
oleic acid	lipid	pSi	Functionalization	no matrix	41	2017
oleic acid	lipid	nano Si	Functionalization	no matrix	64	2016
oxycodone	small molecule	pSi	Derivatization	no matrix	38	2015
oxycodone	small molecule	pSi	Derivatization	no matrix	38	2015
oxytocin	peptide	pSi	Functionalization	no matrix	40	2009
palmitoylcarnitine	small molecule	nano Si	None	no matrix	49	2016
palmitoylcarnitine	small molecule	pSi	None	no matrix	50	2017
palmitoylcarnitine (C10)	small molecule	nano Si	None	no matrix	77	2010
papaverine	small molecule	nano Si	Derivatization	no matrix	68	2008
PC head group	lipid	pSi	Functionalization	no matrix	41	2017
PEG	polymer	nano Si	None	DHB	69	2013
PEG 2300	polymer	pSi	Functionalization	no matrix	40	2009
PEG 400	polymer	pSi	Functionalization	no matrix	40	2009

PEG1000	polymer	SiNP	None	no matrix	59	2012
PEG400	polymer	nano Si	None	no matrix	70	2006
peptide mixture	peptide	SiNP	None	no matrix	54	2012
peptides from human serum and urine	peptide	SiNP	Functionalization	CHCA	56	2010
peptides leucine enkephalin	peptide	SiNP	Derivatization	no matrix	60	2007
phenylalanine	small molecule	pSi	Derivatization	no matrix	34	2004
phosphatidylcholine	lipid	pSi	Derivatization	no matrix	22	2007
phosphatidylethanolamine	lipid	pSi	Derivatization	no matrix	22	2007
phospholipids	lipid	pSi	Derivatization	no matrix	22	2007
phosphopeptides	peptide	pSi	Derivatization and functionalization	DHB	39	2006
PPG1000	polymer	nano Si	None	no matrix	70	2006
prazosin	small molecule	nano Si	Derivatization	no matrix	68	2008
prednisolone	small molecule	pSi	None	no matrix	29	2009
prednisone	small molecule	pSi	Functionalization	no matrix	48	2009
progesterone	small molecule	pSi	Functionalization	no matrix	48	2009
Pro-Leu-Gly tripeptide	peptide	nano Si	None	no matrix	77	2010
propafenone	small molecule	pSi	Derivatization	no matrix	34	2004
propafenone	small molecule	SiNP	Derivatization	no matrix	60	2007
propafenone	small molecule	SiNP	Derivatization	no matrix	60	2007
propafenone	small molecule	SiNW	Derivatization	no matrix	66	2005
propranolol	small molecule	nano Si	Derivatization	no matrix	68	2008
propranolol	small molecule	pSi	Derivatization	no matrix	43	2002
psilocin	small molecule	pSi	Derivatization	no matrix	43	2002
quinidine	small molecule	nano Si	Derivatization	no matrix	68	2008
renin substrate tetrapeptide	peptide	pSi	Derivatization	CHCA or SA	31	2006
reserpine	small molecule	pSi	None	no matrix	23	1999
ropivacaine	small molecule	nano Si	None	no matrix	65	2015
roxithromycin	small molecule	SiNP	None	no matrix	59	2012

serum peptides	peptide	pSi	Functionalization	CHCA	45	2014
somatostatin 28	peptide	nano Si	Derivatization	no matrix	75	2014
spermidine	small molecule	nano Si	None	no matrix	49	2016
squalene	lipid	nano Si	Functionalization	no matrix	64	2016
ss-DNA	oligonucleotides	SiNP	Functionalization	3-HPA	62	2009
STAL-2 (hexapeptide, SFLLRN-NH2)	peptide	nano Si	None	no matrix	49	2016
stearic acid	lipid	pSi	Functionalization	no matrix	41	2017
stearic acid	small molecule	pSi	None	no matrix	24	2006
stearoylcarnitine (C11)	small molecule	nano Si	None	no matrix	77	2010
streptomycin	small molecule	pSi	None	no matrix	50	2017
substance P	peptide	pSi	Derivatization	CHCA or SA	31	2006
substance P	peptide	nano Si	Derivatization	no matrix	75	2014
substance P	peptide	pSi	Derivatization	no matrix	43	2002
sucrose	small molecule	pSi	Functionalization	no matrix	48	2009
sucrose	small molecule	pSi	Functionalization	no matrix	48	2009
sucrose	small molecule	pSi	Derivatization	no matrix	34	2004
Sutent	small molecule	nano Si	Derivatization	no matrix	72	2010
TAG 48:1	lipid	pSi	Functionalization	no matrix	41	2017
temporin-SHf	peptide	SiNP	None	no matrix	59	2012
testosterone	small molecule	pSi	Functionalization	no matrix	48	2009
TMZ	small molecule	nano Si	None	no matrix	69	2013
TPyP	small molecule	pSi	Functionalization	no matrix	40	2009
trans-androsterone	small molecule	pSi	Functionalization	no matrix	48	2009
trioctylamine	small molecule	SiNP	Derivatization	no matrix	60	2007
tripalmitin	lipid	SiNW	Functionalization	no matrix	63	2010
tristearin	lipid	SiNW	Functionalization	no matrix	63	2010
Trx-urodilatin	protein	pSi	Derivatization and functionalization	SA	27	2009
tryptic BSA digest	peptide	SiNP	Functionalization	CHCA	56	2010

tryptic peptide of protein fibronectin	peptide	pSi	Derivatization and functionalization	CHCA	44	2012
tryptophan	small molecule	pSi	None	no matrix	52	2008
tyrian purple	small molecule	pSi	Functionalization	no matrix	41	2017
tyrian purple	small molecule	pSi	Derivatization	no matrix	36	2015
tyrindoleninone	small molecule	pSi	Derivatization	no matrix	36	2015
tyrindoxyl hydrogen sulfate	small molecule	pSi	Derivatization	no matrix	36	2015
tyrindoxyl sulfate	small molecule	pSi	Derivatization	no matrix	35	2012
verapamil	small molecule	nano Si	Derivatization	no matrix	68	2008
verapamil	small molecule	pSi	Derivatization	no matrix	22	2007
verapamil	small molecule	pSi	Derivatization	no matrix	34	2004
verapamil	small molecule	SiNP	Derivatization	no matrix	60	2007
verapamil	small molecule	SiNW	Derivatization	no matrix	66	2005
verapamil	small molecule	nano Si	None	no matrix	49	2016
verapamil	small molecule	nano Si	None	no matrix	65	2015
verapamil	small molecule	nano Si	Derivatization	no matrix	72	2010
vitamin D3	small molecule	pSi	Functionalization	no matrix	48	2009
WE 36:1	small molecule	pSi	Functionalization	no matrix	41	2017
γ-cyclodextrin	peptide	pSi	Functionalization	no matrix	48	2009

UNIVERSITAT ROVIRA I VIRGILI
GOLD-COATED BLACK SILICON NANOSTRUCTURED SURFACES FOR SERS AND SALDI-MS MULTIMODAL IMAGING OF BIOLOGICAL APPLICATIONS
Stefania-Alexandra Iakab

UNIVERSITAT ROVIRA I VIRGILI
GOLD-COATED BLACK SILICON NANOSTRUCTURED SURFACES FOR SERS AND SALDI-MS MULTIMODAL IMAGING OF BIOLOGICAL APPLICATIONS
Stefania-Alexandra Iakab

CHAPTER 2.2: Perspective on Multimodal Imaging Techniques Coupling Mass Spectrometry and Vibrational Spectroscopy: Picturing the Best of Both Worlds

UNIVERSITAT ROVIRA I VIRGILI
GOLD-COATED BLACK SILICON NANOSTRUCTURED SURFACES FOR SERS AND SALDI-MS MULTIMODAL IMAGING OF BIOLOGICAL APPLICATIONS
Stefania-Alexandra Iakab

State of the article:

Accepted in Analytical Chemistry (Manuscript ID: ac-2020-04986u.R1)

Journal metrics:

Impact factor 6.78

Q1 (Analytical chemistry)

Contributing authors:

Stefania Alexandra Iakab, Pere Rafols, Xavier Correig, María García-Altares

Department of Electronic Engineering, Rovira i Virgili University, Tarragona, 43007, Spain

Spanish Biomedical Research Centre in Diabetes and Associated Metabolic Disorders (CIBERDEM), Madrid, 28029, Spain

Institut d'Investigació Sanitària Pere Virgili, Tarragona, 43204, Spain

UNIVERSITAT ROVIRA I VIRGILI
GOLD-COATED BLACK SILICON NANOSTRUCTURED SURFACES FOR SERS AND SALDI-MS MULTIMODAL IMAGING OF BIOLOGICAL APPLICATIONS
Stefania-Alexandra Iakab

2.2.1. Abstract

Studies on complex biological phenomena often combine two or more imaging techniques to collect high-quality comprehensive data directly in-situ, preserving the biological context. Mass Spectrometry Imaging (MSI) and Vibrational Spectroscopy Imaging (VSI) complement each other in terms of spatial resolution and molecular information. In the last decade several combinations of such multimodal strategies arose in research fields as diverse as microbiology, cancer, and forensics, overcoming many challenges towards the unification of these techniques. Here we focus on presenting the advantages and challenges of multimodal imaging from the point of view of studying biological samples, as well as giving a perspective on the up-coming trends regarding this topic. The latest efforts in the field are discussed, highlighting the purpose of the technique for clinical applications.

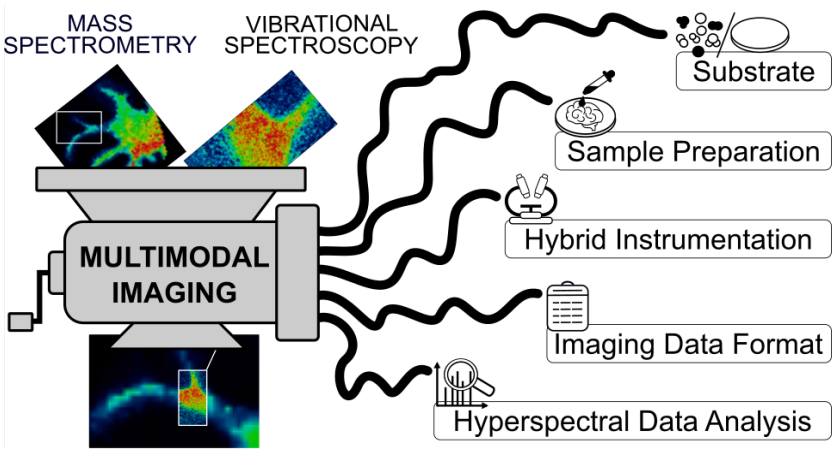

UNIVERSITAT ROVIRA I VIRGILI
GOLD-COATED BLACK SILICON NANOSTRUCTURED SURFACES FOR SERS AND SALDI-MS MULTIMODAL IMAGING OF BIOLOGICAL APPLICATIONS
Stefania-Alexandra Iakab

2.2.2. Introduction

A picture is worth a thousand words, especially when it is a molecular image that can shed light on the composition, function and heterogeneity of a biological tissue. However, one picture might not be enough to fully characterize complex biosystems. That is why multimodal imaging platforms have emerged in the last decade as a coordinated combination of multiple imaging techniques to find solutions in fields as diverse as plant-based renewable energy, microbiology, clinical medicine and forensics.[1–18] Multimodal imaging provides a set of information which characterizes biological samples from two aspects: quantitative and qualitative molecular information, and molecular distribution at both high and low spatial resolution. The coupling of imaging modalities started with optical microscopy techniques such as classical histopathology, fluorescence imaging, and immunohistochemistry being combined with molecular imaging techniques such as Infrared or Raman Spectroscopy Imaging and Mass Spectrometry Imaging (MSI).[1,2,19–24] The classical histology techniques have a major limitation which impedes comprehensive analysis of biological samples: they use labels for targeted imaging.[23,25] This approach involves monitoring a reduced number of compounds (usually two or three proteins) because the chemical stains, immunohistochemical tags or other labels used for imaging are limited. Additionally, molecular discovery is unfeasible as the use of labels requires rational design of targeted strategies based on specific binding between known molecules. Nevertheless, creative workflows that combine classical histology and label-free techniques can yield valuable information that provide insight into complex biological systems.

Mass Spectrometry Imaging (MSI) and Vibrational Spectroscopy Imaging (VSI) techniques are common choices for label-free imaging when studying biological tissues. They complement each other in terms of spatial and

chemical information, and the limitations of one are complemented by the strengths of the other, so spatial resolution images are better and unique molecular formulas can be identified more effectively. The main complementary characteristics of the two techniques are: that VSI can achieve sub-cellular spatial resolution while MSI is generally used for measuring larger areas and morphologies, and that MSI collects specific molecular information (molecular weight of the ion divided by its charge, *m/z*) while VSI adds information about the abundance and specificity of chemical families instead of individual compounds (type of chemical bonds, heavy atoms, *etc.*). Both MSI and VSI have matured greatly in terms of instrumental developments in recent decades. The most commonly used spectrometry techniques for multimodal imaging are: matrix-assisted laser desorption/ionization (MALDI), surface-assisted laser desorption/ionization (SALDI), desorption electrospray ionization (DESI), secondary ion mass spectrometry imaging (SIMS) and laser ablation inductively coupled plasma (LA-ICP). The most commonly used vibrational spectroscopy techniques, on the other hand, are Raman spectroscopy, surface-enhanced Raman scattering (SERS), Fourier-transform infrared spectroscopy (FTIR/IR) and attenuated total reflection Fourier-transform infrared spectroscopy (ATR-FTIR).

2.2.3. Mass Spectrometry Imaging *vs.* Vibrational Spectroscopy Imaging

We have summarized in the Supporting Information file the, sample preparation, data acquisition and data analysis for the most common MSI and VSI techniques used in the latest multimodal imaging applications (Tables S1 and S2). Furthermore, Table S1 provides specificities of each technique (lateral resolution, typical spectral range, sample requirements,

imaging advantages and challenges). Analysts should keep in mind the following aspects when choosing molecular imaging techniques:

2.2.3.1. Sample requirement

Biological samples (usually tissues, plants and cell cultures) have to comply with the instruments' probing chamber. For all MSI techniques samples must be vacuum compatible except for DESI and for a few MALDI sources, where measurements are done in atmospheric conditions. Similarly, all VSI techniques operate in air, however Raman and ATR-IR can also examine samples in liquid. But, each technique has their own requirements regarding sample properties (as reflected in Table S1): polarity, surface roughness, thickness, *etc.* Nevertheless, sample preparation for multimodal imaging can be compatible.

2.2.3.2. Molecular information

In MSI molecules are detected as ions and, depending on the mass spectrometer and the ionization source, different kinds of molecular classes can be analyzed: DESI and MALDI (both soft ionization techniques) are generally used for lipids, peptides, and proteins; SALDI for metabolites, small molecules and lipids; SIMS (a hard ionization technique) for biologically relevant elements, small molecules, metabolites, and sometimes lipids; and LA-ICP for inorganic compounds such as cations, metals and other biologically relevant elements (Figure 1). However, identifying molecules in MSI is sometimes a challenge: isomers, enantiomers, isobars and neutral molecules cannot be recognized. On the other hand, VSI methods examine the vibrations of chemical bonds which provide the fingerprint signature of a molecule. In this case, ATR-IR, FTIR, Raman and SERS examine the abundance, structure and conformation of all biomolecules: lipids, proteins, nucleic acids, sugars, DNA, *etc.* Therefore, the

complementary information of MSI and VSI is key for uncovering molecular mysteries.

2.2.3.3. Type of experiment

Targeted analyses pinpoint specific molecules by looking for their molecular fingerprint or their expected ion formation (the molecular weight of their specific adducts, isotopes, and fragments). Each technique has its own strategy to achieve this: MALDI uses specific ionizing agents (often called "matrices") like 2,5-Dihydroxybenzoic acid for peptides or 9-aminoacridine for lipids, SALDI uses nanomaterials to obtain a clean mass spectrum to distinguish small molecules and metabolites, while SERS employs functionalized nanomaterials to enhance the Raman signal of specific molecules. All these approaches demand careful design and sometimes complex sample preparation which are rarely compatible with multiple measurements on the same sample. On the other hand, untargeted analyses need high specificity techniques which observe many molecules simultaneously in order to establish molecular changes and identify key components. In this case MSI techniques are preferred, however VSI methods can offer complementary information.

2.2.3.4. Required spatial resolution

Based on the sample size and morphology, different imaging experiments require different spatial resolution. For example, larger samples (tissues, plants) are frequently imaged at lower resolution (over 50 μm per pixel) using techniques such as DESI, MALDI, and FTIR,[11–13,15,18] while smaller samples (cells, bacteria) are analyzed using high resolution methods like SIMS, LA-ICP, Raman and SERS[6,7,10,17] that can achieve submicrometer resolution. In multimodal imaging, one technique can be used to obtain a full scan of the sample and another to "zoom in" on a morphologically or compositionally

interesting area. Fortunately, both MSI and VSI can be used for high- or low-resolution imaging as depicted in Figure 1.

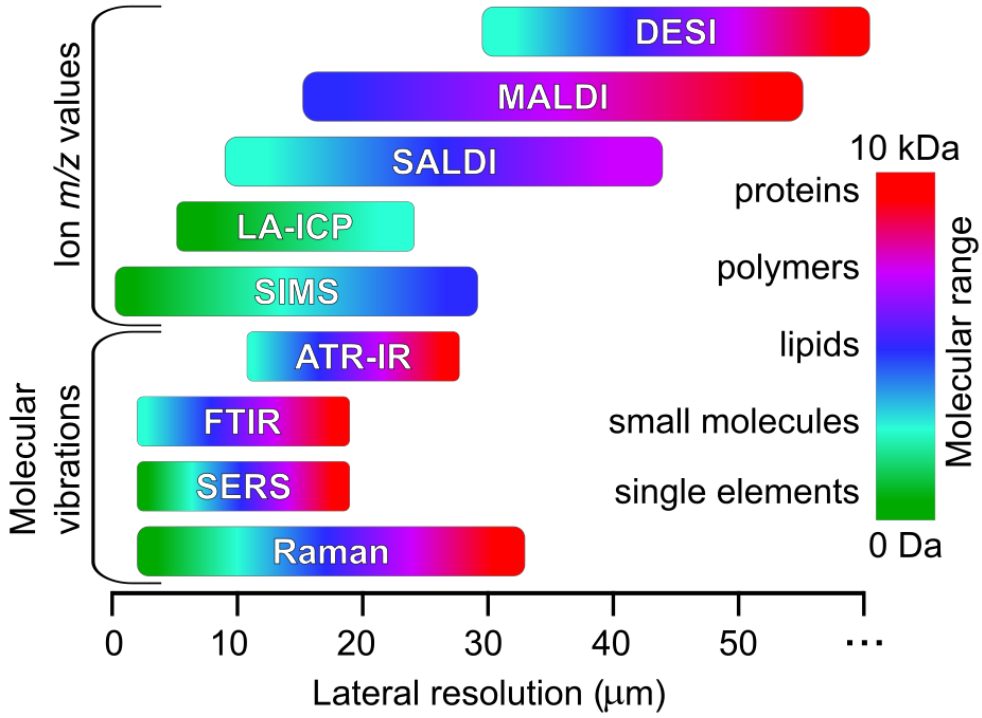

Figure 1. Spatial resolution *vs.* molecular mass range for MSI and VSI techniques

2.2.4. Advantages of Multimodal Imaging

MSI and VSI can be combined to overcome the limitations of one technique and complementing it by the advantages of the other. This combination has been applied in various imaging studies (as illustrated in Table S1 from the Supporting information file): animal brains (mouse,[5,15,16] rat[12,26] and hamster[11]), cell cultures,[6,8] bacterial colonies,[7,10,17] liver metabolism,[1,2] cancerous tissues,[9,13,18] fingermarks[4] and even plants (perennial grass[3] and maize leaves[14]). Label-free multimodal imaging is a new holistic approach which will impact analytical chemistry, especially the

"omics" sciences, for two main reasons: (1) the imaging techniques provide complementary information that identifies molecules and validates results; and (2) the spatial and spectral information have boosted value.

2.2.4.1. Complementarity

The information about the lipid content from MSI can be complemented by the protein information provided by VSI.[1,2,5,9] Even though MALDI-MS is traditionally used for detecting proteins, it also detects lipids when using an organic matrix that facilitates lipid ionization (*e.g.* alpha-cyano 4-hydroxy cinnamic acid[5]); the lipid signal is also specific to Raman and can inform about their level of saturation, as it is frequently used to analyze lipid droplets, layers and membranes.[22] On the other hand, the IR spectra provide specific information about proteins: their composition and secondary structure. For example, Neumann *et al.* used two analytical methods to obtain the chemically specific and spatially resolved information necessary to characterize the chemical heterogeneity of the hippocampus from adult rat brains: the average IR absorption spectrum revealed morphological differences in the protein composition of the different segments within the hippocampus (shift between the amide I and amide II bands), while the average mass spectrum showed significant spatial differences among several phosphatidylcholine lipid species (PC32:0, PC34:1, PC36:4, and PC38:4).[12] Another complementary function of multimodal imaging is to facilitate the identification of macromolecules, such as polymers. For example, combined information from ATR-IR and MALDI was used to identify condom brands on the basis of their composition: the matrix-solvent combination used for MSI failed to show the presence of polydimethylsiloxane (present in condom lubricants) in all samples so Raman was used to identify it using the characteristic 1258 cm^{-1} band.[4] Multimodal techniques have also been used to monitor molecular biosynthesis processes in plants. Burkhow *et al.*

monitored the conversion of phytoenes to carotenoids directly in maize leaves, and how the rate of this conversion changed when they silenced one of the genes involved in the biosynthesis. Raman described the spatial distribution of carotenoids but, due to the lack of Raman signal to detect phytoenes, SALDI was chosen to monitor phytoene accumulation when they silenced the chosen gene.[14] In another study, combined information from SERS and LA-ICP-MS demonstrated that hybrid nanoparticles penetrate fibroblast cells differently from standard silica nanoparticles.[6] The SERS spectra reflected the interaction of several aminoacids of the side chains of proteins with the nanoparticles' surface, while LA-ICP images revealed the cellular uptake of silica nanoparticles with a silver core by monitoring the stable isotope ^{107}Ag.[6] This application promoted the use of multimodal imaging for very much needed qualitative and quantitative nanotoxicology studies.

From the viewpoint of data analysis, multimodal imaging datasets offer a plethora of possibilities for creating both identification and validation algorithms and strategies. The heterospectral data – colocalized mass spectra and vibrational spectra – can be used to identify small variations (*e.g.* highlighted through PCA or clustering analyses) that represent significant differences between physiologically similar regions within tissues.[11,12] One study used PCA on a multimodal dataset to identify the spatial distribution of different molecular classes: the antibiotic compounds quinolones and quinolines from bacterial biofilms.[10] The synergistic data processing of both VSI and MSI data highlights small changes that a single technique often overlooks. For example, fused MALDI and Raman images of rat hippocampus revealed differences in protein (bands 1250 cm^{-1}, 1550 cm^{-1}, and 1680 cm^{-1}) and lipid (ions *m/z* 772.52, *m/z* 789.54, *m/z* 820.52) composition between physiologically similar regions, information otherwise

inaccessible by individual images due to lack of specificity or spatial resolution of Raman and MALDI images, respectively.[12] Small details are often crucial for correct spectral interpretation and the correct identification of molecules. The identification of molecules can also be validated with multimodal imaging datasets, as VSI and MSI are orthogonal methods (*i.e.* methods that use fundamentally different principles). For example, the DESI-MSI and Raman imaging correlation map was used to assign structural features to individual molecular species: the multimodal analysis identified the molecular weight (from MS) and the saturation levels (from Raman) of specific lipids (phosphatidylcholines and phosphatidylethanolamines) involved in the myelination process in multiple sclerosis animal model and human brain samples.[15]

2.2.4.2. Boosted spatial and spectral information

Due to the limited spatial resolution of some molecular imaging techniques (MALDI and DESI), information-rich MS images are often colocalized with higher resolution VS images[3,7,8,13] or *vice versa*.[1,2] In this way, precise localization and molecular identification can be achieved simultaneously. For example, a large area of crop leaves was mapped with LDI-MSI (100 μm lateral resolution) which pinpointed the regions of interest for higher resolution images collected with Raman (~0.6 μm lateral resolution) and SIMS (~2 μm lateral resolution) imaging.[3] In this way high-quality spectra and high-resolution images assigned intracellular globular structures to hemicellulose-rich lignin complexes in perennial grass (*Miscanthus x giganteus*). The coregistration of the two types of image was also ingeniously used to categorize tissue types. This time larger areas were collected by VSI in order to guide and select the regions of interest for MSI. Specifically, FTIR microscopy was used to automatically guide high-resolution MSI data acquisition and interpretation (without prior

histopathological tissue annotation) through *k*-means segmentation algorithms to separate tumors from healthy tissues in mouse brains.[13] Another study used the histopathological analysis of Raman spectra as a guide for MALDI analysis, which differentiated between healthy and altered epithelial growth from a larynx carcinoma sample.[9] In this study, MS revealed many overexpressed ions which are associated with tumor markers (*e.g.* sphingomyelins, several phosphatidylcholines, and a high content of glycerophospholipids). So, changes occurring within small areas of tissues could be monitored with both VSI and MSI, and biomarkers were identified.

2.2.5. Challenges of Multimodal Imaging

Multimodal imaging is a complex analytical tool which involves a variety of high-end instrumentation and software, so it is challenging from two points of view: (1) the experimental workflow and (2) the data processing algorithms.

2.2.5.1. Experimental challenges

Multimodal imaging workflows require multiple optimization steps in each modality to obtain maximum output while maintaining sample and substrate compatibility. Therefore, sample preparation, coregistration strategies that depend on sample preparation, and acquisition parameters have to be optimized for all instruments.

Fortunately, MSI and VSI sample preparation is compatible as the starting point is the same: the biological samples are placed on a substrate. However, the substrate (and thus the analyzed sample) is not always the same for the two techniques. Raman and IR typically use calcium fluoride, but there are other working options such as microscope slides,[1,14,15] ITO slides,[5,8,9,16,18] BVDA gelatine lifters,[4] low emission glass slides,[12] gold-coated slides,[2,13]

silicon wafers,[3,7,10] and sterile cover slips.[6] For MSI the substrates also vary according to the technique and application: ITO slide,[5,8,9,11,16,18] MALDI plate,[4] custom-made SIMS plate,[17] low emission glass slide,[12] gold-coated slide,[2,13] packing tape,[14] silicon wafer,[1,3,7,10] magnesium fluoride slide[15] and sterile cover slips.[6] Choosing a substrate that worked for both imaging techniques soon became an asset, and several studies applied multimodal imaging using the same sample preparation and the same sample.[2,3,5,8,9,12,13,18] One such substrate is the ITO-coated glass slide, on which cells,[8] mouse brain,[5,12,13] mammary tumor,[18] and larynx[9] sections are deposited right after cryosectioning. Generally, the Raman measurements (which are non-destructive) are done first and then the matrix is deposited on the substrate for MALDI analysis. Silicon wafers are another example of a commonly used substrate in SIMS, LDI and Raman,[3,7,10] while gold-coated glass slides are used to couple SIMS and synchrotron FTIR and UV spectroscopy.[2] All these substrates provide excellent spectra in both modalities with minimal preparation and interference in the data acquisition. However, when signal enhancing agents are used (such as organic matrices for MALDI) the sample cannot be further used for other measurements without removing the agents, which may wash analytes away. For this reason, one of the most pressing future steps is to develop more multimodal substrates to enhance both the Raman/IR signal and the ionization efficiency for MSI.

When it comes to instrumentation, sample compatibility is as important as choosing the right substrate. For example, biological samples might be formalin-fixed paraffin embedded. This affects both VSI and MSI measurements because the signal from the paraffin overwhelms the spectra from the sample and conceals relevant information.[27,28] For this reason, the pretreatment of samples (washing, on-tissue digestion, derivatization, *etc.*)

has to be compatible with both imaging techniques. On the other hand, fresh frozen or ice embedded samples might generate artifacts in the VSI spectra due to high water content and autofluorescence. It is also important for the sample to be compatible with vacuum or atmospheric conditions. Dannhorn *et al.* studied the sample preparation methods used in various MSI techniques (DESI, MALDI, and SIMS) to create a universal embedding protocol suited for a broad range of specimens.[29] The hydroxypropyl-methylcellulose and polyvinylpyrrolidone polymer hydrogel outperformed the standard procedures (optimal cutting temperature medium, gelatine, *etc.*), with no interference with MS analysis or histological stains. Although this approach still needs to solve issues such as cold embedding and thaw mounting samples, it also enables using the same sample section for both immunohistochemical staining and MSI.[29]

Before acquisition, however, an additional sample preparation step might be used for easy image registration during data analysis. This step consists of marking the area to be imaged with a mask or specific points that are later used to coordinate the alignment of the molecular images collected. One such strategy aimed to register images by placing a physical mask known as a fiducial mask, on the sample to assist in locating the raster positions for both Raman and MALDI imaging techniques.[8]

After ensuring compatible sample preparation, acquisition order is paramount. All MSI techniques are destructive so the molecules detected are no longer present in the remaining sample after acquisition. The sample itself may deteriorate greatly (*i.e.* total ablation by the laser, dehydration, chemical degradation, *etc.*). Therefore, when the sample is probed subsequently by another molecular imaging method, the quality of the collected data can be compromised. Neumann *et al.* examined how the IR data is altered when measuring the same sample after MALDI acquisition. The IR image quality

was preserved, but a slight red shift in the spectra was associated with increased sample absorbance from the matrix. Other influencing factors were also noted: altered microenvironment, loss of some chemical species, or exposure to atmosphere.[12] Nevertheless, if the first imaging method is non-destructive – which is the case for all VSI methods – then the following acquisition generates reliable information. As such, the latter approach is the norm (see Table S2).

To sum up, for both imaging techniques the analyst must ensure that (1) the acquisition parameters are compatible with obtaining the required spatial and molecular information, (2) the acquisition time is minimal (if sample viability is a concern) and (3) the images are suitable for post-acquisition image coregistration to avoid resolution discrepancy.

2.2.5.2. Data processing challenges

Data processing and analysis strategies are needed to extract the maximum chemical information. In the case of multimodal imaging, these strategies strongly depend on the experimental workflow. Multimodal imaging data is a collection of two datacubes which contain different spectral information but often similar spatial information. Generally, the pre-processing step is done separately for each datacube, in accordance with the techniques' necessities. This involves using different software for each technique and possibly different algorithms for similar signal processing procedures. Figure 2 illustrates a generalized multimodal data processing workflow for MSI and VSI images, where the pre-processing step is done separately for each image followed by the data analysis step which consists of both image and data registration. Several data analysis approaches have been applied to multimodal datasets. The two prominent strategies are image *registration* and image or data *fusion*.

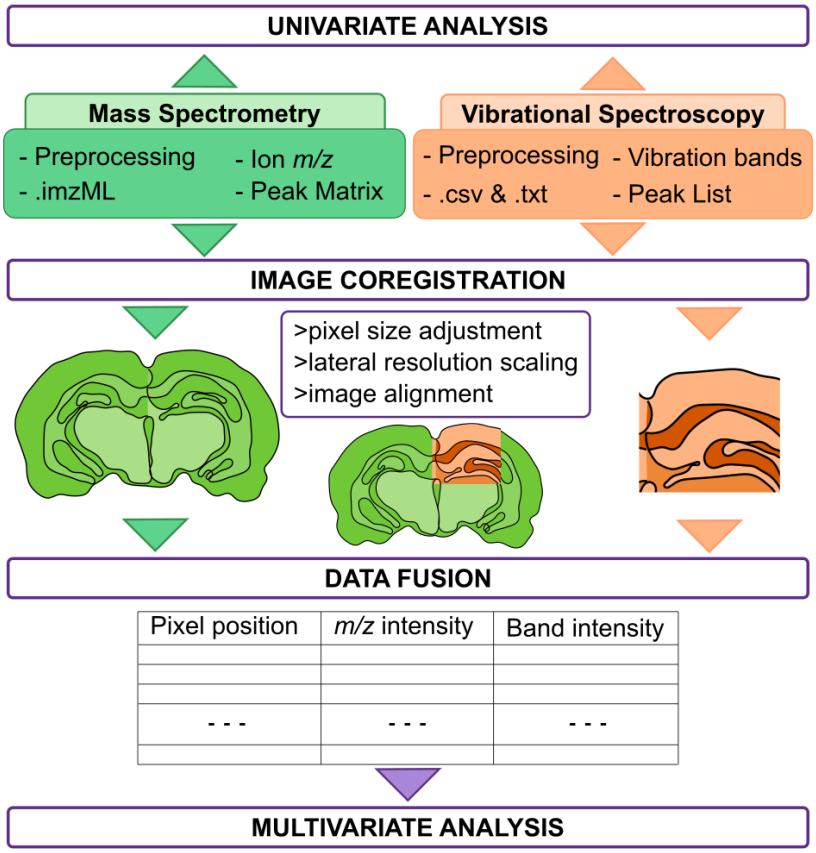

Figure 2. Generalization of the image and data fusion workflow combining one MSI and one VSI technique.

Image registration, also called coregistration, consists of aligning two different images by selecting control points based on anatomical features present in the sample.[30] The points (or fiducial markers) are usually selected on optical images, on molecular images with single or multiple ion or band representation and even on score images from the principal component analysis (PCA). The simplest way to coregister multimodal images is to convert each image (of selected *m/z* or bands) into a single-color intensity plot and then overlap the images using the RGB color schemes.[7,8] This approach is feasible when the images can be aligned and superimposed without distorting the spatial resolution of either image. Another strategy for

coregistration used fiducial markers. Pixel-wise coregistration was done with a high-resolution VSI image (for instance Raman, spatial resolution of ~10 μm) and a low-resolution MSI image (for example DESI, spatial resolution of ~50 μm), where the sequential imaging data from the same sample was coregistered using a fiducial marker-based alignment[15] (see Figure 3). The workflow consisted of placing four markers on each molecular image based on the landmarks on the brain tissue after which an affine transformation was used to coregister the DESI image to match the Raman image. Generally, to correlate the molecular images, more than three marker points should be defined in both images for appropriate registration. A more advanced technique for registering images and sharpening the low-resolution image was based on modeling the distribution of colocalized measurements using partial least square (PLS) regression.[30] Van de Plas *et al.* used molecular images collected with MSI and H&E images from microscopy to predict ion distributions at high spatial resolution in a mouse brain.[30] This coregistration technique is commonly used in image fusion or data fusion experiments, which not only register the images but also correlate the spectral information.

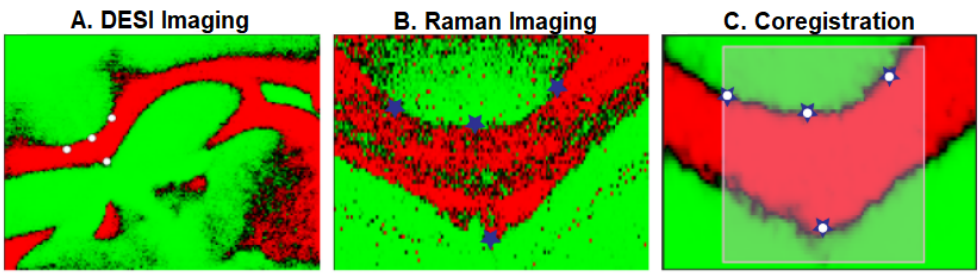

Figure 3. Fiducial markers placed on heterogeneous landmarks in the mouse brain for coregistration by MSI (A) and VSI (B) images. The coregistration results are illustrated in (C) where the fiducial markers from MSI (white circles) are superimposed on the ones from VSI (blue stars).[15] Reproduced with permission from ref 7. Copyright © 2017, American Chemical Society.

Data fusion consists of merging the VSI and MSI spectra into one single multidimensional dataset called a multimodal datacube. The multimodal datacube describes each pixel with three components: one spatial component giving information on the pixel position, and two spectral components (*m/z* intensity and band intensity) associated to each pixel, as seen in Figure 2. This allows the spectral information from each pixel in one image to be correlated with the pixels in the other. In this way, the multimodal dataset can be used to predict an MSI spectrum in a VSI pixel or *vice versa*, on the basis of the interdependence between VSI and MSI. In the scientific literature each study tackles data fusion differently.[12,16,18] Ryabchykov *et al.* fused the spectral data from MALDI and Raman images after interpolating the data in the same spatial grid during coregistration. This data fusion consisted of adjusting the dimensionality and dynamic range of each data set and then merging the two matrices into one.[16] Similarly, Neumann *et al.* coregistered the MS and IR images using anatomical features of the individual PCA score images and then fused the data by up-sampling the MS image and down-sampling the IR image to adjust discrepancies between the spatial resolution.[12] Another data fusion strategy transformed the coordinate system of one imaging modality into the other in order to calculate the mean VSI spectra for regions which exhibit a certain intensity of a MSI peak or MSI fingerprint.[5] This concept was designed to translate any disease marker information from MSI into complex Raman fingerprint, information which can be further used as an *in vivo* application of the marker in a diagnostic procedure.[5]

Multimodal data analysis usually consists of multiple multivariate procedures used to discover otherwise buried signals. The algorithms used in the scientific literature include: PLS to predict MALDI spectral information from the Raman spectra;[5] PLS discriminant analysis (PLS-DA) to classify

Raman spectra for differentiating newly formed myelin and normal myelin in remyelination;[15] maximum margin criterion linear discriminant analysis (MMC-LDA) to determine the most significant mass spectrometry peaks from DESI measurements;[15] multivariate curve resolution-alternating least squares (MCR-ALS) to reveal the composition of lipids and their particular localization;[18] and clustering algorithms for untargeted image segmentation. The most common clustering algorithm is *k*-means clustering,[12,13,15] but unsupervised hierarchical cluster analysis, which is based on interspectral distances obtained from normalized Pearson's product-momentum correlation coefficients and Ward's algorithm, is also used.[11] Figure 4 illustrates the results of a *k*-means clustering on a rat hippocampus, where each cluster is represented spatially (Figure 4A) and has a mean spectrum from each modality (IR absorbance spectra in Figure 4B and MALDI MS spectra in Figure 4C)[12]. The correlated information highlights the differences in lipid (boxplots in Figure 4D) and protein content between clusters, which are associated with different morphological features of the rat hippocampus.

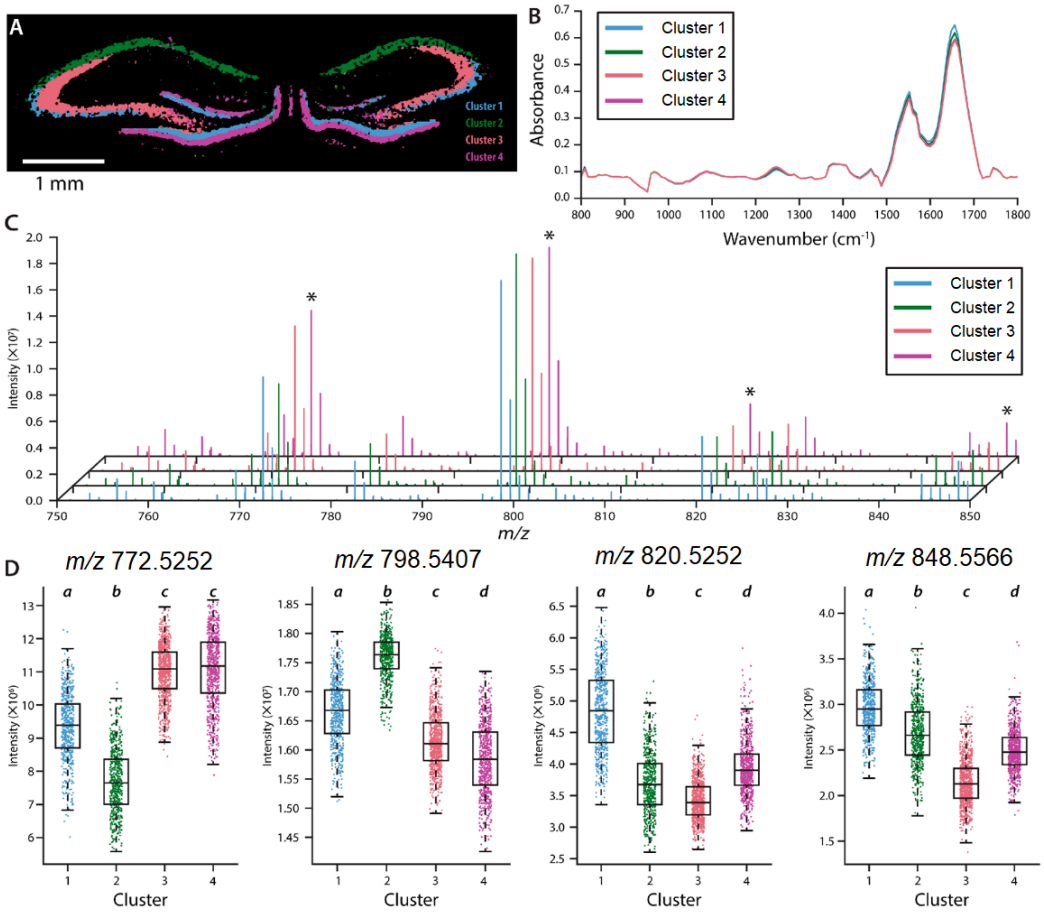

Figure 4. Results of *k*-means clustering of the fused dataset. (A) cluster image with each cluster associated with different anatomical regions in the rat hippocampus; (B) Average IR absorption spectra per cluster; (C) Average MS spectra per cluster; and (D) boxplots illustrating different signal intensities for specific lipid species in each cluster.[12] Reproduced with permission from ref 4. Copyright © 2018, American Chemical Society.

The technical challenges in terms of data processing include the format in which the data is collected and the software used for data analysis. Unfortunately, for imaging experiments there is no universal data format that encompasses both VSI and MSI data. This prevents straightforward data fusion and analysis by a single software package. Recent progress in format

compatibility between Raman and SALDI images proposed imzML (the standard format for MSI files) as a template for Raman imaging data as well.[31] The converter presented in this study transforms Raman imaging data (.txt files) into imzML, and makes it possible to use MSI-specific software for Raman imaging data. This is the first step on the way to creating a common format for all molecular imaging data. On the other hand, multimodal imaging requires several software packages for data export, conversion, processing and analysis. For example, WinCadence (PHI) was used to generate SIMS images, FlexImaging software (Bruker) was used to generate LDI images and WITec software was used for Raman data analysis, all in the same multimodal application.[3] However, some multimodal data analysis approaches use custom-made scripts in R and Matlab[5,9,11,12] but data preprocessing is not always done in the same software. For this reason, multimodal imaging data analysis requires a good set of programming skills and/or multiple licensed software.

2.2.6. Multimodal imaging and its transition to the clinic.

Multimodal imaging is an analytical approach with benefits in the clinical environment that are as yet unexplored. Its high specificity, functional and molecular information, and the label-free aspect of the technique augment the histological data obtained with standard microscopic tools used in the clinics. This approach provides a plethora of possibilities for biomedical applications such as diagnostics, intraoperative guidance, nanotoxicology, and even personalized medicine. For example, modern surgical tools that guide intra-operative interventions already use IR and Raman probing because they are affordable, offer real-time information and enable molecular profiles to be visualized on the microscale.[32] Similarly, MS techniques have been used for surgical guidance tools. In particular, iKnife has identified and distinguished between primary and metastatic tumors *in*

vivo and *ex vivo*.[33] However, the imaging possibilities of VSI and MSI are still barely used in clinical medicine. We suggest some possible examples about the use of label-free multimodal imaging that couples VSI and MSI for the applications described below.

2.2.6.1. Automatic classification of healthy and diseased tissues.

White light histopathology is the gold-standard for diagnosing cancerous cells from samples of human tissues. However, it relies heavily on the experience of the pathologist. Since experts in histopathology are scarce and expensive to train, several applications[34] have arisen so that VSI (especially IR imaging) can be used to screen and classify tissues using the approach known as "spectral histopathology."[24] These applications are complementary to classic histopathology and aim to reduce the number of samples that pathologists need to examine. There are even commercial applications currently being evaluated in clinical trials that exploit IR spectroscopy in the screening of cancerous tissues, such as esophageal and colon cancer, by the company DynamX Medical (https://www.dynamxmedical.com/). The use of MSI to identify biomarkers emerged from the need not only to distinguish between healthy and cancerous tissues but also to distinguish between cancer types and grades.[20,34] As such, ambient mass spectrometry imaging analysis revealed biomarkers representative of different types and subtypes of lung cancer with a sensitivity and a specificity of 93.5% and 100%, respectively.[20] Therefore, multimodal imaging could be used for diagnostic purposes in clinical medicine, where VSI classifies tissues and MSI detects biomarkers of cancer grades, all in an automated procedure with minimum interaction from a pathologist.

2.2.6.2. Development of equipment for the determination of surgical margins

Surgical margins, or margins of resection, are the rims of the apparently healthy tissue around a tumor that has been surgically removed. Normally pathologists examine the surgical margins post-operation to check if tumorous cells are present in the margins of resection. There are devices currently used to characterize surgical margins *in vivo* but they apply MS and vibrational spectroscopy strategies separately: (i) iKnife for electrosurgical dissection of tissues that informs about the tissue lipidomic profiles and discriminates different types of tumours;[33] and (ii) a handheld contact Raman spectroscopy probe for the *in vivo*, local detection of cancer cells in the human brain.[35] Since both methods are handheld, combining the iKnife and the Raman probe into a single instrument could broaden the possibilities of intraoperative procedures, maximize the analysis possibilities and give surgeons accurate guidance.

2.2.6.3. Cell and organoid model imaging

Understanding cell response and cell-cell interactions is crucial for testing compounds such as drugs, cosmetics, pollutants, nanoparticles, *etc.,* or for developing therapies, and designing in vitro organoid models. For example, molecular images collected with SIMS MSI established the silver nanoparticle uptake of Caco-2/TC7 and HT29-MTX cells by analyzing intracellular localization in relation to particle size.[36] Cell-cell interaction analysis is also crucial when designing organoid models such as the coculture model of the alveolar barrier – which includes several types of cells: alveolar type II epithelial cells, endothelial cells, macrophages, and dendritic cells.[37] This model was used to discriminate chemical respiratory sensitizers from irritants. Multimodal imaging could be used to monitor oxidative stress – a

common consequence of exposure to some toxicants, including nanoparticles – in cells and organoid models through DNA damage and changes in lipid peroxidation.[38] For this, Raman can monitor DNA conformational changes following several bands between 600 - 1700 cm^{-1},[39] while MSI can monitor lipid peroxidation by identifying lipid species and their degree of saturation.[40] Therefore, cell response can be characterized in situ as a living system (with VSI) and as a frozen metabolic state (with MSI).

2.2.6.4. Non-invasive testing protocols

Sweat is a biofluid that contains various excretion products: amino acids, urea, metal and nonmetal ions, metabolites and xenobiotics (such as drug molecules).[41] For this reason, non-invasive tests based on sweat composition analysis are becoming popular. MSI approaches were used to monitor illicit drugs from fingerprints[42] and to observe the detoxification of contaminants and medicines,[41] and the biomarkers of diseases.[43] For example, the sweat metabolome analysis by MS revealed that the signal from pilocarpic acid (a metabolite of pilocarpine) and mono(2-ethylhexyl)phthalic acid (a metabolite of the plasticizer bis(2-ethylhexyl) phthalate) can be used to detect cystic fibrosis in asymptomatic infants.[43] Raman spectroscopy was used to investigate the function of a single human sweat gland and the efficiency of aluminium chlorohydrate, a well-known antiperspirant ingredient.[44] Future applications of multimodal imaging regarding non-invasive sampling are appealing, especially because multimodal substrates are bioinert and compatible with aqueous samples such as sweat. Additionally, sweat can be collected from the skin surface (for instance, from the palms of the hand) with no need for a particular volume because both VSI and MSI have low limits of detection.

2.2.7. Perspective and future directions of multimodal imaging

Sample preparation, coregistration and data analysis need to be more user-friendly if multimodal imaging is to be used more commonly. That is why standardizing multimodal imaging based on VSI and MSI protocols, and developing hybrid instrumentation and software for analysis are key to advancements in the field.

2.2.7.1. Universal sample substrate

Here we have focused on the imaging part of multimodal techniques, but *in situ* analysis is not always necessary. Investigating urine, saliva, sweat, blood and even breath does not require spatial information, but does often require multiple analytical techniques for accurate diagnosis and even biomarker identification.[45,46] For this reason, a substrate that is compatible not only with all instruments (both VSI and MSI techniques) but also with all types of sample (liquid, solid and even gases) is still needed. Solid state substrates based on gold and silicon nanostructures are promising, as they have all the necessary requirements for LDI-MSI and SERS imaging.[47,48] Because the fabrication processes of these substrates can be automated, and because these types of substrates are compatible with multiple techniques, they are a potential candidate for the standardized multimodal substrate.

2.2.7.2. Universal sample processing

Universal sample processing is beneficial not only for multimodal imaging, but also for inter-sectoral and multidisciplinary collaborations. For example, samples prepared in the clinic for histological examination can be stored over time and the collected consortia can later be simultaneously analyzed by non-clinical research groups for different purposes: creation of

vast and unbiased spectral reference libraries, disease biomarker identification, development of tissue type classification algorithms, *etc*. Creating a standard coregistration protocol will make it possible to assign two qualitatively different spectra to the same area of a biological sample regardless of the imaging technique used. This will enable fast and accurate data collection over a variety of imaging modalities including MSI, VSI, histology and even magnetic resonance imaging and other routine clinical imaging techniques.

2.2.7.3. Universal data format for imaging

Once imaging data has been collected, the acquisition software should make it possible to export the data in a universal format for imaging. Thus, each imaging dataset, regardless of the acquisition technique, can be straightforwardly visualized and analyzed using a single software package. This would facilitate tremendously the development of correlated data analysis algorithms and software which can bring relevant information buried within the multimodal datasets to light. Along these same lines, the use of the imzML format (common for MSI data) has been suggested for Raman imaging data as well.[31] In fact, the converter presented makes it possible to visualize Raman maps in common MSI software, which provides new opportunities for data analysis. Although the imzML format is missing the nomenclature for Raman measurements such as “Raman Shift” units or diffraction grating definitions (cm^{-1}), in the future it could adopt multiple ontology options which could be chosen during data export or conversion. The universal imaging file should have three components: (1) a metadata section that stores all acquisition details such as laser parameters (wavelength, intensity or power, spot size), area specifications (pixel dimensions, step size), specific details of individual methods (integration time for Raman or shots per pixel for MALDI, *etc*.); (2) a coordinates section

containing information about pixel position and (3) a data section with all the spectral information.

2.2.7.4. Ultra-high-resolution multimodal imaging

Multimodal imaging could also push the limits on spatial resolution. In fact, tip-enhanced Raman spectroscopy (TERS) can attain 8 nm,[49] and Optical Photothermal Infrared (O-PTIR) spectroscopy can reach 100 nm.[50] TERS molecular images at 8 nm spatial resolution can be achieved through simultaneous collection of Raman spectra and nanotopography information. TERS uses a gold or silver tip which scans the sample surface and, when illuminated, generates a locally amplified electromagnetic field resulting in an enhanced Raman spectrum.[49] O-PTIR has beat the diffraction limit of conventional IR microscopes by modulating the changes of photothermal and photoacoustic effects from an intense IR beam source.[50] This enables collecting IR spectra in the order of hundreds of nanometers. Moreover, the instrument collects Raman signal simultaneously from the same location, promoting the use of coregistered multimodal imaging. Van De Plas *et al.* demonstrated that fusing rich chemical information images (MALDI MSI) with high spatial information images (microscopy image) can be beneficial from three points of view: (1) the lower resolution image can be sharpened; (2) out-of-sample prediction can be used for acquisitions which have smaller areas; and (3) the enriched spectral information can be used to discover biological patterns otherwise unnoticed.[30] Therefore, fusing ultra-high resolution images (from TERS or O-PTIR) with information-rich MS images (such as SIMS) enables the exploration of uncharted territories such as intracellular imaging.

2.2.7.5. Hybrid instrumentation development

Having a single instrument which combines multiple imaging methods would considerably simplify both experimental and data analysis procedures. In fact, MS instrumentation equipped with an optical microscope is already available on the market as iMScope™ QT from Shimadzu. A hybrid instrument combining MSI and VSI would analyze the same sample on the same substrate, it would need no coregistration strategy because the coordinate system is identical for both imaging methods, the output data format would be the same, and the data could be analyzed using the same software with no need for multiple data converters. One such multimodal imaging instrument developed in-house already combines atomic force microscopy, IR and MS to acquire topographical and chemical images at 1.6 μm spatial resolution of PVP/PMMA polymer thin films.[51] We could also consider the following combinations:

Ambient multimodal imaging. DESI-MSI combined with Raman spectroscopy using a long working distance objective would enable multimodal imaging in live samples. For example, live bacterial colonies or frozen tissues thawed on a multimodal-compatible substrate could first be sampled with Raman and then immediately sampled with DESI, so after each line acquisition the other modality would measure the same area. The use of an LWD objective could also permit simultaneous acquisition directly from the same pixel if the laser spot size is smaller than the ESI liquid bridge (droplet) and the optical pathway is not hindered by the presence of the capillaries.

Three-dimensional imaging. SIMS and Raman can be used to obtain 3D profiles of tissues. The ability of confocal Raman spectroscopy to acquire in-depth information and create 3D profiles without damaging the sample is

useful for guiding sample discovery.[17] On the other hand, SIMS is a technique which can be used to collect maps layer by layer, or to section (or mill) the sample using the ion beam at the desired depth, previously determined by the Raman profile. Therefore, the fast maps collected with Raman would guide the SIMS analysis, which provides exact information on elements and small molecules.

Laser-based multimodal imaging. SALDI and SERS both need a nanostructured agent which interacts with a laser and enhances the collected molecular signal. Therefore, it is reasonable to modify an LDI instrument (such as MALDI) by coupling multiple lasers (UV for MS and visible for Raman) and installing an additional objective or detector (for collecting the SERS spectra). This instrument can explore vacuum-compatible samples such as frozen tissues sputtered with gold or silver nanoparticles, first analyzed by SERS, because it is non-destructive, and then by SALDI. Similarly, a recently presented MALDI instrument that works in transmission mode[52] can be coupled with an IR laser and detector. This can quickly scan the sample with the IR mode which can help the MALDI acquisition reduce time and increase spatial resolution to the maximum.

2.2.7.6. Software development for multimodal data analysis

Current multimodal workflows collect and preprocess data sets separately and then visualize and analyze single or coregistered images either separately or with data fusion methods. Unfortunately, there is no straightforward way of doing all these data processing steps with the same software. For this reason, software in which the sophisticated computational processes are automatic (such as image registration and data fusion) and users can opt for a friendly interface which requires minimal input are in high demand, especially in clinical medicine where large datasets are routine. For example,

LipostarMSI is a software capable of raw data processing, coregistration, manually drawing or importing of regions annotated by pathologists, image visualization, univariate and multivariate image and spectral analysis, and even annotating lipids and metabolites (https://www.moldiscovery.com/software/lipostarmsi/). We foresee an increase in developing such software not only for multimodal MSI and VSI data analysis but also for optical microscopy images, fluorescence imaging and possibly MRI.

2.2.8. Conclusion

Multimodal imaging based on MSI and VSI techniques blends the advantages of each modality – specificity, sensitivity, and spatial resolution – and sheds light on details otherwise buried under thousands of pixels. The complete integration of imaging techniques from the point of view of the experimental workflow makes it possible to adopt a multidisciplinary approach to sample processing, which uses not only MSI and VSI but also MRI, histology, and other imaging techniques. As far as multimodal data processing is concerned, universal imaging file formats and standard data processing and analysis workflows will soon be available so that multimodal imaging can be used in various fields. We believe that the progress made in standardizing the multimodal imaging workflow and development of hybrid instrumentation will have considerable impact on research in biology, agriculture, nanotoxicology, pharmaceutics, cosmetics and, especially, clinical applications.

2.2.9. Acronyms

MSI - mass spectrometry imaging

VSI - vibrational spectroscopy imaging

MALDI - matrix-assisted laser desorption/ionization

SALDI - surface-assisted laser desorption/ionization

DESI - desorption electrospray ionization

SIMS - secondary ion mass spectrometry imaging

LA-ICP - laser ablation inductively coupled plasma

SERS - surface-enhanced Raman scattering

FTIR - Fourier-transform infrared spectroscopy

ATR-FTIR - attenuated total reflection Fourier-transform infrared spectroscopy

TERS - tip-enhanced Raman spectroscopy

O-PTIR - Optical photothermal infrared spectroscopy

2.2.10. References

(1) Le Naour, F.; Bralet, M.-P.; Debois, D.; Sandt, C.; Guettier, C.; Dumas, P.; Brunelle, A.; Laprévote, O. Chemical Imaging on Liver Steatosis Using Synchrotron Infrared and ToF-SIMS Microspectroscopies. PLoS ONE 2009, 4 (10), e7408. https://doi.org/10.1371/journal.pone.0007408.

(2) Petit, V. W.; Réfrégiers, M.; Guettier, C.; Jamme, F.; Sebanayakam, K.; Brunelle, A.; Laprévote, O.; Dumas, P.; Le Naour, F. Multimodal Spectroscopy Combining Time-of-Flight-Secondary Ion Mass Spectrometry, Synchrotron-FT-IR, and Synchrotron-UV Microspectroscopies on the Same Tissue Section. Analytical Chemistry 2010, 82 (9), 3963–3968. https://doi.org/10.1021/ac100581y.

(3) Li, Z.; Chu, L.-Q.; Sweedler, J. V.; Bohn, P. W. Spatial Correlation of Confocal Raman Scattering and Secondary Ion Mass Spectrometric Molecular Images of Lignocellulosic Materials. Analytical Chemistry 2010, 82 (7), 2608–2611. https://doi.org/10.1021/ac100026r.

(4) Bradshaw, R.; Wolstenholme, R.; Ferguson, L. S.; Sammon, C.; Mader, K.; Claude, E.; Blackledge, R. D.; Clench, M. R.; Francese, S. Spectroscopic Imaging Based Approach for Condom Identification in Condom Contaminated Fingermarks. The Analyst 2013, 138 (9), 2546. https://doi.org/10.1039/c3an00195d.

(5) Bocklitz, T. W.; Crecelius, A. C.; Matthäus, C.; Tarcea, N.; von Eggeling, F.; Schmitt, M.; Schubert, U. S.; Popp, J. Deeper Understanding of Biological Tissue: Quantitative Correlation of MALDI-TOF and Raman Imaging. Analytical Chemistry 2013, 85 (22), 10829–10834. https://doi.org/10.1021/ac402175c.

(6) Drescher, D.; Zeise, I.; Traub, H.; Guttmann, P.; Seifert, S.; Büchner, T.; Jakubowski, N.; Schneider, G.; Kneipp, J. In Situ Characterization of SiO 2 Nanoparticle Biointeractions Using BrightSilica. Advanced Functional Materials 2014, 24 (24), 3765–3775. https://doi.org/10.1002/adfm.201304126.

(7) Lanni, E. J.; Masyuko, R. N.; Driscoll, C. M.; Dunham, S. J. B.; Shrout, J. D.; Bohn, P. W.; Sweedler, J. V. Correlated Imaging with C 60 -SIMS and Confocal Raman Microscopy: Visualization of Cell-Scale Molecular Distributions in Bacterial Biofilms. Analytical Chemistry 2014, 86 (21), 10885–10891. https://doi.org/10.1021/ac5030914.

(8) Ahlf, D. R.; Masyuko, R. N.; Hummon, A. B.; Bohn, P. W. Correlated Mass Spectrometry Imaging and Confocal Raman Microscopy for Studies of Three-Dimensional Cell Culture Sections. The Analyst 2014, 139 (18), 4578. https://doi.org/10.1039/C4AN00826J.

(9) Bocklitz, T.; Bräutigam, K.; Urbanek, A.; Hoffmann, F.; von Eggeling, F.; Ernst, G.; Schmitt, M.; Schubert, U.; Guntinas-Lichius, O.; Popp, J. Novel

Workflow for Combining Raman Spectroscopy and MALDI-MSI for Tissue Based Studies. Analytical and Bioanalytical Chemistry 2015, 407 (26), 7865–7873. https://doi.org/10.1007/s00216-015-8987-5.

(10) Baig, N. F.; Dunham, S. J. B.; Morales-Soto, N.; Shrout, J. D. ; Sweedler, J. V. ;; Bohn, P. W. Multimodal Chemical Imaging of Molecular Messengers in Emerging Pseudomonas Aeruginosa Bacterial Communities. The Analyst 2015, 140 (19), 6544–6552. https://doi.org/10.1039/C5AN01149C.

(11) Lasch, P.; Noda, I. Two-Dimensional Correlation Spectroscopy for Multimodal Analysis of FT-IR, Raman, and MALDI-TOF MS Hyperspectral Images with Hamster Brain Tissue. Analytical Chemistry 2017, 89 (9), 5008–5016. https://doi.org/10.1021/acs.analchem.7b00332.

(12) Neumann, E. K.; Comi, T. J.; Spegazzini, N.; Mitchell, J. W.; Rubakhin, S. S.; Gillette, M. U.; Bhargava, R.; Sweedler, J. V. Multimodal Chemical Analysis of the Brain by High Mass Resolution Mass Spectrometry and Infrared Spectroscopic Imaging. Analytical Chemistry 2018, 90 (19), 11572–11580. https://doi.org/10.1021/acs.analchem.8b02913.

(13) Rabe, J. H.; Sammour, D. A.; Schulz, S.; Munteanu, B.; Ott, M.; Ochs, K.; Hohenberger, P.; Marx, A.; Platten, M.; Opitz, C. A.; Ory, D. S.; Hopf, C. Fourier Transform Infrared Microscopy Enables Guidance of Automated Mass Spectrometry Imaging to Predefined Tissue Morphologies. Scientific Reports 2018, 8 (1), 1–11. https://doi.org/10.1038/s41598-017-18477-6.

(14) Burkhow, S. J.; Stephens, N. M.; Mei, Y.; Dueñas, M. E.; Freppon, D. J.; Ding, G.; Smith, S. C.; Lee, Y. J.; Nikolau, B. J.; Whitham, S. A.; Smith, E. A. Characterizing Virus-Induced Gene Silencing at the Cellular Level with in Situ Multimodal Imaging. Plant Methods 2018, 14 (1), 1–12. https://doi.org/10.1186/s13007-018-0306-7.

(15) Bergholt, M. S.; Serio, A.; McKenzie, J. S.; Boyd, A.; Soares, R. F.; Tillner, J.; Chiappini, C.; Wu, V.; Dannhorn, A.; Takats, Z.; Williams, A.; Stevens, M. M. Correlated Heterospectral Lipidomics for Biomolecular Profiling of Remyelination in Multiple Sclerosis. ACS Central Science 2018, 4 (1), 39–51. https://doi.org/10.1021/acscentsci.7b00367.

(16) Ryabchykov, O.; Popp, J.; Bocklitz, T. Fusion of MALDI Spectrometric Imaging and Raman Spectroscopic Data for the Analysis of Biological Samples. Frontiers in Chemistry 2018, 6, 1–10. https://doi.org/10.3389/fchem.2018.00257.

(17) Morales-Soto, N.; Dunham, S. J. B.; Baig, N. F.; Ellis, J. F.; Madukoma, C. S.; Bohn, P. W.; Sweedler, J. V.; Shrout, J. D. Spatially Dependent Alkyl Quinolone Signaling Responses to Antibiotics in Pseudomonas Aeruginosa Swarms. Journal of Biological Chemistry 2018, 293 (24), 9544–9552. https://doi.org/10.1074/jbc.RA118.002605.

(18) Bedia, C.; Sierra, À.; Tauler, R. Application of Chemometric Methods to the Analysis of Multimodal Chemical Images of Biological Tissues. Analytical and Bioanalytical Chemistry 2020, 412 (21), 5179–5190. https://doi.org/10.1007/s00216-020-02595-8.

(19) Porta Siegel, T.; Hamm, G.; Bunch, J.; Cappell, J.; Fletcher, J. S.; Schwamborn, K. Mass Spectrometry Imaging and Integration with Other Imaging Modalities for Greater Molecular Understanding of Biological Tissues. Molecular Imaging and Biology 2018, 20 (6), 888–901. https://doi.org/10.1007/s11307-018-1267-y.

(20) Li, T.; He, J.; Mao, X.; Bi, Y.; Luo, Z.; Guo, C.; Tang, F. In Situ Biomarker Discovery and Label-Free Molecular Histopathological Diagnosis of Lung

Cancer by Ambient Mass Spectrometry Imaging. Nature Publishing Group 2015, 1–12. https://doi.org/10.1038/srep14089.

(21) Das, N. K.; Dai, Y.; Liu, P.; Hu, C.; Tong, L.; Chen, X.; Smith, Z. J. Raman plus X: Biomedical Applications of Multimodal Raman Spectroscopy. Sensors (Switzerland) 2017, 17 (7). https://doi.org/10.3390/s17071592.

(22) Cheng, J. X.; Xie, X. S. Vibrational Spectroscopic Imaging of Living Systems: An Emerging Platform for Biology and Medicine. Science 2015, 350 (6264). https://doi.org/10.1126/science.aaa8870.

(23) Cornett, D. S.; Reyzer, M. L.; Chaurand, P.; Caprioli, R. M. MALDI Imaging Mass Spectrometry: Molecular Snapshots of Biochemical Systems. Nature Methods 2007, 4 (10), 828–833. https://doi.org/10.1038/nmeth1094.

(24) Bird, B.; Remiszewski, S.; Kon, M.; Diem, M. Infrared Spectral Histopathology (SHP): A Novel Diagnostic Tool for the Accurate Classification of Lung Cancer. 2012. https://doi.org/10.1038/labinvest.2012.101.

(25) Gregson, C. Optimization of MALDI Tissue Imaging and Correlation with Immunohistochemistry in Rat Kidney Sections. Bioscience Horizons 2009, 2 (2), 134–146. https://doi.org/10.1093/biohorizons/hzp016.

(26) Balbekova, A.; Lohninger, H.; van Tilborg, G. A. F.; Dijkhuizen, R. M.; Bonta, M.; Limbeck, A.; Lendl, B.; Al-Saad, K. A.; Ali, M.; Celikic, M.; Ofner, J. Fourier Transform Infrared (FT-IR) and Laser Ablation Inductively Coupled Plasma–Mass Spectrometry (LA-ICP-MS) Imaging of Cerebral Ischemia: Combined Analysis of Rat Brain Thin Cuts Toward Improved Tissue Classification. Applied Spectroscopy 2018, 72 (2), 241–250. https://doi.org/10.1177/0003702817734618.

(27) Dukor, R. K. Vibrational Spectroscopy in the Detection of Cancer. Handbook of Vibrational Spectroscopy 2006. https://doi.org/10.1002/0470027320.s8107.

(28) Norris, J. L.; Caprioli, R. M. Analysis of Tissue Specimens by Matrix-Assisted Laser Desorption/Ionization Imaging Mass Spectrometry in Biological and Clinical Research. Chemical Reviews 2013, 113 (4), 2309–2342. https://doi.org/10.1021/cr3004295.

(29) Dannhorn, A.; Kazanc, E.; Ling, S.; Nikula, C.; Karali, E.; Serra, M. P.; Vorng, J.-L.; Inglese, P.; Maglennon, G.; Hamm, G.; Swales, J.; Strittmatter, N.; Barry, S. T.; Sansom, O. J.; Poulogiannis, G.; Bunch, J.; Goodwin, R. J.; Takats, Z. Universal Sample Preparation Unlocking Multimodal Molecular Tissue Imaging. Analytical Chemistry 2020, 92 (16), 11080–11088. https://doi.org/10.1021/acs.analchem.0c00826.

(30) Van De Plas, R.; Yang, J.; Spraggins, J.; Caprioli, R. M. Image Fusion of Mass Spectrometry and Microscopy: A Multimodality Paradigm for Molecular Tissue Mapping. Nature Methods 2015, 12 (4), 366–372. https://doi.org/10.1038/nmeth.3296.

(31) Iakab, S. A.; Sementé, L.; Altares, M. G.; Correig, X.; Ràfols, P. Raman2imzML Converts Raman Imaging Data into the Standard Mass Spectrometry Imaging Format. 2020, 1–7. https://doi.org/10.1186/s12859-020-03789-8.

(32) Mascagni, P.; Longo, F.; Barberio, M.; Seeliger, B.; Agnus, V.; Saccomandi, P.; Hostettler, A.; Marescaux, J.; Diana, M. New Intraoperative Imaging Technologies: Innovating the Surgeon's Eye toward Surgical Precision. Journal of Surgical Oncology 2018, 118 (2), 265–282. https://doi.org/10.1002/jso.25148.

(33) Balog, J.; Sasi-Szabó, L.; Kinross, J.; Lewis, M. R.; Muirhead, L. J.; Veselkov, K.; Mirnezami, R.; Dezso, B.; Damjanovich, L.; Darzi, A.; Nicholson, J. K.; Takáts, Z. Intraoperative Tissue Identification Using Rapid Evaporative Ionization Mass Spectrometry. Science Translational Medicine 2013, 5 (194). https://doi.org/10.1126/scitranslmed.3005623.

(34) Willetts, K.; Farr, L.; Foreman, L.; Willetts, K.; Farr, L.; Foreman, L. From Stellar Composition to Cancer Diagnostics. Contemporary Physics 2019, 0 (0), 1–15. https://doi.org/10.1080/00107514.2019.1645492.

(35) Jermyn, M.; Mok, K.; Mercier, J.; Desroches, J.; Pichette, J.; Saint-arnaud, K.; Bernstein, L.; Guiot, M.; Petrecca, K.; Leblond, F. Intraoperative Brain Cancer Detection with Raman Spectroscopy in Humans. 2015, 7 (274), 1–10.

(36) Georgantzopoulou, A.; Serchi, T.; Cambier, S.; Leclercq, C. C.; Renaut, J.; Shao, J.; Kruszewski, M.; Lentzen, E.; Grysan, P.; Eswara, S.; Audinot, J. N.; Contal, S.; Ziebel, J.; Guignard, C.; Hoffmann, L.; Murk, A. T. J.; Gutleb, A. C. Effects of Silver Nanoparticles and Ions on a Co-Culture Model for the Gastrointestinal Epithelium. Particle and Fibre Toxicology 2016, 13 (1). https://doi.org/10.1186/s12989-016-0117-9.

(37) Chary, A.; Serchi, T.; Moschini, E.; Hennen, J.; Cambier, S.; Ezendam, J.; Blömeke, B.; Gutleb, A. C. An in Vitro Coculture System for the Detection of Sensitization Following Aerosol Exposure. Altex 2019, 36 (3), 403–418. https://doi.org/10.14573/altex.1901241.

(38) Manke, A.; Wang, L.; Rojanasakul, Y. Mechanisms of Nanoparticle-Induced Oxidative Stress and Toxicity. BioMed Research International 2013, 2013. https://doi.org/10.1155/2013/942916.

(39) Sofińska, K.; Wilkosz, N.; Szymoński, M.; Lipiec, E. Molecular Spectroscopic Markers of DNA Damage. Molecules 2020, 25 (3), 1–24. https://doi.org/10.3390/molecules25030561.

(40) Sparvero, L.; Amoscato, A.; Kochanek, P.; Pitt, B.; Kagan, V.; Bayır, H. Mass-Spectrometry Based Oxidative Lipidomics and Lipid Imaging: Applications in Traumatic Brain Injury. Journal of Neurochemistry 2010, 115 (6), 1322–1336. https://doi.org/10.1111/j.1471-4159.2010.07055.x.Mass-Spectrometry.

(41) Jadoon, S.; Karim, S.; Akram, M. R.; Kalsoom Khan, A.; Zia, M. A.; Siddiqi, A. R.; Murtaza, G. Recent Developments in Sweat Analysis and Its Applications. International Journal of Analytical Chemistry 2015, 2015. https://doi.org/10.1155/2015/164974.

(42) Guinan, T.; Della Vedova, C.; Kobus, H.; Voelcker, N. H. Mass Spectrometry Imaging of Fingerprint Sweat on Nanostructured Silicon. Chem. Commun. 2015, 51, 6088–6091. https://doi.org/10.1039/C4CC08762C.

(43) MacEdo, A. N.; Mathiaparanam, S.; Brick, L.; Keenan, K.; Gonska, T.; Pedder, L.; Hill, S.; Britz-McKibbin, P. The Sweat Metabolome of Screen-Positive Cystic Fibrosis Infants: Revealing Mechanisms beyond Impaired Chloride Transport. ACS Central Science 2017, 3 (8), 904–913. https://doi.org/10.1021/acscentsci.7b00299.

(44) Chen, X.; Gasecka, P.; Formanek, F.; Galey, J. B.; Rigneault, H. In Vivo Single Human Sweat Gland Activity Monitoring Using Coherent Anti-Stokes Raman Scattering and Two-Photon Excited Autofluorescence Microscopy. British Journal of Dermatology 2016, 174 (4), 803–812. https://doi.org/10.1111/bjd.14292.

(45) Bakry, R.; Rainer, M.; Huck, C. W.; Bonn, G. K. Analytica Chimica Acta Protein Profiling for Cancer Biomarker Discovery Using Matrix-Assisted Laser Desorption / Ionization Time-of-Flight Mass Spectrometry and Infrared Imaging : A Review. Analytica Chimica Acta 2011, 690 (1), 26–34. https://doi.org/10.1016/j.aca.2011.01.044.

(46) Rüther, A.; Perez-guaita, D.; Heraud, P.; Stone, N.; Dudgeon, A.; Gardner, B.; Reddy, R.; Mayerich, D.; Bhargava, R. Care Medicine : A Review. 2019, 72, 52–84. https://doi.org/10.1177/0003702818791939.Application.

(47) Iakab, S. A.; Ràfols, P.; Tajes, M.; Correig-Blanchar, X.; García-Altares, M. Gold Nanoparticle-Assisted Black Silicon Substrates for Mass Spectrometry Imaging Applications. ACS Nano 2020, 14 (6), 6785–6794. https://doi.org/10.1021/acsnano.0c00201.

(48) Milewska, A.; Zivanovic, V.; Merk, V.; Arnalds, U. B.; Sigurjónsson, Ó. E.; Kneipp, J.; Leosson, K. Gold Nanoisland Substrates for SERS Characterization of Cultured Cells. Biomedical Optics Express 2019, 10 (12), 6172. https://doi.org/10.1364/boe.10.006172.

(49) Touzalin, T.; Joiret, S.; Lucas, I. T.; Maisonhaute, E. Electrochemical Tip-Enhanced Raman Spectroscopy Imaging with 8 nm Lateral Resolution. Electrochemistry Communications 2019, 108 (September), 106557. https://doi.org/10.1016/j.elecom.2019.106557.

(50) Marcott, C.; Kansiz, M.; Dillon, E.; Cook, D.; Mang, M. N.; Noda, I. Two-Dimensional Correlation Analysis of Highly Spatially Resolved Simultaneous IR and Raman Spectral Imaging of Bioplastics Composite Using Optical Photothermal Infrared and Raman Spectroscopy. Journal of Molecular Structure 2020, 1210, 128045. https://doi.org/10.1016/j.molstruc.2020.128045.

(51) Tai, T.; Karácsony, O.; Bocharova, V.; Van Berkel, G. J.; Kertesz, V. Topographical and Chemical Imaging of a Phase Separated Polymer Using a Combined Atomic Force Microscopy/Infrared Spectroscopy/Mass Spectrometry Platform. Analytical Chemistry 2016, 88 (5), 2864–2870. https://doi.org/10.1021/acs.analchem.5b04619.

(52) Niehaus, M.; Soltwisch, J.; Belov, M. E.; Dreisewerd, K. Transmission-Mode MALDI-2 Mass Spectrometry Imaging of Cells and Tissues at Subcellular Resolution. Nature Methods 2019, 16 (9), 925–931. https://doi.org/10.1038/s41592-019-0536-2.

(53) Lanekoff, I.; Heath, B. S.; Liyu, A.; Thomas, M.; Carson, J. P.; Laskin, J. Automated Platform for High-Resolution Tissue Imaging Using Nanospray Desorption Electrospray Ionization Mass Spectrometry. Analytical Chemistry 2012, 84 (19), 8351–8356. https://doi.org/10.1021/ac301909a.

(54) Kompauer, M.; Heiles, S.; Spengler, B. Atmospheric Pressure MALDI Mass Spectrometry Imaging of Tissues and Cells at 1.4-Mm Lateral Resolution. Nature Methods 2016, 14 (1), 90–96. https://doi.org/10.1038/nmeth.4071.

(55) Wang, H. A. O.; Grolimund, D.; Giesen, C.; Borca, C. N.; Shaw-Stewart, J. R. H.; Bodenmiller, B.; Günther, D. Fast Chemical Imaging at High Spatial Resolution by Laser Ablation Inductively Coupled Plasma Mass Spectrometry. Analytical Chemistry 2013, 85 (21), 10107–10116. https://doi.org/10.1021/ac400996x.

(56) Limbeck, A.; Galler, P.; Bonta, M.; Bauer, G.; Nischkauer, W.; Vanhaecke, F. Recent Advances in Quantitative LA-ICP-MS Analysis: Challenges and Solutions in the Life Sciences and Environmental Chemistry ABC Highlights: Authored by Rising Stars and Top Experts. Analytical and

Bioanalytical Chemistry 2015, 407 (22), 6593–6617. https://doi.org/10.1007/s00216-015-8858-0.

(57) Kollmer, F.; Paul, W.; Krehl, M.; Niehuis, E. Ultra High Spatial Resolution SIMS with Cluster Ions - Approaching the Physical Limits. Surface and Interface Analysis 2013, 45 (1), 312–314. https://doi.org/10.1002/sia.5093.

(58) Yoon, S.; Lee, T. G. Biological Tissue Sample Preparation for Time-of-Flight Secondary Ion Mass Spectrometry (ToF–SIMS) Imaging. Nano Convergence 2018, 5 (1). https://doi.org/10.1186/s40580-018-0157-y.

(59) Bertasa, M.; Possenti, E.; Botteon, A.; Conti, C.; Sansonetti, A.; Fontana, R.; Striova, J.; Sali, D. Close to the Diffraction Limit in High Resolution ATR FTIR Mapping: Demonstration on Micrometric Multi-Layered Art Systems. Analyst 2017, 142 (24), 4801–4811. https://doi.org/10.1039/c7an00873b.

(60) Kazarian, S. G.; Chan, K. L. A. Applications of ATR-FTIR Spectroscopic Imaging to Biomedical Samples. Biochimica et Biophysica Acta - Biomembranes 2006, 1758 (7), 858–867. https://doi.org/10.1016/j.bbamem.2006.02.011.

2.3.11. Supporting Information

Table S1. Specificities of the MSI and VSI methods used in (multimodal) imaging.

Method	Lat. res.*	Max. lat. res.**	Typical Spectral Range	Sample requirement	Sample preparation	Imaging challenges	Imaging advantages
DESI-MS (e.g. Q-TOF)	20-50 µm	10 µm[53]	0-2 kDa	Intermediate polarity to non-polar Flat surface Stable over time	Mounting on non-conductive surface Electrospray composition optimization	Lack of high spatial resolution Electrospray may damage soft samples	Ambiental ionization conditions Soft ionization
MALDI-MS (e.g. TOF, QTOF, FTICR)	20-150 µm	1.4 µm[54]	0-70 kDa	Vacuum compatible (dry) Flat surface Stable over time	Mounting on conductive surface Matrix selection and application	Low mass range info missing Matrix effects Analyte delocalization	Wide range of molecules Soft ionization
SALDI-MS (e.g. TOF, LTQ-Orbitrap)	20 µm	1.4 µm[54]	0-1 kDa	Vacuum compatible (dry) Flat surface Stable over time	Mounting on conductive surface Nanostructure application	Reproducibility	Analysis in the low mass range (low background) Soft ionization
LA-ICP-MS (e.g. Q)	7-40 µm	1 µm[55]	7-250 Da	Vacuum compatible (dry) Flat surface	Mounting on solid support Thin metal layer deposition	Hard ionization “Elemental fractionation” Matrix effects [56]	High precision elemental analysis
SIMS-MS (e.g. TOF, QTOF)	1-200 µm	120 nm[57]	0-1 kDa	Vacuum compatible (dry) Flat surface Cryogenic temperature compatible[58]	Mounting on solid support	Low production yield of secondary ions Extensive fragmentation	3D imaging Matrix-free detection High spatial resolution
ATR-IR	18 µm	1 µm[59]	7000–650 cm^{-1}	Flat surface Lower refractive index then ATR crystal	Mounting on ATR crystal Improving contact with ATR crystal by flattening/pressing sample	Water content	Label-free & Non-destructive Measurements in liquid Time dependent analysis Thick samples[60]

FTIR	5-25 µm	diffraction limited ~2.5 µm	4000-700 cm^{-1}	Flat surface Dry sample (low water content) Thin sample	Mounting on low IR absorption transparent substrates	Lack of high resolution Water content	Label-free & Non-destructive Fast acquisition
Raman	0.3-250 µm	diffraction limited ~ƛ/2 ~250 nm	4000-10 cm^{-1}	Flat surface*** Stable over time	Mounting on low refractive index and absorption substrate	Autofluorescence Long acquisition time Lack of specificity	Label-free & Non-destructive Molecular fingerprint Time dependent analysis
SERS	2 µm	diffraction limited ~ƛ/2 ~250 nm	4000-10 cm^{-1}	Flat surface*** Stable over time	Mounting on low refractive index and absorption substrate and nanostructure application Mounting on nanostructured surface	Autofluorescence Long acquisition time Lack of reproducibility	Targeted detection Time dependent analysis

*- lateral resolution range used in multimodal imaging applications presented in this perspective

**- maximum lateral resolution reported in literature

***- The inVia Qontor from Renishaw uses LiveTrack™ focus tracking technology to enable users to analyze samples with uneven, curved or rough surfaces. (https://www.renishaw.com/en/invia-qontor-confocal-raman-microscope--38125)

Table S2. Multimodal imaging approaches from the last decade (Img. Acq. Order = order of acquisition; Lat. Res. = lateral resolution)

Table S2. (page 1)

		Sample Preparation		Acquisition		Data			Results
Ref.	Method (Img. Acq. Order)	Sample	Substrate + enhancing agent	Same section	Lat. Res. (µ m)	Time	Format/ software	Processing	Analysis	Specific Info	Synergy
Ahlf 2014	MALDI-TOF (2nd)	Cell cultures	ITO slide + CHCA / DHB / SA	YES	50	N/A	ASCII Bruker	Background correction; matrix peak removal; peak alignment; normalization; PCA	PC correlation; image co-localization	Small molecules; lipids; proteins lipids	50 µm pixel of MALDI corresponds to an entire Raman image; PC score images are fused for colocalization; PCA used to extract chemically informative factors responsible for spatial variation in the spectra from MSI and VSI
	Raman (1st)		ITO slide	YES	1	3h	ASCII WITec	Cosmic ray removal; autofluorescence removal; spectra alignment; normalization; PCA			
Baig 2015	SIMS-QTOF (N/A)	P. aeruginosa bacterial biofilm	Si wafer	N/A	200 and 21	N/A	.wiff .img BioMap	Normalization	Univariate analysis (ion map)	Metabolites	SIMS and Raman imaging characterized the spatial distribution of several quinolone quorum sensing molecules and quinoline secondary metabolites across the surface of P. aeruginosa at various states of organization. Raman in conjunction with PCA identified broad molecular classes (e.g. quinolones and quinolines)
	Raman (N/A)		Si wafer	N/A	0.3	16 min	WITec Matlab	Cosmic ray removal, PCA	Univariate analysis (band map)	Proteins, carbohydrate moieties	

Table S2. (page 2)

	Sample Preparation			Acquisition		Data			Results	
Ref.	Method (Img. Acq. Order)	Sample	Substrate + enhancing agent	Same section	Lat. Res. (µ m)	Time	Format/ software	Processing	Analysis	Specific Info	Synergy
Balbekova 2018	LA-ICP-Q (N/A)	Ischemic stroke rat brain	Immunohistochemistry microscope slides	NO	40	120 µm/s	N/A Imagelab	Normalization	Anchor-points defined spatial alignment; data sets were merged to a hyperspectral datacube; PLS-DA and RDF classification models	Biologically relevant elements	Reliable multivariate analysis: no false-positives or false-negatives were observed for the classification results obtained from models based on the hyperspectral dataset; The RDF classifier built on the combined data sets appeared to be more precise compared to classifiers built on the individual data sets
	FTIR (N/A)		IR-reflecting microscope slides	NO	N/A	N/A	OPUS Imagelab	Baseline correction, normalization, smoothing,		Proteins, nucleic acids, lipids, lipid acyl chain, fatty acids	
Bedia 2020	MALDI-TOF (2nd)	Primary breast carcinoma implanted in the intra-mammary fat path of nude mice	ITO slide + DHB	YES	150	N/A	.imzML Matlab	Peak picking; normalization	x-y orientation correction; image size adjustments by resizing to the same spatial dimensions of the MALDI-MS image (31 × 50); multivariate curve resolution-alternating least squares (MCR-ALS)	Lipids: PC(P-30:1), PA(30:2), PA, PE, PG, PI	The multimodal resolution of the fused images revealed the different lipid compositions associated with specific IR fingerprints, their particular localizations; the limitation of the low spatial resolution of MALDI was compensated for with the higher resolution IR image. The spectra resolved during the analysis of the low spatial resolution images can be used in a second step to recover the distribution maps of the constituents at high spatial resolution by spectral projection
	IR (1st)		ITO slide	YES	25	N/A	.csv Matlab	Baseline correction		Proteins, ester lipids, alcohols, alkyl chains, carboxylic acids	

Table S2. (page 3)

		Sample Preparation			Acquisition		Data			Results	
Ref.	Method (Img. Acq. Order)	Sample	Substrate + enhancing agent	Same section	Lat. Res. (µ m)	Time	Format/ software	Processing	Analysis	Specific Info	Synergy
Bergholt 2018	DESI-QTOF (2nd)	Mouse model brain; human multiple sclerosis brain sections	Magnesium fluoride slides	YES/ NO	20 mice/ 50 human	N/A	Matlab	Normalization; ANOVA between control and lesion groups; FDR correction; MMC-LDA	DESI and Raman images coregistered using a fiducial marker-based alignment; pixelwise approach	Lipids	A heterospectral DESI-MS and Raman correlation map enables structural features detected by vibrational spectroscopy to be assigned to individual molecular species detected by mass spectrometry; This technique revealed the subtle and apparently buried Raman peaks; approach to profile the lipidomics of de- and re-myelinated tissue at both the structural and compositional levels
	Raman (1st)		Superfrost Plus adhesive glass slides	YES/ NO	6 mice/ 150 human	34h / 41 min human	WITec	Tissue autofluorescence removal; normalization; PLS-DA; k-means clustering		Lipids Proteins; DNA	
Bocklitz 2013	MALDI-TOF (2nd)	Mouse brain	ITO slide + CHCA	YES	75	14h	imzML Bruker	Background correction	PLD correlation	lipids	MALDI signal translated into a Raman fingerprint by multivariate calibration model; predicting the MALDI peak intensity based on the transformed and preprocessed Raman scan
	Raman (1st)		ITO slide	YES	25	3s/ spectrum	WITec	Background correction		proteins	

Table S2. (page 4)

		Sample Preparation			Acquisition		Data				Results	
Ref.	Method (Img. Acq. Order)	Sample	Substrate + enhancing agent	Same section	Lat. Res. (µ m)	Time	Format/ software	Processing	Analysis	Specific Info	Synergy
Bocklitz 2015	MALDI-TOF (2nd)	Larynx carcinoma	ITO slide + CHCA	YES	25	20h	imzML Bruker	Vector normalization; PCA	Co-registration by rigid registration	Cancer markers; lipidome	Co-registering Raman and H&E image to the MALDI grid; Raman spectroscopy used to determine the tissue type and MALDI imaging used to investigate changes occurring in this tissue type
	Raman (1st)		ITO slide	YES	12.5	21h	WITec	Background correction; vector normalization; PCA		Lipids; proteins; nucleic acids	
Bradshaw 2013	MALDI-QTOF (2nd)	Condom lubricant-contaminated fingermarks	MALDI plate + CHCA	Remaining deposit	N/A	N/A	wiff .txt Analyst	Spectra recalibration; normalization	Univariate (ion map)	Polymers; endogenous exogenous compounds	Complementary information to identify condom brands
	ATR-IR (1st)		BDVA gelatine lifter	First lift	18	N/A	Resolutio ns Pro	N/A	Univariate (band map)	Polymers	
Burkhow 2018	SALDI-LTOQ Orbitrap (N/A)	Gene modified maize leaves	Packing tape + Ag nanolayer	N/A	20	N/A	ImageQue st	N/A	Univariate (ion map)	Phytoene	The accumulation of phytoene by MS imaging agrees with the reduced carotenoid Raman signal within the same area; biochemical changes in carotenoid expression from gene silencing; sensitivity of MS imaging enables the imaging of phytoene and Raman imaging provides high selectivity for downstream carotenoids
	Raman (N/A)		Glass slide	N/A	3	15 s	Igor Pro Matlab	Gaussian batch fit and extraction of the 1520 cm^{-1} peak amplitudes and maxima; noise quantification in specific region	Univariate analysis (band map)	Vascular bundles; mesophyll and epidermal cells	

Table S2. (page 5)

	Sample Preparation			Acquisition		Data			Results	
Ref.	Method (Img. Acq. Order)	Sample	Substrate + enhancing agent	Same section	Lat. Res. (μ m)	Time	Format/ software	Processing	Analysis	Specific Info	Synergy
Drescher 2014	LA-ICP-MS (N/A)	Mouse fibroblast cells and macrophages	Sterile cover slip + silica-coated Au and Ag nanoparticles	NO	7-8	N/A	Origin ImageJ	N/A	Univariate analysis (map)	Number of nanoparticles	Investigation of intra- and extracellular biomolecules; spatially resolved LA-ICP-MSI showed differences in the uptake of nanoparticles into cells and SERS spectra characterized nanoparticle biomolecule interactions; nanoparticles enabled multimodal qualitative and quantitative characterization
	SERS (N/A)			NO	2	N/A	Matlab	N/A	Univariate (band map)	Biomolecules; culture medium components; pATP reporter	
Lanni 2014	SIMS-QTOF (2nd)	*Pseudomonas aeruginosa* bacterial biofilm	Si wafer	YES	10	N/A	.img BioMap	N/A	Univariate(ion map)	Metabolites	The nanometer-scale spatial resolution provided by Raman is complemented by the chemical specificity of SIMS; correlated detection of at least nine quinolones and additional related metabolites present in biofilms
	Raman (1st) *a*		Si wafer	YES	0.3	16 min	WITec Igor Pro	N/A	Univariate (band map)	Proteins, carbohydrate moieties	
Lasch 2017	MALDI-TOF (3rd)	Hamster brain	ITO slide + DHB	NO	60	N/A	Cytospec	Smoothing; vector normalization;	*k*-means cluster analysis	Sphingolipids; cholesterol;	Spectra interpretation, band assignment and identification of a very subtle heterospectral correlation pattern; Spectral resolution enhancement procedures, like Pareto-scaling and node attenuation, enabled the assignment of overlapping bands in HSI data
	Raman (2nd)		CaF2 slide	YES	1	1.1 h	WITec Cytospec	Baseline correction; cosmic ray	Unsupervised hierarchical cluster analysis	Sphingolipids; cholesterol;	
	FTIR (1st)		CaF2 slide	YES	25	N/A	Bruker Cytospec	Spectral quality test; vector normalization; first derivative		Sphingolipids	

Table S2. (page 6)

	Sample Preparation			Acquisition		Data			Results		
Ref.	Method (Img. Acq. Order)	Sample	Substrate + enhancing agent	Same section	Lat. Res. (µ m)	Time	Format/ software	Processing	Analysis	Specific Info	Synergy
Le Naour 2009	SIMS-TOF (2nd)	Liver biopsies	Si wafer	NO	1-2	N/A	IonSpec IonImage	normalizatio n	Univariate (ion map)	Lipids	One of the first studies to emphasize the advantages of combining different spectroscopies for investigating in situ the chemical composition of tissues; lipid content characterization and visualization of small lipid droplets
	FTIR (1st)		Glass slide	NO	6-10	N/A	OMNIC	N/A	Univariate (band map)	Proteins, lipids	
Li 2010	SIMS-TOF (2nd)	*Miscanthus x giganteus*, a tall perennial grass	Si wafer	YES	2	N/A	WinCadence	N/A	Univariate (ion map)	Lignin and cellulose fragment ions	Spatially correlated LDI, SIMS and Raman imaging provide high-quality, high-resolution subcellular images of Miscanthus cross sections, and the combination of information from the mass spectrometry and Raman scattering allows specific chemical assignments of observed structures, difficult to assign from either imaging approach alone
	LDI (3rd		Si wafer	YES	100	N/A	ruker	N/A	Univariate (ion map)	High MW compounds	
	Raman (1st)		Si wafer	YES	0.65	37 min	WITec	N/A	Univariate (band map)	Lignin and cellulose	
Moreales Soto 2018	SIMS-TOF (N/A)	*P. aeruginosa* bacterial biofilm planktonic cells	Custom aluminium SIMS plate	NO	50	7 min	.imzML MsiReader	PCA	Univariate (ion map)	Targeted alkyl quinolones: PQS, C9-PQS, HQNO, and NQNO	SIMS PCA image results corroborate the relative quantification results and validate the CRM observations, indicating that when exposed to the aminoglycoside tobramycin, *P. aeruginosa* cells undergo a metabolite shift; multimodal imaging for spatial heterogeneity in signaling is possible within a *P. aeruginosa* community
	Raman (N/A		N/A	NO	0.5	2.5 h	WITec Matlab	Removed cosmic ray spikes; PCA	Univariate (band and PCA map)	DNA, proteins, lipids, PQS, AQNO	

Table S2. (page 7)

	Sample Preparation			Acquisition		Data			Results	
Ref.	Method (Img. Acq. Order)	Sample	Substrate + enhancing agent	Same section	Lat. Res. (μ m)	Time	Format/ software	Processing	Analysis	Specific Info	Synergy
Neumann 2018	MALDI-FT-ICR (1st)	Rat brain	Low emission glass slide + DHB	YES	25	N/A	.imzML SCILS Matlab	Normalization; spectra alignment; peak picking	Pan sharpening to sharpen MSI images with higher spatial resolution IR image	lipids	Data fusion and unsupervised clustering for detecting significant chemical differences; exploring chemical heterogeneity present in the brain
	FTIR (2nd)		Low emission glass slide	YES	5	N/A	.mat Matlab	N/A		Lipids, proteins	
Petit 2010	SIMS-TOF (2nd)	Liver cirrhosis	Au-coated glass slide	YES	1-2	6 min	IonSpec IonImage	N/A	Univariate (ion map)	Lipids	Investigating biological tissue without any treatment, labeling, or staining of the sample and using a single sample holder; characterization of liver cirrhosis ester lipid species
	FTIR (1st)		Au-coated glass slide	YES	6-10	N/A	OMNIC	N/A	Univariate (band map)	Lipids, proteins, nucleic acids, sugars	
Rabe 2018	MALDI-TOF (2nd)	Mouse brain / PhCCAA	Au-coated slide + DHB	YES	20	18.3 h	R, Cardinal package	Peak picking; normalization; baseline correction	Spatially aware segmentation	Lipids; metabolites	FTIR image segmentation guides MSI acquisition; this allows the exclusive acquisition of regions of interest to increase throughput in cases where the acquisition of whole tissue sections at high resolution is impractical or even infeasible
	FTIR (1st)	Human gastrointestinal stromal tumor	Au-coated slide	YES	6.5	1h	Matlab	Baseline correction; first derivative; normalization; spectral quality test	*k*-means clustering	Cell groups by molecular feature	

Table S2. (page 8)

	Sample Preparation			Acquisition		Data				Results	
Ref.	Method (Img. Acq. Order)	Sample	Substrate + enhancing agent	Same section	Lat. Res. (μ m)	Time	Format/ software	Processing	Analysis	Specific Info	Synergy
Ryabchykov 2018	MALDI-TOF (2nd)	Mouse brain	ITO slide + CHCA	YES	75	N/A	Bruker FlexData	Noise removal, background correction, and TIC normalization	Before preprocessing and data fusion, the MALDI and Raman spectra were interpolated to the same spatial grid; data fusion; PCA	Lipids	Changes in the lipid content observed by a high correlation of the Raman spectral region with MALDI mass spectra; data fusion increases reliability not only for the spectral features but also for the spatial features present in the data
	Raman (1st)		ITO slide	YES	25	3s/ spectrum	WITec	Corrected for fluorescence background and vector normalized		Lipids, proteins and DNA	

2.3.12. Supporting Information References

(1) Lanekoff, I.; Heath, B. S.; Liyu, A.; Thomas, M.; Carson, J. P.; Laskin, J. Automated Platform for High-Resolution Tissue Imaging Using Nanospray Desorption Electrospray Ionization Mass Spectrometry. Analytical Chemistry 2012, 84 (19), 8351–8356. https://doi.org/10.1021/ac301909a.

(2) Kompauer, M.; Heiles, S.; Spengler, B. Atmospheric Pressure MALDI Mass Spectrometry Imaging of Tissues and Cells at 1.4-Mm Lateral Resolution. Nature Methods 2016, 14 (1), 90–96. https://doi.org/10.1038/nmeth.4071.

(3) Wang, H. A. O.; Grolimund, D.; Giesen, C.; Borca, C. N.; Shaw-Stewart, J. R. H.; Bodenmiller, B.; Günther, D. Fast Chemical Imaging at High Spatial Resolution by Laser Ablation Inductively Coupled Plasma Mass Spectrometry. Analytical Chemistry 2013, 85 (21), 10107–10116. https://doi.org/10.1021/ac400996x.

(4) Limbeck, A.; Galler, P.; Bonta, M.; Bauer, G.; Nischkauer, W.; Vanhaecke, F. Recent Advances in Quantitative LA-ICP-MS Analysis: Challenges and Solutions in the Life Sciences and Environmental Chemistry ABC Highlights: Authored by Rising Stars and Top Experts. Analytical and Bioanalytical Chemistry 2015, 407 (22), 6593–6617. https://doi.org/10.1007/s00216-015-8858-0.

(5) Kollmer, F.; Paul, W.; Krehl, M.; Niehuis, E. Ultra High Spatial Resolution SIMS with Cluster Ions - Approaching the Physical Limits. Surface and Interface Analysis 2013, 45 (1), 312–314. https://doi.org/10.1002/sia.5093.

(6) Yoon, S.; Lee, T. G. Biological Tissue Sample Preparation for Time-of-Flight Secondary Ion Mass Spectrometry (ToF–SIMS) Imaging. Nano Convergence 2018, 5 (1). https://doi.org/10.1186/s40580-018-0157-y.

(7) Bertasa, M.; Possenti, E.; Botteon, A.; Conti, C.; Sansonetti, A.; Fontana, R.; Striova, J.; Sali, D. Close to the Diffraction Limit in High Resolution ATR FTIR Mapping: Demonstration on Micrometric Multi-Layered Art Systems. Analyst 2017, 142 (24), 4801–4811. https://doi.org/10.1039/c7an00873b.

(8) Kazarian, S. G.; Chan, K. L. A. Applications of ATR-FTIR Spectroscopic Imaging to Biomedical Samples. Biochimica et Biophysica Acta - Biomembranes 2006, 1758 (7), 858–867. https://doi.org/10.1016/j.bbamem.2006.02.011.

(9) Ahlf, D. R.; Masyuko, R. N.; Hummon, A. B.; Bohn, P. W. Correlated Mass Spectrometry Imaging and Confocal Raman Microscopy for Studies of Three-Dimensional Cell Culture Sections. The Analyst 2014, 139 (18), 4578. https://doi.org/10.1039/C4AN00826J.

(10) Baig, N. F.; Dunham, S. J. B.; Morales-Soto, N.; Shrout, J. D.; Sweedler, J. V.;; Bohn, P. W. Multimodal Chemical Imaging of Molecular Messengers in Emerging Pseudomonas Aeruginosa Bacterial Communities. The Analyst 2015, 140 (19), 6544–6552. https://doi.org/10.1039/C5AN01149C.

(11) Balbekova, A.; Lohninger, H.; van Tilborg, G. A. F.; Dijkhuizen, R. M.; Bonta, M.; Limbeck, A.; Lendl, B.; Al-Saad, K. A.; Ali, M.; Celikic, M.; Ofner, J. Fourier Transform Infrared (FT-IR) and Laser Ablation Inductively Coupled Plasma–Mass Spectrometry (LA-ICP-MS) Imaging of Cerebral Ischemia: Combined Analysis of Rat Brain Thin Cuts Toward Improved

Tissue Classification. Applied Spectroscopy 2018, 72 (2), 241–250. https://doi.org/10.1177/0003702817734618.

(12) Bedia, C.; Sierra, À.; Tauler, R. Application of Chemometric Methods to the Analysis of Multimodal Chemical Images of Biological Tissues. Analytical and Bioanalytical Chemistry 2020, 412 (21), 5179–5190. https://doi.org/10.1007/s00216-020-02595-8.

(13) Bergholt, M. S.; Serio, A.; McKenzie, J. S.; Boyd, A.; Soares, R. F.; Tillner, J.; Chiappini, C.; Wu, V.; Dannhorn, A.; Takats, Z.; Williams, A.; Stevens, M. M. Correlated Heterospectral Lipidomics for Biomolecular Profiling of Remyelination in Multiple Sclerosis. ACS Central Science 2018, 4 (1), 39–51. https://doi.org/10.1021/acscentsci.7b00367.

(14) Bocklitz, T. W.; Crecelius, A. C.; Matthäus, C.; Tarcea, N.; von Eggeling, F.; Schmitt, M.; Schubert, U. S.; Popp, J. Deeper Understanding of Biological Tissue: Quantitative Correlation of MALDI-TOF and Raman Imaging. Analytical Chemistry 2013, 85 (22), 10829–10834. https://doi.org/10.1021/ac402175c.

(15) Bocklitz, T.; Bräutigam, K.; Urbanek, A.; Hoffmann, F.; von Eggeling, F.; Ernst, G.; Schmitt, M.; Schubert, U.; Guntinas-Lichius, O.; Popp, J. Novel Workflow for Combining Raman Spectroscopy and MALDI-MSI for Tissue Based Studies. Analytical and Bioanalytical Chemistry 2015, 407 (26), 7865–7873. https://doi.org/10.1007/s00216-015-8987-5.

(16) Bradshaw, R.; Wolstenholme, R.; Ferguson, L. S.; Sammon, C.; Mader, K.; Claude, E.; Blackledge, R. D.; Clench, M. R.; Francese, S. Spectroscopic Imaging Based Approach for Condom Identification in Condom Contaminated Fingermarks. The Analyst 2013, 138 (9), 2546. https://doi.org/10.1039/c3an00195d.

(17) Burkhow, S. J.; Stephens, N. M.; Mei, Y.; Dueñas, M. E.; Freppon, D. J.; Ding, G.; Smith, S. C.; Lee, Y. J.; Nikolau, B. J.; Whitham, S. A.; Smith, E. A. Characterizing Virus-Induced Gene Silencing at the Cellular Level with in Situ Multimodal Imaging. Plant Methods 2018, 14 (1), 1–12. https://doi.org/10.1186/s13007-018-0306-7.

(18) Drescher, D.; Zeise, I.; Traub, H.; Guttmann, P.; Seifert, S.; Büchner, T.; Jakubowski, N.; Schneider, G.; Kneipp, J. In Situ Characterization of SiO 2 Nanoparticle Biointeractions Using BrightSilica. Advanced Functional Materials 2014, 24 (24), 3765–3775. https://doi.org/10.1002/adfm.201304126.

(19) Lanni, E. J.; Masyuko, R. N.; Driscoll, C. M.; Dunham, S. J. B.; Shrout, J. D.; Bohn, P. W.; Sweedler, J. V. Correlated Imaging with C 60 -SIMS and Confocal Raman Microscopy: Visualization of Cell-Scale Molecular Distributions in Bacterial Biofilms. Analytical Chemistry 2014, 86 (21), 10885–10891. https://doi.org/10.1021/ac5030914.

(20) Lasch, P.; Noda, I. Two-Dimensional Correlation Spectroscopy for Multimodal Analysis of FT-IR, Raman, and MALDI-TOF MS Hyperspectral Images with Hamster Brain Tissue. Analytical Chemistry 2017, 89 (9), 5008–5016. https://doi.org/10.1021/acs.analchem.7b00332.

(21) Le Naour, F.; Bralet, M.-P.; Debois, D.; Sandt, C.; Guettier, C.; Dumas, P.; Brunelle, A.; Laprévote, O. Chemical Imaging on Liver Steatosis Using Synchrotron Infrared and ToF-SIMS Microspectroscopies. PLoS ONE 2009, 4 (10), e7408. https://doi.org/10.1371/journal.pone.0007408.

(22) Li, Z.; Chu, L.-Q.; Sweedler, J. V.; Bohn, P. W. Spatial Correlation of Confocal Raman Scattering and Secondary Ion Mass Spectrometric Molecular Images of Lignocellulosic Materials. Analytical Chemistry 2010, 82 (7), 2608–2611. https://doi.org/10.1021/ac100026r.

(23) Morales-Soto, N.; Dunham, S. J. B.; Baig, N. F.; Ellis, J. F.; Madukoma, C. S.; Bohn, P. W.; Sweedler, J. V.; Shrout, J. D. Spatially Dependent Alkyl Quinolone Signaling Responses to Antibiotics in Pseudomonas Aeruginosa Swarms. Journal of Biological Chemistry 2018, 293 (24), 9544–9552. https://doi.org/10.1074/jbc.RA118.002605.

(24) Neumann, E. K.; Comi, T. J.; Spegazzini, N.; Mitchell, J. W.; Rubakhin, S. S.; Gillette, M. U.; Bhargava, R.; Sweedler, J. V. Multimodal Chemical Analysis of the Brain by High Mass Resolution Mass Spectrometry and Infrared Spectroscopic Imaging. Analytical Chemistry 2018, 90 (19), 11572–11580. https://doi.org/10.1021/acs.analchem.8b02913.

(25) Petit, V. W.; Réfrégiers, M.; Guettier, C.; Jamme, F.; Sebanayakam, K.; Brunelle, A.; Laprévote, O.; Dumas, P.; Le Naour, F. Multimodal Spectroscopy Combining Time-of-Flight-Secondary Ion Mass Spectrometry, Synchrotron-FT-IR, and Synchrotron-UV Microspectroscopies on the Same Tissue Section. Analytical Chemistry 2010, 82 (9), 3963–3968. https://doi.org/10.1021/ac100581y.

(26) Rabe, J. H.; Sammour, D. A.; Schulz, S.; Munteanu, B.; Ott, M.; Ochs, K.; Hohenberger, P.; Marx, A.; Platten, M.; Opitz, C. A.; Ory, D. S.; Hopf, C. Fourier Transform Infrared Microscopy Enables Guidance of Automated Mass Spectrometry Imaging to Predefined Tissue Morphologies. Scientific Reports 2018, 8 (1), 1–11. https://doi.org/10.1038/s41598-017-18477-6.

(27) Ryabchykov, O.; Popp, J.; Bocklitz, T. Fusion of MALDI Spectrometric Imaging and Raman Spectroscopic Data for the Analysis of Biological Samples. Frontiers in Chemistry 2018, 6, 1–10. https://doi.org/10.3389/fchem.2018.00257.

UNIVERSITAT ROVIRA I VIRGILI
GOLD-COATED BLACK SILICON NANOSTRUCTURED SURFACES FOR SERS AND SALDI-MS MULTIMODAL IMAGING OF BIOLOGICAL APPLICATIONS
Stefania-Alexandra Iakab

CHAPTER 3: Gold Nanoparticle-Assisted Black Silicon Substrates for Mass Spectrometry Imaging Applications

UNIVERSITAT ROVIRA I VIRGILI
GOLD-COATED BLACK SILICON NANOSTRUCTURED SURFACES FOR SERS AND SALDI-MS MULTIMODAL IMAGING OF BIOLOGICAL APPLICATIONS
Stefania-Alexandra Iakab

State of the article:

Published in ACS Nano 2020, 14, 6785−6794, https://dx.doi.org/10.1021/acsnano.0c00201 and reproduced by permission from © 2020 American Chemical Society.

Journal metrics:

Impact factor 14.58 (2019)

Q1 (Engineering - miscellaneous)

Contributing authors:

Stefania Alexandra Iakab[†‡], Pere Ràfols[†‡], Marta Tajes[₸], Xavier Correig-Blanchar[†‡§], María García-Altares[†‡]

[†]Department of Electronic Engineering, Rovira i Virgili University, Tarragona, 43007, Spain

[‡]Spanish Biomedical Research Centre in Diabetes and Associated Metabolic Disorders (CIBERDEM), Madrid, 28029, Spain

[₸]Group of Biomedical Research in Heart Diseases, IMIM (Hospital del Mar Medical Research Institute), Barcelona, 08003, Spain.

[§]Institut d'Investigacio Sanitària Pere Virgili, Tarragona, 43204, Spain

UNIVERSITAT ROVIRA I VIRGILI
GOLD-COATED BLACK SILICON NANOSTRUCTURED SURFACES FOR SERS AND SALDI-MS MULTIMODAL IMAGING OF BIOLOGICAL APPLICATIONS
Stefania-Alexandra Iakab

3.1. Abstract

Mass spectrometry imaging (MSI) based on matrix-assisted laser desorption ionization (MALDI) is widely used in proteomics. However, matrix-free technologies are gaining popularity for detecting low molecular mass compounds. Small molecules were analyzed with nanostructured materials as ionization promoters, which produce low-to-no background signal, and facilitate enhanced specificity and sensitivity through functionalization. We investigated the fabrication and the use of black silicon and gold-coated black silicon substrates for surface-assisted laser desorption/ionization mass spectrometry imaging (SALDI-MSI) of animal tissues and human fingerprints. Black silicon was created using dry etching while gold nanoparticles were deposited by sputtering. Both methods are safe for the user. Physicochemical characterization and MSI measurements revealed the optimal properties of the substrates for SALDI applications. The gold-coated black silicon worked considerably better than black silicon as LDI-MSI substrate. The substrate was also compatible with imprinting, as a sample-simplification method that allows the efficient transference of metabolites from the tissues to the substrate surface, without compound delocalization. Moreover, by modifying the surface with hydrophilic and hydrophobic groups specific interactions were stimulated between surface and sample, leading to a selective analysis of molecules. Thus, our substrate facilitates targeted and/or untargeted *in situ* metabolomics studies for various fields such as clinical, environmental, forensics and pharmaceutical research.

UNIVERSITAT ROVIRA I VIRGILI
GOLD-COATED BLACK SILICON NANOSTRUCTURED SURFACES FOR SERS AND SALDI-MS MULTIMODAL IMAGING OF BIOLOGICAL APPLICATIONS
Stefania-Alexandra Iakab

Keywords: black silicon, gold, nanostructured surface, functionalization, mass spectrometry imaging, imprinting

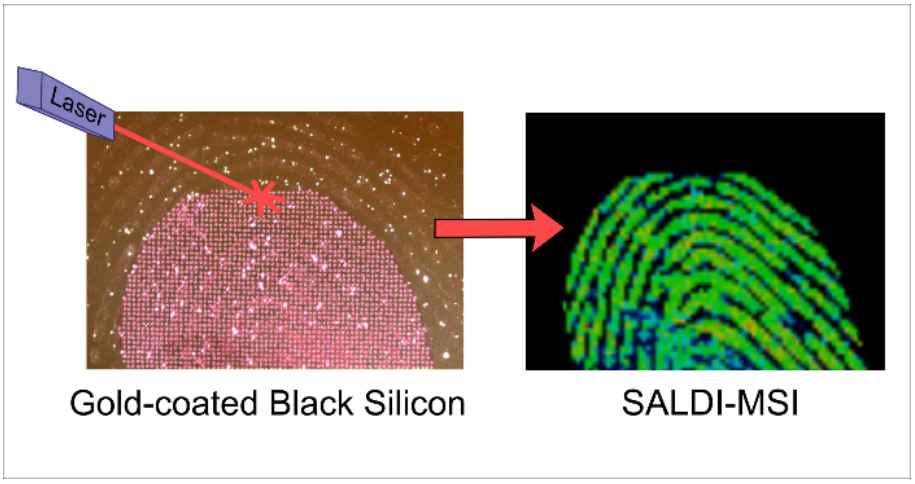

UNIVERSITAT ROVIRA I VIRGILI
GOLD-COATED BLACK SILICON NANOSTRUCTURED SURFACES FOR SERS AND SALDI-MS MULTIMODAL IMAGING OF BIOLOGICAL APPLICATIONS
Stefania-Alexandra Iakab

3.2. Introduction

Mass spectrometry imaging (MSI) is a technique of considerable interest in the omics sciences, especially in proteomics and metabolomics. One of the most commonly used methods for recording molecular images is matrix-assisted laser desorption ionization (MALDI).[1,2] This technique uses a matrix – usually an organic acid – to promote the ionization and desorption of large molecules. However, there are several drawbacks for the detection of molecules in the low mass range (<500 Da).[3] The signals from matrix, analyte-matrix adducts, and fragmented species appear mostly in the low range of the mass spectra, making it challenging to differentiate between sample-related signals and background signals. Additionally, the organic acids co-crystallize heterogeneously with the analytes to create hot-spots that render qualitative high-resolution imaging impossible. Consequently, replacing the organic matrix with other more reliable agents that promote desorption and ionization is now a topic of great interest.[4]

Many research groups are developing matrix-free laser desorption/ionization mass spectrometry (LDI-MS) procedures that reduce spectral interferences from the matrix and improve lateral resolution. Some of the most common alternative techniques are surface-assisted laser desorption ionization (SALDI),[5,6] desorption ionization on silicon (DIOS),[7] and nanostructure-initiator mass spectrometry (NIMS).[8] In these techniques ionization is supported by nanostructured materials, porous silicon, and molecules trapped in nanostructured surfaces, respectively. Considering the success of these techniques, there is a strong possibility that solid-state substrates with nanostructured surfaces are ideal candidates to complement or replace organic matrices. The laser-nanostructure interaction can result in high heating rates, prolonged interaction time and, most importantly,

improved ionization. Moreover, the ideal "non-matrix" ionization promoter should make efficient use of laser pulse energy to generate ions from the adsorbates with minimal to no fragmentation.

Nanostructured silicon surfaces such as porous silicon (pSi) and black silicon (BSi) substrates are common alternatives used for matrix-free LDI.[9] Unfortunately, the pSi surface is not stable over time and its fabrication method involves the manipulation of dangerous reagents such as cleaning and etching solutions containing sulphuric acid, hydrofluoric acid or hydrogen peroxide.[10,11] On the other hand, BSi surfaces are stable over time and their fabrication method is safe for the user. BSi is mostly known in the solar cell industry for its physicochemical properties.[12] The predominant characteristic of BSi is its black surface that is built up by an array of silicon nanopillars which absorbs up to 99% of visible light. Black silicon fabrication methods are extensively reported in the literature.[12] Dry plasma etching is one of the most advantageous fabrication methods for three main reasons. Firstly, reactive ion etching (RIE) is a non-toxic and well-controlled etching method that does not use any harmful substances for the user. Secondly, plasma etching yields black silicon substrates that are stable and free of contaminants. Lastly, it is a highly repetitive fabrication method. Jansen *et al.* described the black silicon method as a synergistic mechanism of plasmas: one etching plasma (fluorine radicals) and one passivating plasma (oxygen radicals).[13]

Black silicon with different surface morphologies has been used previously as NIMS substrate.[14] Gao *et al.* demonstrated that optimal ionization can be achieved by enhancing the sensitivity of the substrate for pure compounds with the help of the initiator. The BSi surfaces can be soaked with a perfluorinated compound that enhances the efficiency of analyte desorption/ionization. Since BSi needs a complimentary

desorption/ionization boosting element for its proper use in SALDI applications, safer and more practical alternatives to perfluorinated initiators have been explored, such as noble metals (Au, Ag.) or metal oxide (TiO_2, Fe_3O_4, ZnO, *etc.*) nanoparticles.[15]

Gold nanostructures are excellent candidates for developing substrates for SALDI. They have a high absorption coefficient in the UV-vis optical range that favors the absorption of laser light and the efficient transfer of absorbed energy to the metabolites. Gold nanostructures provide a source of ionization that ensures minimal interference in the low mass range, contrary to approaches based on organic matrices. They are also cost-friendly, present high stability and can be easily functionalized using surface modification protocols based on the gold-thiol (Au-SH) interaction.[16] Several studies have used gold nanoparticles to analyze biomolecules by SALDI-MS and achieved an effective ionization of low mass range metabolites with very low background noise. [16–21] The two most popular methods to create gold nanoparticles are through wet-chemistry methods (in water-repellent solvents)[16,18] and dry-etching plasma or sputtering.[19,20]

However, using gold nanoparticles deposited on a substrate as ionization agents limits the SALDI-MSI approach to analyzing tissues because the analytes need to be in direct contact with the gold nanoparticles for desorption and ionization. This means that typical tissue sections (between 10 and 20 μm)[2] used for MALDI-MSI cannot be placed on nanostructured substrates decorated with gold nanoparticles. To solve this problem, similar matrix-free strategies used thinner tissue sections (2 - 4 μm)[22] or direct imprinting methods for the analysis of fingerprints.[23,24] The molecular imprinting methods demonstrated that transferring the molecules onto the SALDI surface was sufficient to obtain high quality MS data.

This study focuses on the design and fabrication of solid-state substrates based on black silicon and gold nanostructures. The substrates were optimized for SALDI-MSI applications and physicochemically characterized by scanning electron microscopy (SEM), atomic force microscopy (AFM), UV-vis absorption and contact angle measurements. Their use as LDI substrates was assessed by transferring metabolites from animal tissues and human fingerprints. The surface was also functionalized with hydrophobic and hydrophilic functional groups and used to adhere molecules in a selective manner. Our results demonstrate that our silicon-based nanostructured surfaces covered with Au nanoparticles can be used to perform targeted and untargeted SALDI-MSI approaches.

3.3. Results and Discussion

3.3.1. Substrate fabrication

Black silicon was created using dry etching because it is a safe, reproducible and reliable method. Dry etching using a mixture of oxygen and sulfur hexafluoride plasma created an array of vertical silicon spikes, also known as black silicon. The gold nanolayer was deposited *via* sputtering because it yielded thickness-controlled nanolayers. Dry etching was used to functionalize the AuBSi surface to reduce the possibility of contamination through wet chemistry methods. When exposed to oxygen plasma and fluoroform plasma, the surface became hydrophilic and hydrophobic, respectively. Figure 1 shows a schematic representation of the fabrication and functionalization methods. Considering that both silicon and gold are often functionalized in MS applications,[9] our AuBSi substrates could also be further developed for targeted analysis by modifying the surface chemistry to selectively detect specific compounds.

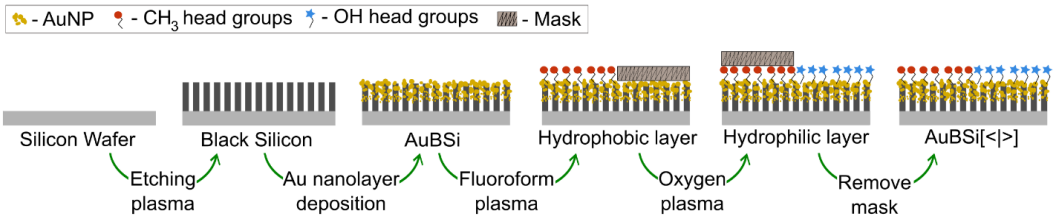

Figure 1. Schematic representation of the BSi, AuBSi and functionalized AuBSi fabrication method

3.3.2. Substrate characterization

The black silicon nanostructure is produced by the synergistic interaction between etching and masking gases during RIE. Briefly, oxygen radicals mask the silicon wafer surface and fluorine radicals etch the unmasked silicon surface.13 The masking and etching occur randomly and produce arrays of irregularly shaped spikes. The morphology of the black silicon substrate is shown in Figure 2. The SEM images show the black silicon nanostructure with unordered nanopillars or spikes with average height of 300 nm, average diameter of 60 nm (Figure S1, Supporting Information), and average spacing between nanopillars of ~45 nm. The structure of the 10 nm layer of gold deposited via sputtering can be seen in the SEM diagrams as gold nanoislands/nanoparticles decorating the silicon pillars creating asparagus-like nanostructures.

The large surface area and roughness of the nanostructures are important characteristics of the substrates because they demonstrate mechanical stability for imprinting. These properties justify the adhesion of a large number of molecules onto the substrate. The 3D roughness profiles in Figure S2 demonstrate that the 300 nm-high nanopillar forest serves as a robust surface with an average roughness of ~16 nm. This height variation of the BSi and AuBSi indicates that the surface is flatter than that of micron-scaled objects, such as tissues. Therefore, the tissue can be stamped onto the black

silicon surface without breaking the nanostructure. This was also demonstrated by SEM images (Figure S3) of the AuBSi nanostructure before and after fingerprint imprinting and MSI analysis.

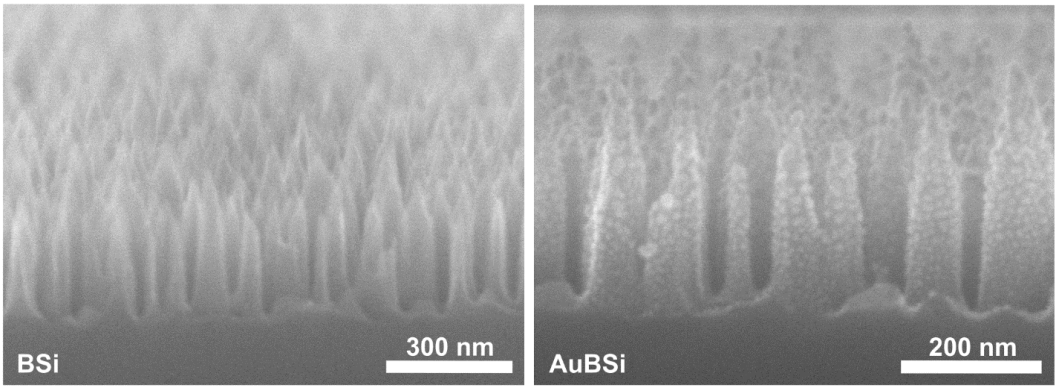

Figure 2. SEM images of the cross-section of BSi (left) and AuBSi (right)

The reflectance measurements shown in Figure S4 show that black silicon can absorb most of the visible light. Compared with bare silicon surfaces, which have a reflectance higher than 50 %, BSi reflects less than 6 % of UV light, while both AuBSi and hydrophilic/hydrophobic functionalized AuBSi have even lower reflectance values (< 4 %). This suggests that modifying the surface using hydrophilic or hydrophobic ligands does not make major modifications to the black silicon's property of absorbing light. It may also encourage the use of other surface modification methods such as thiol-terminated oligonucleotides, aptamers and ethylene glycol for improved selectivity of various biomolecules.[17] The laser used in this study was a Nd:YAG laser, with a 335 nm wavelength (marked with a dashed line in Figure S4). The energy of this specific wavelength is > 95% absorbed by the black silicon surfaces and, most probably, it is converted into energy (heat and localized plasma) for desorption and ionization processes.

Contact angle (CA) measurements were made to describe the chemical properties of the functionalized hydrophobic/hydrophilic surfaces. By

convention, surfaces with a mean CA below 90° are considered hydrophilic and surfaces with a mean CA above 90° are considered hydrophobic. For bare silicon we measured a mean contact angle of 53°, for BSi it was 7° and for AuBSi it was 133°. All values of the mean CA and the visual data are represented in Figure S5. These results indicate that the pristine silicon wafer is slightly hydrophilic while the BSi nanostructure turns the silicon surface superhydrophilic. Also, the Au nanoisland layer has an active role in modifying the BSi surface property because it creates a hydrophobic layer. For the AuBSi[<|>] the contact angles were measured immediately after surface modification and then after 2 months of storage in laboratory conditions (in air, 20°C room temperature). The polymer plasma treatment yielded hydrophobic surfaces with CA > 123°, while the oxygen plasma created hydrophilic surfaces with CA < 17°. After 2 months of storage, the hydrophilic AuBSi did not maintain this property, as the CA was slightly over 90° while the hydrophobic layer slightly increased with a mean CA of 137°. This suggests that the hydroxyl-terminated surface is not stable over time. Therefore, substrates should be used shortly after the surface has been modified.

3.3.3. Substrate performance

To assess the suitability of AuBSi as SALDI-MSI substrates, a first set of measurements was done using standard solutions of glucose, folic acid and phosphocholine (1000 ppm). Droplets of 1.5 µl of each solution were spotted onto an array of hydrophilic AuBSi wells – described in the Supporting Information file (Figure S6). MS images of all spotted wells and 3 blank wells (water/methanol 1:1, v/v) were acquired with approximately 35-40 pixels per well, as shown in Figure S7. The mean spectra of the three replicates of each standard on both BSi and AuBSi are represented in Figure 3. On AuBSi. glucose and folic acid were detected as $[M+Na]^+$ and $[M+K]^+$ adducts, and

we detected the typical in-source fragments of folic acid and phosphocholine as $[M+H]^+$ adducts. However, we could barely detect glucose and folic acid on BSi (Figure S8). All standards were detected in the pool on AuBSi but not on BSi, suggesting that the AuBSi substrate is appropriate for the analysis of complex samples. Sensitivity was evaluated in quantitative terms as the slope of the standard calibration curve[25] for glucose using both substrates. We measured glucose on BSi and AuBSi substrates in the range of 1 - 1000 ppm, which encompasses relevant glucose concentrations in saliva, blood and urine[26–28] (Figure S9). Results show that the AuBSi substrate was 45 times more sensitive for the detection of glucose than the BSi substrate – due to the presence of gold ($BSi_{intensity} = 2.3 + 0.0033 \cdot [C_{glucose}]$, $R^2 = 0.3$; *vs.* $AuBSi_{intensity} = 21 + 1.5 \cdot [C_{glucose}]$, $R^2 = 0.8$; Figure S9).

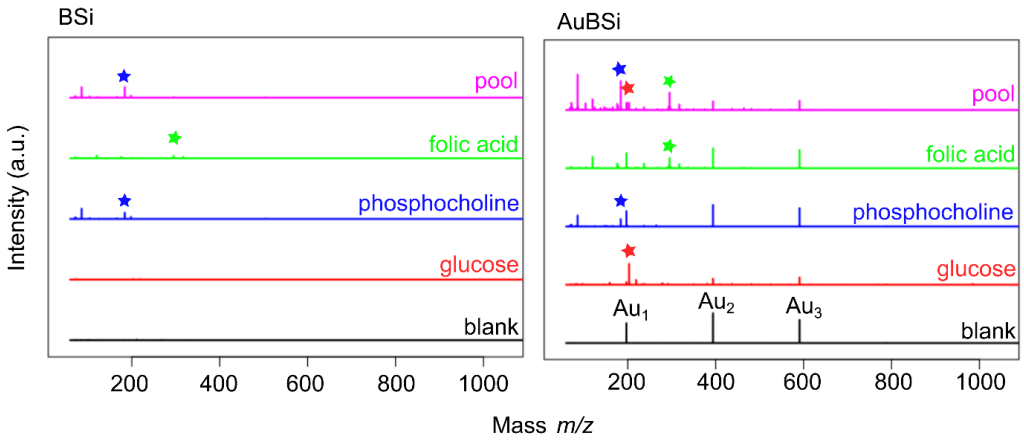

Figure 3. Mean spectra of glucose, folic acid, phosphocholine, pool and blank measured on BSi and AuBSi well arrays. Red star: *m/z* 203.05 $[M+Na]^+$ adduct of glucose; blue star: *m/z* 184.07 $[M+H]^+$ adduct of phosphocholine in-source fragment; green star: *m/z* 295.09 $[M+H]^+$ adduct of folic acid in-source fragment. Intensity scale is the same in all spectra.

To assess the suitability of the substrates for imaging experiments, LDI-MS spectra (approx. 350 spectra for each condition) were acquired from

blank substrates and from fingerprints adhered to BSi and AuBSi surfaces, in positive and negative ionization modes. The mean spectra acquired from the blank substrates in positive and negative ionization modes (illustrated in Figure S10) show clean spectra with a few background peaks with very low intensity in the low mass range (*m/z* 50-300). The mean spectrum acquired from the fingerprint on each substrate (BSi and AuBSi) and with each ionization mode is represented in Figure 4. Both substrates provided an adequate setting for MSI, but AuBSi proved to be considerably more effective in both positive and negative modes. The total sum of intensities (Total Ion Count) from the peak matrix (MS signals detected at a signal-to-noise ratio of 5) of AuBSi was 9 times greater than that of BSi in positive mode and 17 times greater in negative mode. The spectra on AuBSi display more signals than BSi surfaces, including very prominent signals from Au ion clusters used as references for the mass recalibration during data processing.

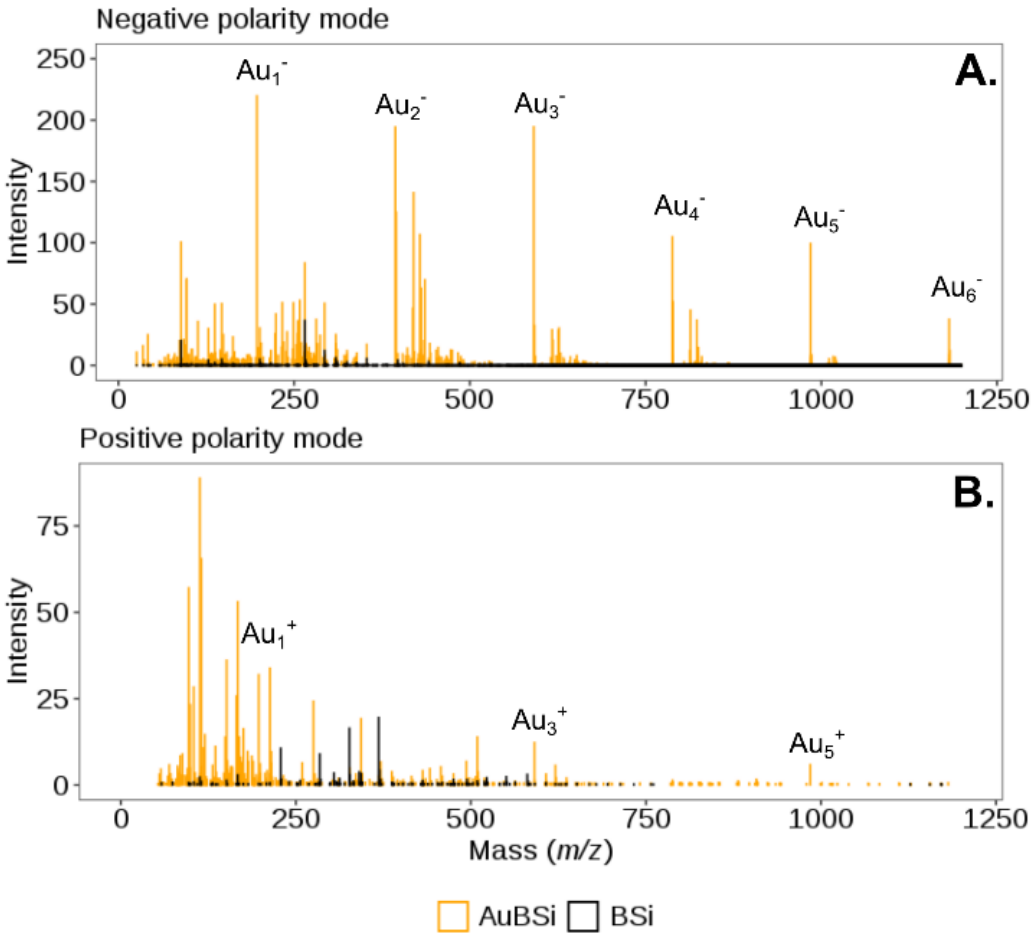

Figure 4. Mean spectra of fingerprint acquired in negative (A) and positive (B) polarity modes from BSi (in black) and AuBSi (in yellow)

The morphology of AuBSi substrates mostly influences the ionization method through thermal confinement and the large surface area of the material. When vertical arrays of silicon nanowires (SiNW) are used, Chen *et al.*[29] describe the tip of the SiNW as a lightning rod where most of the laser energy is accumulated. The ionization mechanisms that occur in these systems are explained by dynamic models of ultraviolet matrix-assisted laser desorption/ionization (UV-MALDI).[30] Ionization is described as: (1) photoinduced electron transfer to the analyte adsorbed on the SiNW tip, in

negative ionization mode; (2) photoinduced electron transfer followed by secondary ionization mechanisms from intramolecular recombination of ions, which results in cationization of the analytes, in positive ionization mode. Our substrates have sharp silicon tips decorated with gold nanoparticles which form a conductive nanolayer that promotes the tunneling effect for electron transfer. This might explain the significantly increased signal in the negative ionization mode in our experiments, which are in agreement with the observations by Chen *et al.*[29] However, spectra in both positive and negative ionization modes can be acquired with our AuBSi substrates, which make the substrates potentially useful for detecting a wide range of small molecules. The gold nanoparticles are believed to mainly assist in the desorption process, as a portion of the laser energy is transformed into thermal energy needed for the ablation of molecules.[16,20] Therefore, the synergistic effect between gold nanoparticles and black silicon results in a soft desorption process. When it comes to the ionization process, cationization is also promoted by the gold nanoparticles due to their unique properties[8,9,17] but the adduct formation ($[M+Na]^+$, $[M+K]^+$, *etc.*) is the result of the intrinsic presence of these elements in the tissue.

Other studies have proposed different alternatives to improve sensitivity, such as the addition of fluorinated compounds (1H,1H,2H,2H-perfluorooctanethiol or 1H,1H,2H,2H-perfluorodecanethiol)[16,18], salts (sodium acetate[20], potassium bromide[31]) and other additives (citrate, citric acid, trifluoroacetic acid, *etc.*)[17]. These additional preparation steps requiring a mixture with, or modification of, the nanoparticles could be compatible with AuBSi substrates.

3.3.4. Detection of fingerprint metabolites on functionalized AuBSi substrates

Metabolites from sweat glands and sebaceous glands, and compounds adhered to fingerprints were detected on the AuBSi using positive and negative ionization modes, as shown in the mean spectra from Figure 4. The abundance of peaks in the spectra shows that metabolites and compounds are directly transferred onto the AuBSi substrate. We detected several ions in the range *m/z* 150-900, which could be both endogenous (*e.g.* fatty acids and lipids)[32] and exogenous compounds (residues from soap or laboratory gloves).

One big advantage of using AuBSi as the LDI substrate is that silicon and gold can be easily functionalized. For this reason, various plasma treatments were used to modify the surface of AuBSi, leading to hydrophilic and hydrophobic AuBSi (named as AuBSi [<|>]). To test the functionality of AuBSi[<|>], fingerprints were imprinted on the AuBSi[<|>] and analyzed in positive ionization mode. Principal component analysis (PCA) was used to assess the influence of the functionalization on the AuBSi[<|>] surface. Figure 5A shows the PCA score plot, in which each dot represents one pixel from the acquired dataset and the color of which represents where it is located: the red dots are pixels from the hydrophobic area and the blue dots are in the hydrophilic area. The first two principal components (PC1 and PC2) explained more than 50 % of the variance in the dataset and showed a significant separation of both regions, which indicated that the surface modification is one of the main factors that influences the variance in the dataset. Figure 5B and 5C are showing the spatial distribution of PC1 and PC2, respectively. These images show that PC1, and PC2 to a lesser extent, can separate the hydrophobic and hydrophilic regions, which suggests that the modification of the surface into hydrophilic and hydrophobic areas

affects molecule adhesion and possibly the ionization process. The fold change plot in Figure S11 shows the different ions localized predominantly in the hydrophilic and the hydrophobic regions, respectively. The PC2 image in Figure 5C, on the other hand, seems to capture the morphology of the fingerprints, revealing some of the sebaceous glands.

We expect the molecules detected in each region to have the same hydrophilic or hydrophobic behavior as the surface they were adhere to and thus desorbed from. For instance, we putatively identified *m/z* 135.02 as lactic acid ($[M+2Na-H]^+$) mostly desorbed from the hydrophilic region, as shown in Figure 5D. Lactic acid is commonly found in sweat[33] and sometimes forms salts (*i.e.* sodium lactate), since sweat has a high sodium and potassium content.[33,34] On the other hand, we found several *m/z* values mostly in the hydrophobic region that were putatively identified as lipids, such as glycerophospholipid PA(8:0/14:0) *m/z* 547.25 ($[M+K]^+$) (Figure 5E). Glycerophospholipids are one class of many lipids produced by the sebaceous glands together with non-polar lipids such as wax esters and squalenes.[35] Other morphologically representative ions such as *m/z* 550.65 (putatively identified as Cer(d18:0/18:0), $[M+H-H2O]^+$) and *m/z* 138.12 (unidentified) were also found, even though they did not seem to have any specific affinity to the surface functionalization and were found all over the substrate (Figure 5F). The distribution of these ions matched the position of pores through which the eccrine and sebaceous gland secretions are excreted to the surface.

Therefore, our results suggest that a straightforward functionalization technique that modifies the hydrophobicity of the surface enables the selective adhesion of different compounds, presumably according to their polarity.

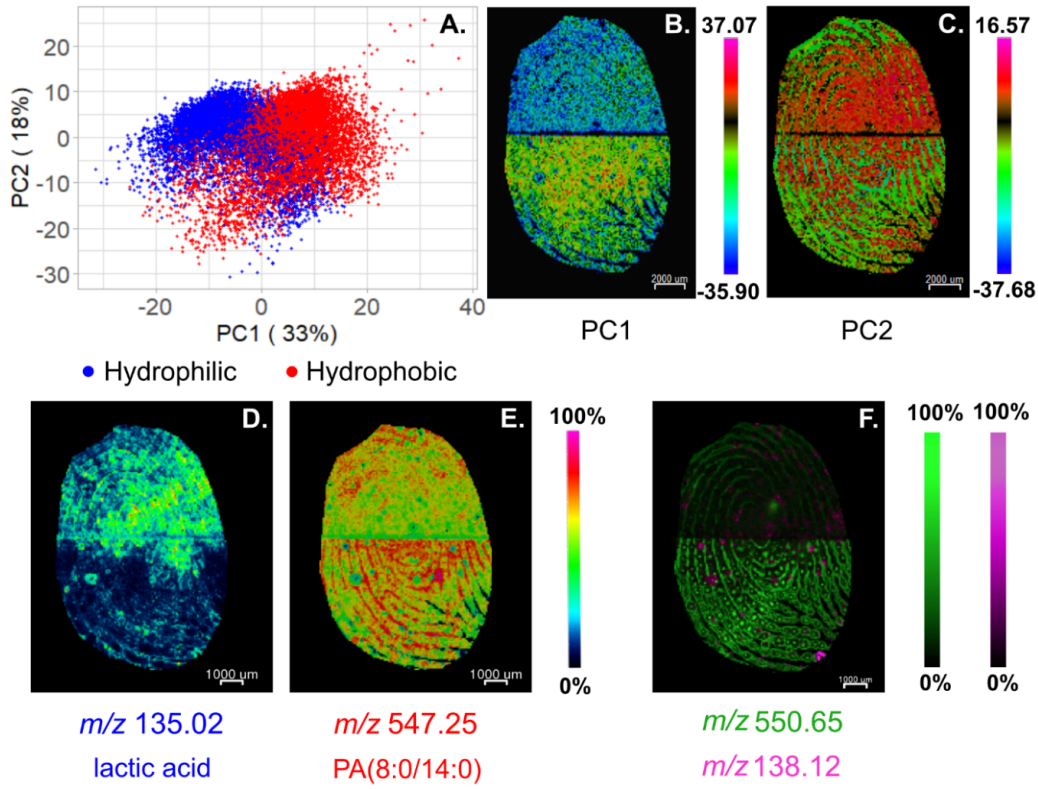

Figure 5. Score plot of PC1 and PC2 from principal component analysis (A), PC1 image (B), PC2 image (C), representative ion from the hydrophilic region *m/z* 135.02 ($[M+2Na-H]^+$ adduct of lactic acid) (D), representative ion from the hydrophobic region, *m/z* 547.25 ($[M+K]^+$ adduct of a glycerophospholipid) (E) and ions *m/z* 522.66 (green) and 138.12 (magenta) with morphological significance (F)

3.3.5. Detection of paracetamol on fingerprint

We then investigated if our AuBSi surface could be used to monitor exogenous compounds on fingerprints in a targeted manner, such as drug residues from someone who has touched or manipulated a powdered compound. For this example, we attempted to detect the commercial drug paracetamol.

First, we used the functionalized AuBSi[<|>] substrate to collect a reference spectrum of paracetamol from a pill dissolved in water and spotted on the surface. Then a fingerprint was stamped onto another AuBSi[<|>] after a volunteer rubbed a paracetamol pill on her finger. A control fingerprint from the same volunteer was also stamped on the AuBSi[<|>]. The acquired data showed that paracetamol was detected from the paracetamol droplet and the fingerprint. The representative peaks of paracetamol ($[M+Na]^+$ and $[M+K]^+$ cations, *m/z* 174.04 and *m/z* 190.01) were detected in positive mode from both the liquid sample and the fingerprints. Figure 6 shows the spectrum obtained from the paracetamol pill dissolved in Milli-Q water deposited on the hydrophilic AuBSi, together with MS images of the paracetamol adducts $[M+Na]^+$ and $[M+K]^+$ from the fingerprint exposed to paracetamol, which are absent in the control fingerprint.

Since paracetamol is a polar molecule, it is noticeable that the hotspots with the highest intensity of paracetamol are located on the hydrophilic part of the surface. We believe paracetamol was detected across the whole surface because it was present on the fingerprint in excess and because the majority of the molecules from the composition of fingermark are hydrophobic molecules (lipids, fatty acids, *etc.*) and our imprinting method favors the transference of the same hydrophobicity molecules to the same hydrophobicity surface. This explains why the transference of the paracetamol residue is more widespread on the hydrophobic surface (maybe aided by the waxes of the skin), but less intense than in the hydrophilic part. Therefore, the AuBSi surface can be used to monitor exogenous compounds on fingermarks in a targeted way, such as in the control of prohibited substances and in forensic applications. The sample preparation of this workflow is compatible with non-invasive clinical applications, for instance

with the measurement of disease biomarkers from sweat excreted by finger sebaceous glands.[32]

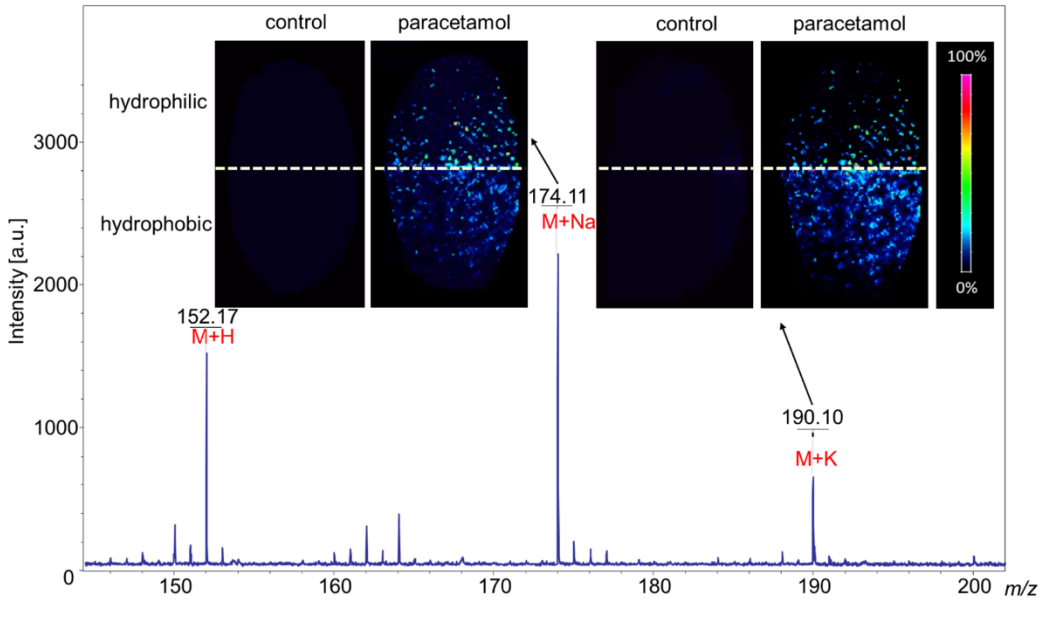

Figure 6. Mass spectrum of paracetamol pill dissolved in water, and MS images of control (A, C) and paracetamol-exposed (B, D) fingerprints

3.3.6. Mass spectrometry imaging of molecules transferred from animal tissues

Sample preparation methods in traditional MALDI-MSI struggle with consistency and reproducibility because of the use of organic matrix. Signal suppression and inaccurate quantitation are some of the undesired effects caused by inhomogeneous matrix deposition.[36] The imprinting technique used to measure the metabolites from fresh frozen animal tissues was molecule transfer (described above). Liver was used to determine the optimal tissue thickness to be used for molecule transfer, since liver tissues do not present marked morphological regions and differences among consecutive sections are minimal. We sliced 1, 5 and 10 μm thick liver sections to acquire

MS images together with an image of the bare substrate (or background) for comparison. Sections were allowed to interact with the substrate for 60 seconds, and then they were washed away with milli-Q water. Our results indicate that thinner sections lead to more intense signals in the MSI spectra (Figure S12). However, most animal tissues are very fragile and sections thinner than 4 μm are difficult to handle. Therefore, we chose 5 μm as the most appropriate tissue thickness for the MSI of molecule transfer. This molecule transfer method has several advantages over traditional MALDI sample preparation. For instance: (1) there is no matrix deposition step; (2) the spectra are less complex because interferences by salts and matrix components are removed, which makes it easier to identify endogenous compounds; (3) the washing steps can be modified to selectively favor the detection of a specific group of molecules (*e.g.* focus on the detection of lipids by removing polar contaminants through washing the sections with water).[37,38]

Fresh frozen kidney and brain tissues were sectioned at 5 μm and MSI data were acquired in negative mode, because of the greater sensitivity shown in the preliminary measurements. The mean spectra and ion intensity images of representative ions from kidney and brain tissues are represented in Figure 7 and Figure 8, respectively. MSI of kidney sections revealed several representative ions of the different morphological regions of the organ: for example, *m/z* 283.27 is mainly found in the outer medulla region and ions *m/z* 778.53 and 906.68 are found in the cortex region (Figure 7). We tentatively identified some of these ions as phosphatidylethanolamine (*e.g.* *m/z* 906.68 as $[M-H]^-$ of PE-NMe2(46:4)) and stearic acid (*m/z* 283.28 as $[M-H]^-$) with a distribution that was similar to that reported in Liu *et. al.*[39]

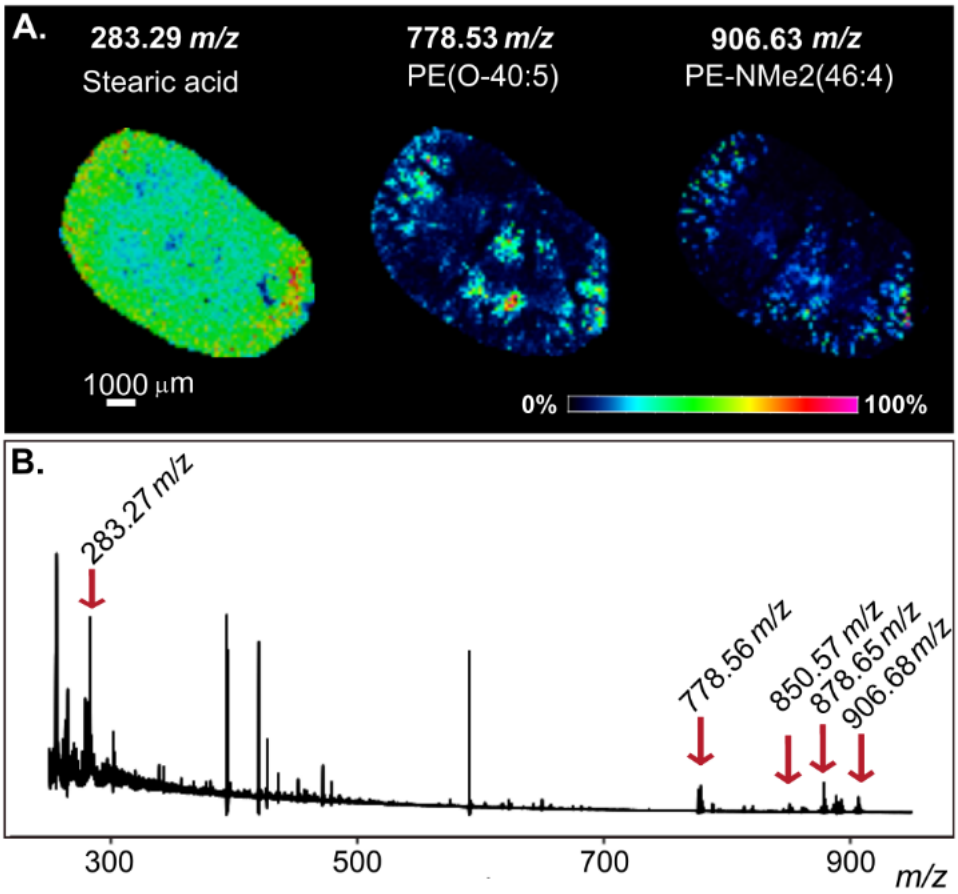

Figure 7. MS images of ions tentatively identified from mouse kidney (A.) and average spectrum (B.)

For brain tissue, several ions in the range *m/z* 800-900 were found in the grey matter of the mouse cerebellum, corpus callosum, fornix, pons and medulla oblongata (Figure 8). Most of these ions have already been reported by Cerruti *et. al* [40] who used 9-aminoacridine as an organic matrix, negative ionization mode, and MS/MS experiments for identification. Our results agree with those in Cerruti *et al.*, as we identified most ions as 3-O-sulfogalactosylceramides (*e.g.* *m/z* 888.59 as (3'-sulfo)Galβ-Cer(d18:1/24:1(15Z)); and *m/z* 904.58 as (3'-sulfo)Galβ-Cer(d18:1/24:1(15Z)(2OH))) which are found in particularly high

concentrations in myelin. Both kidney and brain ions were putatively identified according to the experimental section. The results are shown in Table S1 (Supporting Information).

We consider that the innate hydrophobic property of the AuBSi surface promoted the adhesion of hydrophobic compounds from brain and kidney, mainly of molecules with hydrophobic groups such as long aliphatic chains. Putatively identified molecules transferred to AuBSi are lipid species that illustrate specific morphological areas at high spatial resolution with no delocalization. The AuBSi substrates could also be designed for targeted analysis using common functionalization methods such as gold-thiol chemistry protocols[16,18] and surface-ligand-molecule interactions.[21]

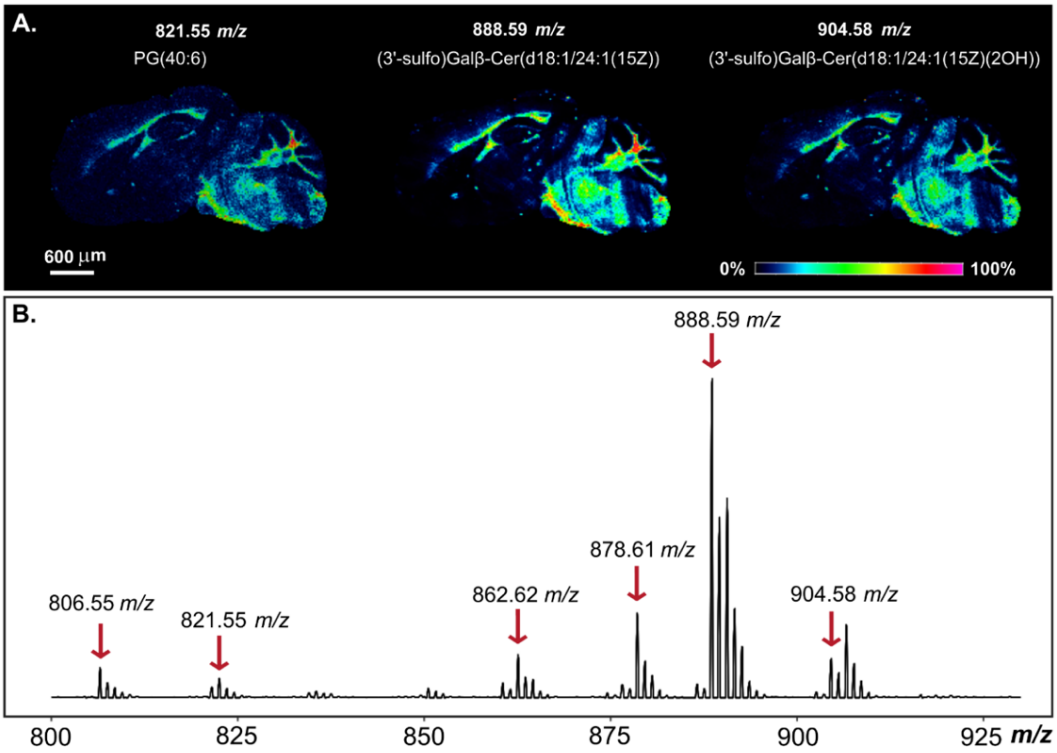

Figure 8. MS images of ions identified as 3-O-sulfogalactosylceramides (A.) and average spectrum (zoom in the region *m/z* 800-925) highlighting identified ions from imprinted brain tissue (B.)

3.4. Conclusions

We developed a surface on which matrix-free LDI-MS Imaging experiments based on black silicon decorated with gold can be performed. The surface is produced with a straightforward protocol that is easy to replicate and poses no risk for users. By sputtering Au nanoparticles onto the black silicon surfaces, we increased their efficiency as SALDI-MS substrates, and enabled detection of metabolites from fingerprints and molecules transferred from animal tissues in both positive and negative ionization modes. With this technique, we acquired high quality images from mouse brain and liver tissues. Moreover, our surfaces can easily be functionalized to selectively monitor compounds in terms of their physicochemical properties. We envisage that versatile substrates based on safe materials like silicon and gold will have a considerable impact as a matrix-free strategy for performing *in situ* metabolomics on biological samples.

3.5. Experimental Section

3.5.1. Materials

The silicon wafers used were 4-inch diameter, *n*-type (Phosphor) CZ-Si wafers, with a thickness of 520 μm and a resistivity of 1-20 Ohm·cm, from MicroChemicals GmbH (Ulm, Germany). The gold target (purity grade > 99.995%) was obtained from Kurt J. Lesker Company (Hastings, England). A 5 mm thick inox mask was custom made by the Scientific and Technical Resources Service at the Rovira i Virgili University with an array of 2.5 mm diameter holes of and 2.5 mm pitch. Folic acid, 1,2-dioleoyl-sn-glycero-3-phosphocholine (18:1 (Δ9-Cis)), and D-(+) Glucose standards were purchased from Sigma-Aldrich.

3.5.2. Fabrication of substrates

As bought Si wafers were used to obtain black silicon by applying plasma treatment in a reactive ion etching (RIE) chamber from Oxford Instruments, Plasma Technology PlasmaPro®80. The plasma used was a mixture of oxygen (O_2) and sulfur hexafluoride (SF_6) gases in a ratio of 1:1, at specific pressure, RF power and etching time (30 mTorr, 200 W, 10 min). After the black silicon was created, a 10 nm layer of gold was deposited to obtain the gold-coated black silicon (AuBSi) substrate. The Au layer was deposited using an ATC Orion 8-HV sputtering system (AJA International, N. Scituate, MA, USA) in an argon atmosphere at a pressure of 30 mTorr to create the plasma in the gun. The working distance of the plate was set to 35 mm and RF mode was used at 100 W for 72 s. Similarly, arrays of hydrophilic BSi and AuBSi wells were prepared for measuring diluted standards. The detailed fabrication steps are described in the Supporting Information file.

3.5.3. Functionalization of substrates

The AuBSi were further treated in the same RIE chamber with different plasma to obtain hydrophilic and hydrophobic surfaces. A fluoroform (CHF_3) plasma (50 sccm, 50 W, 20 mTorr, 7 min) was used to obtain the super-hydrophobic surface and an oxygen plasma (50 sccm, 150 W, 50 mTorr, 7 min) was used to obtain the hydrophilic surface. For each treatment a silicon wafer piece was used as a physical mask to cover half of the AuBSi. The functionalized substrate was labelled AuBSi[<|>], and had a half hydrophilic and half hydrophobic surface.

3.5.4. Substrate characterization methods

The surface morphology of BSi and AuBSi was analyzed with a Field Emission Scanning Electron Microscope (SEM) FEG INSPECT 50 operating

at an accelerating voltage of 20 keV. Reflectance measurements were carried out with a Lambda-950 spectrophotometer, equipped with deuterium and tungsten lamps (Perkin-Elmer, Waltham, MA, USA) scanning in the 200 - 800 nm range. Surface roughness was characterized by atomic force microscope Agilent 5500. The hydrophobic and hydrophilic behavior was determined by measuring the contact angle using Optical Tensiometer Theta Lite 100 together with Oneattension software from Biolin Scientific Holding.

3.5.5. Sample preparation

Standard solutions of 1000 ppm were prepared by diluting each standard in water/methanol (1:1 v/v). A pool solution was created where equal amounts of each standard solution were mixed. To obtain the linear calibration curve, the glucose solution was further diluted into 10 concentrations from 1000 ppm to 1 ppm. Droplets of 1.5 µl were spotted in 3 replicates onto the BSi and AuBSi wells and let to dry at room temperature before SALDI-MS measurement.

Fingerprints were obtained from a volunteer working in the laboratory. The direct stamping method was used to imprint the fingerprint molecules onto the substrate. The fingerprint was placed against the nanostructured surface for 5 seconds to ensure that the fingerprint sweat was thoroughly transferred. To detect paracetamol on fingerprints, the volunteer's index finger was coated with paracetamol powder (crushed paracetamol pill, 1 g pills EFG, produced by Ratiopharm Spain, S.A. purchased from a local drugstore) prior to imprinting. Another finger from the same volunteer was used to imprint the control. A fraction of the paracetamol pill was dissolved in water, spotted (2 µL) and dried at room temperature on the AuBSi so that a reference mass spectrum could be measured.

Fresh frozen mouse liver, kidney and brain tissues were received from the Research Unit on Lipids and Atherosclerosis (Reus, Spain). Briefly, six-week-old C57BL/6J male mice (Charles River Laboratories, Spain) were maintained on standard light-dark cycle (12 h light/dark cycle) and temperature (21±1°C) conditions with ad libitum access to food and water. Mice were euthanized and the liver, kidney and brain tissues were immediately frozen in liquid nitrogen and stored at -80°C. Animal handling was conformed to the Guide for the Care and Use of Laboratory Animals published by the U.S. National Institutes of Health (NIH publication no. 85-23, revised 1996). All procedures were approved by the University Rovira i Virgili Bioethics Committee, as stated in Law 5/21 July 1995 passed by the Generalitat de Catalunya (Autonomous Government of Catalonia). The fresh frozen animal tissues were cross-sectioned at different thicknesses (1-10 μm) using a Leica CM-1950 cryostat (Leica Biosystems Nussloch GmbH) at a working temperature of -20°C. The molecule transfer method was used to imprint the tissue molecules onto the surface.[37] In this case, tissue sections were placed on the AuBSi and allowed to interact for one minute. Then the tissues were removed with a constant stream of Milli-Q water.

4.5.6. MSI acquisition

MSI data was acquired using a MALDI TOF/TOF UltrafleXtreme instrument with SmartBeam II Nd:YAG/355 nm laser from Bruker Daltonics. Acquisitions were carried out in the 50-1200 Da range in reflectron mode, and positive and negative ionization mode using the large laser spot size settings (25 μm diameter), operated at 2 kHz, and collecting a total of 500 shots per pixel. We adjusted the laser power for each acquisition to avoid in-source fragmentation as described in a previous work.[19] Lateral resolution was 200 μm for standard droplets, 60 μm for brain tissue, 100 μm for kidney tissue and 80 μm for fingermark.

3.5.7. MSI image data processing

The raw data acquired was visualized using rMSI[41] and processed using rMSIproc[42], an open source software specifically designed to efficiently handle large MSI data sets. Spectral smoothing was done using Savitzky-Golay, mass calibration was based on the linear or loess mass error fitting model using the Au cluster peaks as internal references, intensity was normalized by total ion count (TIC), and the peak matrix was created after peak picking and binning. All processing parameters were the default rMSIproc settings, unless otherwise mentioned.

Whenever possible, a tentative identification has been provided for detected metabolites. Identification was based on the Human Metabolome Database[43] (http://www.hmdb.ca/) and the LIPID MAPS Structure Database (LMSD)[44] (https://www.lipidmaps.org/data/structure/index.php) with the exact precursor mass of metabolites after spectral calibration.

3.5.8. Safety considerations

The substrates were created in a well-controlled environment without using any harmful chemicals. All fabrication steps took place inside reactive chambers with controlled plasma. The proper use of all instrumentation guarantees no risk for users.

3.6. References

(1) Hillenkamp, F.; Karas, M.; Beavis, R. C.; Brian, T. C. Matrix-Assisted Laser Desorption/Ionization Mass Spectrometry of Biopolymers. *Anal. Chem.* **1991**, *63*, 1193–1203.

(2) McDonnell, L. A.; Heeren, R. M. A. Imaging Mass Spectrometry. *Mass Spectrom. Rev.* **2007**, *26*, 606–643.

(3) Puolitaival, S. M.; Burnum, K. E.; Cornett, D. S.; Caprioli, R. M. Solvent-Free Matrix Dry-Coating for MALDI Imaging of Phospholipids. *J. Am. Soc. Mass Spectrom.* **2008**, *19*, 882–886.

(4) Muthu, M.; Chun, S.; Wu, H.-F.; Duncan, M. W.; Gopal, J. The Ongoing Evolution of Laser Desorption/Ionization Mass Spectrometry: Some Observations on Current Trends and Future Directions. *J. Mass Spectrom.* **2018**, 525–540.

(5) Law, K. P.; Larkin, J. R. Recent Advances in SALDI-MS Techniques and Their Chemical and Bioanalytical Applications. *Anal. Bioanal. Chem.* **2011**, *399*, 2597–2622.

(6) Sunner, J.; Dratz, E.; Chen, Y. C. Graphite Surface-Assisted Laser Desorption/Ionization Time-of-Flight Mass Spectrometry of Peptides and Proteins from Liquid Solutions. *Anal. Chem.* **1995**, *67*, 4335–4342.

(7) Thomas, J. J.; Shen, Z.; Crowell, J. E.; Finn, M. G.; Siuzdak, G. Desorption/Ionization on Silicon (DIOS): A Diverse Mass Spectrometry Platform for Protein Characterization. *Proc. Natl. Acad. Sci. U. S. A.* **2001**, *98*, 4932–4937.

(8) Northen, T. R.; Yanes, O.; Northen, M. T.; Marrinucci, D.; Uritboonthai, W.; Apon, J.; Golledge, S. L.; Nordström, A.; Siuzdak, G. Clathrate Nanostructures for Mass Spectrometry. *Nature* **2007**, *449*, 1033–1036.

(9) Iakab, S. A.; Rafols, P.; García-Altares, M.; Yanes, O.; Correig, X. Silicon-Based Laser Desorption Ionization Mass Spectrometry for the Analysis of Biomolecules: A Progress Report. *Adv. Funct. Mater.* **2019**, *1903609*.

(10) Piret, G.; Drobecq, H.; Coffinier, Y.; Melnyk, O.; Boukherroub, R. Matrix-Free Laser Desorption/Ionization Mass Spectrometry on Silicon Nanowire Arrays Prepared by Chemical Etching of Crystalline Silicon. *Langmuir* **2010**, *26*, 1354–1361.

(11) Wen, X.; Dagan, S.; Wysocki, V. H. Small-Molecule Analysis with Silicon-Nanoparticle-Assisted Laser Desorption/Ionization Mass Spectrometry. *Anal. Chem.* **2007**, *79*, 434–444.

(12) Liu, X.; Coxon, P. R.; Peters, M.; Hoex, B.; Cole, J. M.; Fray, D. J. Black Silicon: Fabrication Methods, Properties and Solar Energy Applications. *Energy Environ. Sci.* **2014**, *7*, 3223–3263.

(13) Jansen, H.; de Boer, M.; Legtenberg, R.; Elwenspock, M. The Black Silicon Method: A Universal Method for Determining the Parameter Setting of a Fluorine- Based Reactive Ion Etcher in Deep Silicon Trench Etching with Profile Control. *J Micromech. Microeng.* **1995**, *5*.

(14) Gao, J.; De Raad, M.; Bowen, B. P.; Zuckermann, R. N.; Northen, T. R. Application of Black Silicon for Nanostructure-Initiator Mass Spectrometry. *Anal. Chem.* **2016**, *88*, 1625–1630.

(15) Chiang, C.-K.; Chen, W.-T.; Chang, H.-T. Nanoparticle-Based Mass Spectrometry for the Analysis of Biomolecules. *Chem. Soc. Rev.* **2011**, *40*, 1269–1281.

(16) Palermo, A.; Forsberg, E. M.; Warth, B.; Aisporna, A. E.; Billings, E.; Kuang, E.; Benton, H. P.; Berry, D.; Siuzdak, G. Fluorinated Gold Nanoparticles for Nanostructure Imaging Mass Spectrometry. *ACS Nano* **2018**, *12*, 6938–6948.

(17) Pilolli, R.; Palmisano, F.; Cioffi, N. Gold Nanomaterials as a New Tool for Bioanalytical Applications of Laser Desorption Ionization Mass Spectrometry. *Anal. Bioanal. Chem.* **2012**, *402*, 601–623.

(18) Kurczy, M. E.; Zhu, Z. J.; Ivanisevic, J.; Schuyler, A. M.; Lalwani, K.; Santidrian, A. F.; David, J. M.; Giddabasappa, A.; Roberts, A. J.; Olivos, H. J.; O'Brien, P. J.; Franco, L.; Fields, M. W.; Paris, L. P.; Friedlander, M.; Johnson, C. H.; Epstein, A. A.; Gendelman, H. E.; Wood, M. R.; Felding, B. H.; *et al.* Comprehensive Bioimaging with Fluorinated Nanoparticles Using Breathable Liquids. *Nat. Commun.* **2015**, *6*, 6–13.

(19) Ràfols, P.; Vilalta, D.; Torres, S.; Calavia, R.; Heijs, B.; McDonnell, L. A.; Brezmes, J.; del Castillo, E.; Yanes, O.; Ramírez, N. I.; CorreigID, X. Assessing the Potential of Sputtered Gold Nanolayers in Mass Spectrometry Imaging for Metabolomics Applications. *PLoS One* **2018**.

(20) Dufresne, M.; Masson, J. F.; Chaurand, P. Sodium-Doped Gold-Assisted Laser Desorption Ionization for Enhanced Imaging Mass Spectrometry of Triacylglycerols from Thin Tissue Sections. *Anal. Chem.* **2016**, *88*, 6018–6025.

(21) Huang, Y. F.; Chang, H. T. Analysis of Adenosine Triphosphate and Glutathione through Gold Nanoparticles Assisted Laser Desorption/Ionization Mass Spectrometry. *Anal. Chem.* **2007**, *79*, 4852–4859.

(22) Greving, M. P.; Patti, G. J.; Siuzdak, G. Nanostructure-Initiator Mass Spectrometry Metabolite Analysis and Imaging. *Anal. Chem.* **2011**, *83*, 2–7.

(23) Guinan, T.; Della Vedova, C.; Kobus, H.; Voelcker, N. H. Mass Spectrometry Imaging of Fingerprint Sweat on Nanostructured Silicon. *Chem. Commun.* **2015**, *51*, 6088–6091.

(24) Sekuła, J.; Nizioł, J.; Rode, W.; Ruman, T. Gold Nanoparticle-Enhanced Target (AuNPET) as Universal Solution for Laser Desorption/Ionization Mass Spectrometry Analysis and Imaging of Low Molecular Weight Compounds. *Anal. Chim. Acta* **2015**, *875*, 61–72.

(25) Taverniers, I.; De Loose, M.; Van Bockstaele, E. Trends in Quality in the Analytical Laboratory. II. Analytical Method Validation and Quality Assurance. *TrAC - Trends Anal. Chem.* **2004**, *23*, 535–552.

(26) Wasserman, D. H. Four Grams of Glucose. *Am. J. Physiol. - Endocrinol. Metab.* **2009**, *296*, 11–21.

(27) Sener, A.; Jurysta, C.; Bulur, N.; Oguzhan, B.; Satman, I.; Yilmaz, T. M.; Malaisse, W. J. Salivary Glucose Concentration and Excretion in Normal and Diabetic Subjects. *J. Biomed. Biotechnol.* **2009**.

(28) Lawrence, R. D. Renal Threshold for Glucose : Normal and in Diabetics. *Br. Med. J.* **1940**, *1*, 766.

(29) Chen, X.; Wang, T.; Lin, L.; Wo, F.; Liu, Y.; Liang, X.; Ye, H.; Wu, J. Tip-Enhanced Photoinduced Electron Transfer and Ionization on Vertical Silicon Nanowires. *ACS Appl. Mater. Interfaces* **2018**, *10*, 14389–14398.

(30) Knochenmuss, R. The Coupled Chemical and Physical Dynamics Model of MALDI. *Annu. Rev. Anal. Chem.* **2016**, *9*, 365–385.

(31) Wahl, M. C.; Kim, H. S.; Wood, T. D.; Guan, S.; Marshall, A. G. Thin Gold Film-Assisted Laser Desorption/Ionization Fourier Transform Ion Cyclotron Resonance Mass Spectrometry of Biomolecules. *Anal. Chem.* **1993**, *65*, 3669–3676.

(32) Mena-Bravo, A.; Luque de Castro, M. D. Sweat: A Sample with Limited Present Applications and Promising Future in Metabolomics. *J. Pharm. Biomed. Anal.* **2014**, *90*, 139–147.

(33) De Paoli, G.; Lewis, S. A.; Schuette, E. L.; Lewis, L. A.; Connatser, R. M.; Farkas, T. Photo- and Thermal-Degradation Studies of Select Eccrine Fingerprint Constituents. *J. Forensic Sci.* **2010**, *55*, 962–969.

(34) Sonner, Z.; Wilder, E.; Heikenfeld, J.; Kasting, G.; Beyette, F.; Swaile, D.; Sherman, F.; Joyce, J.; Hagen, J.; Kelley-Loughnane, N.; Naik, R. The Microfluidics of the Eccrine Sweat Gland, Including Biomarker Partitioning, Transport, and Biosensing Implications. *Biomicrofluidics* **2015**, *9*.

(35) Pappas, A. Epidermal Surface Lipids. *Dermatoendocrinol.* **2009**, *1*, 72–76.

(36) Gemperline, E.; Chen, B.; Li, L. Challenges and Recent Advances in Mass Spectrometric Imaging of Neurotransmitters. *Bioanalysis* **2014**, *6*, 525–540.

(37) Vidová, V.; Novák, P.; Strohalm, M.; Pól, J.; Havlíček, V.; Volný, M. Laser Desorption-Ionization of Lipid Transfers: Tissue Mass Spectrometry Imaging without Maldi Matrix. *Anal. Chem.* **2010**, *82*, 4994–4997.

(38) Škrášková, K.; Heeren, R. M. A. A Review of Complementary Separation Methods and Matrix Assisted Laser Desorption Ionization-Mass Spectrometry Imaging: Lowering Sample Complexity. *J. Chromatogr. A* **2013**, *1319*, 1–13.

(39) Liu, H.; Li, W.; He, Q.; Xue, J.; Wang, J.; Xiong, C.; Pu, X.; Nie, Z. Mass Spectrometry Imaging of Kidney Tissue Sections of Rat Subjected to Unilateral Ureteral Obstruction. *Sci. Rep.* **2017**, *7*, 1–9.

(40) Cerruti, C. D.; Benabdellah, F.; Laprévote, O.; Touboul, D.; Brunelle, A. MALDI Imaging and Structural Analysis of Rat Brain Lipid Negative Ions with 9-Aminoacridine Matrix. *Anal. Chem.* **2012**, *84*, 2164–2171.

(41) Rafols, P.; Torres, S.; Ramirez, N.; del Castillo, E.; Yanes, O.; Brezmes, J.; Correig, X. RMSI : An R Package for MS Imaging Data Handling and Visualization. *Bioinformatics* **2017**, *33*, 2427–2428.

(42) Ràfols, P.; Castillo, E. del; Yanes, O.; Brezmes, J.; Correig, X. Novel Automated Workflow for Spectral Alignment and Mass Calibration in MS Imaging Using a Sputtered Ag Nanolayer. *Anal. Chim. Acta* **2018**, *1022*, 61–69.

(43) Wishart, D. S.; Feunang, Y. D.; Marcu, A.; Guo, A. C.; Liang, K.; Vázquez-Fresno, R.; Sajed, T.; Johnson, D.; Li, C.; Karu, N.; Sayeeda, Z.; Lo, E.; Assempour, N.; Berjanskii, M.; Singhal, S.; Arndt, D.; Liang, Y.; Badran, H.; Grant, J.; Serra-Cayuela, A.; *et al.* HMDB 4.0: The Human Metabolome Database for 2018. *Nucleic Acids Res.* **2018**, *46*, D608–D617.

(44) Sud, M.; Fahy, E.; Cotter, D.; Brown, A.; Dennis, E. A.; Glass, C. K.; Merrill, A. H.; Murphy, R. C.; Raetz, C. R. H.; Russell, D. W.; Subramaniam, S. LMSD: LIPID MAPS Structure Database. *Nucleic Acids Res.* **2007**, *35*, 527–532.

3.6. Supporting information

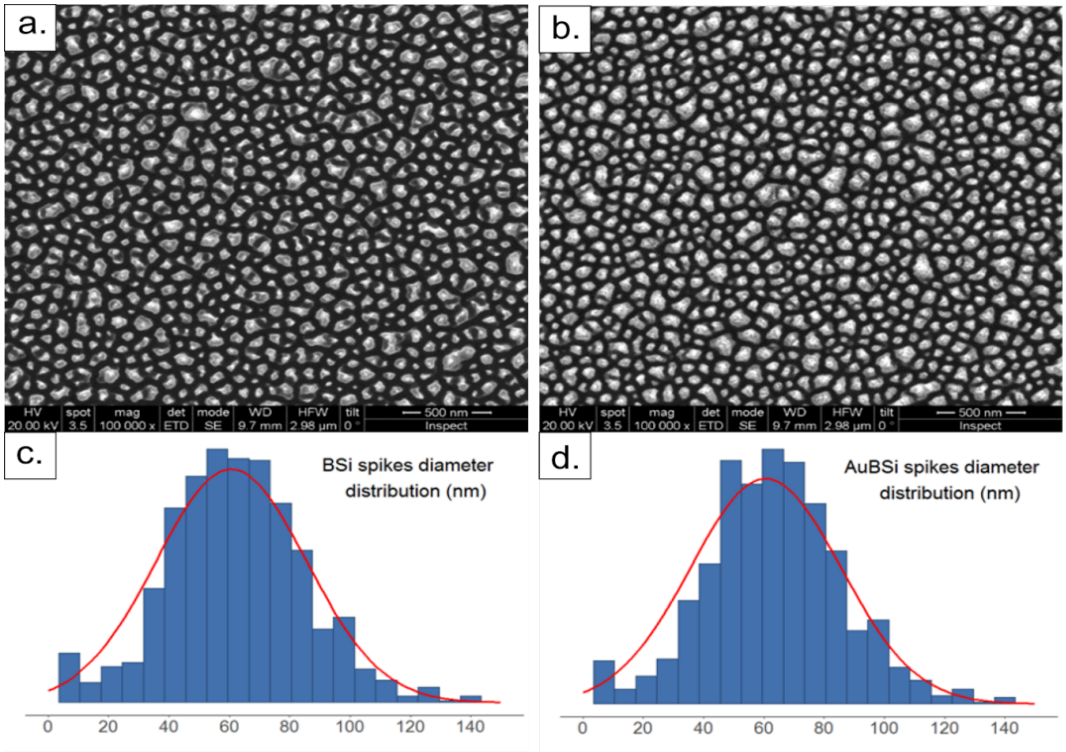

Figure S1. SEM images of the top view of BSi (a) and AuBSi (b) with their respective mean diameter size distribution around 60 nm (c and d)

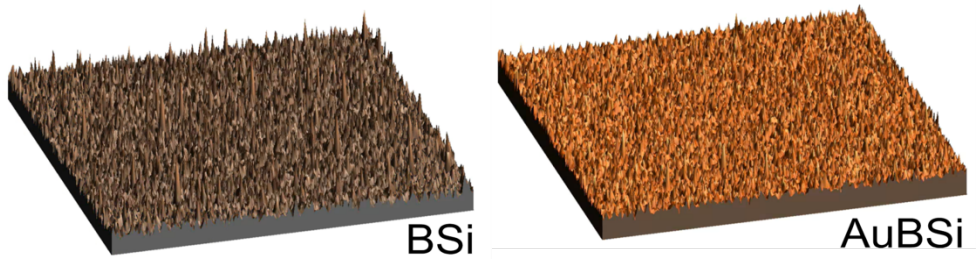

Figure S2. 3D profile roughness measurements of BSi and AuBSi. The average Roughness of BSi and AuBSi surfaces is 15.9378 nm and 16.0352 nm, respectively. The Root Mean Square (RMS) of BSi and AuBSi is 20.8494 and 20.6259, respectively. These values that describe the height variations on the

surface indicate that the surfaces are very similar to each other and they are flatter than micron-scaled objects, such as tissues

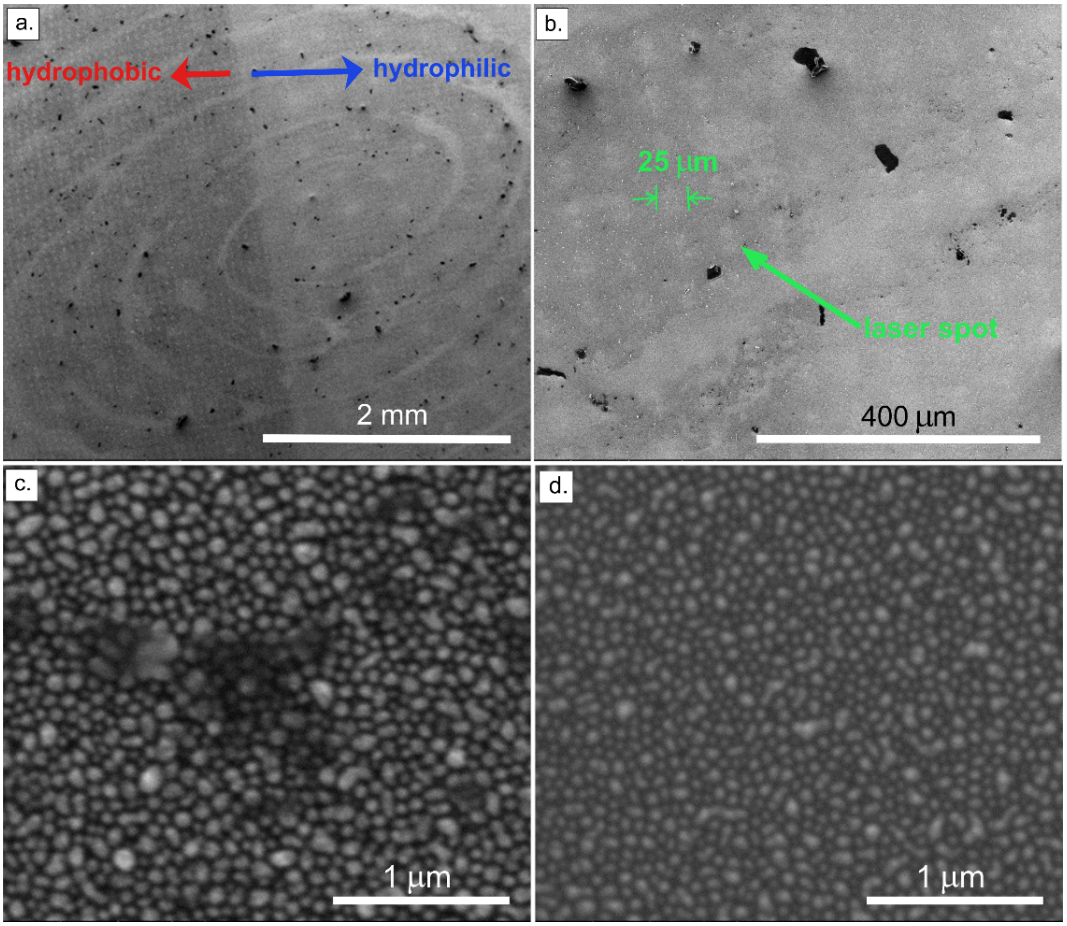

Figure S3. SEM images of the AuBSi nanostructure after fingerprint stamping and MSI acquisition (a, b, c) and SEM image of a clean AuBSi (d). Image a. shows the morphology of the fingerprint (ridges and valleys), with some parts that are darker than others because of the presence of carbon from the biomolecules adhered to the surface; image b shows the laser spots with average diameter around 25 µm (in light grey color), small circular-like areas where the molecules desorbed from the AuBSi; image c is a close up inside one of the laser spots from image b., where the darker grey indicates the presence of carbon and the lighter grey shows the presence of metal, in

this case gold. The nanostructures in image c (after fingerprint imprinting and MSI analysis) and image d. (clean AuBSi surface) are very similar, indicating that the AuBSi structure is robust enough to stamp samples onto the surface

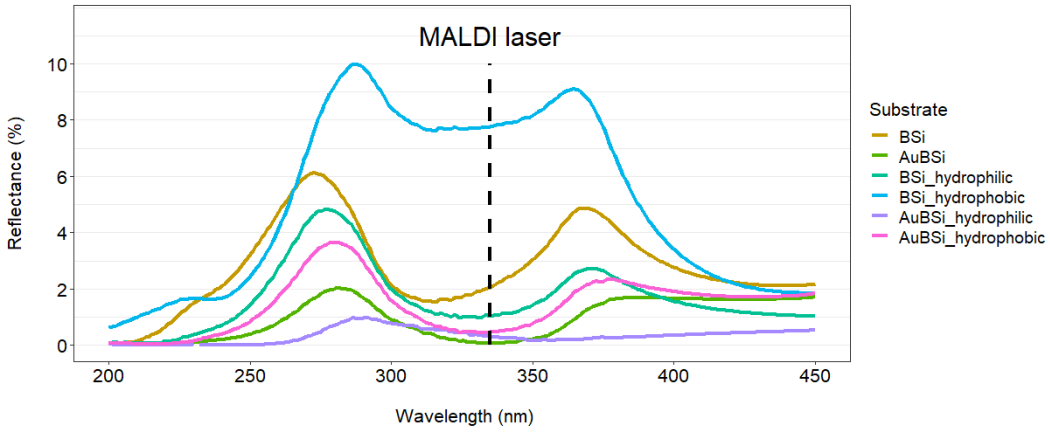

Figure S4. Reflectance of bare Si, BSi and AuBSi substrates and their modified surfaces. The dashed line marks the MALDI UV laser wavelength at 335 nm. The value of reflectance for bare silicon for the range 200-450 nm is higher than 50%

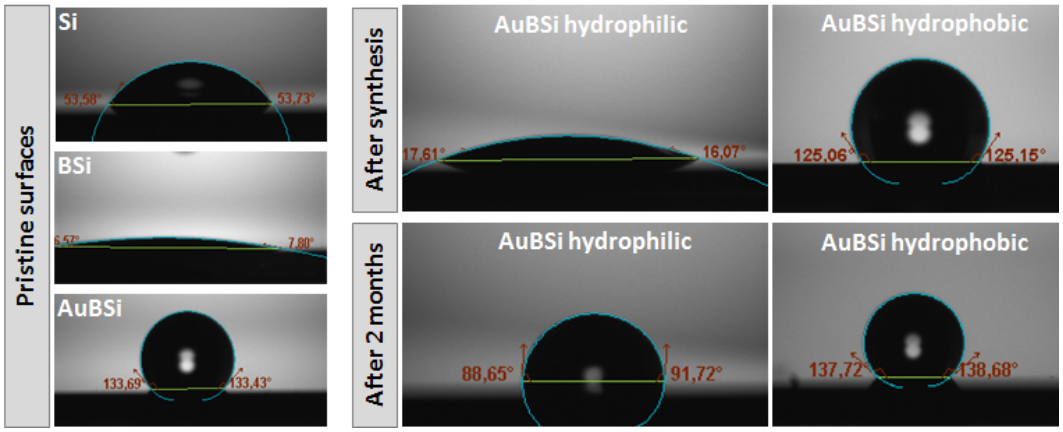

Figure S5. Contact angle measurements of bare Si, BSi, AuBSi and functionalized AuBSi surfaces after synthesis and 2 months after synthesis

Fabrication protocol of BSi and AuBSi array of wells

For the analysis of liquid samples we created an array of black silicon (BSi) and gold-coated black silicon (AuBSi) wells on which the liquid standards would be spotted. For this, we used a custom made inox mask to cover the Si wafer while creating the BSi. First we placed the wafer into the RIE chamber, then we placed the inox mask on the wafer and used a mixture of oxygen (O2) and sulfur hexafluoride (SF6) gasses of ratio 1:1 (30 mTorr, 200 W, 10 min) to create the BSi wells, only where the wafer was exposed (in the holes of the mask). Then we removed the mask and placed the wafer into the Sputtering chamber and deposited 10 nm Au layer (Ar atmosphere 30 mTorr, 35 mm working distance, RF mode at 100 W for 72 s) to obtain AuBSi wells. The Au layer deposited on the Si wafer created a hydrophobic surface, therefore we changed the hydrophobicity of the wells for optimizing the sample deposition. For this, we placed the gold-coated wafer into the RIE chamber and put the inox mask onto the wafer so the wells aligned with the holes of the mask. We then used oxygen plasma (50 sccm, 150 W, 50 mTorr, 75 min)

to create hydrophilic AuBSi wells. Figure S6 represents the fabrication steps for the BSi and AuBSi well array.

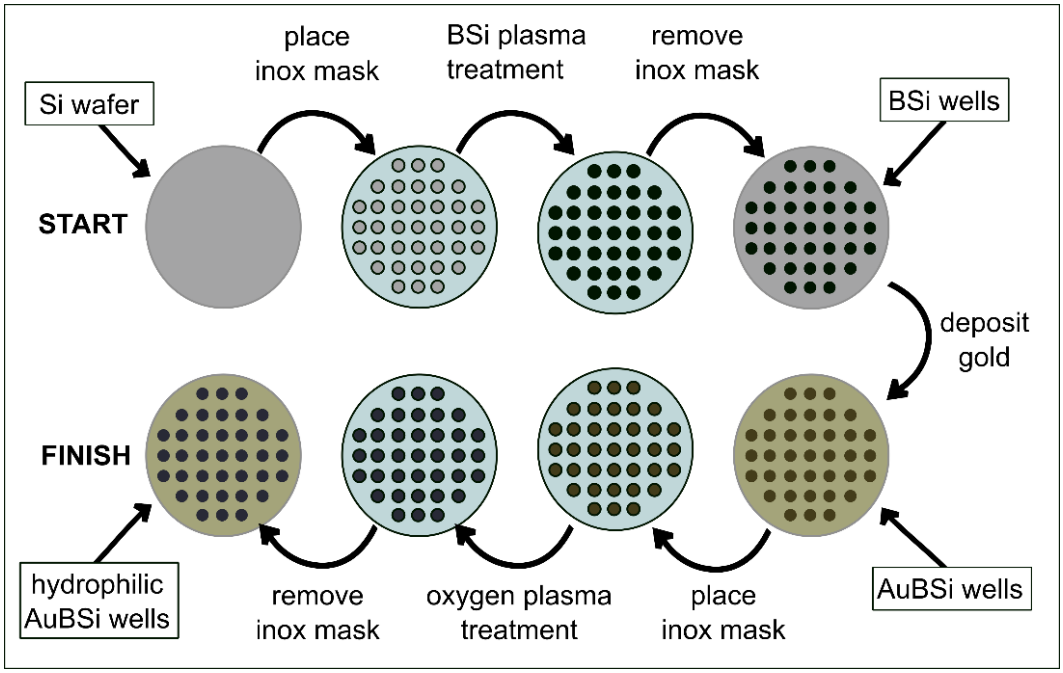

Figure S6. Fabrication steps for the array of hydrophilic AuBSi wells.

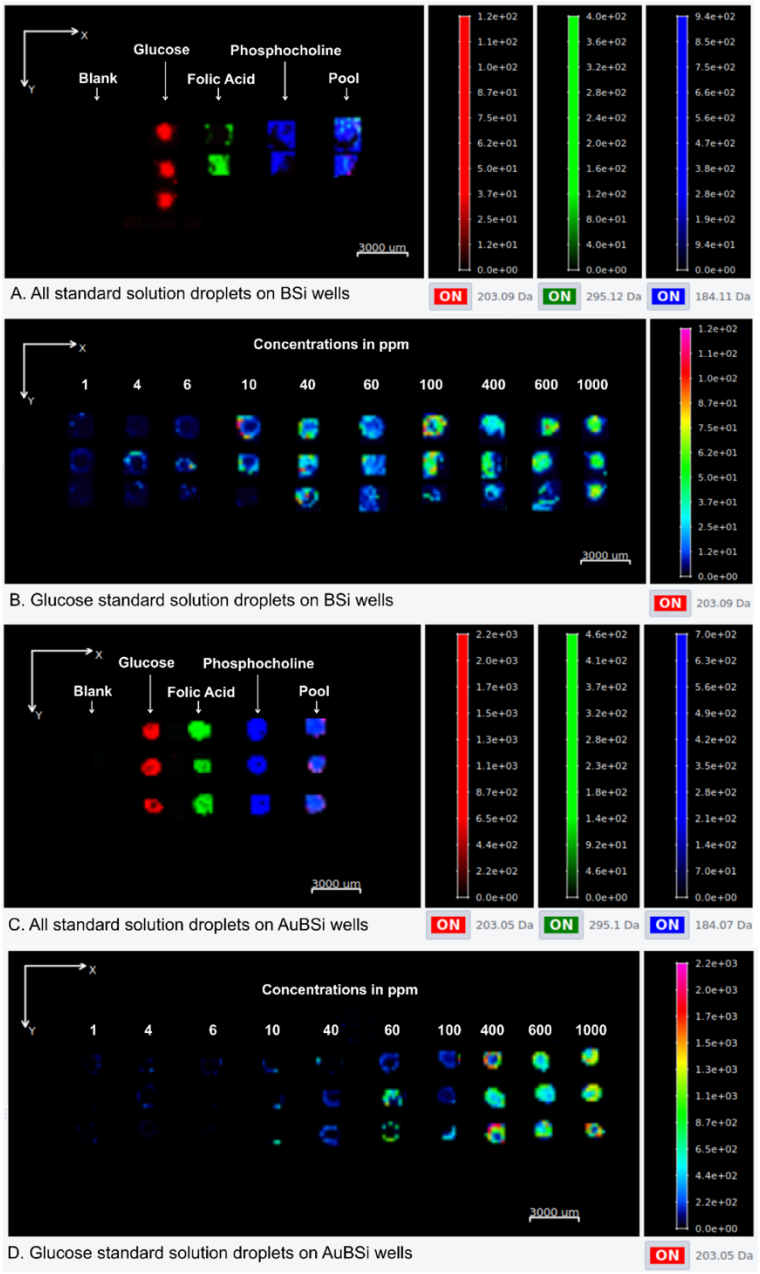

Figure S7. MS images of standard droplets on BSi and AuBSi normalized by TIC. (A, C) Visualization of the three standards (1000 ppm in water/methanol 1:1, v/v), the pool and the blank using 3 color channels: red for glucose *m/z* 203.05, green for folic acid *m/z* 295.1 and blue for

phosphocholine *m/z* 184.07. (B, D) Visualization of the 10 concentrations of glucose (1-1000 ppm in water/methanol 1:1, v/v).

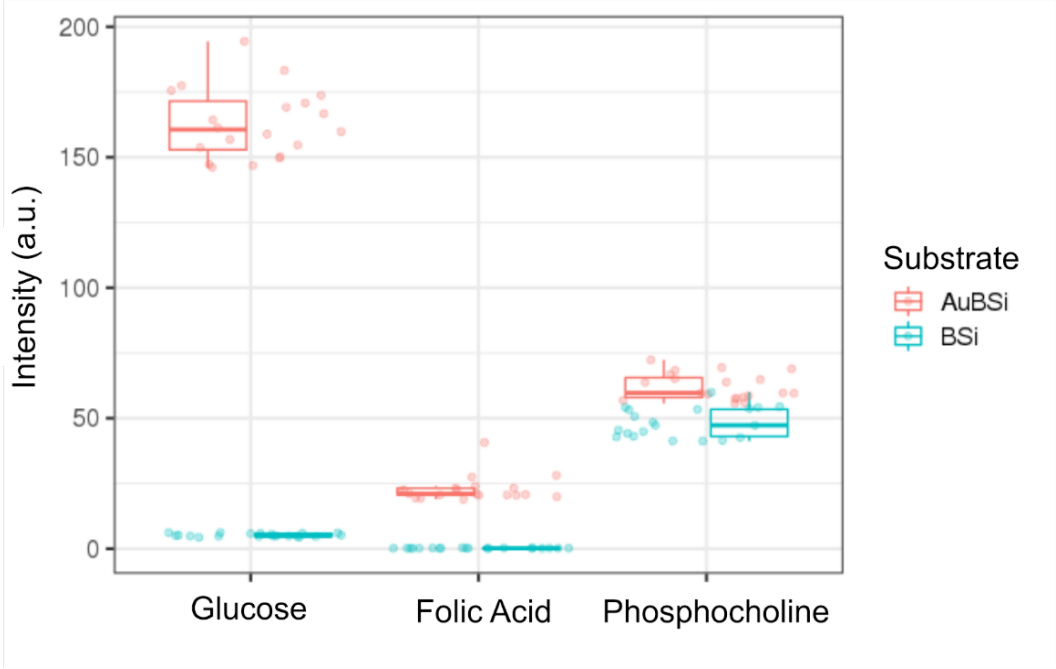

Figure S8. Boxplot chart comparing the intensity values of the representative ions of the three standards measured on BSi and AuBSi substrates (glucose *m/z* 203.05; folic acid *m/z* 295.1; phosphocholine *m/z* 184.07). Each boxplot contains the 20 most intense pixels from the 3 droplets measured (see in Figure S7).

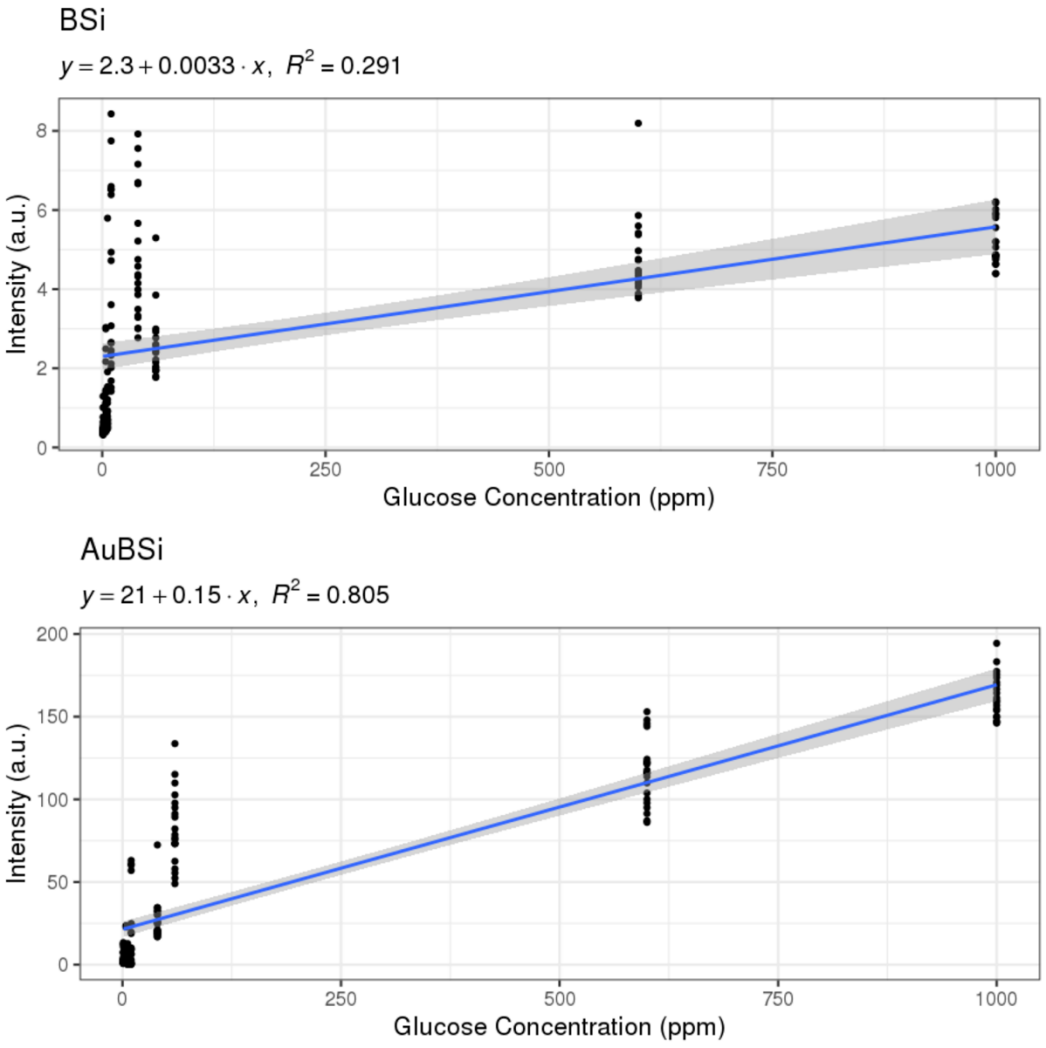

Figure S9. Linear calibration curves of glucose in the range of 1-1000 ppm measured on BSi and AuBSi. For each glucose concentration the 20 most intense pixels are used for calculations.

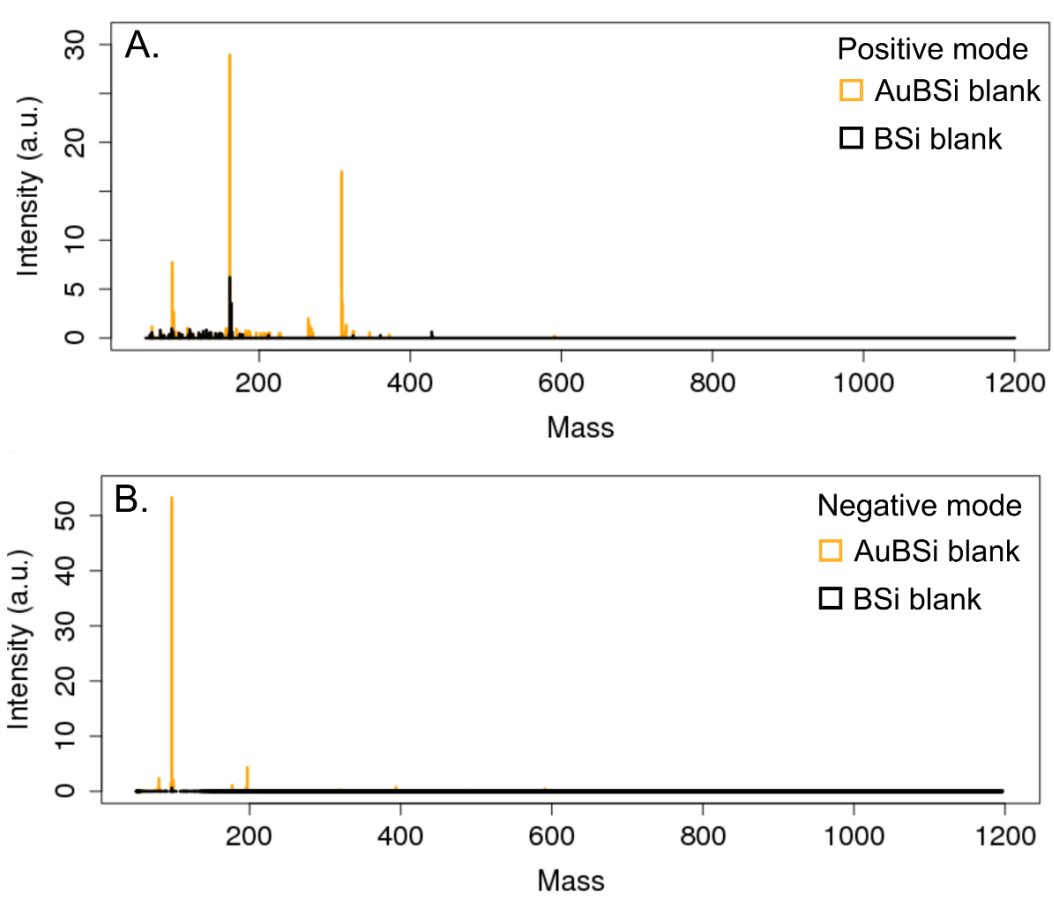

Figure S10. Background (blank) mass spectra from BSi and AuBSi in positive (A.) and negative mode (B.). Peaks detected in these background samples are situated in the low mass region of the spectra (*m/z* 50-300) with low intensity compared to intensity from fingermarks, Figure 3 in the main manuscript.

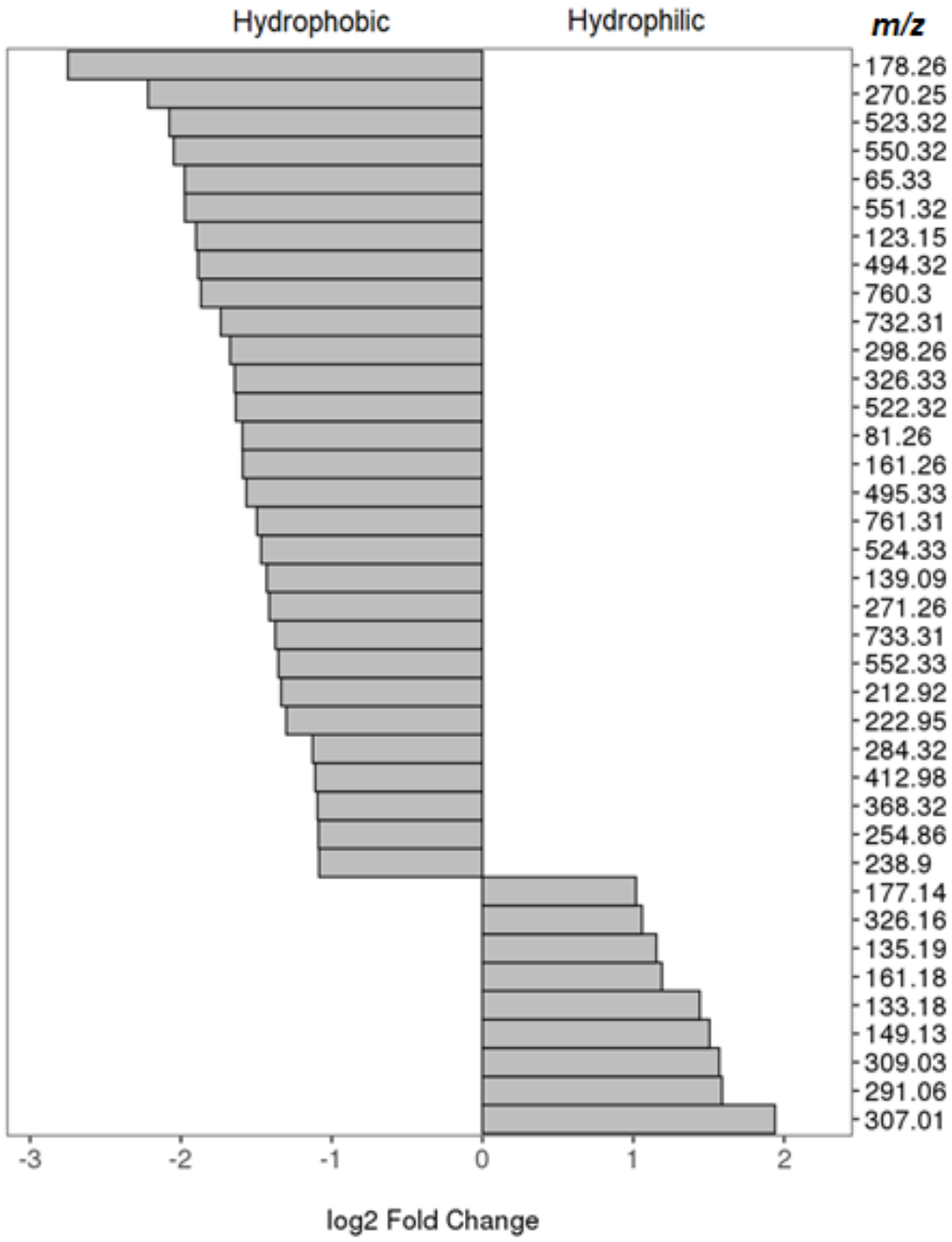

Figure S11. Fold change plot showing the predominant ions (*m/z*) in the hydrophobic and hydrophilic regions

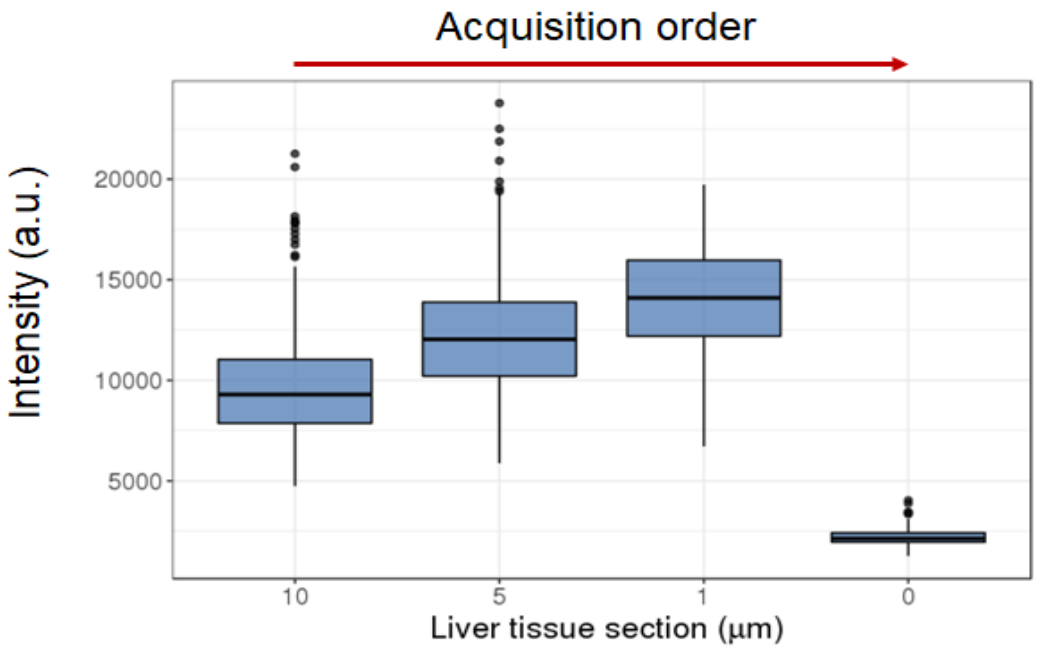

Figure S12. Boxplot representation of total ion count for the different liver sections used for the molecule transfer method in acquisition order

Table S1. Putative identification of brain and kidney ions detected on AuBSi

Compound Name	Chemical Formula	Adduct	Theoretical *m/z*	Experimental *m/z*	Error [ppm]	Sample	Ref
(3'-sulfo)Galβ-Cer(d18:1/18:0)	C42H81NO11S	[M-H]$^-$	806.5458	806.5535	9.546	brain	[1,2]
PG(40:6)	C46H79O10P	[M-H]$^-$	821.5338	821.5591	30.796	brain	[1–3]
(3'-sulfo)Galβ-Cer(d18:1/18:0(2OH))	C42H81NO12S	[M-H]$^-$	822.5407	822.5328	9.604	brain	[2,3]
(3'-sulfo)Galβ-Cer(d18:1/22:0)	C46H89NO11S	[M-H]$^-$	862.6084	862.6261	20.519	brain	[1–3]
(3'-sulfo)Galβ-Cer(d18:1/22:0(2OH))	C46H89NO12S	[M-H]$^-$	878.6033	878.6169	15.479	brain	[2,3]
(3'-sulfo)Galβ-Cer(d18:1/24:1(15Z))	C48H91NO11S	[M-H]$^-$	888.624	888.591	37.136	brain	[1–3]
(3'-sulfo)Galβ-Cer(d18:1/24:0)	C48H93NO11S	[M-H]$^-$	890.6397	890.6341	6.287	brain	[1–3]
(3'-sulfo)Galβ-Cer(d18:1/24:1(15Z)(2OH))	C48H91NO12S	[M-H]$^-$	904.6189	904.5851	37.363	brain	[2,3]
(3'-sulfo)Galβ-Cer(d18:1/24:0(2OH))	C48H93NO12S	[M-H]$^-$	906.6346	906.6489	15.772	brain	[2,3]
stearic acid	C18H36O2	[M-H]$^-$	283.2643	283.27911	52.283	kidney	[1,2,4]
PE(P-18:0/22:4(7Z,10Z,13Z,16Z))	C45H82NO7P	[M-H]$^-$	778.5756	778.5687	8.862	kidney	[2,3]
PE(MonoMe(11,3)/MonoMe(13,5))	C47H82NO10P	[M-H]$^-$	850.5604	850.5736	15.519	kidney	[1]
PE(22:4(7Z,10Z,13Z,16Z)/24:0)	C51H94NO8P	[M-H]$^-$	878.6644	878.6532	12.746	kidney	[1]
PE-NMe2(46:4)	C53H98NO8P	[M-H]$^-$	906.6957	906.68	17.315	kidney	[1]

3.7. Supporting information references

(1) Wishart, D. S.; Feunang, Y. D.; Marcu, A.; Guo, A. C.; Liang, K.; Vázquez-Fresno, R.; Sajed, T.; Johnson, D.; Li, C.; Karu, N.; Sayeeda, Z.; Lo, E.; Assempour, N.; Berjanskii, M.; Singhal, S.; Arndt, D.; Liang, Y.; Badran, H.; Grant, J.; Serra-Cayuela, A.; *et al.* HMDB 4.0: The Human Metabolome Database for 2018. *Nucleic Acids Res.* **2018**, *46*.

(2) Sud, M.; Fahy, E.; Cotter, D.; Brown, A.; Dennis, E. A.; Glass, C. K.; Merrill, A. H.; Murphy, R. C.; Raetz, C. R. H.; Russell, D. W.; Subramaniam, S. LMSD: LIPID MAPS Structure Database. *Nucleic Acids Res.* **2007**, *35*, 527–532.

(3) Cerruti, C. D.; Benabdellah, F.; Laprévote, O.; Touboul, D.; Brunelle, A. MALDI Imaging and Structural Analysis of Rat Brain Lipid Negative Ions with 9-Aminoacridine Matrix. *Anal. Chem.* **2012**, *84*, 2164–2171.

(4) Liu, H.; Li, W.; He, Q.; Xue, J.; Wang, J.; Xiong, C.; Pu, X.; Nie, Z. Mass Spectrometry Imaging of Kidney Tissue Sections of Rat Subjected to Unilateral Ureteral Obstruction. *Sci. Rep.* **2017**, *7*, 1–9.

UNIVERSITAT ROVIRA I VIRGILI
GOLD-COATED BLACK SILICON NANOSTRUCTURED SURFACES FOR SERS AND SALDI-MS MULTIMODAL IMAGING OF BIOLOGICAL APPLICATIONS
Stefania-Alexandra Iakab

Chapter 4: Gold-Coated Black Silicon for Multimodal Imaging Combining Surface Assisted Laser Desoprtion/Ionization Mass Spectrometry (SALDI-MS) and Surface Enhanced Raman Spectroscopy (SERS) Imaging

UNIVERSITAT ROVIRA I VIRGILI
GOLD-COATED BLACK SILICON NANOSTRUCTURED SURFACES FOR SERS AND SALDI-MS MULTIMODAL IMAGING OF BIOLOGICAL APPLICATIONS
Stefania-Alexandra Iakab

Chapter 4.1: *Raman2imzML* Converts Raman Imaging Data Into The Standard Mass Spectrometry Imaging Format

UNIVERSITAT ROVIRA I VIRGILI
GOLD-COATED BLACK SILICON NANOSTRUCTURED SURFACES FOR SERS AND SALDI-MS MULTIMODAL IMAGING OF BIOLOGICAL APPLICATIONS
Stefania-Alexandra Iakab

State of the article:

Published in BMC Bioinformatics (2020) 21:448 https://doi.org/10.1186/s12859-020-03789-8 and reproduced by permission from the authors

Journal metrics:

Impact factor 3.24 (2019)

Q1 (Applied Mathematics)

Contributing authors:

Stefania Alexandra Iakab[†‡⧫], *Lluc Sementé*[†⧫], *María García-Altares*[†‡*], *Xavier Correig*[†‡§], *Pere Ráfols*[†]

[†]Department of Electronic Engineering, Rovira i Virgili University, Tarragona, 43007, Spain

[‡]Spanish Biomedical Research Centre in Diabetes and Associated Metabolic Disorders (CIBERDEM), Madrid, 28029, Spain

[§]Institut d'Investigació Sanitària Pere Virgili, Tarragona, Spain

[⧫]Both authors contributed equally to this work

UNIVERSITAT ROVIRA I VIRGILI
GOLD-COATED BLACK SILICON NANOSTRUCTURED SURFACES FOR SERS AND SALDI-MS MULTIMODAL IMAGING OF BIOLOGICAL APPLICATIONS
Stefania-Alexandra Iakab

4.1.1. Abstract

Background: Multimodal imaging that combines Mass Spectrometry Imaging (MSI) with Raman imaging is a rapidly developing multidisciplinary analytical method used by a growing number of research groups. Computational tools that can visualize and aid the analysis of datasets by both techniques are in demand. **Results:** *Raman2imzML* was developed as an open-source converter that transforms Raman imaging data into imzML, a standardized common data format created and adopted by the mass spectrometry community. We successfully converted Raman datasets to imzML and visualized Raman images using open-source software designed for MSI applications. **Conclusion:** *Raman2imzML* enables both MSI and Raman images to be visualized using the same file format and the same software for a straightforward exploratory imaging analysis.

Keywords: converter, Raman Imaging, imzML, R, Mass Spectrometry Imaging

UNIVERSITAT ROVIRA I VIRGILI
GOLD-COATED BLACK SILICON NANOSTRUCTURED SURFACES FOR SERS AND SALDI-MS MULTIMODAL IMAGING OF BIOLOGICAL APPLICATIONS
Stefania-Alexandra Iakab

4.1.2. Background

In recent years, mass spectrometry imaging (MSI) has become an important analytical technique because of its capacity to spatially localize a wide range of biomolecules from plant, animal and human tissues (1). The main advantage of MSI is its high specificity, which makes it possible to identify endogenous and exogenous compounds such as metabolites, lipids, peptides and proteins. Consequently, a considerable number of advanced data analysis tools have emerged as proprietary or open source software, with a tendency towards data format standardization (2).

However, the most common MSI instruments and sample preparation protocols have difficulty in acquiring high spatial resolution images. The spatial resolution of current acquisitions is limited to a few micrometres, which prevents the detailed molecular characterization at the micron scale so necessary for the study of microorganisms and cells (3). Thus, it was suggested that the molecular images produced by MSI could be combined with images obtained by other high spatial resolution techniques. Several studies proposed correlating MSI with optical or fluorescence images (4–6) or with molecular images of spectroscopic techniques such as Fourier Transformed-Infrared Spectroscopy (FTIR) (7,8) and Raman Spectroscopy imaging (9–17). The combination of MSI and Raman imaging is becoming increasingly popular for exploring biological tissues because Raman is a non-destructive label-free technique which characterizes tissues at a submicron lateral resolution. Moreover, Raman imaging provides MSI proteomic studies with complimentary information about the chemical composition of the sample, such as lipid-to-protein ratio or changes in lipid content (10).

Nonetheless, collecting molecular information for sample characterization with two analytical instruments means that there are two different data

formats, which need two different software to visualize and analyse the two datasets. A unified data format, common to all spectral imaging techniques, would benefit and promote the development of multimodal imaging applications. So far, only a few studies have visualized and analysed datasets using techniques such as spectroscopic, mass spectrometric, and X-ray diffraction data within the same software (18–20). However, the data format supported in these cases was common text (.txt) which is not suitable for MSI datasets because it cannot encode a complete MSI dataset in a text file because of its large data size. The standard data format adopted by the MSI community to exchange and process data is imzML (21). Currently instrument manufacturers and the scientific community are not using a standard file format for Raman imaging data. Due to the similarities between MSI and Raman imaging data structure, we suggest adapting Raman imaging datasets to the standardized open format imzML. In this way, MSI and Raman imaging data can be explored with the same software, so that data from different imaging experiments can be visualized more straightforwardly.

Here, we present *Raman2imzML,* an open-source data converter distributed as an R package which converts Raman data acquired with Renishaw and WITec instruments to imzML. We converted Raman imaging datasets collected from mouse brain tissue, and then visualized them with commonly used MSI software tools. The *Raman2imzML* package together with its documentation is available online (github.com).

4.1.3. Implementation

Raman2imzML converts text files (.txt) exported from imaging data acquired using Renishaw and WITec Raman instruments to imzML format (Figure 1). To convert the Raman data to imzML, the Raman text file (.txt) is

parsed to extract the imaging information: number of pixels, pixel coordinates and number of data points in each spectrum. Then, the imaging information is used to calculate the binary offsets according to the imzML format specification and stored in an intermediate data structure. Immediately, the binary part of the imzML format is written by directly transferring each Raman spectrum to binary stream encoded as 32-bit floating-point numbers. Finally, the *Raman2imzML* converter uses the imzML parser in the rMSI package (22) to write the XML part of the imzML using the imaging information (metadata) stored in the intermediate data structure. The *Raman2imzML* converter is distributed as an R package and includes a converter function for each instrument manufacturer to simplify user access. A Raman2imzML R project that includes a markdown and a set of example measurements from Renishaw and WITec to test the package is available as supplementary material.

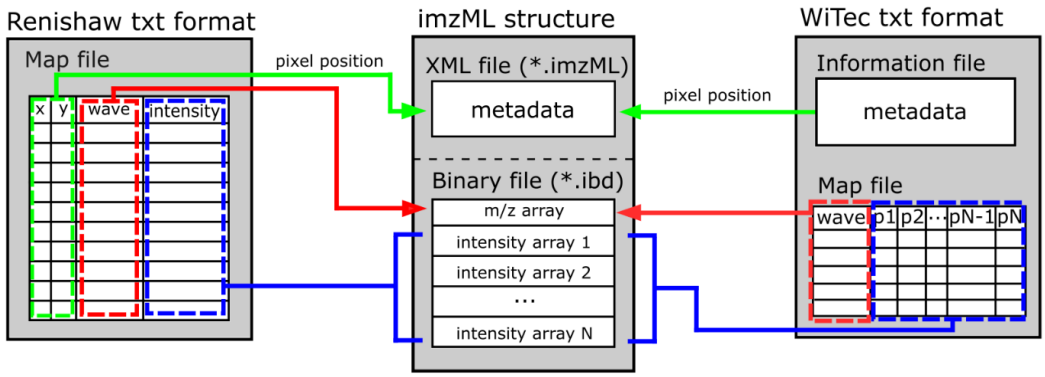

Figure 1. Data conversion from Raman *.txt files (exported from datasets collected with Renishaw and WITec spectrometers) into the imzML format. Coloured arrows indicate how and where the information is stored in the imzML format.

The imzML format was designed to store mass spectrometry data, so it has some limitations when it is used for Raman data. Several specific words

defined in the imzML ontology do not suit Raman experiments or do not exist. For example, "Raman Shift" units or diffraction grating definitions (cm^{-1}) are nonexistent in the imzML format. Therefore, after the conversion, only numeric imaging information such as pixel position, intensity values and Raman shift axis values are preserved. It should also be pointed out that some information (integration time, excitation wavelength, etc.) is not preserved by the converter, as it is lost when the data is exported to text. Nevertheless, we suggest that the imzML specification be extended to handle imaging modalities other than MSI. This will enable future versions of *Raman2imzML* to perform data conversion without losing any information.

4.1.4. Results and Discussion

Figure 2 illustrates how images produced by MSI and Raman imaging can be visualized and explored using the same software. First, we used laser desorption/ionization (LDI) MSI and Raman to acquire molecular images from consecutive histological sections of a fresh-frozen mouse brain. For MSI (Figure 2 A), we placed the tissue section onto an ITO-coated glass slide and covered the surface of the tissue with a thin Au nanolayer by sputtering (23). For Raman measurements (Figure 2 B), we placed the consecutive tissue slice onto a CaF_2 slide. Images were acquired using MALDI TOF/TOF UltrafleXtreme (50-1200 Da mass range, positive reflectron mode, large laser spot size, 500 shots per pixel, 20 μm lateral resolution) for MSI, and Renishaw (633 nm excitation wavelength, 50x objective, 2 s integration time, 50% laser power, 2 μm step) for Raman imaging. To explore both imaging datasets, we exported the MSI data using Bruker's software flexImaging™ directly into imzML and converted the Raman text data using *Raman2imzML* into the imzML format. Finally, we imported both imzML files independently, and visualized the molecular images using the rMSI package (22) although other MSI software can be used for data exploration:

for example, open-source options such as Datacube Explorer (24), CARDINAL (25), MSiReader (26) and msiQuant (27) and commercial options such as SCiLS Lab and MALDIVision.

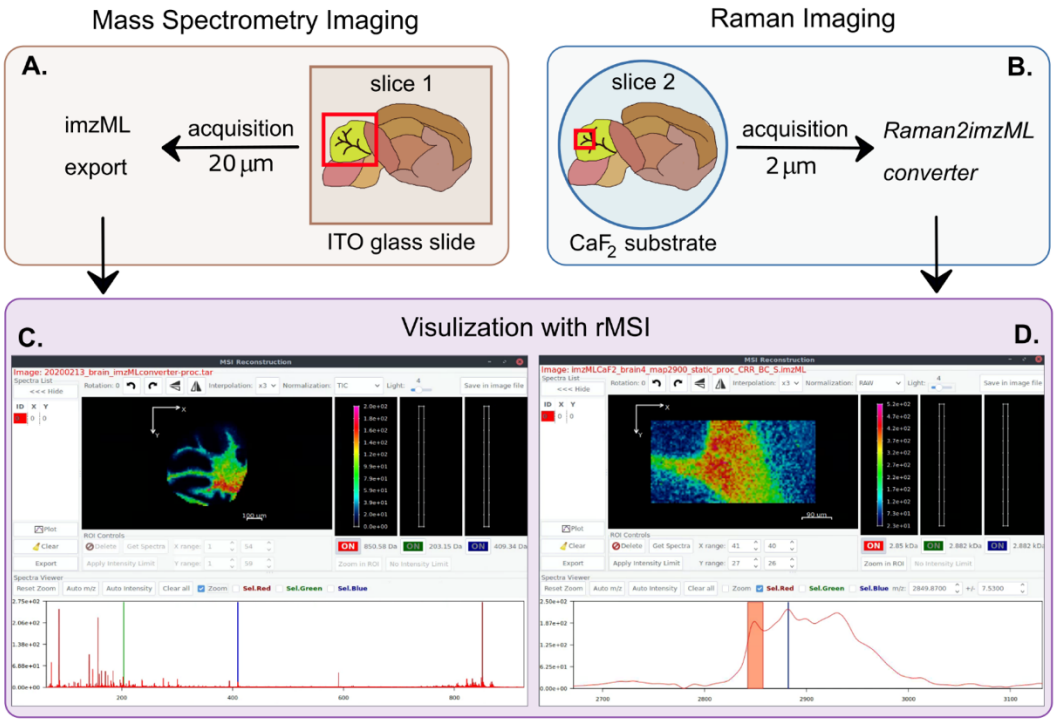

Figure 2. Imaging mouse brain sections: MSI (A) and Raman imaging (B) sample preparation steps and visualization within the same open-source software (rMSI) of each dataset (C and D); rMSI: R package for MSI data handling and visualization, Copyright© 2014 Pere Rafols Soler

For MSI (Figure 2 C), we showed the spatial distribution of ion *m/z* 850 (putatively annotated as a glycerophospholipid - phosphatidylcholine(38:3), experimental *m/z* 850.58 as $[M+K]^+$ adduct, mass error 9 ppm) (28) on the whole mouse cerebellum. For Raman (Figure 2 D) we chose to illustrate the band at 2850 cm^{-1} Raman shift, which is specific for lipids (29) on one specific nerve tract in the cerebellum. The possible merger of the two molecular images (Figure 2 C and D) is shown in Figure 3. The high spatial resolution

image from Raman clearly enhances the low-resolution image obtained with MSI. When co-registration strategies are used together with multimodal imaging techniques it can accurately coordinate the relationship between pixel position and information between the two images. This way Raman2imzML could also enable hyperspectral data analysis of Raman and MSI datasets within the same software.

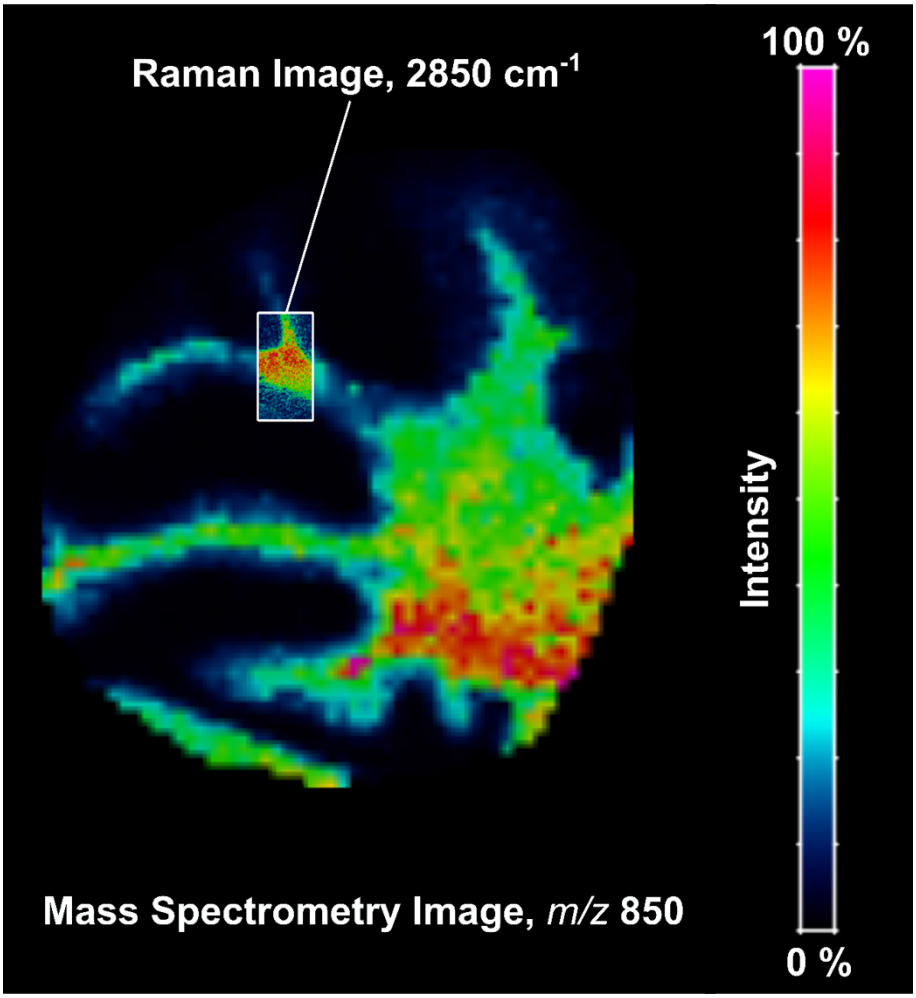

Figure 3. Merged molecular images collected from MSI (20 μm lateral resolution) and Raman (2 μm lateral resolution). Molecular images are the same as Figure 2.

4.1.5. Conclusion

The *Raman2imzML* converter was created so that the same software could be used to visualize different imaging datasets, and in particular to explore Raman images using MSI software tools. We demonstrated that the similarities between Raman imaging and MSI data structures favour the use of the same data visualization software. Therefore, we recommend that a comprehensive multimodal strategy be created to facilitate the combination of spectral imaging techniques such as Raman and MSI. We propose that imzML be used as a template for a standardized file format for Raman imaging and other spectral imaging techniques, and that specific Raman ontology be included in future imzML format iterations.

4.1.6. Availability and Requirements

Project name: Raman2imzML

Project home page: https://github.com/LlucSF/Raman2imzML

Operating system(s): Platform independent

Programming language: R and C++

Other requirements: R, Rtools, RStudio

License: GNU GPL-3.0

Any restrictions to use by non-academics: none

The datasets generated and/or analysed during the current study are available in the GitHub repository, https://github.com/LlucSF/Raman2imzML. The associated supplementary material contains the Raman2imzML R project that includes a markdown and a set of example measurements to test this package.

4.1.7. List of Abbreviations

MSI - mass spectrometry imaging

FTIR – Fourier Transformed-Infrared Spectroscopy

LDI-MSI - laser desorption/ionization mass spectrometry imaging

4.1.8. Declarations

Ethics approval and consent to participate

Animal handling was conformed to the Guide for the Care and Use of Laboratory Animals published by the U.S. National Institutes of Health (NIH publication no. 85-23, revised 1996). All procedures were approved by the University Rovira i Virgili Bioethics Committee, as stated in Law 5/21 July 1995 passed by the Generalitat de Catalunya (Autonomous Government of Catalonia). No animals were sacrificed specifically for this work. The tissues used were unused in previous experiments.

Authors' contributions

The manuscript was written through contributions of all authors. All authors have given approval to the final version of the manuscript.

SAI: Data curation, Investigation, Validation, Visualization, Writing - original draft

LS: Methodology, Software, Validation, Visualization, Writing - original draft

MG-A: Conceptualization, Supervision, Writing - review & editing

XC: Conceptualization, Funding acquisition, Writing - review & editing

PR: Conceptualization, Supervision, Software, Writing - review & editing

4.1.9. References

1. McDonnell LA., Heeren RMA. Imaging Mass Spectrometry. Mass Spectrom Rev. 2007;26:606–43.

2. Rafols P, Vilalta D, Brezmes J, Cañellas N, Del Castillo E, Yanes O, et al. Signal preprocessing, multivariate analysis and software tools for MA(LDI)-TOF mass spectrometry imaging for biological applications. Mass Spectrom Rev. 2018;37:281–306.

3. Buchberger AR, DeLaney K, Johnson J, Li L. Mass Spectrometry Imaging: A Review of Emerging Advancements and Future Insights. Anal Chem. 2018;90(1):240–65.

4. Van De Plas R, Yang J, Spraggins J, Caprioli RM. Image fusion of mass spectrometry and microscopy: A multimodality paradigm for molecular tissue mapping. Nat Methods. 2015;12(4):366–72.

5. Lenz B, Brink A, Siam M, De Paepe AD, Bassett S, Eichinger-Chapelon A, et al. Application of imaging techniques to cases of drug-induced crystal nephropathy in preclinical studies. Toxicol Sci. 2018;163(2):409–19.

6. Porta Siegel T, Hamm G, Bunch J, Cappell J, Fletcher JS, Schwamborn K. Mass Spectrometry Imaging and Integration with Other Imaging Modalities for Greater Molecular Understanding of Biological Tissues. Mol Imaging Biol. 2018;20(6):888–901.

7. Rabe JH, Sammour DA, Schulz S, Munteanu B, Ott M, Ochs K, et al. Fourier Transform Infrared Microscopy Enables Guidance of Automated Mass Spectrometry Imaging to Predefined Tissue Morphologies. Sci Rep. 2018;8(1):1–11.

8. Neumann EK, Comi TJ, Spegazzini N, Mitchell JW, Rubakhin SS, Gillette MU, et al. Multimodal Chemical Analysis of the Brain by High Mass Resolution Mass Spectrometry and Infrared Spectroscopic Imaging. Anal Chem. 2018;90(19):11572–80.

9. Bradshaw R, Wolstenholme R, Ferguson LS, Sammon C, Mader K, Claude E, et al. Spectroscopic imaging based approach for condom identification in condom contaminated fingermarks. Analyst. 2013;138(9):2546–57.

10. Ryabchykov O, Popp J, Bocklitz T. Fusion of MALDI spectrometric imaging and Raman spectroscopic data for the analysis of biological samples. Front Chem. 2018;6(JUL):1–10.

11. Bergholt MS, Serio A, McKenzie JS, Boyd A, Soares RF, Tillner J, et al. Correlated heterospectral lipidomics for biomolecular profiling of remyelination in multiple sclerosis. ACS Cent Sci. 2018;4(1):39–51.

12. Fagerer SR, Schmid T, Ibáñez AJ, Pabst M, Steinhoff R, Jefimovs K, et al. Analysis of single algal cells by combining mass spectrometry with Raman and fluorescence mapping. Analyst. 2013;138(22):6732–6.

13. Jadoul L, Malherbe C, Calligaris D, Longuespée R, Gilbert B, Eppe G, et al. Matrix-assisted laser desorption/ionization mass spectrometry and Raman spectroscopy: An interesting complementary approach for lipid detection in biological tissues. Eur J Lipid Sci Technol. 2014;116(8):1080–6.

14. Bocklitz TW, Crecelius AC, Matthäus C, Tarcea N, Von Eggeling F, Schmitt M, et al. Deeper understanding of biological tissue: Quantitative correlation of MALDI-TOF and Raman imaging. Anal Chem. 2013;85(22):10829–34.

15. Ahlf DR, Masyuko RN, Hummon AB, Bohn PW. Correlated mass spectrometry imaging and confocal Raman microscopy for studies of three-dimensional cell culture sections. Analyst. 2014;139(18):4578–85.

16. Bocklitz T, Bräutigam K, Urbanek A, Hoffmann F, von Eggeling F, Ernst G, et al. Novel workflow for combining Raman spectroscopy and MALDI-MSI for tissue based studies. Anal Bioanal Chem. 2015;407(26):7865–73.

17. Lasch P, Noda I. Two-Dimensional Correlation Spectroscopy for Multimodal Analysis of FT-IR, Raman, and MALDI-TOF MS Hyperspectral Images with Hamster Brain Tissue. Anal Chem. 2017;89(9):5008–16.

18. Race AM, Palmer AD, Dexter A, Steven RT, Styles IB, Bunch J. SpectralAnalysis: Software for the Masses. Anal Chem. 2016;88(19):9451–8.

19. Rubens U, Hoyoux R, Vanosmael L, Ouras M, Tasset M, Hamilton C, et al. Cytomine: Toward an Open and Collaborative Software Platform for Digital Pathology Bridged to Molecular Investigations. Proteomics - Clin Appl. 2019;13(1):1–4.

20. Foose DP, Sizemore IEP. Vespucci: A Free, Cross-Platform Tool for Spectroscopic Data Analysis and Imaging. J Open Res Softw. 2016;4.

21. Schramm T, Hester A, Klinkert I, Both JP, Heeren RMA, Brunelle A, et al. ImzML - A common data format for the flexible exchange and processing of mass spectrometry imaging data. J Proteomics. 2012;75(16):5106–10.

22. Rafols P, Torres S, Ramirez N, Del Castillo E, Yanes O, Brezmes J, et al. rMSI : an R package for MS imaging data handling and visualization. Bioinformatics. 2017;33(March):2427–8.

23. Ràfols P, Vilalta D, Torres S, Calavia R, Heijs B, McDonnell LA, et al. Assessing the potential of sputtered gold nanolayers in mass spectrometry imaging for metabolomics applications. PLoS One. 2018;13(12).

24. Klinkert I, Chughtai K, Ellis SR, Heeren RMA. Methods for full resolution data exploration and visualization for large 2D and 3D mass spectrometry imaging datasets. Int J Mass Spectrom. 2014;362(1):40–7.

25. Bemis KD, Harry A, Eberlin LS, Ferreira C, Van De Ven SM, Mallick P, et al. Cardinal: An R package for statistical analysis of mass spectrometry-based imaging experiments. Bioinformatics. 2015;31(14):2418–20.

26. Robichaud G, Garrard KP, Barry JA, Muddiman DC. MSiReader: An open-source interface to view and analyze high resolving power MS imaging files on matlab platform. J Am Soc Mass Spectrom. 2013;24(5):718–21.

27. Källback P, Nilsson A, Shariatgorji M, Andrén PE. MsIQuant - Quantitation Software for Mass Spectrometry Imaging Enabling Fast Access, Visualization, and Analysis of Large Data Sets. Anal Chem. 2016 May 3;88(8):4346–53.

28. Cerruti CD, Benabdellah F, Laprévote O, Touboul D, Brunelle A. MALDI imaging and structural analysis of rat brain lipid negative ions with 9-aminoacridine matrix. Anal Chem. 2012;84(5):2164–71.

29. Dybas J, Marzec KM, Pacia MZ, Kochan K, Czamara K, Chrabaszcz K, et al. Raman spectroscopy as a sensitive probe of soft tissue composition – Imaging of cross-sections of various organs vs. single spectra of tissue homogenates. TrAC - Trends Anal Chem. 2016;85:117–27.

4.1.10. Supporting Information Script

```
# script for converting Raman maps exported to text files into imzML


# for Renishaw
txt_path <- "C:/"
imzML_path <- "C:/"
Raman2imzML::WiRe_convert(txt_path = txt_path,
                          imzML_path = imzML_path)
# visualize image with rMSI
rMSI::OpenMSI()


# for WITec
info_txt_path <- "C:/"
table_txt_path <- "C:/"
spectrum_txt_path <- "C:/"
imzML_path <- "C:/"
Raman2imzML::FIVE_convert(info_txt_path = info_txt_path,
                          table_txt_path = table_txt_path,
                          spectrum_txt_path = spectrum_txt_path,
                          imzML_path = imzML_path)


# end of script
```

UNIVERSITAT ROVIRA I VIRGILI
GOLD-COATED BLACK SILICON NANOSTRUCTURED SURFACES FOR SERS AND SALDI-MS MULTIMODAL IMAGING OF BIOLOGICAL APPLICATIONS
Stefania-Alexandra Iakab

Chapter 4.2: SALDI-MS and SERS Multimodal Imaging: one nanostructured substrate to rule them both

UNIVERSITAT ROVIRA I VIRGILI
GOLD-COATED BLACK SILICON NANOSTRUCTURED SURFACES FOR SERS AND SALDI-MS MULTIMODAL IMAGING OF BIOLOGICAL APPLICATIONS
Stefania-Alexandra Iakab

State of the article:

In preparation

Contributing authors:

Stefania-Alexandra Iakab[1,2], Gerard Baquer[1], Marta Lafuente[3,4], Pilar Pina[3,4,5], Miriam Alvarado[1], José Luís Ramírez[1], Pere Ràfols[1,2], Xavier Correig[1,2,6], María García-Altares[1,2]

[1]Department of Electronic Engineering, Rovira i Virgili University, Tarragona, 43007, Spain

[2]Spanish Biomedical Research Centre in Diabetes and Associated Metabolic Disorders (CIBERDEM), Madrid, 28029, Spain

[3]Instituto de Nanociencia y Materiales de Aragón (INMA), CSIC-Universidad de Zaragoza, 50009 Zaragoza, Spain

[4]Department of Chemical & Environmental Engineering, University of Zaragoza, 50018 Zaragoza, Spain

[5]Networking Research Center on Bioengineering, Biomaterials and Nanomedicine, CIBER-BBN, 28029 Madrid, Spain

[6]Institut d'Investigació Sanitària Pere Virgili, Tarragona, Spain

UNIVERSITAT ROVIRA I VIRGILI
GOLD-COATED BLACK SILICON NANOSTRUCTURED SURFACES FOR SERS AND SALDI-MS MULTIMODAL IMAGING OF BIOLOGICAL APPLICATIONS
Stefania-Alexandra Iakab

4.2.1. Abstract

Imaging techniques based on mass spectrometry or spectroscopic methods inform in situ about the chemical composition of biological tissues or organisms, but they are sometimes limited by their specificity, sensitivity or spatial resolution. Multimodal imaging addresses these limitations by combining several imaging modalities, however, measuring the same sample with the same preparation using multiple imaging techniques is still uncommon due to the incompatibility between substrates, sample preparation protocols and data formats. We present a multimodal imaging approach that employs a gold-coated nanostructured silicon substrate to couple Surface Assisted Laser Desorption/Ionization Mass Spectrometry (SALDI-MS) and Surface Enhanced Raman Spectroscopy (SERS). Our approach integrates both imaging modalities by using the same substrate, sample preparation and data analysis software on the same sample, allowing the coregisteration of both images. We transferred molecules from clean fingertips and fingertips covered with plasticine modelling clay onto our nanostructured substrate and analyzed their chemical composition and distribution by SALDI-MS and SERS. Multimodal analysis located the traces of plasticine on fingermarks and provided chemical information on the composition of the clay. Our multimodal approach effectively combines the advantages of mass spectrometry and vibrational spectroscopy with the signal enhancing abilities of our nanostructured substrate.

Chapter 4.2

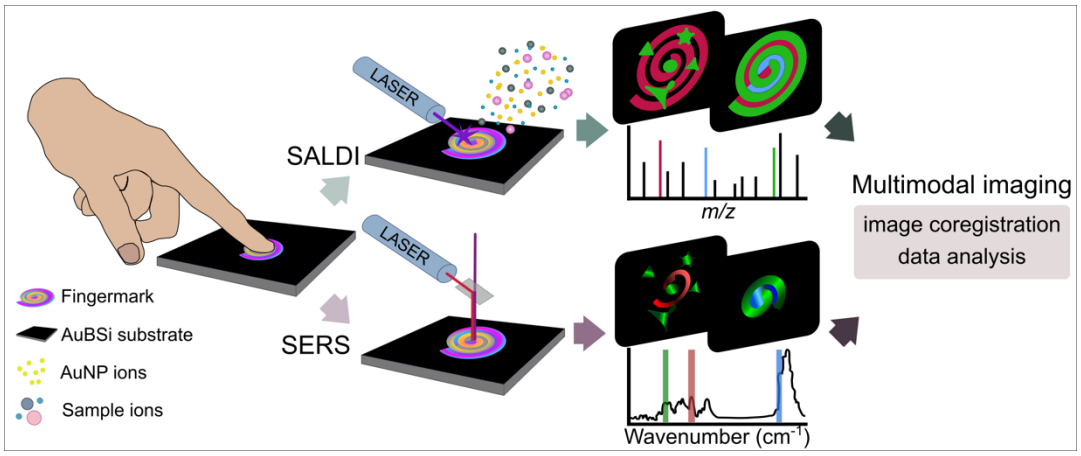

Keywords: multimodal imaging, nanostructure, image coregistration, SERS, SALDI-MSI

4.2.2. Introduction

Label-free imaging techniques are crucial for understanding biological mechanisms at a molecular level. They are used for investigating a wide range of issues such as plant-based renewable energy, microbiological essays, diseases (in clinical medicine) and even forensic specimens.[1–6] Vibrational spectroscopy and mass spectrometry imaging techniques are the most popular choices to specifically and simultaneously map a wide range of biomolecules present in living organisms or frozen tissues.[1]

Raman imaging is frequently used for exploring the chemical composition of biological samples.[7] It offers high spatial resolution maps (down to ~250 nm lateral resolution) with information about molecular structure (the secondary structure of proteins, the saturation level of lipids, etc.),[8] but with limited sensitivity and specificity. Surface enhanced Raman spectroscopy (SERS) boosts Raman sensitivity and specificity through electromagnetic enhancement - when the signal is amplified by the surface plasmon resonances in metallic nanoparticles - and chemical enhancement - when a charge transfer is established between analyte and metal surface.[9] Gold and silver nanoparticles are popular SERS substrates, as they are stable in air and can be used over a wide range of laser wavelengths (400 - 1000 nm for Ag and 600 - 1200 nm for Au).[10–13] SERS is frequently used for body fluid analyses, such as pathogen detection (*e.g.* bacteria from urine and blood)[12], but also for imaging applications such as tumor margin determination,[11] single cell analysis[13] and even for revealing chemical information from latent fingermarks.[10] However, sample preparation for SERS imaging using metallic nanoparticles is difficult to control.[14–16]

Matrix-assisted laser desorption/ionization mass spectrometry imaging (MALDI-MSI) is commonly used in proteomics and metabolomics studies[17]

as it offers rich, high quality spectra, with specific chemical information (such as molecular weight and isotopic pattern), and even tandem mass spectrometry information (MS2) that makes the identification of molecules possible.[18] However, MALDI has limitations: the ions from the organic matrices generate noise in the low mass range, the spatial resolution is lower compared to Raman imaging (often down to ~20 μm, due to the heterogeneous co-crystallization of matrix and analyte, and delocalization of analytes caused during sample preparation), and sometimes the mass analyzer is not sensitive enough. Surface enhanced laser desorption/ionization mass spectrometry imaging (SALDI-MSI) eliminates the limitations of the matrix and enables imaging at higher lateral resolutions with cleaner spectra.[19] SALDI-MS uses nanostructured surfaces often made of gold, silver and silicon[19,20] to promote the desorption and ion formation of small molecules with the help of laser energy and localized laser plume.[21] For instance, Au and Ag nanoparticles have been sputtered on top of tissue sections to examine several biomolecules: cholesterol and olefinic compounds,[22] triaglycerols[23] and different low molecular weight compounds.[24] As for solid-state substrates, nanostructured silicon surfaces have various applications for SALDI imaging: embedded with siloxane compounds they can characterize peptide microarrays, single cells, tissues, blood and urine,[25] and decorated with gold nanoparticles they can selectively detect metabolites from tissue surfaces.[26] However, the most popular mass spectrometers used for imaging are still limited to spatial resolutions >10 μm.

Molecular imaging data is described by two keywords: spectral information and lateral resolution. As a result, MALDI and Raman have been combined as a multimodal imaging approach to encompass the best of both worlds.[27] The main advantage of multimodal imaging is the complementarity of the two techniques: the high spatial resolution images from Raman and

the rich spectral information from MALDI. Multimodal data image coregistration merges the spatial and spectral information from the two source acquisitions into a single multimodal dataset. This enables a more accurate description of the sample by an improved interpretation of structure-composition relationships.[28] For example, correlation features between MSI, Raman and IR images allowed the characterization of lipids from hamster brains in terms of species identification (MSI) and located the areas of the brain that are protein-rich in α-helical and β-sheet secondary structures (Raman and IR).[28] Unfortunately, sample preparation, image acquisition and data processing workflows are challenging for multimodal imaging. The use of different substrates and sample preparation protocols as well as the impossibility to measure the same sample are still issues to be addressed (Table S1). For example, groups which used the same substrate (ITO glass slide) to perform Raman imaging and MALDI-MSI had to add an additional step while preparing the sample for MSI analysis: organic matrix deposition for MALDI[29,30] or an unconventional silicon-based nanoparticle system for SALDI.[31] Multimodal data processing also struggles with different file formats, and different data preprocessing (Table S1). For instance, MALDI spectra need to be aligned and binned while Raman spectra need to be cleaned from cosmic rays and have their baseline corrected.[24,32] These steps are often performed with software provided by instrument manufacturers or developed in-house. Nevertheless, there is no standardized workflow for either sample preparation or data processing in multimodal imaging.

We created a multimodal imaging approach to acquire molecular images by SERS and MSI from the same sample using the same nanostructured silicon substrate with a one-step sample preparation method. To demonstrate our approach, we stamped a clean fingertip and a fingertip

covered by residues of plasticine modelling clay onto our substrate. SERS and SALDI imaging analyses revealed *in-situ* the complex molecular information of fingermarks described not only by endogenous compounds (secreted by the eccrine and sebaceous glands), but also by exogenous (plasticine) molecules at a micron-scale resolution.

4.2.3. Results

4.2.3.1. Optimization using inks

AuBSi substrate

The gold-coated black silicon (AuBSi) nanostructured substrate used in this work was previously developed by our group for surface-assisted laser desorption/ionization mass spectrometry imaging applications.[26] Briefly, the substrate is a silicon wafer with a homogeneous nanostructured surface which consists of ~500 nm tall silicon nanopillars decorated with 10-20 nm gold nanoparticles, resembling a forest of nano asparagus (Figure 1). The roughness of the nanostructure is ideal for capturing a high number of molecules from liquid or solid samples due to the high surface area of the nanopillars (Figure S1A). The substrate's surface chemistry is stable over a long period of time (we tested after 17 months) ensuring its correct functionality after storage in normal conditions (room temperature and atmospheric pressure; Figure S1B). Lastly, the substrate absorbs >90% of light, including the wavelengths of the lasers used in this study: 355nm for SALDI and 514 nm, 633 nm and 785 nm for Raman (Figure S1C).

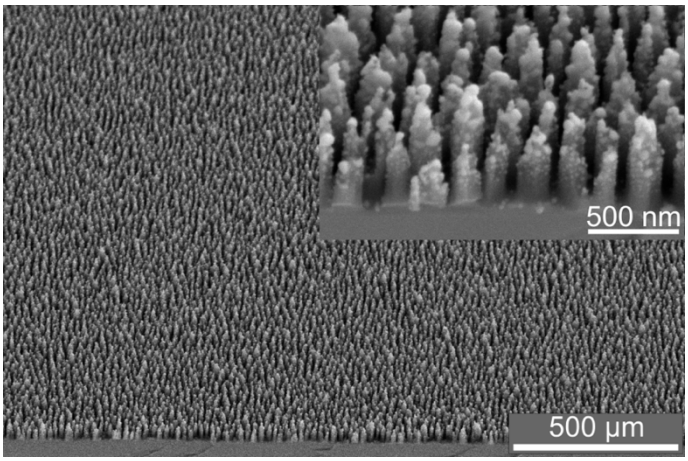

Figure 1. Electron images of the AuBSi nanostructure. Images (collected at 45 degrees) represent the nanostructure, the silicon nanopillars (in dark grey) and the gold nanoparticles (in bright grey or white) create a nano-asparagus architecture, better visualized in the inset.

AuBSi for SALDI MS imaging

First, we demonstrated the use of the AuBSi substrate in MSI. Aqueous solutions (1 mM) of rhodamine 6G (R6G) and malachite green (MG) were spotted with an inkjet printer on the substrate for testing the optimal LDI performance. Figure S3A. shows the average spectra of an area collected in negative mode with the most intense peak at *m/z* 96 putatively associated with a fragment of the molecules or background signal and the typical peaks of Au (*m/z* 196) and its clusters (*m/z* 393, 590, 787, 984). In this case, the signal from rhodamine 6G and malachite green cannot be detected, as they are cationic basic dyes that do not ionize in negative mode. Figure S3B shows the average spectra of the same area as in Figure S3A collected in positive ionization mode. The most intense peaks at *m/z* 443 and *m/z* 329 come from rhodamine 6G ($[M+H-2H_2O]^+$ adduct) and malachite green ($[M+H-2H_2O]^+$ adduct), respectively. No signal interference from the background or the Au nanoparticles was observed.

AuBSi for SERS imaging

The characteristics of the AuBSi substrate are also optimal for SERS measurements. First, we tested which laser works best with the AuBSi substrate by mapping the printed R6G and MG droplets with three different laser wavelengths: 514 nm, 633 nm and 785 nm. Single spectra from R6G and MG droplets collected with each laser, together with images representing the intensity distribution of the specific bands of R6G and MG are illustrated in Figure S4. The best quality spectra were collected with the 633 nm laser, with the highest intensity and the best definition between different bands (Figure S4A). We chose to represent R6G with the band 1513 cm^{-1} (characteristic for C-C stretching)[33] and MG with the band 1620 cm^{-1} (characteristic of benzene ring C-C stretching)[34] as they were the most intense bands characteristic to each standard. AuBSi with the 633 nm works best for detecting both R6G and MG due to: (1) effective adsorption of molecules to the surface, (2) high absorption of the laser energy by the substrate and (3) the presence of Au nanoparticles which lead to enhanced electromagnetic fields. The localized heating and enhanced electromagnetic field promote energy transfer from the nanostructure to the adjacent molecules, enhancing their vibration and implicitly the collected signal expected in SERS measurements.[27,35]

Then we characterized the surface homogeneity, a paramount property for imaging experiments. For this we mapped the AuBSi surface after R6G immersion. Figure 2 shows the mean spectra of map collected and the distributions of the most intense band of R6G. The bands at 1315 cm^{-1}, 1360 cm^{-1}, and 1513 cm^{-1} are associated with aromatic C-C stretching vibrations. The heatmap shows uniform distribution of band intensity at 1 μm lateral resolution, without any significant hot spots that might mislead qualitative or quantitative analyses. Therefore, the AuBSi substrates can be used for imaging fine morphological and chemical details. Next, we calculated the

analytical enhancement factor of the substrate as explained by Lafuente et al.[35] As controls, we measured the normal Raman spectrum for R6G by immersing a bare silicon (Si) and a black silicon (BSi) piece in an aqueous R6G solution (10^{-3} M) for 1h and, the SERS spectra by immersing the AuBSi piece in an aqueous R6G solution (10^{-5} M) for 1 h. To avoid measuring molecules not directly attached to the surface, each piece was rinsed by dipping in distilled water 3 times. Adapting the formula from Lafuente et al.[35] (explained in the supporting information file), we calculated the AuBSi substrate's analytical enhancement factor: $5.4 \cdot 10^5$ when comparing to Si and $2.3 \cdot 10^5$ when comparing to BSi. Figure S5 illustrates the enhancing ability of the AuBSi for malachite green as well ($7.5 \cdot 10^3$ when compared to Si and $2.3 \cdot 10^3$ when compared to BSi). We finally tested the linearity of the AuBSi substrate as SERS spectroscopy can also be used for quantitative studies.[14,33] In our case, the intensity of the band 1513 cm^{-1} was linearly correlated to the rhodamine 6G concentration between the ranges of 1 μM and 1 mM (Figure S6).

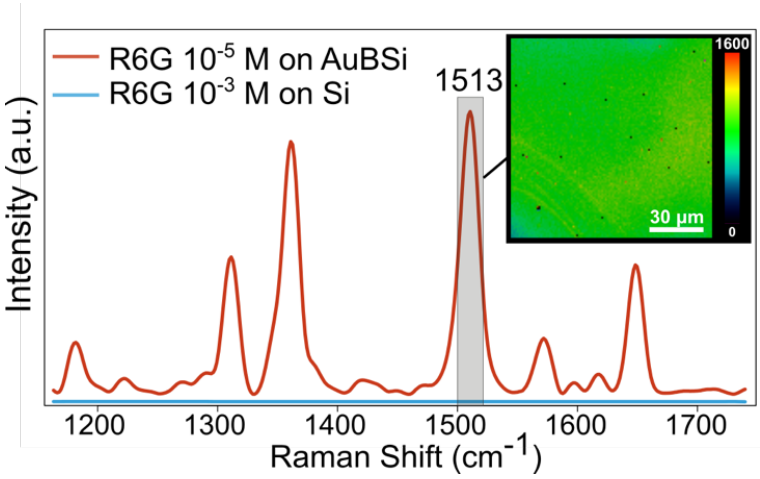

Figure 2. Characteristics of AuBSi substrate for SERS imaging measurements. Mean spectrum of 50x50 µm² area mapped on Si (in blue) and AuBSi (in red) substrate immersed in 10^{-5} M and 10^{-3} M Rhodamine 6G solution, respectively; the spatial distribution of the 1510 cm^{-1} band of R6G is represented in the inset (arbitrary intensity units, 0 to 1600). Black pixels are zapped spectra during pre-processing.

AuBSi for Multimodal Imaging

To perform SALDI and SERS imaging on the same sample we first determined the optimal acquisition order. We acquired maps of AuBSi immersed in R6G solution first by SALDI and then by SERS and *vice versa*. The maps from Figure S7 show that the lasers did not damage the sample or substrate, as the SALDI laser ablation spots could not be distinguished, regardless of the order of acquisition. The SALDI spectra were not negatively affected by SERS measurement, but the SERS spectra intensity decreased after SALDI measurement (this was expected, as MS techniques are destructive). This behavior was maintained even when the SERS map was acquired at 20 times higher resolution (Figure S8). Even though we could not detect any serious sample deterioration from the molecular maps, or substrate damage through optical images (Figure S9), we consider that it is

best to measure with SERS first and with SALDI last to retain the best signal intensity.

For comparing the lateral resolution capabilities of SERS and SALDI, R6G and MG microliter droplets were spotted with an inkjet printer in the shape of two overlapping squares (represented in Figure S2). The intensity maps of the characteristic peaks and bands are illustrated in Figure 3. For the SALDI-MS image, the best lateral resolution we could achieve was 20 µm (apparatus limitation), while for the SERS image we acquired at 1 µm lateral resolution. Figure 3 B and E show the region where the R6G and MG droplets are overlapping, displaying the poorer lateral resolution capabilities of SALDI-MSI.

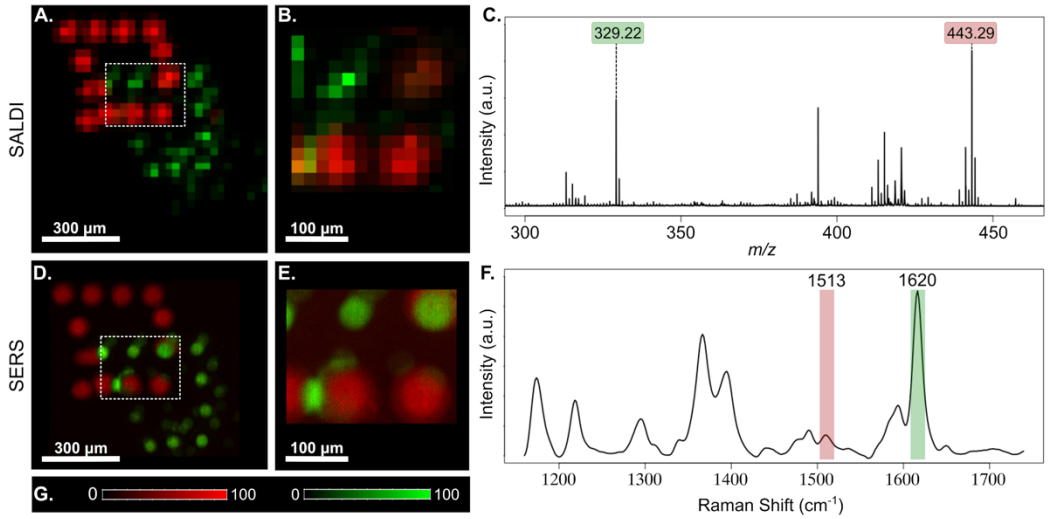

Figure 3. SALDI and SERS images and their average spectra of rhodamine 6G and malachite green. 30 µm resolution (A) and 20 µm resolution (B) ion maps: *m/z* 329.22 in green and *m/z* 443.29 in red detected as $[M+H-2H_2O]^+$ adducts; (B) is the zoomed area marked with dashed line in (A); average mass spectrum of (B) highlighting the represented ions (C); 5 µm resolution (D) and 1 µm resolution (E) SERS maps: 1513 cm^{-1} band in red is C-C stretching vibration of rhodamine 6G and 1620 cm^{-1} band in green is

benzene ring C-C stretching vibration of malachite green; (E) is the "magnified" area marked with dashed lines in (D); average SERS spectrum of (E) highlighting the represented bands (F); intensity scales for the red and green channels (G).

Image coregistration strategy

Coregistration allows us to integrate data from multiple imaging modalities by aligning them in space.[36] The simple and distinct morphologies of the ink droplets allowed us to optimize and validate our coregistration script (illustrated in Figure S10). In spite of the two images having very different lateral resolutions, they could be coregistered correctly. Once the images are coregistered, pixels between the two techniques are linked, allowing the retrieval of SERS and SALDI-MS spectra for the same location. To further explore the potential of these coregistered images we propose two multimodal data analysis strategies based on performing *k*-means spatial clustering on one technique and transforming the resulting clusters to the pixels in the other technique.

Figure S11 shows the first strategy, where the spatial clustering on the SERS image is transformed to the SALDI pixels. This allows us to directly compare the average SERS and SALDI spectra for each region - background (cluster 1), rhodamine 6G (cluster 2) and malachite green (cluster 3). Distinct *m/z* features 443.29 for rhodamine 6G and 329.22 for malachite green were more prominent in their respective transformed clusters. Additionally, if we compare the SERS-to-SALDI transformed clustering to the one directly obtained on the SALDI dataset (shown in Figure S11) we can appreciate that the latter does not yield a malachite green cluster. We hypothesize that the variability introduced by the malachite green *m/z* features is insufficient to be represented in a separate cluster. This is a clear example where the

spectral information from one technique can complement the analysis of the other technique: the clusters defined by SERS could be used on the SALDI image to retrieve the specific *m/z* of the Raman reporters

Figure S12 shows the second strategy, where the spatial clustering on the SALDI image is transformed to the SERS pixels. The clustering on SALDI does not differentiate between the Raman reporter droplets and transforming it to the SERS pixels does not add new insights. Therefore, the rest of the analyses in this study follow the first strategy SERS-to-SALDI.

4.2.3.2. Multimodal imaging detects residues from fingermarks

We developed a multimodal imaging approach with the help of the AuBSi substrate to analyse the molecules transferred onto the substrate surface. We tested our approach by analysing endogenous and exogenous molecules from fingermarks. The workflow consists of five steps: (1) molecule transfer (*i.e.* stamping the fingermark); (2) image acquisitions (first SERS then SALDI); (3) separate data pre-processing; (4) image coregistration; and (5) data analysis.

SERS images were collected at high resolution (5 and 7 μm) to study the morphological details of a clean fingermark and a fingermark stamped after rubbing the finger with plasticine modelling clay (clean FM and stained FM respectively). Although Raman maps are generally acquired at ~1 μm resolution, we chose to collect maps at 5 and 7 μm for three reasons: (1) the spatial resolution is enough to reflect the morphology of fingermarks, as the sweat and eccrine glands pore size can be distinguished at this resolution;[37] (2) SERS and SALDI image coregistration is favored when the spatial resolution discrepancy is not too high;[29] and (3) these parameters ensure reduced acquisition time (although at this resolution it is long: ~7.5 and ~12 hours). Figure 4 illustrates the distribution of skin-related compounds

(represented by the bands at 1588 cm^{-1} in blue for the valley and 1644 cm^{-1} in red for the ridge) and of plasticine molecules (tentatively associated with the 1550 cm^{-1} band in green for the stain). The morphology of the fingermark can be easily distinguished as the 1588 cm^{-1} band (tentatively associated with amino acids - Tyr, Phe, Trp - due to the aromatic ring breathing)[38] is representative of the valley and the 1644 cm^{-1} band (associated with proteins due to the amide I vibrations)[39,40] is representative of the ridge. The average spectrum of the clean (in grey) and stained (in black) fingerprint maps show the typical bands and shoulder bands of biomolecules found in the fingermark composition, while the reference spectrum collected from plasticine (Figure S13) shows different bands specific to the molecules composing the plasticine modelling clay. All putatively identified bands and shoulder bands are listed in Table S2.

SALDI-MS images were collected from the fingerprint residue transferred onto the AuBSi surface using low resolution (50 and 100 μm). We detected a wide range of *m/z* signals possibly associated with molecules originating from the sebaceous and eccrine glands, but also from contaminants such as dust, cosmetics, food residue, plastics, and their metabolites.[41] Figure S14 illustrates the average spectrum (full range) of the clean and stained fingermark maps together with the reference spectrum collected from the plasticine. We detected several morphologically relevant *m/z* features: exogenous from the plasticine and endogenous from the finger sweat (*e.g.* lipids, proteins, amino acids, fatty acids, wax esters, *etc.* of eccrine and sebaceous origin).[40]

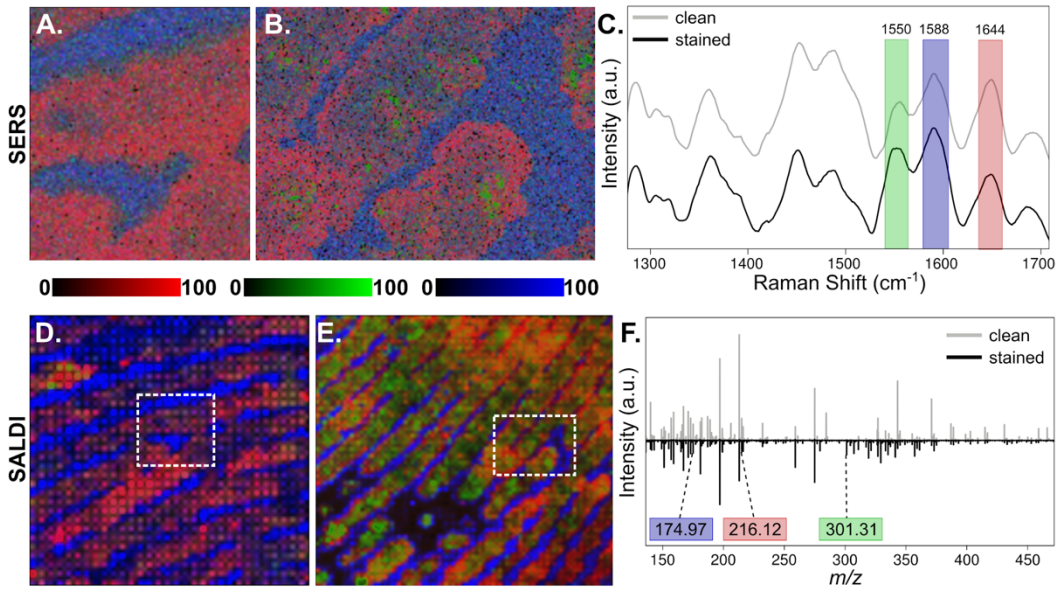

Figure 4. SALDI and SERS measurements of clean and stained fingermarks. 5 µm resolution (A) and 7 µm resolution (B) RGB channel band maps for clean and stained fingermarks, respectively: bands 1644 cm^{-1} in red (ridge), 1588 cm^{-1} in green (stain) and 1550 cm^{-1} in blue (valley) are represented in the average SERS spectra in (C); 50 µm resolution RGB channel ion maps for clean (D) and stained (E) fingermarks: ions *m/z* 216.12 in red (ridge), *m/z* 301.31 in green (stain) and *m/z* 174.97 in blue (valley) are highlighted in the average mass spectra from (F); dashed squares mark the SERS area measurement.

Multimodal approach

Associating and identifying the SERS bands of the staining molecules present in the fingermark from the mean spectra is difficult. For this reason, we coregistered the SERS and SALDI images using the SERS-to-SALDI strategy. Then, we generated clusters on the SERS image by *k*-means clustering, which we transferred to the SALDI image data, as illustrated in Figure 5. The average spectra of each cluster from the SERS image reveal

bands that were not distinguished in the mean spectrum of the whole image (Figure 4C). Specifically, cluster 1 seems to represent the staining molecules from the fingermark, as its pattern is very distinct from the fingermark composition from the other two clusters or the average spectrum of the image (Figure 4C). The transformed SALDI cluster 1 also shows prominent *m/z* features not present in other clusters, marked with a star in Figure 5E. The spatial distribution of these ions (as reflected in the ion images from Figure S15) coincide with the position of SALDI cluster 1 in Figure 5C.

According to the label that the manufacturer includes in the package of the plasticine modelling clay, the material is composed by: wax, starch, white oil and pigments. Several ions specifically concentrated in cluster 1 were putatively identified as long-chain aliphatic hydrocarbons and long chain fatty acids (e.g. *m/z* 279.33, $[M+H-H_2O]^+$, $C_{20}H_{42}O_2$; *m/z* 301.3162, $[M+H-2H_2O]^+$, $C_{22}H_{40}O_2$; *m/z* 307.35, $[M+H-2H_2O]^+$, $C_{21}H_{42}O_3$). On the other hand, the SERS average spectra of cluster 1 has its maximum band at 1540 cm^{-1}, common in Cu-Phthalocyanine dyes like Pigment Green 7 (PG7)[42] due to the stretching of the C-N bonds in the macrocycle. To corroborate these findings, we analyzed by SALDI and SERS three samples of plasticine of three different colors: white, yellow, and green (the latter was the same plasticine used in the fingermarks experiments). We found that all plasticine samples contained the ions between *m/z* 279 and *m/z* 327 that we putatively identified as hydrocarbons, thus these ions are most likely associated with the wax and white oil. However, the band at 1540 cm^{-1} in the SERS spectra was only present in the green plasticine but not in the white or yellow samples, therefore this band is definitively linked to the green pigment.

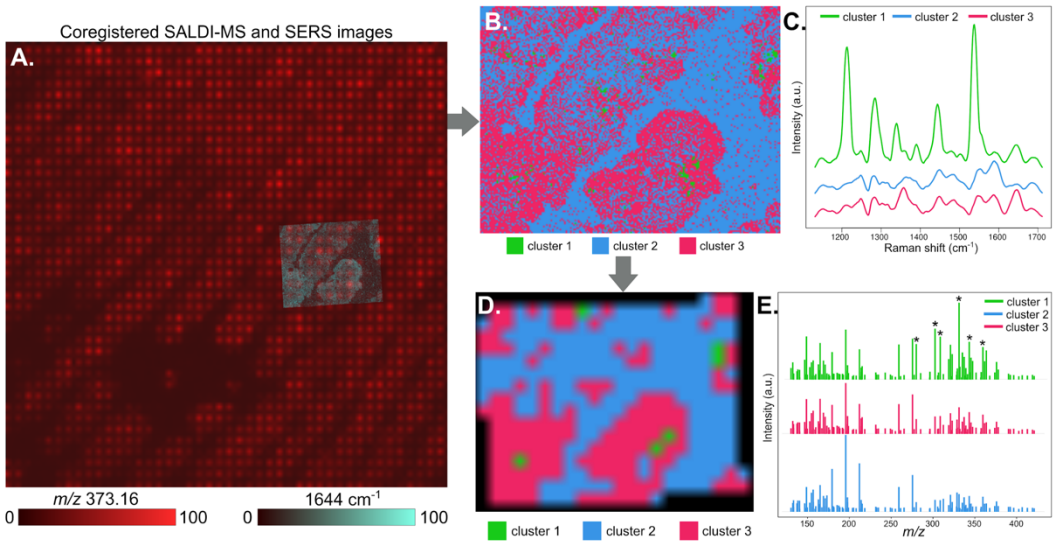

Figure 5. Multimodal analysis strategy. Coregistered SALDI-MS and SERS images (A); SERS *k*-means cluster map (B) and the associated average spectra (C); SERS clusters transformed to the SALDI-MS pixels (D) and the average mass spectra of each transformed cluster (E). SALDI-MS image area 4 x 5 mm² was acquired at 50 µm resolution and SERS image area 1.1 x 0.7 mm² at 7 µm resolution.

4.2.4. Discussion

Our multimodal imaging approach uses an AuBSi substrate to combine SALDI-MS and SERS imaging with simple sample preparation suitable for both techniques. The AuBSi substrate is ideal for a cost-effective and user-friendly substrate for molecule detection using laser-based imaging techniques. Moreover, the gold nanoparticles decorating the substrate are ideal enhancing agents for both SALDI and SERS, as they ensure background-free and enhanced signals, and promote measurements with the highest lateral resolution. AuBSi performed best in positive mode in SALDI measurements (due to the nature of the Raman reporters) and worked best with the 633 nm laser with SERS (due to the resonance of the Au

nanoparticles). The effectiveness of the substrate for SERS imaging was evidenced by its analytical enhancement factor (in the order of 10^5); its ability to detect molecules from solutions or from solid samples; and its homogeneous surface which allows mapping at micron-scale resolution. Using two fundamentally different analytical techniques to measure the same sample, on the same substrate with the same sample preparation, promotes synergistic analysis: the limitations of one technique can be addressed by the advantages of the other and *vice versa*. We combined SALDI MSI and SERS to achieve three main goals:

- *Easy sample preparation*. Sample preparation for multimodal imaging using AuBSi substrate is straightforward because it only consists in depositing the analytes onto the substrate. After this, measurements can be done either in atmospheric conditions or in vacuum, depending on the technique. Printing Raman reporter inks, immersion in Raman reporter solutions or even touching the finger to the surface of the substrate are convenient sample preparation protocols that can be reproduced easily. It is important to note that the AuBSi substrate also supports non-imaging applications.

- *Improved lateral resolution*. SERS maps can provide high resolution images which can be spatially analyzed with multivariate tools such as *k*-means clustering, to define regions of interest in otherwise overlooked areas in MSI studies. Fingermark morphology can be easily distinguished by both SALDI and SERS univariate analyses, but the presence of staining molecules cannot be confidently represented without image coregistration and multimodal data analysis. For example, the plasticine contaminants were considerably lower in size than the SALDI pixel (<20% of their area). Because of the coregistration of the two modalities, we were able to label as stained,

SALDI pixels that overlapped with at least 15% of stained SERS pixels. Coregistration with SERS allowed us to overcome the intrinsic resolution limitation of SALDI and detect contaminants smaller than its pixel size.

- *Complementary molecular information*. SERS and SALDI are orthogonal techniques which provide complementary molecular information. SERS informs on the types of molecular bonds, their vibrations and secondary structure, while SALDI gives precise information about the mass-to-charge ratio of monomers, isotopes, adducts and fragments. In targeted studies - such as the experiment from Figure 3 - identifying molecules is straightforward in both SALDI and SERS, but for untargeted studies identifying biomolecules with a single technique is challenging. In these cases, having complementary molecular information is very valuable. The SERS bands detected describe the general fingermark composition at high resolution (tentative assignments in Table S2) and the SALDI peaks putatively identified confirm these assignments. The staining molecules on the fingermark were detected by *k*-means clustering on the two spatially correlated datasets. Specifically, the multimodal approach linked SERS and SALDI pixels and their respective spectral data, which enabled identifying features such as the bands 1215 cm^{-1} and 1540 cm^{-1} and ions *m/z* 301.31 and *m/z* 307.35 associated with the staining molecules from the plasticine.

Still, not all challenges of the two modalities can be overcome by multimodal imaging. For example, our substrate enhances the Raman signal of the molecules in the close vicinity to the AuNP, so SERS imaging of thicker samples, such as tissues - which have far greater amounts of molecules residing outside the enhancing electromagnetic field - is troublesome. In

SALDI a similar challenge appeared: the laser could not interact with the AuNP due to the thickness of the tissue sample, which resulted in poor ionization yield. Our solution for SALDI-MSI was to remove the excess material by washing,[26] which concentrated the analysis exclusively on the molecules adhered to the surface of the nanostructure. This approach was successful for investigating fingermarks but similarly prepared samples, such as imprinted molecules from plants or even liquid samples can be analyzed.

Our AuBSi substrate works as a sample support which enhances the Raman signal in SERS imaging and promotes the ionization of molecules in SALDI-MSI, independently of the method. The possibility to measure from the same sample and to coregister the acquired images allow high confidence identification of molecules based on multivariate data analysis.

4.2.5. Conclusion

Our multimodal imaging approach uses the same substrate, the same sample, the same sample preparation method and the same data analysis procedures. We mapped the molecular composition of fingermark residues at high lateral resolution using SERS and detected endogenous and exogenous compounds using SALDI. This approach can be translated into fields such as clinical, environmental, forensics, and pharmaceutical research, where Raman spectroscopy is an established technique.

4.2.6. Materials and Methods

Multimodal imaging substrate

Pristine n-type silicon wafers from MicroChemicals GmbH (Ulm, Germany) were used in a reactive ion etching chamber to obtain the black silicon. High purity grade gold target was obtained from Kurt J. Lesker Company (Hastings, England) and used in a magnetron sputtering chamber

to deposit gold on the black silicon and obtain the final substrate labelled AuBSi. A more detailed fabrication process is described in our previous work.[26] Morphological characterization of the substrate was done with a field emission scanning electron microscope (FESEM) equipped with a focused ion beam (FIB) from ThermoScientific, model Scios2; reflectance measurements were carried out with a Lambda-950 spectrophotometer, equipped with deuterium and tungsten lamps; the surface roughness was characterized by atomic force microscope; and the hydrophobic behavior of the substrate was determined by measuring the contact angle of milli-Q water droplets using a tensiometer together with Oneattension software (Biolin Scientific).

Sample preparation

The same sample preparation was used for both SALDI MSI and SERS imaging acquisitions. For drawing the pattern using inks, 2 mg of rhodamine 6G (R6G) and malachite green (MG) (Sigma-Aldrich) were diluted in two separate 10 ml butanol:terpineol (1:1) solutions. These solutions were sonicated for 15 minutes and were printed on the AuBSi substrate using a Dimatix DMP-2850 materials printer equipped with a DMC-11610 cartridge (Fujifilm Dimatix Inc., Santa Clara, CA, USA). 13 layers of two partially overlapping squares (one square printed with R6G solution and the other with MG solution) were drawn to assess the specificity and lateral resolution capabilities of each imaging technique. For substrate evaluation, the AuBSi substrate was immersed in different concentrations of R6G and MG in ethanol (from 1 μM to 1 mM). In case of fingermark imaging, the clean and stained fingermarks were obtained from a volunteer working in the laboratory. The clean fingermark was obtained after rubbing the finger with a disinfectant alcoholic hydrogel and the stained fingermark (from the same finger) was obtained after playing with modelling clay (or plasticine) model

Art. 70 JOVI in green color. Molecules from the same finger (first clean then stained) were transferred onto the nanostructured substrate by lightly pressing the finger on the surface of the AuBSi substrate for 10 seconds. The stained finger's surface was inspected for cleanliness prior to imprinting to avoid transferring plasticine residue.

Image acquisitions

MSI data was acquired using a MALDI TOF/TOF UltrafleXtreme instrument with SmartBeam II Nd:YAG/355 nm laser from Bruker Daltonics. Acquisitions were carried out in the 50-1200 Da range in reflectron mode, positive and negative ionization modes using the large laser spot size settings, operated at 2 kHz, and collecting a total of 1000 shots per pixel.

SERS/Raman measurements were performed on a Renishaw inVia™ confocal Raman microscope. All maps were recorded at room temperature with 514 nm, 633 nm and 785 nm excitation wavelengths using the 1200 l/mm grating for the 633 nm and 785 nm lasers and the 2400 l/mm grating for the 514 nm laser, optical lens 50x with NA 0.75, and 1 s integration time, unless otherwise indicated.

Data pre-processing and visualization

The raw SERS images were pre-processed using WiRE 5 software (from Renishaw) following basic chemometric algorithms: baseline correction (polynomial fitting), cosmic ray removal (software's built-in algorithms Nearest Neighbor and Width of Features) and smoothing (Savitzky-Golay). Saturated spectra were zapped during pre-processing. Spectral axis alignment was done before each map acquisition by adjusting the silicon peak to 520.5 cm^{-1} Raman shift. The pre-processed datasets were exported into .txt files and converted into the imzML format using the open-source

Raman2imzML R package.[43] The converter package uses the spectral and spatial information to create an imzML file, the standard imaging file format used in the mass spectrometry community. This step is necessary to visualize both Raman and MS images with the same software.

The raw SALDI MSI data was exported into imzML files and processed using rMSIproc,[44] an open source software specifically designed to efficiently handle large MSI data sets. Spectral smoothing was done using Savitzky-Golay, mass calibration was based on the linear or loess mass error fitting model using the Au cluster peaks as internal references, and the peak matrix was created after peak picking and binning. All processing parameters were the default rMSIproc settings, unless otherwise mentioned.

Image coregistration protocol

Image coregistration was performed using a set of R and MATLAB in-house scripts available under the General Public Licence v3.0 at https://github.com/gbaquer/rMSIcoregistration. A single image (corresponding to a band in SERS or an ion in SALDI) was manually selected for each dataset to represent distinct morphology. The R package RNiftyReg available at CRAN[45] was used to automatically register these representative images in the ink datasets used during optimization. The highly complex morphologies presented by the fingermark datasets required manual registration using “teaching points". MATLAB functions “cpselect” (selection of point pairs) and “fitgeotrans” (generation of transformation matrix) were used for this purpose as, unlike any available R counterpart, they provide a user-friendly GUI. The “affine” transformation type was used in both cases. Regardless of the registration type (automatic or manual) RNiftyReg was used to transform all datasets (SERS into SALDI and *vice versa*). The result is an R vector linking each pixel in the SERS dataset to its closest counterpart

in the SALDI dataset and *vice versa*. This result is fully compatible with the rMSI dataset class (rMSIprocPeakMatrix)[44] and it enables downstream multimodal analysis (such as transforming *k*-means clustering from one technique to the other). A diagram of the complete coregistration protocol is shown in Figure S10.

4.2.7. Acknowledgements

The authors acknowledge the financial support of the Spanish Ministry of Economy and Competitivity (MINECO) for S. A. Iakab's pre-doctoral grant BES-2016-076483, the Spanish Ministry of Science, Innovation and Universities (MICIN) for project RTI2018-096061-B-I00, and the Agency for the Management of University and Research Grants of the Generalitat de Catalunya (AGAUR) for the 2017-SGR-1119 grant and for M. García-Altares' post-doctoral grant 2018-BP-00188. GB acknowledges the financial support of the European Union's Horizon 2020 research and innovation programme under the Marie Skłodowska-Curie grant agreement No. 713679 and the Universitat Rovira i Virgili (URV). SAI acknowledges the help of Xavier Blanch and Miriam Alvarez for the work with the InkJet printer.

4.2.8. References

(1) Prentice, B. M.; Caprioli, R. M.; Vuiblet, V. Label-Free Molecular Imaging of the Kidney. *Kidney International* **2017**, *92* (3), 580–598. https://doi.org/10.1016/j.kint.2017.03.052.

(2) Li, Z.; Chu, L. Q.; Sweedler, J. v.; Bohn, P. W. Spatial Correlation of Confocal Raman Scattering and Secondary Ion Mass Spectrometric Molecular Images of Lignocellulosic Materials. *Analytical Chemistry* **2010**, *82* (7), 2608–2611. https://doi.org/10.1021/ac100026r.

(3) Lanni, E. J.; Masyuko, R. N.; Driscoll, C. M.; Dunham, S. J. B.; Shrout, J. D.; Bohn, P. W.; Sweedler, J. v. Correlated Imaging with C 60 -SIMS and Confocal Raman Microscopy: Visualization of Cell-Scale Molecular Distributions in Bacterial Biofilms. *Analytical Chemistry* **2014**, *86* (21), 10885–10891. https://doi.org/10.1021/ac5030914.

(4) Kanodarwala, F. K.; Moret, S.; Spindler, X.; Lennard, C.; Roux, C. Nanoparticles Used for Fingermark Detection—A Comprehensive Review. *Wiley Interdisciplinary Reviews: Forensic Science* **2019**, *1* (5), 1–41. https://doi.org/10.1002/wfs2.1341.

(5) Rabe, J. H.; Sammour, D. A.; Schulz, S.; Munteanu, B.; Ott, M.; Ochs, K.; Hohenberger, P.; Marx, A.; Platten, M.; Opitz, C. A.; Ory, D. S.; Hopf, C. Fourier Transform Infrared Microscopy Enables Guidance of Automated Mass Spectrometry Imaging to Predefined Tissue Morphologies. *Scientific Reports* **2018**, *8* (1), 1–11. https://doi.org/10.1038/s41598-017-18477-6.

(6) Bergholt, M. S.; Serio, A.; McKenzie, J. S.; Boyd, A.; Soares, R. F.; Tillner, J.; Chiappini, C.; Wu, V.; Dannhorn, A.; Takats, Z.; Williams, A.; Stevens, M. M. Correlated Heterospectral Lipidomics for Biomolecular Profiling of Remyelination in Multiple Sclerosis. *ACS Central Science* **2018**, *4* (1), 39–51. https://doi.org/10.1021/acscentsci.7b00367.

(7) Pahlow, S.; Weber, K.; Popp, J.; Wood, B. R.; Kochan, K.; Rüther, A.; Perez-Guaita, D.; Heraud, P.; Stone, N.; Dudgeon, A.; Gardner, B.; Reddy, R.; Mayerich, D.; Bhargava, R. Application of Vibrational Spectroscopy and Imaging to Point-of-Care Medicine: A Review. *Applied Spectroscopy* **2018**, *72* (1_suppl), 52–84. https://doi.org/10.1177/0003702818791939.

(8) Jadoul, L.; Malherbe, C.; Calligaris, D.; Longuespée, R.; Gilbert, B.; Eppe, G.; de Pauw, E. Matrix-Assisted Laser Desorption/Ionization Mass Spectrometry and Raman Spectroscopy: An Interesting Complementary

Approach for Lipid Detection in Biological Tissues. *European Journal of Lipid Science and Technology* **2014**, *116* (8), 1080–1086. https://doi.org/10.1002/ejlt.201300198.

(9) Sharma, B.; Frontiera, R. R.; Henry, A. I.; Ringe, E.; van Duyne, R. P. SERS: Materials, Applications, and the Future. *Materials Today* **2012**, *15* (1–2), 16–25. https://doi.org/10.1016/S1369-7021(12)70017-2.

(10) Kolhatkar, G.; Parisien, C.; Ruediger, A.; Muehlethaler, C. Latent Fingermark Imaging by Single-Metal Deposition of Gold Nanoparticles and Surface Enhanced Raman Spectroscopy. *Frontiers in Chemistry* **2019**, *7* (JUN), 1–8. https://doi.org/10.3389/fchem.2019.00440.

(11) Kircher, M. F.; de La Zerda, A.; Jokerst, J. v.; Zavaleta, C. L.; Kempen, P. J.; Mittra, E.; Pitter, K.; Huang, R.; Campos, C.; Habte, F.; Sinclair, R.; Brennan, C. W.; Mellinghoff, I. K.; Holland, E. C.; Gambhir, S. S. A Brain Tumor Molecular Imaging Strategy Using a New Triple-Modality MRI-Photoacoustic-Raman Nanoparticle. *Nature Medicine* **2012**, *18* (5), 829–834. https://doi.org/10.1038/nm.2721.

(12) Premasiri, W. R.; Sauer-Budge, A. F.; Lee, J. C.; Klapperich, C. M.; Ziegler, L. D. Rapid Bacterial Diagnostics via Surface Enhanced Raman Microscopy. *Spectroscopy (Springfield, Or.)* **2012**, *27* (6), s8-31.

(13) Yang, J.; Wang, Z.; Zong, S.; Song, C.; Zhang, R.; Cui, Y. Distinguishing Breast Cancer Cells Using Surface-Enhanced Raman Scattering. *Analytical and Bioanalytical Chemistry* **2012**, *402* (3), 1093–1100. https://doi.org/10.1007/s00216-011-5577-z.

(14) Chisanga, M.; Muhamadali, H.; Ellis, D.; Goodacre, R. Enhancing Disease Diagnosis: Biomedical Applications of Surface-Enhanced Raman

Scattering. *Applied Sciences* **2019**, *9* (6), 1163. https://doi.org/10.3390/app9061163.

(15) Davis, R.; Campbell, J.; Burkitt, S.; Qiu, Z.; Kang, S.; Mehraein, M.; Miyasato, D.; Salinas, H.; Liu, J.; Zavaleta, C. A Raman Imaging Approach Using CD47 Antibody-Labeled SERS Nanoparticles for Identifying Breast Cancer and Its Potential to Guide Surgical Resection. *Nanomaterials* **2018**, *8* (11), 953. https://doi.org/10.3390/nano8110953.

(16) Verdin, A.; Malherbe, C.; Müller, W. H.; Bertrand, V.; Eppe, G. Multiplex Micro-SERS Imaging of Cancer-Related Markers in Cells and Tissues Using Poly(Allylamine)-Coated Au@Ag Nanoprobes. *Analytical and Bioanalytical Chemistry* **2020**, *412* (28), 7739–7755. https://doi.org/10.1007/s00216-020-02927-8.

(17) McDonnell, L. A.; Heeren, R. M. A. IMAGING MASS SPECTROMETRY. *Mass Spectrometry Reviews* **2007**, *26*, 606–643. https://doi.org/10.1002/mas.20124.

(18) Ahlf, D. R.; Masyuko, R. N.; Hummon, A. B.; Bohn, P. W. Correlated Mass Spectrometry Imaging and Confocal Raman Microscopy for Studies of Three-Dimensional Cell Culture Sections. *Analyst* **2014**, *139* (18), 4578–4585. https://doi.org/10.1039/c4an00826j.

(19) Silina, Y. E.; Volmer, D. A. Nanostructured Solid Substrates for Efficient Laser Desorption/Ionization Mass Spectrometry (LDI-MS) of Low Molecular Weight Compounds. *Analyst* **2013**, *138* (23), 7053–7065. https://doi.org/10.1039/c3an01120h.

(20) Iakab, S. A.; Rafols, P.; García-Altares, M.; Yanes, O.; Correig, X. Silicon-Based Laser Desorption Ionization Mass Spectrometry for the Analysis of Biomolecules: A Progress Report. *Advanced Functional*

Materials **2019**, *1903609*, 1903609. https://doi.org/10.1002/adfm.201903609.

(21) Iakab, S. A.; Rafols, P.; García-Altares, M.; Yanes, O.; Correig, X. Silicon-Based Laser Desorption Ionization Mass Spectrometry for the Analysis of Biomolecules: A Progress Report. *Advanced Functional Materials* **2019**, *29* (45), 1–18. https://doi.org/10.1002/adfm.201903609.

(22) Dufresne, M.; Thomas, A.; Breault-Turcot, J.; Masson, J.-F.; Chaurand, P. Silver-Assisted Laser Desorption Ionization For High Spatial Resolution Imaging Mass Spectrometry of Olefins from Thin Tissue Sections. *Analytical Chemistry* **2013**, *85* (6), 3318–3324. https://doi.org/10.1021/ac3037415.

(23) Dufresne, M.; Masson, J.-F. F.; Chaurand, P. Sodium-Doped Gold-Assisted Laser Desorption Ionization for Enhanced Imaging Mass Spectrometry of Triacylglycerols from Thin Tissue Sections. *Analytical Chemistry* **2016**, *88* (11), 6018–6025. https://doi.org/10.1021/acs.analchem.6b01141.

(24) Rafols, P.; Vilalta, D.; Brezmes, J.; Cañellas, N.; del Castillo, E.; Yanes, O.; Ramírez, N.; Correig, X. Signal Preprocessing, Multivariate Analysis and Software Tools for MA(LDI)-TOF Mass Spectrometry Imaging for Biological Applications. *Mass Spectrometry Reviews* **2018**, No. 37, 281–306. https://doi.org/10.1002/mas.

(25) Northen, T. R.; Yanes, O.; Northen, M. T.; Marrinucci, D.; Uritboonthai, W.; Apon, J.; Golledge, S. L.; Nordström, A.; Siuzdak, G. Clathrate Nanostructures for Mass Spectrometry. *Nature* **2007**, *449* (7165), 1033–1036. https://doi.org/10.1038/nature06195.

(26) Iakab, S. A.; Ràfols, P.; Tajes, M.; Correig-Blanchar, X.; García-Altares, M. Gold Nanoparticle-Assisted Black Silicon Substrates for Mass Spectrometry Imaging Applications. *ACS Nano* **2020**, *14* (6), 6785–6794. https://doi.org/10.1021/acsnano.0c00201.

(27) Masyuko, R.; Lanni, E. J.; Sweedler, J. v.; Bohn, P. W. Correlated Imaging-a Grand Challenge in Chemical Analysis. *Analyst* **2013**, *138* (7), 1924–1939. https://doi.org/10.1039/c3an36416j.

(28) Lasch, P.; Noda, I. Two-Dimensional Correlation Spectroscopy for Multimodal Analysis of FT-IR, Raman, and MALDI-TOF MS Hyperspectral Images with Hamster Brain Tissue. *Analytical Chemistry* **2017**, *89* (9), 5008–5016. https://doi.org/10.1021/acs.analchem.7b00332.

(29) Ryabchykov, O.; Popp, J.; Bocklitz, T. Fusion of MALDI Spectrometric Imaging and Raman Spectroscopic Data for the Analysis of Biological Samples. *Frontiers in Chemistry* **2018**, *6* (JUL), 1–10. https://doi.org/10.3389/fchem.2018.00257.

(30) Bocklitz, T.; Bräutigam, K.; Urbanek, A.; Hoffmann, F.; von Eggeling, F.; Ernst, G.; Schmitt, M.; Schubert, U.; Guntinas-Lichius, O.; Popp, J. Novel Workflow for Combining Raman Spectroscopy and MALDI-MSI for Tissue Based Studies. *Analytical and bioanalytical chemistry* **2015**, *407* (26), 7865–7873. https://doi.org/10.1007/s00216-015-8987-5.

(31) Alessandri, I.; Vassalini, I.; Bertuzzi, M.; Bontempi, N.; Memo, M.; Gianoncelli, A. "RaMassays": Synergistic Enhancement of Plasmon-Free Raman Scattering and Mass Spectrometry for Multimodal Analysis of Small Molecules. *Scientific Reports* **2016**, *6* (September), 1–8. https://doi.org/10.1038/srep34521.

(32) Lasch, P. Spectral Pre-Processing for Biomedical Vibrational Spectroscopy and Microspectroscopic Imaging. *Chemometrics and Intelligent Laboratory Systems* **2012**, *117*, 100–114. https://doi.org/10.1016/j.chemolab.2012.03.011.

(33) Lafuente, M.; Pellejero, I.; Sebastián, V.; Urbiztondo, M. A.; Mallada, R.; Pina, M. P.; Santamaría, J. Highly Sensitive SERS Quantification of Organophosphorous Chemical Warfare Agents: A Major Step towards the Real Time Sensing in the Gas Phase. *Sensors and Actuators, B: Chemical* **2018**, *267*, 457–466. https://doi.org/10.1016/j.snb.2018.04.058.

(34) Gu, G. H.; Suh, J. S. Silver Nanorods Used to Promote SERS as a Quantitative Analytical Tool. *Journal of Raman Spectroscopy* **2010**, *41* (6), 624–627. https://doi.org/10.1002/jrs.2487.

(35) Lafuente, M.; Pellejero, I.; Clemente, A.; Urbiztondo, M. A.; Mallada, R.; Reinoso, S.; Pina, M. P.; Gandía, L. M. In Situ Synthesis of SERS-Active Au@POM Nanostructures in a Microfluidic Device for Real-Time Detection of Water Pollutants. *ACS Applied Materials and Interfaces* **2020**, *12* (32), 36458–36467. https://doi.org/10.1021/acsami.0c06725.

(36) Race, A. M.; Sutton, D.; Hamm, G.; Maglennon, G.; Morton, J. P.; Strittmatter, N.; Campbell, A.; Sansom, O. J.; Wang, Y.; Barry, S. T.; Takáts, Z.; Goodwin, R. J. A.; Bunch, J. Deep Learning-Based Annotation Transfer between Molecular Imaging Modalities: An Automated Workflow for Multimodal Data Integration. *Analytical Chemistry* **2021**. https://doi.org/10.1021/acs.analchem.0c02726.

(37) Chen, X.; Gasecka, P.; Formanek, F.; Galey, J. B.; Rigneault, H. In Vivo Single Human Sweat Gland Activity Monitoring Using Coherent Anti-Stokes Raman Scattering and Two-Photon Excited Autofluorescence

Microscopy. *British Journal of Dermatology* **2016**, *174* (4), 803–812. https://doi.org/10.1111/bjd.14292.

(38) Liu, X.; Lu, L.; Li, Z.; Song, W.; Lu, Y.; Mao, Z.; Zhao, B. Detection of Protein Deposition within Latent Fingerprints by Surface-Enhanced Raman Spectroscopy Imaging. *Nanoscale* **2012**, *4* (7), 2333. https://doi.org/10.1039/c2nr12030e.

(39) Cennamo, G.; Montorio, D.; Morra, V. B.; Criscuolo, C.; Lanzillo, R.; Salvatore, E.; Camerlingo, C.; Lisitskiy, M.; Delfino, I.; Portaccio, M.; Lepore, M. Surface-Enhanced Raman Spectroscopy of Tears: Toward a Diagnostic Tool for Neurodegenerative Disease Identification. *Journal of Biomedical Optics* **2020**, *25* (08), 1. https://doi.org/10.1117/1.jbo.25.8.087002.

(40) Dorakumbura, B. N.; Boseley, R. E.; Becker, T.; Martin, D. E.; Richter, A.; Tobin, M. J.; van Bronswjik, W.; Vongsvivut, J.; Hackett, M. J.; Lewis, S. W. Revealing the Spatial Distribution of Chemical Species within Latent Fingermarks Using Vibrational Spectroscopy. *Analyst* **2018**, *143* (17), 4027–4039. https://doi.org/10.1039/c7an01615h.

(41) Girod, A.; Ramotowski, R.; Weyermann, C. Composition of Fingermark Residue: A Qualitative and Quantitative Review. *Forensic Science International* **2012**, *223* (1–3), 10–24. https://doi.org/10.1016/j.forsciint.2012.05.018.

(42) Scherrer, N. C.; Stefan, Z.; Francoise, D.; Annette, F.; Renate, K. Synthetic Organic Pigments of the 20th and 21st Century Relevant to Artist's Paints: Raman Spectra Reference Collection. *Spectrochimica Acta - Part A: Molecular and Biomolecular Spectroscopy* **2009**, *73* (3), 505–524. https://doi.org/10.1016/j.saa.2008.11.029.

(43) Iakab, S. A.; Sementé, L.; García-Altares, M.; Correig, X.; Ràfols, P. Raman2imzML Converts Raman Imaging Data into the Standard Mass Spectrometry Imaging Format. *BMC Bioinformatics* **2020**, *21* (1). https://doi.org/10.1186/s12859-020-03789-8.

(44) Rafols, P.; Heijs, B.; del Castillo, E.; Yanes, O.; McDonnell, L. A.; Brezmes, J.; Pérez-Taboada, I.; Vallejo, M.; García-Altares, M.; Correig, X. RMSIproc: An R Package for Mass Spectrometry Imaging Data Processing. *Bioinformatics* **2020**, *36* (11), 3618–3619. https://doi.org/10.1093/bioinformatics/btaa142.

(45) Modat, M.; Cash, D. M.; Daga, P.; Winston, G. P.; Duncan, J. S.; Ourselin, S. Global Image Registration Using a Symmetric Block-Matching Approach. *Journal of Medical Imaging* **2014**, *1* (2), 024003. https://doi.org/10.1117/1.jmi.1.2.024003.

4.2.8. Supporting Information

Table S1. Comparison between standard SERS and SALDI imaging and our approach to multimodal imaging on AuBSi substrate.

Technique/ Aspect	SERS	SALDI	Multimodal imaging on AuBSi
Substrate	Low fluorescence CaF_2 substrate	ITO-covered glass slide	AuBSi multimodal substrate
Sample Preparation	● Tissue mounted on CaF_2 substrate + nanoparticle deposition; ● Tissue incubated with nanostructured material	● Tissue mounted on ITO-covered glass slide + nanoparticle deposition; ● Tissue mounted on nanostructured substrate	Tissue mounted on AuBSi substrate followed by tissue removal for molecular transfer

Spatial Resolution	<1µm	>20µm	Both
Spectrum Quality	low	high	Multimodal data
Sensitivity	low	high	Multimodal data
Specificity	medium	high	Multimodal data
Acquisition Time	Medium to long: Parameter and instrument dependent	Long: Parameter and instrument dependent	Depends on acquisition technique/method
Data Format	Instrument specific formats; Exported .txt files	imzML	imzML*
Data Processing	Baseline Correction Cosmic Ray Removal Smoothing Normalization	Alignment Smoothing Peak Picking Normalization	All
Type of Experiment	Targeted Analysis (not metabolomics)	Targeted Untargeted Analysis	All
Chemical Information	Functional Groups Chemical Bonds Molecular Conformation	Molecular Weight (and ion fragmentation patterns) Isotopic Patterns Adduct Formation	All

*SERS imaging data is converted into imzML using Raman2imzML converter

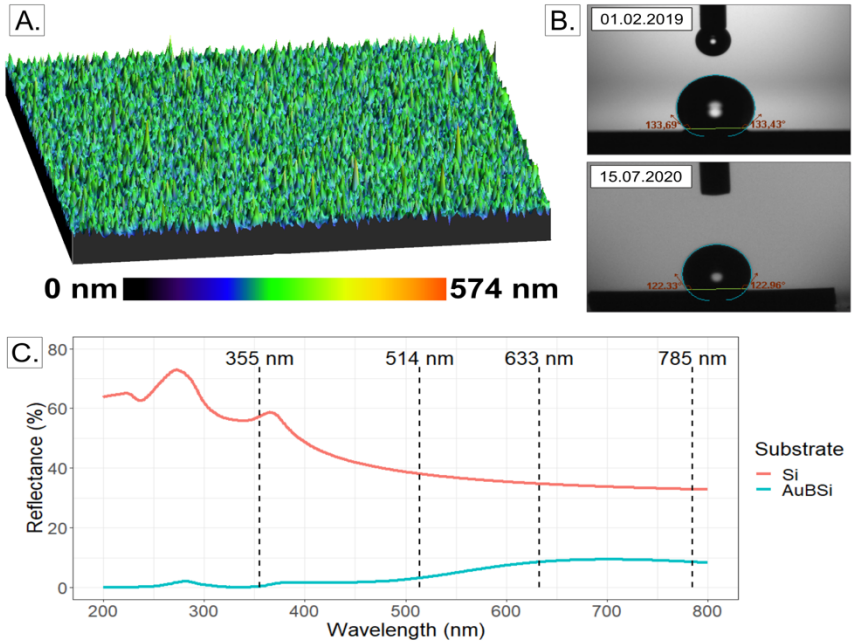

Figure S1. AuBSi surface properties. AFM roughness map of the AuBSi surface (A); Contact angle measurements with water on the AuBSi over a period of 17 months (B) and Reflectance measurements comparing normal Si wafer and AuBSi behaviour when interacting with the lasers used in MSI (355 nm) and Raman (514 nm, 633 nm, 785 nm) measurements (C).

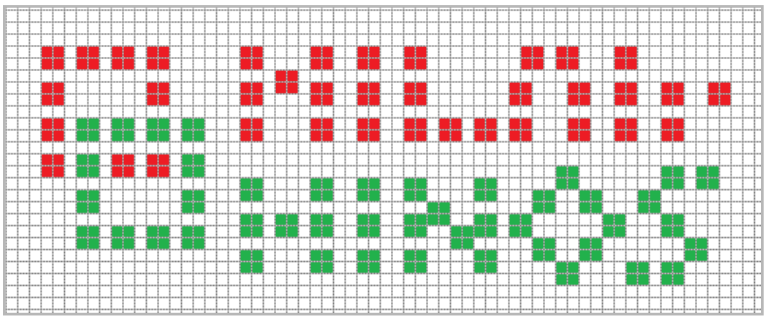

Figure S2. Inkjet printer drawing sheet. Two overlapping squares and the names of two research groups from the department where the research was carried out. The ink used for the red spots contains rhodamine 6G and the one used for the green spots contains malachite green. Printing method can be found in the methods section in the main manuscript.

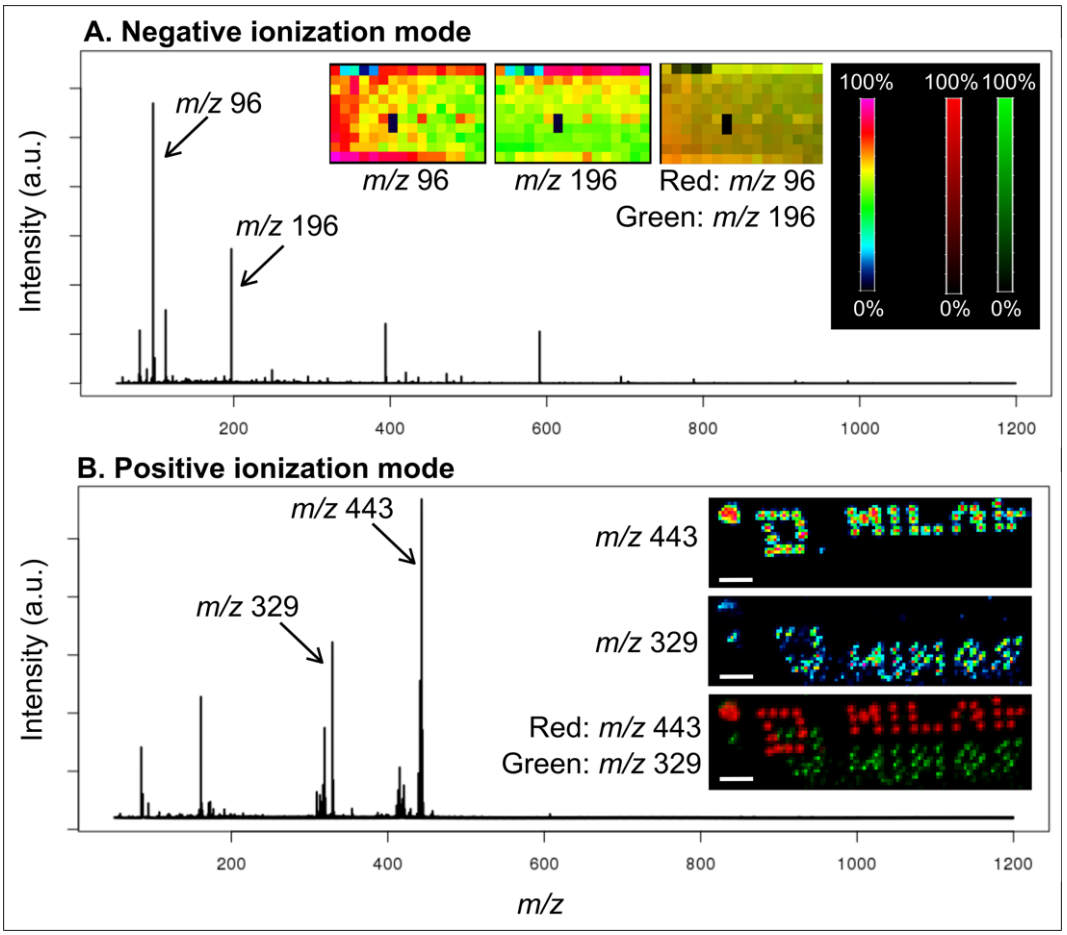

Figure S3. Negative and positive ionization modes on AuBSi. (A) Average spectra and ion intensity distribution images of the first two most intense peaks: *m/z* 96 from background and *m/z* 196 from Au^- ions in negative ionization mode; scale bar is 300 µm. (B) Average spectra and ion images (30 µm lateral resolution) of rhodamine 6G (in red, *m/z* 443.29) and malachite green (in green, *m/z* 329.22) ions detected as $[M+H-2H_2O]^+$ adducts, printed on the AuBSi substrate as the acronyms of two research groups (MILAB and MINOS - represented in Figure S2) from our department; scale bar is 300 µm.

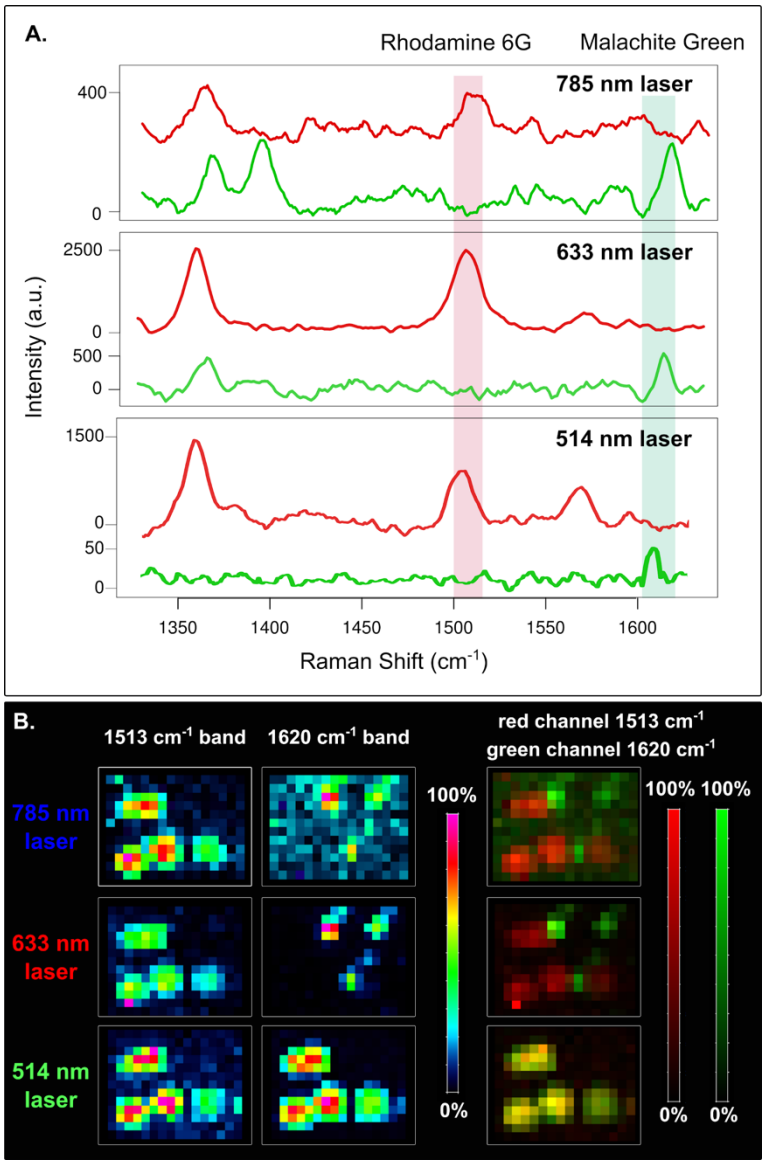

Figure S4. (A) Single pixel spectra from the rhodamine 6G droplet (in red) and from the malachite green droplet (in green) with three lasers: 514 nm, 633 nm and 785 nm wavelength; bands specific to Rhodamine 6G (1513 cm^{-1}) and malachite green (1620 cm^{-1}) are highlighted with transparent red and green, respectively. (B) Raman images collected with the three lasers: individual and two channel representation of the distribution of the two bands 1513 cm^{-1} and 1620 cm^{-1} and for each laser.

Calculating the analytical enhancement factor (AEF):

The AEF quantifies the increase of signal intensity compared to normal Raman spectroscopy under specific experimental conditions and is calculated using the following equation:

$$\mathrm{AEF} = \frac{I_{\mathrm{SERS}}/(t_{\mathrm{SERS}} \times P_{\mathrm{SERS}} \times C_{\mathrm{SERS}})}{I_{\mathrm{Raman}}/(t_{\mathrm{Raman}} \times P_{\mathrm{Raman}} \times C_{\mathrm{Raman}})}$$

where C_{Raman} and C_{SERS} are the R6G concentration in the Raman (1 mM) and SERS (1 μM) measurement conditions, respectively and I_{Raman} and I_{SERS} are the intensity values of the R6G characteristic band at 1510 cm−1, for the normal Raman and SERS measurements, respectively.[1] Similarly, P_{Raman} and t_{Raman} and P_{SERS} and t_{SERS} refer to the laser power and acquisition time values for the normal Raman and SERS measurements, respectively. In our case, laser power and exposure time were the same, but the normal Raman R6G spectrum was measured immersing a bare silicon wafer in 10^{-3} M R6G solution and the AuBSi substrate in 10^{-5} M R6G solution for 1 h then rinsed with distilled water by dipping 3 times to remove excess molecules not adhered to the surface. Thus, I_{SERS} is the intensity of the R6G molecules that remain adsorbed on the SERS substrate and I_{Raman} is the intensity of the R6G molecules adsorbed on the bare Si. Based on this calculation approach, the AuBSi substrate has an AEF of $2.3 \cdot 10^5$ when compared to BSi and $5.4 \cdot 10^5$ when compared to Si. Similarly, when using the most intense band from malachite green for the calculation, the AEF of AuBSi is $7.5 \cdot 10^3$ when compared to Si and $2.3 \cdot 10^3$ when compared to BSi.

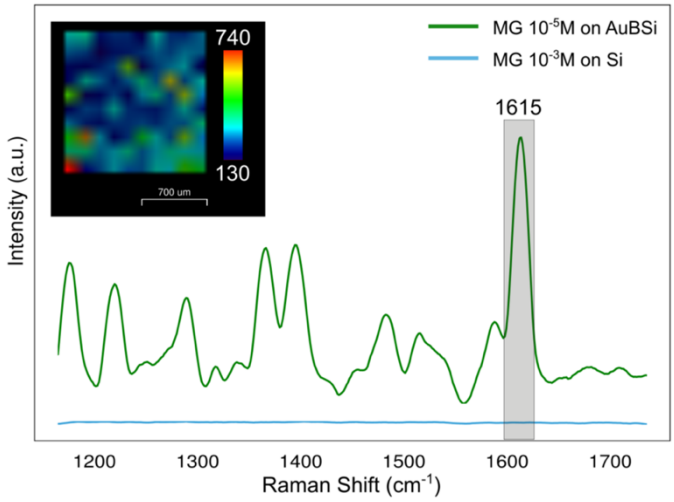

Figure S5. Malachite green average spectra of 100 pixels (over a 1.5 x 1.5 mm² area with 150 µm resolution) collected from AuBSi and from Si (silicon wafer) at different concentrations 10^{-5} M for AuBSi and 10^{-3}M for Si. The band at 1615 cm^{-1} is used for representing the spatial distribution of the 10^{-5} M MG concentration measured on the AuBSi substrate and for calculating the analytical enhancement factor.

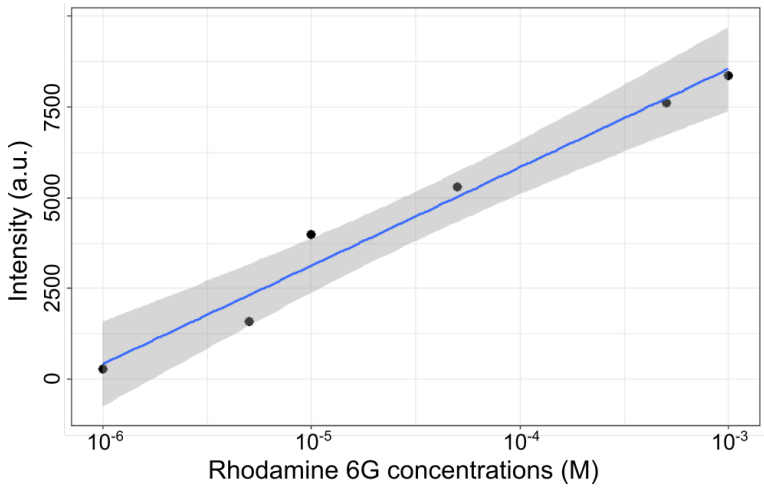

Figure S6. Substrate linearity. Regression line obtained from the average intensity of the 1513 cm^{-1} band from different R6G concentrations.

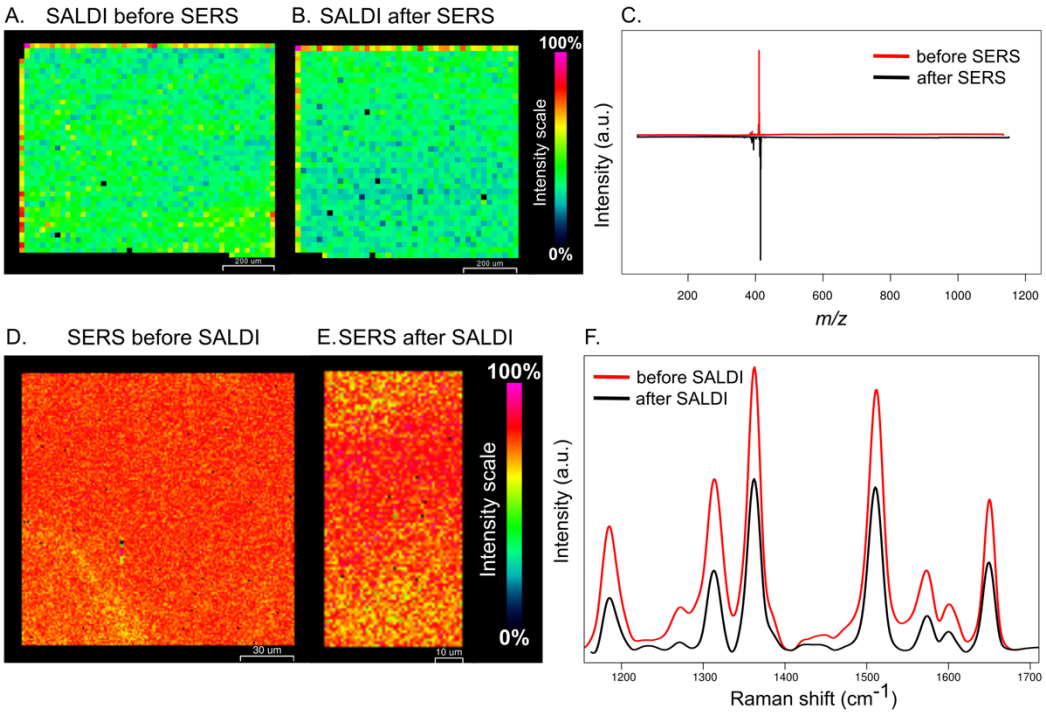

Figure S7. Imaging acquisition order assessment. All maps were acquired at 20 microns lateral resolution.

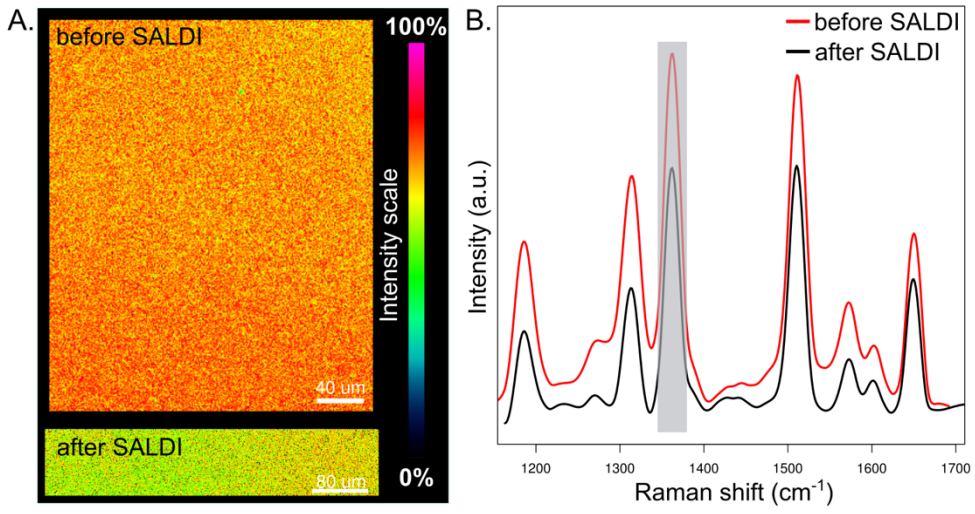

Figure S8. Imaging acquisition order assessment for high resolution (2 microns) SERS maps.

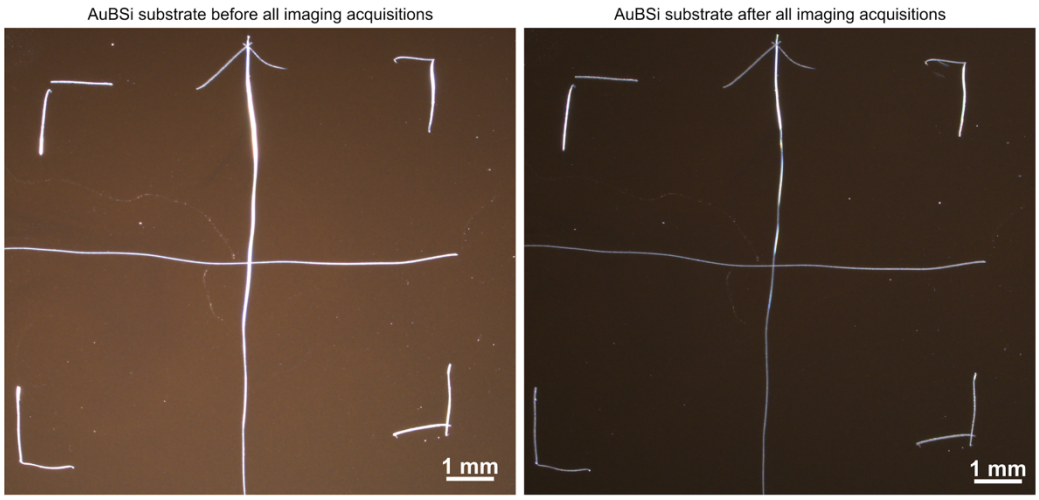

Figure S9. Optical images of the AuBSi substrate before and after imaging acquisitions. The substrate was removed from the Rhodamine 6G solution, dipped 3 times in milli-Q water and then dried at room temperature for 30 minutes.

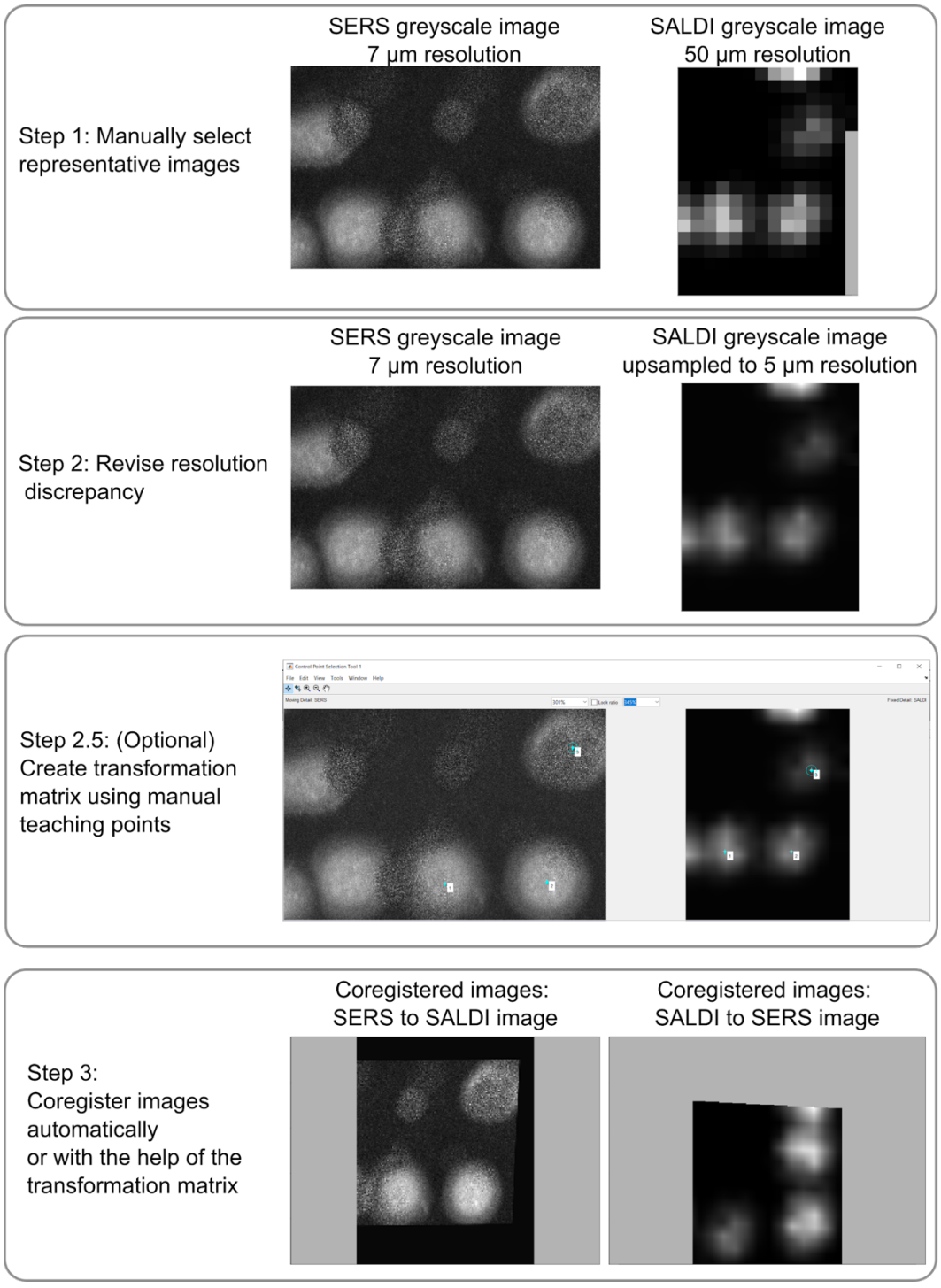

Figure S10. Coregistration algorithm steps, illustrated with the images from the inkjet-printed Raman reporters.

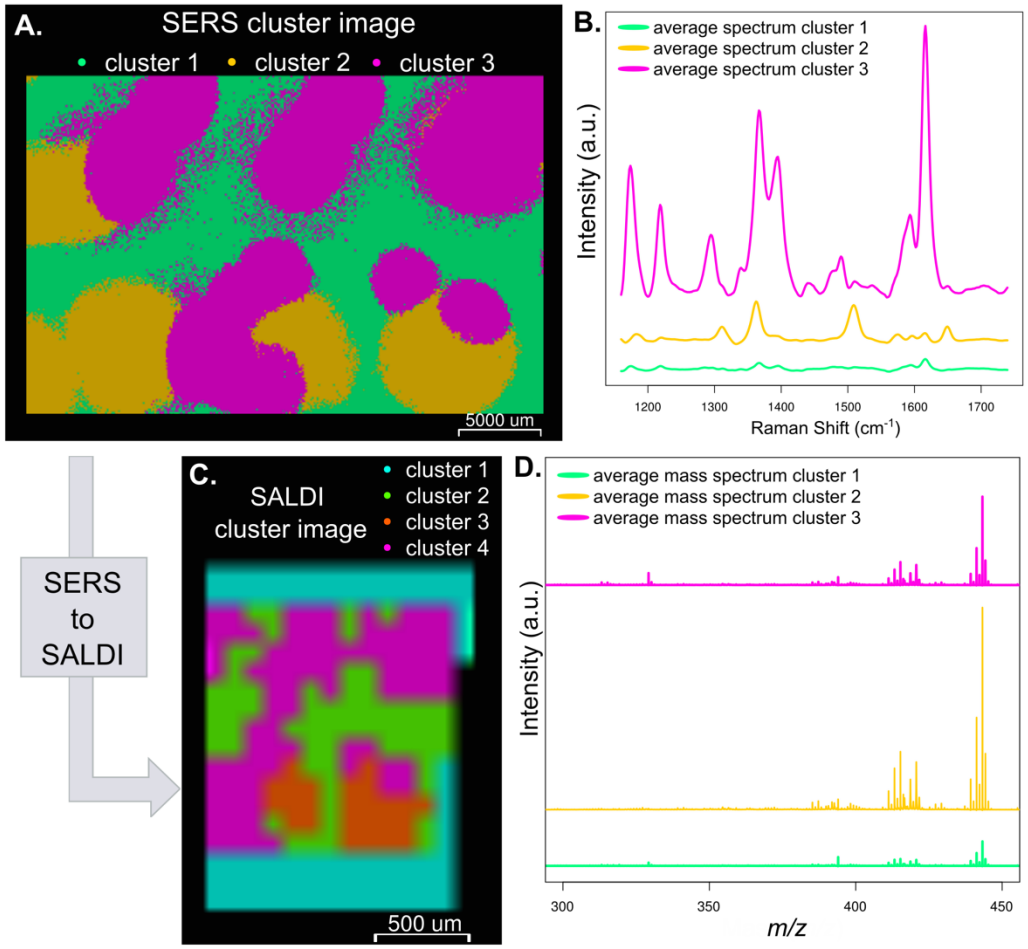

Figure S11. Data analysis strategy 1: SERS-to-SALDI. SERS k-means clusters (A) are transformed into the SALDI image (C) using the image coregistration transformation. Spectral features of the average spectrum of each cluster of the SERS (B) can be recognized as *m/z* information in the corresponding SALDI clusters (D).

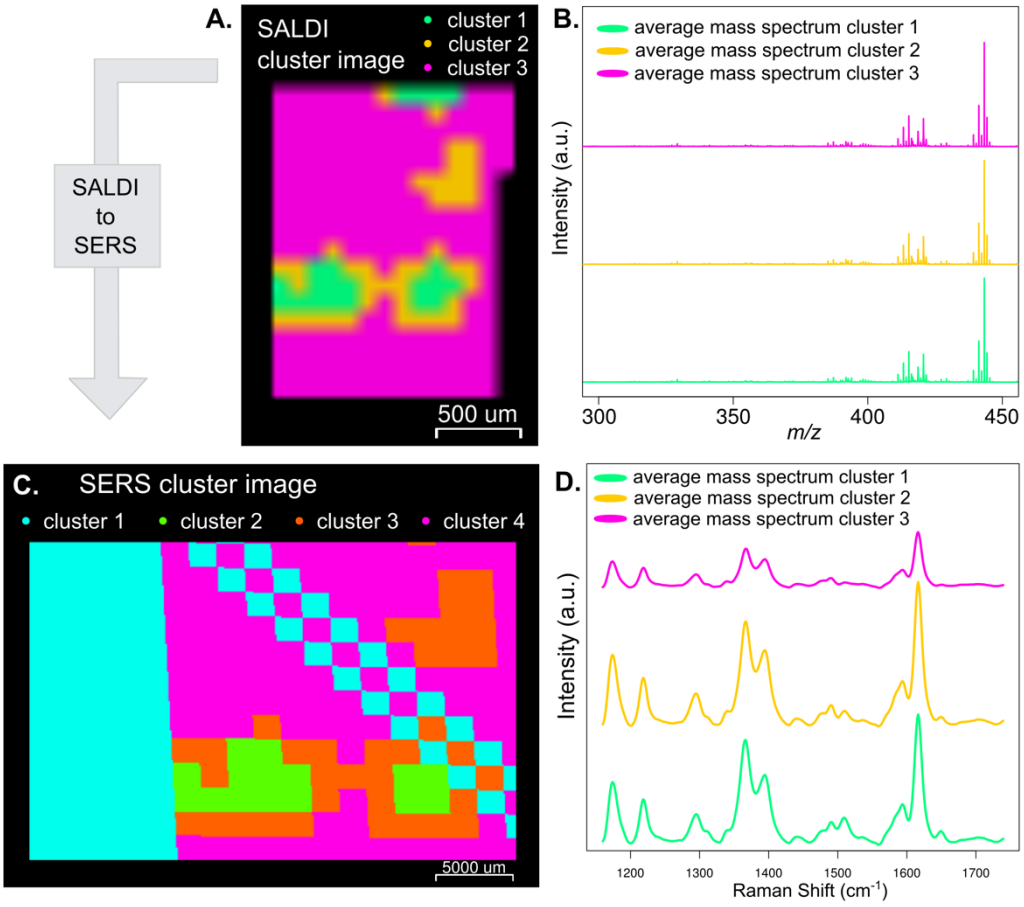

Figure S12. Data analysis strategy 2: SALDI-to-SERS. SALDI k-means clusters (A) are transformed into the SERS image (C) using the image coregistration transformation. *m/z* features of the clusters cannot be distinguished, and the transformed SERS clusters (B) reflect this.

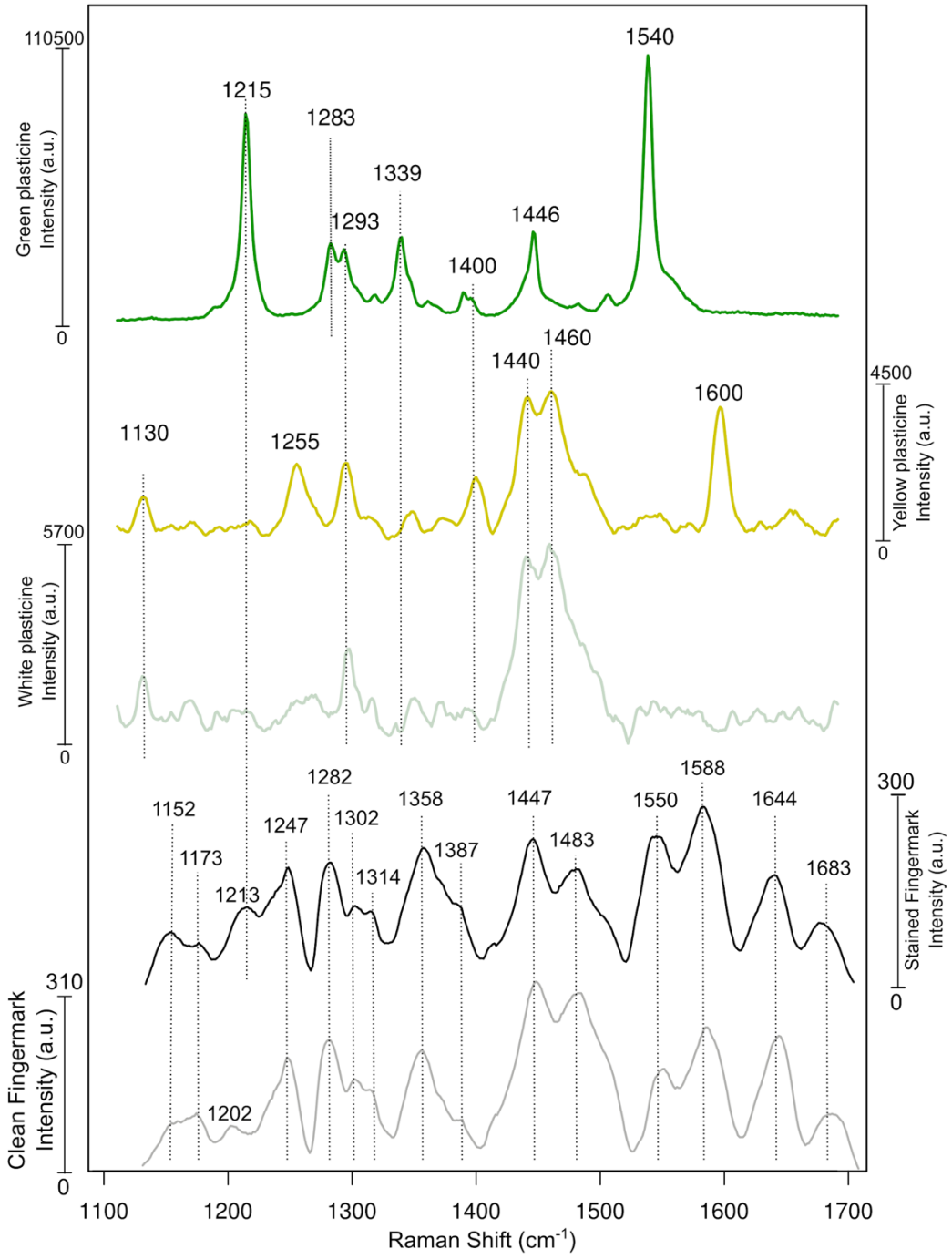

Figure S13. Raman reference spectra collected from white, yellow and green plasticine and average spectra for clean and stained fingermark.

Table S2. Raman band tentative assignments

Band (cm^{-1})	Vibration	Assignment	Predominant in	Ref.
1152	C-C stretching	carotenoids	both	2
1173	C-C stretching	aliphatic carbon chains	both	3
1202	ring breathing	tyrosine	clean	2
1213	C-C6H5 stretching	tyrosine and phenylalanine	stained	4
1215	ring C-C stretching	Pigment Green 7 (PG7), Cu-Phthalocyanine	green plasticine	5
1247	β-sheet	Amide III (LF, LZ)	both	6
1282	amide III, CH2 wagging	glycine, proline	both	7
1302	twisting CH2, dCH3, dCH2	lipids, aliphatic carbon chains	both	2,3
1314		collagen, lipids; or guanine	both	4
1358	C-H deformation; CH2 def	Trp, LF, LZ; Guanine/tryptophan; aliphatic carbon chains	both	3,6,7
1387	CH3 band	squalene?	stained	2,4
1447	δ(CH2/CH3)	lipids	both	2
1483	ring breathing	G, A (ring breathing modes in the DNA bases)	both	4
1540	C-N_m-C stretching vibration	Pigment Green 7 (PG7), Cu-Phthalocyanine	green plasticine	5
1551	indole ring vibration	tryptophan	both	2
1587	aromatic ring vibrations, C=C	amino acids: Phe, Tyr, Trp	both	8
1646	amide I	Alpha-helix proteins	both	3,6
1683	Amide I	disordered structure, non hydrogen bonded	both	4

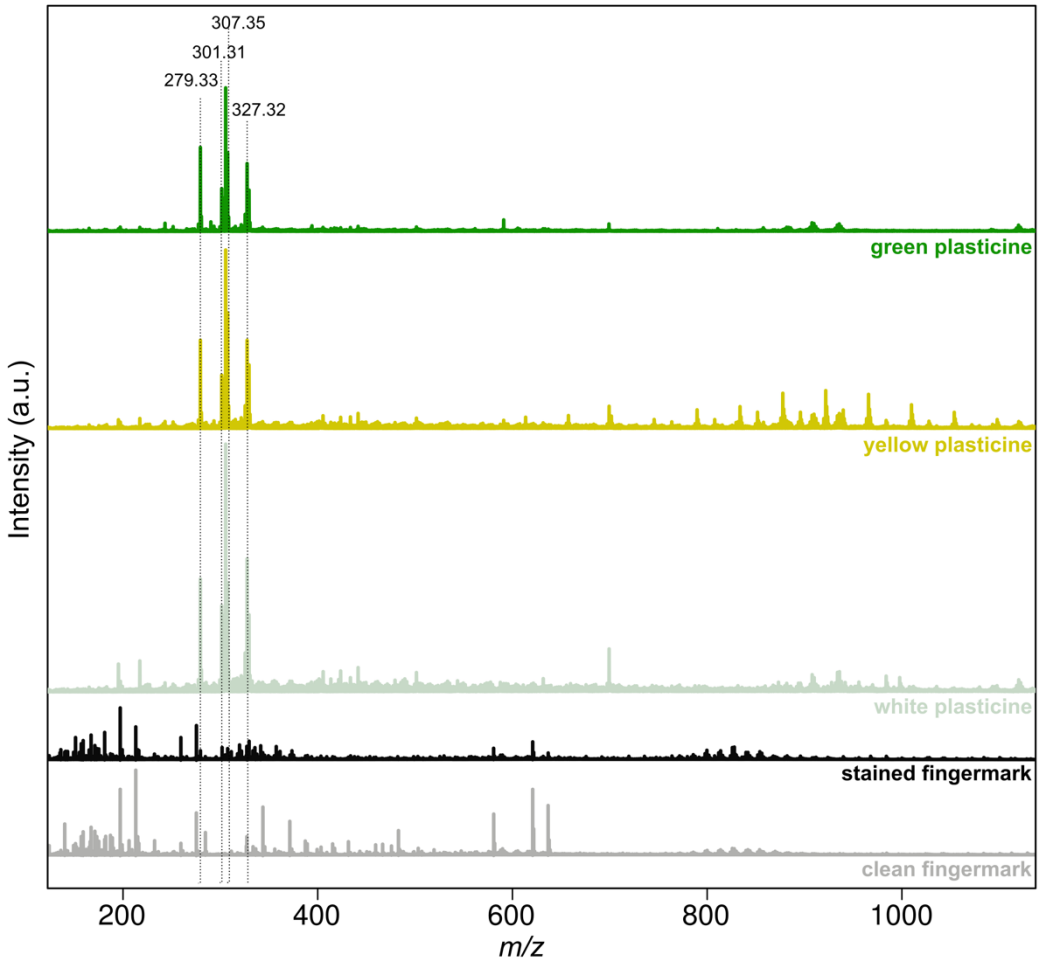

Figure S14. Average spectra of clean (in grey) and stained (in black) fingermarks and reference spectra of white, yellow and green plasticine (in light grey, yellow and green). *m/z* features specific to plasticine are marked with a dashed line.

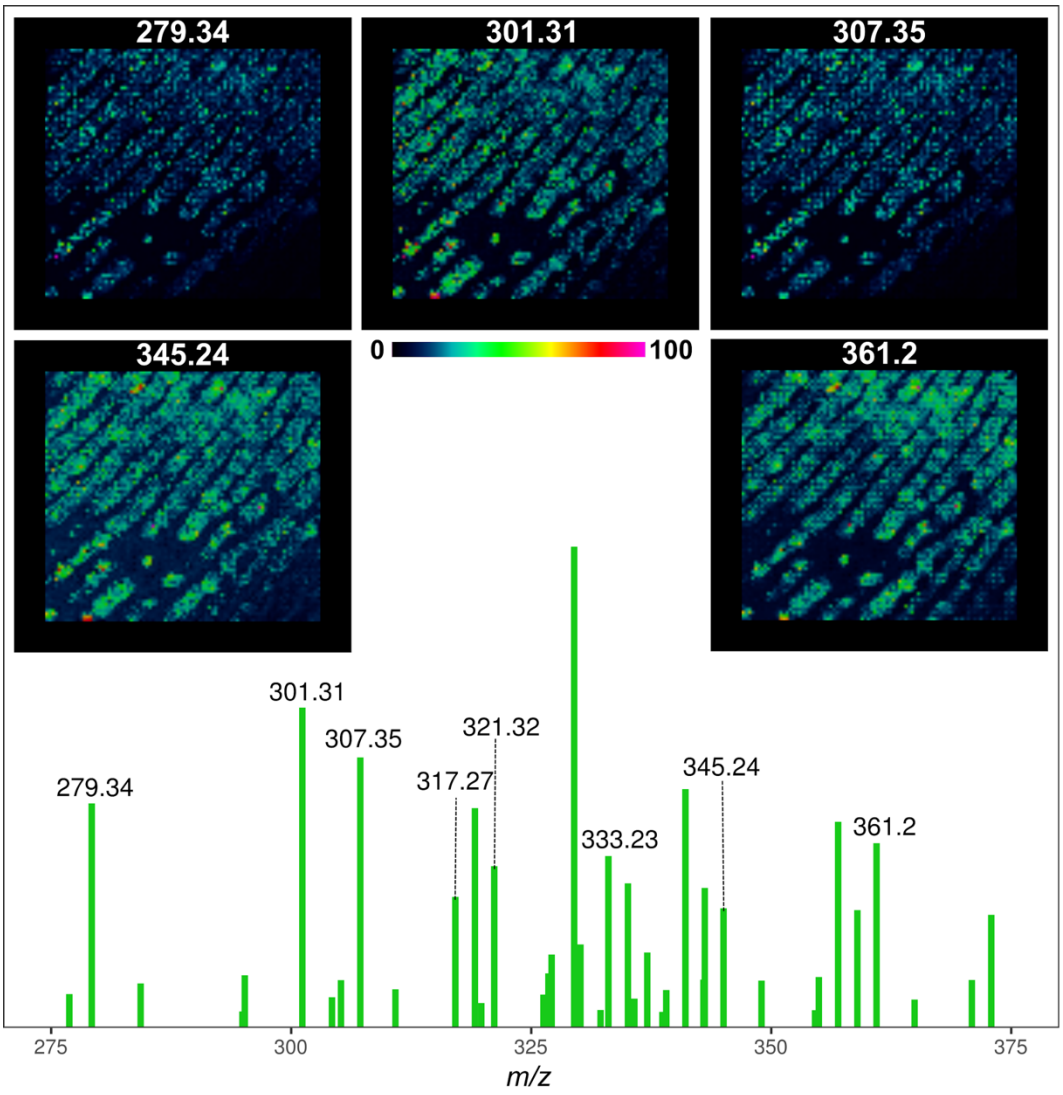

Figure S15. Average spectra of SERS-to-SALDI-MS cluster 1 in the range *m/z* 275-375; Labelled ions appear only in this cluster, which was associated with signal from the stain. The *m/z* images illustrate the distribution of the most intense stain-associated ions.

4.2.9. Supporting Information References

(1) Lafuente, M.; Pellejero, I.; Clemente, A.; Urbiztondo, M. A.; Mallada, R.; Reinoso, S.; Pina, M. P.; Gandía, L. M. In Situ Synthesis of SERS-Active Au@POM Nanostructures in a Microfluidic Device for Real-Time Detection of Water Pollutants. *ACS Appl. Mater. Interfaces* **2020**, *12* (32), 36458–36467. https://doi.org/10.1021/acsami.0c06725.

(2) Andersson, P. O.; Lejon, C.; Mikaelsson, T.; Landström, L. Towards Fingermark Dating: A Raman Spectroscopy Proof-of-Concept Study. *ChemistryOpen* **2017**, *6* (6), 706–709. https://doi.org/10.1002/open.201700129.

(3) Dorakumbura, B. N.; Boseley, R. E.; Becker, T.; Martin, D. E.; Richter, A.; Tobin, M. J.; Van Bronswjik, W.; Vongsvivut, J.; Hackett, M. J.; Lewis, S. W. Revealing the Spatial Distribution of Chemical Species within Latent Fingermarks Using Vibrational Spectroscopy. *Analyst* **2018**, *143* (17), 4027–4039. https://doi.org/10.1039/c7an01615h.

(4) Movasaghi, Z.; Rehman, S.; Rehman, I. U. Raman Spectroscopy of Biological Tissues. *Appl. Spectrosc. Rev.* **2007**, *42* (5), 493–541. https://doi.org/10.1080/05704920701551530.

(5) Scherrer, N. C.; Stefan, Z.; Francoise, D.; Annette, F.; Renate, K. Synthetic Organic Pigments of the 20th and 21st Century Relevant to Artist's Paints: Raman Spectra Reference Collection. *Spectrochim. Acta - Part A Mol. Biomol. Spectrosc.* **2009**, *73* (3), 505–524. https://doi.org/10.1016/j.saa.2008.11.029.

(6) Cennamo, G.; Montorio, D.; Morra, V. B.; Criscuolo, C.; Lanzillo, R.; Salvatore, E.; Camerlingo, C.; Lisitskiy, M.; Delfino, I.; Portaccio, M.; Lepore, M. Surface-Enhanced Raman Spectroscopy of Tears: Toward a Diagnostic

Tool for Neurodegenerative Disease Identification. *J. Biomed. Opt.* **2020**, *25* (08), 1. https://doi.org/10.1117/1.jbo.25.8.087002.

(7) Kolhatkar, G.; Parisien, C.; Ruediger, A.; Muehlethaler, C. Latent Fingermark Imaging by Single-Metal Deposition of Gold Nanoparticles and Surface Enhanced Raman Spectroscopy. *Front. Chem.* **2019**, *7* (JUN), 1–8. https://doi.org/10.3389/fchem.2019.00440.

(8) Liu, X.; Lu, L.; Li, Z.; Song, W.; Lu, Y.; Mao, Z.; Zhao, B. Detection of Protein Deposition within Latent Fingerprints by Surface-Enhanced Raman Spectroscopy Imaging. *Nanoscale* **2012**, *4* (7), 2333. https://doi.org/10.1039/c2nr12030e.

UNIVERSITAT ROVIRA I VIRGILI
GOLD-COATED BLACK SILICON NANOSTRUCTURED SURFACES FOR SERS AND SALDI-MS MULTIMODAL IMAGING OF BIOLOGICAL APPLICATIONS
Stefania-Alexandra Iakab

CHAPTER 5: Discussion, Conclusions and Perspectives

UNIVERSITAT ROVIRA I VIRGILI
GOLD-COATED BLACK SILICON NANOSTRUCTURED SURFACES FOR SERS AND SALDI-MS MULTIMODAL IMAGING OF BIOLOGICAL APPLICATIONS
Stefania-Alexandra Iakab

5.1. Discussion

Objective 1: To design, fabricate and characterize a nanostructured substrate based on black silicon and gold nanoparticles compatible with both SALDI-MS and SERS imaging of biological samples¶

The results from this thesis have demonstrated in Chapters 3 and 4 that nanostructured surfaces based on silicon and gold are excellent candidates for SALDI-MS and SERS imaging. The AuBSi substrate created in this thesis can be considered the evolution of DIOS[1] and NIMS[2] substrates. All three approaches use the physicochemical properties of nanostructured silicon surfaces for enhancing the ionization of molecules for MSI applications. However, the AuBSi overcomes the limitations of the DIOS and NIMS substrates: it is stable under vacuum and over long periods of time while stored in normal conditions; does not cause interferences or clutter in the collected signal; it is more sensitive; it is easier and safer to manufacture; and it allows reproducible results. Additionally, AuBSi incorporates gold nanoparticles for promoting desorption/ionization and the signal from the Au ion can be used for spectral calibration, which is important for long acquisition times where changes in the ionization source or detector can result in shifted spectra.[3] Furthermore, dry fabrication guarantees a homogeneous, contaminant free and reliable nanostructure on the surface of the substrate, otherwise difficult or impossible to achieve through wet methods (such as surface functionalization with AuNP).

Objective 2: To obtain SALDI-MS images of biological samples using the nanostructured substrate and to implement data processing methods

Nanostructured solid-state substrates with homogeneous surfaces are advantageous for MSI applications because: the MS signal can be collected in both positive and negative ionization modes; the signal is clean, with low-to-

no background signal, less fragmentation and no analyte-substrate adduct formation; and the analytes are not delocalized nor detected from hot spots that interfere with high-resolution imaging applications. The need for nanostructured substrates in MSI is reflected by the appearance of several commercial substrates such as the DIOS chip, patented by Dr. Gary Siuzdak from Mass Consortium Corporation (San Diego, CA, USA),[4] the NALDI target (based on Si nanowires), which was available for a limited time from Bruker,[5] and lately DIUTHAME[a] from Hamamatsu, which offers substrates in various shapes and sizes. The AuBSi could be a strong competitor on the market due to its versatility (it can be functionalized with both dry and wet methods), stability over time, mechanical robustness, sensitivity and overall user-friendly operation.

Objective 3: To collect optimal SERS images using the nanostructured substrate and to implement data analysis methods

SERS imaging also requires nanostructured solid-state substrates with homogeneous surfaces because current SERS approaches are difficult to control and cannot be used for untargeted analysis. Therefore, SERS substrates for imaging should enhance the Raman signal uniformly all over the substrate, with no hot spots which interfere with high-resolution imaging, should generate reproducible results, be easy to handle and store, be compatible with a variety of samples and offer opportunities for surface modifications (if necessary). Available commercial substrates focus only on measuring liquid samples. For example, the substrate from SERSitive,[b] the

[a] https://www.hamamatsu.com/sp/etd/mktg-LP/201807_diuthame_en/index-en.html
[b] https://sersitive.eu

SERS substrate J12853 from Hamamatsu[c] and the SERS substrates based on Ag, Au and Cu from HORIBA[d] are designed for spotting droplets onto their surface and are not stable in air. Milewska et al.[6] demonstrated that gold-based nanostructured substrates are compatible with imaging fixed cells cultured directly on the substrate. Therefore, AuBSi offers the possibility to monitor biological samples *in situ* and perhaps *in vivo* by real-time measurements on different types of cultures grown on the substrate's surface (*e.g.* cells, bacteria, fungi).

On the side of data processing, SERS (or Raman) imaging is lacking a unified data format. Instrument manufacturers use different types of file formats compatible only with their proprietary software. The only option to access the SERS imaging data is to export these files in .txt format. Chapter 4.1 demonstrated that for easy data visualization and processing, Raman text files can be converted into imzML, the MSI standard format. So, the imzML format is capable of bringing together two fundamentally different molecular imaging techniques, by allowing their image analysis on the same platform/software. This is an opportunity for the imaging community (optical, molecular and nuclear imaging) to consider merging all the image processing knowledge from each separate technique into one all-powerful universal image processing tool.

Objective 4: To develop a multimodal imaging workflow

Multimodal imaging based on nanostructured materials is not a popular approach, because the nanostructure properties and the sample preparation

[c] https://www.hamamatsu.com/jp/en/product/type/J12853/index.html
[d] https://www.horiba.com/en_en/products/detail/action/show/Product/sers-substrates-1635/

are difficult to control and compatibilize for each modality.[7] Therefore, it is paramount to implement a nanostructured material that acts as a sample holder and also promotes detection of molecules, regardless of the imaging mechanism. The AuBSi substrate presented in this thesis succeeds in both SERS and SALDI-MS imaging, with some minor challenges, but sample preparation is simple, reproducible and compatible with both imaging modalities. Also, an accessible substrate could pave the way for translational research: routine experiments with SERS can be translated into new methods with SALDI-MS, and *vice versa*. For example, SERS and Raman spectroscopy are quantitative analytical tools rapidly advancing in clinical diagnostics,[8] but applied in a multimodal approach, they could accelerate the use of SALDI-MS in clinical research.

Using the same sample holder is also beneficial for the data analysis part: it's surface can be marked with unique marker points which facilitate image coregistration. Image coregistration enables linking two fundamentally different spectra through their location in space. This enables multiple approaches to univariate and multivariate image analysis, such as image sharpening, out-of-sample prediction, spectral enrichment, data fusion, etc.[9,10] Thus, a rich multimodal dataset will be indispensable for uncovering features unnoticeable with a single technique.

Limitations of the AuBSi substrate

The use of AuBSi for both modalities simplifies the sample preparation and allows measuring intact molecules from both solid and liquid samples. However, there are still some challenges (for both SALDI and SERS): (1) liquid deposition is difficult and (2) tissue imprinting has to be optimized for each type of sample.

(1) Reproducible droplet deposition is difficult to obtain on a surface with no modifications (special geometry or chemical functionalization) but it is necessary for reliable measurements. The research in this thesis is focused on the imaging opportunities that the AuBSi substrate offers, but it also includes measurements from liquid standards (in Chapters 3 and 4), as *in situ* analysis is not always necessary. Investigating urine, saliva, sweat, blood and even breath does not require spatial information, but does often require multiple analytical techniques for accurate diagnosis and even biomarker identification.[11,12] In chapter 3 we modified physically and chemically the AuBSi substrate surface for measuring standard solutions by creating hydrophilic wells surrounded by hydrophobic walls. This approach could be adapted and improved for creating micron-scaled wells which need very low amounts of sample, in an accessible geometry for automatic measurements, similar to microarrays,[13] biochips[14] and biosensors,[15] which offer reliable and reproducible results for all kinds of biological samples.

(2) The ionizing and enhancing capabilities of the AuBSi are closely tied with the sample imprinting method. In the case of SALDI-MSI, the synergy between UV laser and nanostructure promotes the detection of molecules adhered to the substrate surface. So, the focal point of the laser has to be on the substrate surface. For example, tissue sections mounted on the NIMS substrate had to be ablated until the interface between tissue and nanostructured surface was uncovered for optimal measurements.[2] Our imprinting approach removes the excess material from the substrate by mounting the section and washing, which leaves only the adhered molecules on the nanostructured surface. But for SERS, this layer of molecules is still too thick and the AuNP cannot provide enough enhancement. The SERS effect happens only in the close vicinity of AuNPs, so imaging the great number of molecules from a tissue is difficult. As a matter of fact, AuNPs have

desirable surface properties which allow their functionalization with molecules such as SERS tags (Raman active molecules) or aptamers.[16,17] In fact, we demonstrated that the AuBSi can be functionalized with hydrophilic or hydrophobic plasma treatments, which enabled selective detection of molecules (*e.g.* polar and nonpolar lipid molecules from the hydrophobic-AuBSi from fingermarks). This strategy could be adapted for targeted imaging of biomolecules of interest.

5.2. Conclusions

Conclusion 1: AuBSi is an excellent nanostructured substrate compatible with both SALDI-MS and SERS imaging of biological samples

The first objective of the thesis has been achieved through the development of the AuBSi substrate. This novel nanostructured substrate is reproducible, user-friendly, cost effective, highly reliable and has a contaminant free surface with physicochemical properties which ensure optimal signal acquisition with SALDI-MS and SERS imaging of tissues, fingermarks and standard solutions.

Conclusion 2: AuBSi can be used to produce reliable SALDI-MS images without compound delocalization and offers the possibility of surface functionalization

The second objective was completed in Chapter 3 when the AuBSi substrate was used for imaging standard solutions, animal tissues (mouse liver, kidney and brain) and fingermarks. In this work we functionalized the AuBSi surface with hydrophilic and hydrophobic plasma treatment which promoted selective adhesion and ionization of molecules based on their hydrophobicity. SALDI imaging on AuBSi proved to be robust, user-friendly and versatile methods.

Conclusion 3: AuBSi can also be used to produce high-resolution SERS images, due to its highly homogeneous nanostructure.

Conclusion 4: Raman imaging data can be converted into imzML in a straightforward way.

The third objective was completed in Chapter 4 when the AuBSi demonstrated that its properties are also optimal for SERS imaging. We

mapped inks and fingermarks deposited on the AuBSi surface with high lateral resolution and reproducible signal. For data analysis we had to convert the SERS imaging data using our in-house developed converter, which proved to be easy to use. Therefore, SERS imaging on AuBSi is reliable and data conversion is possible and straightforward.

Conclusion 5: The compatibility of the AuBSi substrate with both SALDI-MS and SERS imaging promotes multimodal imaging on the same substrate and sample, supporting easy coregistration and data analysis.

The fourth, and last objective was accomplished in Chapter 4 where we proved that measuring the same sample prepared on the AuBSi substrate is possible with both SALDI-MS and SERS imaging. We demonstrated a simple approach for multimodal imaging using inks and fingermarks: 1) measuring the same sample is possible with both techniques, 2) image coregistration and multivariate analysis using the same software is convenient and straightforward, and 3) the versatility of AuBSi together with the customizable open-source software open a path to countless opportunities.

5.3. Perspectives

Universal sample substrate: AuBSi a possible solution

Solid state substrates based on gold and silicon nanostructures are promising, as they have all the necessary requirements for SALDI-MSI and SERS imaging of both solid and liquid samples. Because the fabrication processes of these substrates can be automated, are reliable, reproducible and safe, and because these types of substrates are compatible with multiple techniques, they are a potential candidate for the standardized multimodal substrate. Creating a standard coregistration protocol will make it possible to assign two qualitatively different spectra to the same area of a biological sample regardless of the imaging technique used. This will enable fast and accurate data collection over a variety of imaging modalities.

Universal data format for imaging: imzML a possible solution

Once imaging data has been collected, the acquisition software should make it possible to export the data in a universal format for imaging. Thus, each imaging dataset, regardless of the acquisition technique, can be straightforwardly visualized and analyzed using a single software package. This would facilitate tremendously the development of correlated data analysis algorithms and software which can bring relevant information buried within the multimodal datasets to light. The use of the imzML format for Raman imaging data makes it possible to visualize Raman and MALDI maps with the MSI software, which provides new opportunities for data analysis. Although the imzML format is missing the nomenclature for Raman measurements such as “Raman Shift” units or diffraction grating definitions (cm^{-1}), in the future it could adopt multiple ontology options which could be chosen during data export or conversion. The universal imaging file should have three components: (1) a metadata section that stores all acquisition

details such as laser parameters (wavelength, intensity or power, spot size), area specifications (pixel dimensions, step size), specific details of individual methods (integration time for Raman or shots per pixel for MALDI, *etc.*); (2) a coordinates section containing information about pixel position and (3) a data section with all the spectral information.

Software development for multimodal imaging data analysis

Current multimodal workflows collect and preprocess data sets separately and then visualize and analyze single or coregistered images either separately or with data fusion methods. Unfortunately, there is no straightforward way of doing all these data processing steps with the same software. Accessible, user-friendly software which require minimum input and compute sophisticated processes automatically (such as image coregistration and data fusion) are in high demand. For example, in clinical research, where large datasets are routine, users need fast, efficient and reliable tools. Therefore, developing such software for multimodal data analysis which includes MSI, VSI, optical microscopy images, fluorescence imaging and possibly MRI is forthcoming. Moreover, this software will not only help with the data processing in the multimodal imaging community, but also with the transition of unfamiliar imaging modalities into the clinic.

5.4. References

(1) Thomas, J. J.; Shen, Z.; Crowell, J. E.; Finn, M. G.; Siuzdak, G. Desorption/Ionization on Silicon (DIOS): A Diverse Mass Spectrometry Platform for Protein Characterization. *Proc. Natl. Acad. Sci. U. S. A.* **2001**, *98* (9), 4932–4937. https://doi.org/10.1073/pnas.081069298.

(2) Northen, T. R.; Yanes, O.; Northen, M. T.; Marrinucci, D.; Uritboonthai, W.; Apon, J.; Golledge, S. L.; Nordström, A.; Siuzdak, G. Clathrate Nanostructures for Mass Spectrometry. *Nature* **2007**, *449* (7165), 1033–1036. https://doi.org/10.1038/nature06195.

(3) Ràfols, P.; Vilalta, D.; Torres, S.; Calavia, R.; Heijs, B.; McDonnell, L. A.; Brezmes, J.; del Castillo, E.; Yanes, O.; Ramírez, N. I.; CorreigID, X. Assessing the Potential of Sputtered Gold Nanolayers in Mass Spectrometry Imaging for Metabolomics Applications. **2018**. https://doi.org/10.1371/journal.pone.0208908.

(4) Budimir, N.; Blais, J. C.; Fournier, F.; Tabet, J. C. The Use of Desorption/Ionization on Porous Silicon Mass Spectrometry for the Detection of Negative Ions for Fatty Acids. *Rapid Commun. Mass Spectrom.* **2006**, *20* (4), 680–684. https://doi.org/10.1002/rcm.2363.

(5) DANIELS, R.; DIKLER, S.; LI, E.; STACEY, C. Break Free of the Matrix: Sensitive and Rapid Analysis of Small Molecules Using Nanostructured Surfaces and LDI-TOF Mass Spectrometry. *J. Assoc. Lab. Autom.* **2008**, *13* (6), 314–321. https://doi.org/10.1016/j.jala.2008.07.005.

(6) Milewska, A.; Zivanovic, V.; Merk, V.; Arnalds, U. B.; Sigurjónsson, Ó. E.; Kneipp, J.; Leosson, K. Gold Nanoisland Substrates for SERS Characterization of Cultured Cells. *Biomed. Opt. Express* **2019**, *10* (12), 6172. https://doi.org/10.1364/boe.10.006172.

(7) Alessandri, I.; Vassalini, I.; Bertuzzi, M.; Bontempi, N.; Memo, M.; Gianoncelli, A. "RaMassays": Synergistic Enhancement of Plasmon-Free Raman Scattering and Mass Spectrometry for Multimodal Analysis of Small Molecules. *Sci. Rep.* **2016**, *6* (September), 1–8. https://doi.org/10.1038/srep34521.

(8) Henry, A. I.; Sharma, B.; Cardinal, M. F.; Kurouski, D.; Van Duyne, R. P. Surface-Enhanced Raman Spectroscopy Biosensing: In Vivo Diagnostics and Multimodal Imaging. *Anal. Chem.* **2016**, *88* (13), 6638–6647. https://doi.org/10.1021/acs.analchem.6b01597.

(9) Neumann, E. K.; Comi, T. J.; Spegazzini, N.; Mitchell, J. W.; Rubakhin, S. S.; Gillette, M. U.; Bhargava, R.; Sweedler, J. V. Multimodal Chemical Analysis of the Brain by High Mass Resolution Mass Spectrometry and Infrared Spectroscopic Imaging. *Anal. Chem.* **2018**, *90* (19), 11572–11580. https://doi.org/10.1021/acs.analchem.8b02913.

(10) Van De Plas, R.; Yang, J.; Spraggins, J.; Caprioli, R. M. Image Fusion of Mass Spectrometry and Microscopy: A Multimodality Paradigm for Molecular Tissue Mapping. *Nat. Methods* **2015**, *12* (4), 366–372. https://doi.org/10.1038/nmeth.3296.

(11) Bakry, R.; Rainer, M.; Huck, C. W.; Bonn, G. K. Analytica Chimica Acta Protein Profiling for Cancer Biomarker Discovery Using Matrix-Assisted Laser Desorption / Ionization Time-of-Flight Mass Spectrometry and Infrared Imaging : A Review. *Anal. Chim. Acta* **2011**, *690* (1), 26–34. https://doi.org/10.1016/j.aca.2011.01.044.

(12) Rüther, A.; Perez-guaita, D.; Heraud, P.; Stone, N.; Dudgeon, A.; Gardner, B.; Reddy, R.; Mayerich, D.; Bhargava, R. Care Medicine : A

Review. **2019**, *72*, 52–84. https://doi.org/10.1177/0003702818791939.Application.

(13) Jaluria, P.; Konstantopoulos, K.; Betenbaugh, M.; Shiloach, J. A Perspective on Microarrays: Current Applications, Pitfalls, and Potential Uses. *Microb. Cell Fact.* **2007**, *6*, 1–14. https://doi.org/10.1186/1475-2859-6-4.

(14) Stumpf, A.; Brandstetter, T.; Hübner, J.; Rühe, J. Hydrogel Based Protein Biochip for Parallel Detection of Biomarkers for Diagnosis of a Systemic Inflammatory Response Syndrome (SIRS) in Human Serum. *PLoS One* **2019**, *14* (12), 1–19. https://doi.org/10.1371/journal.pone.0225525.

(15) Baganizi, D. R.; Leroy, L.; Laplatine, L.; Fairley, S. J.; Heidmann, S.; Menad, S.; Livache, T.; Marche, P. N.; Roupioz, Y. A Simple Microfluidic Platform for Long-Term Analysis and Continuous Dual-Imaging Detection of T-Cell Secreted IFN-γ and IL-2 on Antibody-Based Biochip. *Biosensors* **2015**, *5* (4), 750–767. https://doi.org/10.3390/bios5040750.

(16) Chisanga, M.; Muhamadali, H.; Ellis, D.; Goodacre, R. Enhancing Disease Diagnosis: Biomedical Applications of Surface-Enhanced Raman Scattering. *Appl. Sci.* **2019**, *9* (6), 1163. https://doi.org/10.3390/app9061163.

(17) Verdin, A.; Malherbe, C.; Müller, W. H.; Bertrand, V.; Eppe, G. Multiplex Micro-SERS Imaging of Cancer-Related Markers in Cells and Tissues Using Poly(Allylamine)-Coated Au@Ag Nanoprobes. *Anal. Bioanal. Chem.* **2020**, *412* (28), 7739–7755. https://doi.org/10.1007/s00216-020-02927-8.

UNIVERSITAT ROVIRA I VIRGILI
GOLD-COATED BLACK SILICON NANOSTRUCTURED SURFACES FOR SERS AND SALDI-MS MULTIMODAL IMAGING OF BIOLOGICAL APPLICATIONS
Stefania-Alexandra Iakab